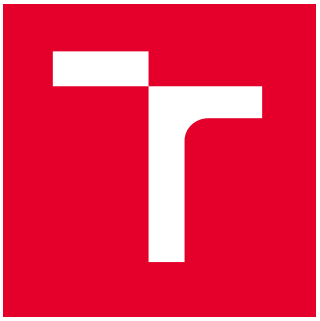


BRNO UNIVERSITY OF TECHNOLOGY

VYSOKÉ UČENÍ TECHNICKÉ V BRNĚ

FACULTY OF ELECTRICAL ENGINEERING AND COMMUNICATION

FAKULTA ELEKTROTECHNIKY
A KOMUNIKAČNÍCH TECHNOLOGIÍ

DEPARTMENT OF CONTROL AND INSTRUMENTATION

ÚSTAV AUTOMATIZACE A MĚŘICÍ TECHNIKY

CLOSED-LOOP PHASE MODULATION METHODS FOR INTERFEROMETRIC MEASUREMENT

METODY FÁZOVÉ MODULACE SE ZPĚTNOU VAZBOU PRO INTERFEROMETRICKÉ MĚŘENÍ

DOCTORAL THESIS
DIZERTAČNÍ PRÁCE

AUTHOR — **Ing. Michal Skalský**
AUTOR PRÁCE

SUPERVISOR — **Ing. Zdeněk Havránek, Ph.D.**
ŠKOLITEL

BRNO 2024

ABSTRACT

The thesis deals with the methods of phase modulation and closed-loop phase shift compensation for interferometric measurement. The interferometry belongs to the most advanced and accurate sensing principles, providing outstanding performance, especially for the measurement of mechanical quantities. In the two-beam interferometry, frequently addressed task concerns the transfer of the detected phase to the output signal through the nonlinear interference function with the elimination of the unwanted effect of other parasitic variables. Many of the related problems can be solved by the closed-loop phase shift compensation and appropriate signal processing methods, as successfully shown by this work. Two specific applications are herein explored, embodying the well-established utilizations of the interferometric measurement, on which novel types of closed-loop processing and compensation methods are demonstrated.

Firstly, an unconventional combination of an interferometric fiber-optic gyroscope and a simple piezoelectric modulator presents a use case where the proposed methods can notably increase the viability of this architecture, and thus constitute a high-performance angular velocity sensor with reasonable costs. The second application shows the method's employment in the thickness vibrations sensing through the double-beam Mach-Zehnder interferometer employing an electro-optical modulator, where not only the adoption of the proposed techniques ensures a superior performance, but also brings a capability of vibrations profile scanning. In both cases, the theoretical analysis is verified through the practical measurement setups implementation and testing.

In addition to the demonstration of the methods for the specific use cases, the work shows indisputable benefits of the closed-loop processing interferometric measurement, as many of the general problems of the interferometric sensors and the corresponding modulation methods are addressed as well. Therefore, the principles and conclusions presented herein could also apply to other quantities‘ sensors and measurement mechanisms relying on the phenomenon of light interference.

KEYWORDS

Phase modulation, interferometry, closed-loop measurement, sensors, fiber-optic gyroscope, vibrations measurement.

ABSTRAKT

Disertační práce se zabývá metodami fázové modulace a zpětnovazební fázové kompenzace v interferometrickém měření. Interferometrie se řadí k nejpokročilejším a nejpřesnějším principům detekce, poskytující vynikající parametry zejména pro měření mechanických veličin. Často řešenou problematikou dvousvazkových interferometrů je převod detekované fáze přes nelineární interferenční funkci na výstupní signál se současnou eliminací nežádoucích parazitních vlivů. Velkou část s tím spojených problémů lze úspěšně vyřešit pomocí kompenzace fázového posunu v uzavřené smyčce a vhodných metod zpracování signálu, jak úspěšně ukazuje tato práce. Jsou zkoumány dvě konkrétní aplikace, zahrnující zavedené využití interferometrického měření, na nichž jsou demonstrovány nové typy zpracování signálu se zavedenou zpětnou vazbou a metody kompenzace.
V prvním případě se jedná o netradiční kombinaci interferometrického optovláknového gyroskopu a jednoduchého piezoelektrického modulátoru, kde lze díky navrženým metodám zvýšit potenciál této architektury, a vytvořit tak snímač kombinující kvalitními parametry a relativně nízké výrobní náklady. Druhá aplikace demonstruje využití metod pro snímání tloušťkových vibrací pomocí dvousvazkového Machova-Zehnderova interferometru s elektrooptickým modulátorem, kde navržené techniky přináší nejen možnost velmi dobré měřicí parametry, ale také schopnost skenování profilů vibrací. V obou případech je pak teoretická analýza ověřena prostřednictvím praktických měření a testování.
Vedle demonstrace metod pro zmíněné případy, práce ukazuje obecné přínosy interferometrického měření se zpracováním se zpětnou vazbou, neboť se zabývá i mnoha obecnými problémy interferometrických snímačů a s nimi spojenými modulačními metodami. Prezentované mechanismy a postupy lze tak využít i v rámci jiných snímačů a měřicích principů, založené na fenoménu interference světla.

KLÍČOVÁ SLOVA

Fázová modulace, interferometrie, měření v uzavřené smyčce, snímače, optovláknový gyroskop, měření vibrací.

SKALSKÝ, Michal. *Closed-loop phase modulation methods for interferometric measurement*. Brno, 2024, 171 p. Doctoral thesis. Brno University of Technology, Faculty of Electrical Engineering and Communication, Department of Control and Instrumentation. Advised by Ing. Zdeněk Havránek, Ph.D.

DECLARATION

I declare that I have written the Doctoral Thesis titled "Closed-loop phase modulation methods for interferometric measurement" independently, under the guidance of the advisor and using exclusively the technical references and other sources of information cited in the thesis and listed in the comprehensive bibliography at the end of the thesis.

As the author I furthermore declare that, with respect to the creation of this Doctoral Thesis, I have not infringed any copyright or violated anyone's personal and/or ownership rights. In this context, I am fully aware of the consequences of breaking Regulation § 11 of the Copyright Act No. 121/2000 Coll. of the Czech Republic, as amended, and of any breach of rights related to intellectual property or introduced within amendments to relevant Acts such as the Intellectual Property Act or the Criminal Code, Act No. 40/2009 Coll., Section 2, Head VI, Part 4.

Brno ....

author's signature

ACKNOWLEDGEMENT

I would like to thank my supervisor, Ing. Zdeněk Havránek, Ph.D., for his guidance, encouragement, and particularly for providing me with the opportunity to participate in the research on this interesting topic.

I would also like to extend my gratitude to my colleagues and close collaborators, especially Jiří Fialka for his inspiration and support in measurement systems development, Ladislav Kopečný for his invaluable input in software development, and Jakub Hnidka, to whom I am very grateful not only for numerous consultations and assistance provided during the research but also for his careful reading and commenting on this work.

Special thanks go to my family for their support and patience during my studies and to my fiancée, Jana, for her encouragement in the thesis preparation.

The research presented here could not be conducted without the instrumentation and infrastructure of Central European Institute of Technology under the project CEITEC 2020 (LQ1601) and Centre for Research and Utilization of Renewable Energy under the project Energy for Sustainable Development (EN-PUR) (LO1210), both with financial support from the Ministry of Education, Youth and Sports of the Czech Republic under the National Sustainability Program; the infrastructure of RICAIP that has received funding from the European Union's Horizon 2020 research and innovation programme under grant agreement No. 857306 and from Ministry of Education, Youth and Sports under OP RDE grant agreement No. CZ.02.1.01/0.0/0.0/17043/0010085.

The support was further provided by the R&D projects, especially, the project NewControl: Integrated, Fail-Operational, Cognitive Perception, Planning and Control Systems for Highly Automated Vehicles, under grant agreement No. 826653/8A19006; publications support by the Internal science fund of Brno University of Technology under the grant No. FEKT-S-20-6205 "Research in Automation, Cybernetics and Artificial Intelligence within Industry 4.0"; and Brno Ph.D. Talent Scholarship funded by the Brno City Municipality.

Brno ....

author's signature

Contents

Introduction **15**

1 State of the art **19**
1.1 Laser Interferometry . . . 19
1.2 Detection techniques . . . 21
1.3 Phase modulation principles . . . 23
1.3.1 Electro-optical phase modulators . . . 23
1.3.2 Piezoelectric phase modulators . . . 24
1.3.3 Other principles of phase modulation . . . 25
1.4 Detection methods in fiber-optic gyroscopes . . . 25
1.4.1 Sagnac effect in the fiber-optic gyroscopes . . . 27
1.4.2 Open-loop detection methods . . . 28
1.4.3 Closed-loop detection methods . . . 34
1.5 Detection methods in vibrations measurement homodyne interferometers . . . 38
1.5.1 Interferometer arrangements for piezoelectric materials characterization . . . 39
1.5.2 Quadrature point closed-loop stabilization . . . 40
1.5.3 Phase modulation . . . 41

2 Aims and objectives **43**
2.1 Aims summary . . . 44

3 Closed-loop fiber optic gyroscope with piezoelectric modulator **45**
3.1 Closed-loop modulation methods . . . 46
3.1.1 Double-sine modulation . . . 46
3.1.2 Quadruple-sine modulation . . . 49
3.1.3 Modulation parasitic effects . . . 52
3.1.4 Modulation depth control . . . 54
3.1.5 Stabilization of the modulation signal parameters . . . 63
3.2 Test setup . . . 70
3.2.1 Optical setup . . . 71
3.2.2 Control unit and data processing . . . 74
3.3 Verification and results . . . 76
3.3.1 Closed-loop phase shift compensation . . . 76
3.3.2 Scale-factor stability control . . . 81

4 Scanning double-beam laser interferometer with closed-loop compensation and phase stabilization 88
4.1 Closed-loop modulation methods . . . 89
4.1.1 Quadrature point stabilization . . . 89
4.1.2 Sample vibrations closed-loop compensation . . . 91
4.1.3 Modulation gain detection . . . 93
4.2 Implementation . . . 95
4.2.1 Optical setup . . . 96
4.2.2 Control unit and data processing . . . 98
4.3 Verification and results . . . 101
4.3.1 Quadrature point stabilization . . . 101
4.3.2 Sample vibrations closed-loop compensation . . . 103

5 Conclusions and future perspectives 109

Bibliography 112

List of symbols, physical constants, and abbreviations 131

List of appendices 137

A Supplementary materials on the closed-loop IFOG prototypes 138
A.1 Optical setup development . . . 139
A.1.1 Superfluorescent fiber source . . . 139
A.1.2 Piezoelectric modulator . . . 141
A.1.3 Lyot depolarizer . . . 143
A.2 Mechanical assembly . . . 144
A.3 Electronics and control software development . . . 145
A.3.1 Hardware design . . . 145
A.3.2 Software design . . . 148
A.4 Supplementary measurement results . . . 150
A.4.1 Laboratory testing . . . 150
A.4.2 Practical testing . . . 153
A.4.3 Additional results . . . 154

B Supplementary materials on the closed-loop DBMZI setup 158
B.1 Optical setup development . . . 159
B.1.1 Sample clamping . . . 161
B.1.2 Probing beam focusing . . . 162
B.2 Electronics and control software development . . . 164
B.2.1 Hardware design . . . 164

B.2.2 Software design 166
B.3 Supplementary measurement results 168

List of Figures

1.1 Ideal response of the two-beam interferometer. 22
1.2 Closed-loop phase shift detection. 22
1.3 Path difference between the counterpropagating waves in the rotating system. 28
1.4 The minimal configuration of the IFOG satisfying the principle of reciprocity. 28
1.5 Square-wave biasing modulation scheme. 29
1.6 Sinusoidal biasing modulation scheme. 30
1.7 Analog and digital sawtooth compensation modulation scheme. . . . 34
1.8 Four-state biasing modulation scheme. 35
1.9 Schematic of the SBMI and the DBMZI. 39
3.1 Schematic of the IFOG testbench for the closed-loop modulation methods design. 45
3.2 Sinusoidal compensation modulation. 47
3.3 Simulated dependency of $\Delta\phi_s$ detection error caused by the non-zero length of sample acquisition for different modulation harmonic components combinations and a relative white noise level suppression. 50
3.4 Biasing and compensation modulation waveforms with the double-sine and the quadruple-sine modulation 51
3.5 Sample PEM radial displacement frequency spectrum and the harmonic components distribution for the quadruple-sine modulation scheme. 51
3.6 Components of closed-loop IFOG linear distortion approximation. . . 53
3.7 Closed-loop IFOG linearity error - comparison of experimental (P1) and simulated response including PEM linearity distortion model with separate effects of individual components. 53
3.8 Schematic of the compensation modulation depth control in the PEM-based closed-loop IFOG. 56
3.9 Residual phase shift detection error of the quadratic criterion error function with the linearity distortion model ($\gamma = 1$) and the original uncompensated absolute error. 57
3.10 Iterative procedure of the K_{PEM} estimation. 58
3.11 Parameters estimator employing the NNCLE method. 59
3.12 Phase shift detection error with the NNCLE correction method for different NN size and relative parasitic effects distortion levels γ. . . . 61
3.13 Phase shift detection error with the LSCFE correction method for different relative parasitic effects distortion levels γ. 61

3.14 Error function minimum $E\left(\hat{I}(k), I(k)\right)$ and the corresponding error of the modulation depth estimate $\Delta\hat{\Phi}_c$ in dependence on the γ coefficient level. 63
3.15 The intensity signal with the parasitic effects model and its model-based estimate. 64
3.16 Error functions for different $\Delta\phi_s$: $E_{\psi b}$ under the effect of ψ_{b1} and ψ_{b3}, $E_{\psi c}$ under the effect of ψ_{c1} and ψ_{c5}. 65
3.17 Compensation of the modulation components phase error. 66
3.18 Error functions for different $\Delta\phi_s$: E_{Gb} in dependency on δG_b, E_{Gc} in dependency on δG_c. 67
3.19 Compensation of the modulation components gain error. 68
3.20 The cross-coupling functions between the parameters errors and their estimated values. 68
3.21 Schematic of the PEM-based closed-loop IFOG signal processing with the compensation modulation depth control and modulation errors compensation. 69
3.22 The intensity signal with the parasitic effects model and its model-based estimate. 70
3.23 The optical architecture of the P1 and P2 IFOG testing prototypes. . 71
3.24 Designed WF-DPB SFS configuration with optimal cleave and fusion arc modified fiber end and pure angle cleave temperature gradient characteristics and the SFS mean wavelength temperature dependency for different fiber endings. 73
3.25 Layout of the P1b test setup. 75
3.26 Layout of the P1c test setup. 75
3.27 Layout of the P2 test setup. 76
3.28 Comparison of the designed closed-loop and the open-loop P1a setup response. 77
3.29 Relative change of the closed-loop and the open-loop IFOG (P1a) output with temperature. 78
3.30 The Allan deviation of the closed-loop and the open-loop IFOG operation for zero angular velocity and the angular velocity $\Omega_{ref} = 10\ ^\circ/\mathrm{s}$, with table encoder data as a reference. 80
3.31 The frequency transfer characteristics of the angular velocity measurement with the P1a IFOG setup and the designed closed-loop processing method. 81
3.32 Comparison of the direct closed-loop output and the LSCFE method output temperature dependency. 82

3.33 Allan deviation of the direct closed-loop output and the LSCFE method output, measured at different temperature profiles. 84
3.34 Comparison of the direct data, corrected data, and the estimated data in the time domain and as an Allan deviation for the temperature drop from 40 to 29 °C. 85
3.35 Comparison of the direct data, corrected data, and the estimated data in the time domain and as an Allan deviation for the temperature rise from -10 to 29 °C. 86
3.36 Comparison of the direct data, corrected data, and the estimated data in the time domain and as an Allan deviation for stabilized temperature at 27 °C. 86
4.1 Schematic of the DBMZI setup with a phase difference modulation by EOM. 89
4.2 Schematic of the quadrature point stabilization in the DBMZI. 90
4.3 Schematic of the sample-induced phase shift compensation. 92
4.4 The optical architecture of the DBMZI testing setup. 96
4.5 Layout of the DBMZI control and processing setup. 99
4.6 Comparison of the quadrature point phase drift when it is set to an optimal fixed $\Delta\phi_{stab}$ value and when it is stabilized by the closed-loop method. 102
4.7 Comparison of the relative drift of the sample vibrations compensation error signal for the case when the $\Delta\phi_{stab}$ is set to an optimal fixed value and when it is stabilized by the closed-loop method. . . . 103
4.8 Scanning of the thickness displacement of the PZT sample (cylinder, NCE41) demonstrating the reflectivity-induced error of the measured displacement determined from the open-loop demodulated output and through the closed-loop compensation method. 104
4.9 Scanning the thickness vibrations profile of the AlN film on a Si substrate. 104
4.10 The frequency response (thin AlN film) measured with the open-loop and the closed-loop method and the closed-loop method noise level. . 105
4.11 The frequency response (bulk PZT disc) measured with the closed-loop method within a low-frequency region. 106
4.12 Measured displacement with the driving voltage of the thin films and the PZT samples and the corresponding linearity error in absolute and relative scales. 107
A.1 The P1a and the uncovered P2 IFOG setups on the rotary table inside the temperature chamber. 138

A.2 Optimized SFS output spectrum and its mean wavelength temperature drift. . . . 140
A.3 Assembly and integration of the SFS in the P2 case. . . . 140
A.4 Impedance characteristics of the PZT tube actuator used for the PEM (at 20 °C). . . . 141
A.5 Impedance characteristics of the PZT tube actuator used for the PEM around the employed biasing and compensation modulation frequency components at different temperatures. . . . 142
A.6 Detail of the fiber winding on the PZT actuator. . . . 142
A.7 Detail of PM fiber segments (L_1, L_2) alignment during the Lyot depolarizer manufacturing. . . . 143
A.8 Exploded view of the P2 IFOG prototype case design structure. . . . 144
A.9 Stages of the optical components integration in the P2 IFOG prototype. 145
A.10 Schematic of the electronic module comprising the IU2 and CU2. . . . 146
A.11 Interface unit (IU2) board of the P2 and its major blocks. . . . 147
A.12 Block diagram of the methods implementation and functions distribution within the CU2. . . . 149
A.13 A PC application for the P2 IFOG software parameters configuration. 151
A.14 Laboratory verification of the IFOG P2 parameters – scale factor and corresponding linearity error. . . . 152
A.15 Laboratory verification of the IFOG P2 parameters – stability of the bias and the scale factor. . . . 152
A.16 Layout of the testbench for a practical verification of the IFOG P2 performance installed in a car. . . . 153
A.17 Comparison of the integrated angular position for the reference drive in CW and CCW direction. . . . 154
A.18 Comparison of the measured trajectories for the reference drive in CCW direction. . . . 155
A.19 An examination of the bias stability limitation posed by various light sources usage within the IFOG P2. . . . 156
A.20 An examination of the Shupe effect on the angular velocity error at rest induced by temperature sweep with a singlepole and a quadrupole windings. . . . 156
B.1 An overall DBMZI setup layout. . . . 158
B.2 DBMZI optical components layout. . . . 159
B.3 The frequency spectrum of the d_{33} coefficient at different clamping forces within the 1 MHz range, and a detail near the first resonance frequency (measured at sample center, quartz x-cut, $10 \times 11 \times 1$ mm, $U_s \in \langle 0.01; 0.5 \rangle$ V). . . . 161

B.4 Examples of custom-made sample holders with optimized clamping. . 162
B.5 Demonstration of the speckle noise effect on the resulting output data (PZT disc sample, 20 mm diameter, measured at $f_s = 20$ kHz). . . . 163
B.6 Demonstration of measurement with and without using a pinhole in case of a poorly reflective sample producing high speckle noise (PZT NCE40 disc sample, 20 mm diameter, measured at $f_s = 1$ kHz). . . . 163
B.7 Schematic of the Filter & Gain switch module. 165
B.8 Block diagram of the processes in the DBMZI control application. . . 166
B.9 A PC application for the DBMZI measurement control. 167
B.10 Scanning of the PZT disc thickness displacement profile in a radial direction in the original state and after a break along the longitudinal axis (NCE51 material, 50 mm diameter, 1 mm thickness). 169
B.11 Scanning of the PZT disc edge with an electrode wear, resulting in a thickness displacement fading (20 mm diameter, measured at $f_s =$ 20 kHz, $U_s = 0.5$ V). 169
B.12 Scanning of the PZT disc thickness displacement profile near the center (NCE51 material, 30 mm diameter, 2 mm thickness). 170
B.13 Scanning of the PZT disc thickness displacement profile in near lines along the radial axis (NCE51 material, 30 mm diameter, 2 mm thickness). 170

List of Tables

3.1 Comparison of the higher harmonics components of the biasing and compensation modulation. 50
4.1 Comparison of results measured with DBMZI to the reference results measured with the direct (quasistatic) and the frequency (resonance) method. 108
A.1 Overall IFOG prototypes dimensions 138
A.2 List of the P2 optical setup's components and their key parameters. . 139
A.3 IFOG P2 key measurement parameters. 153
B.1 Overall DBMZI optical setup dimensions. 159
B.2 List of the DBMZI optical components and their key parameters. . . 160
B.3 List of the DBMZI electronic components. 164

Introduction

Although light has illuminated our understanding of the world since ancient times, it took a considerable amount of time to uncover one of its most intriguing properties. When Robert Hook first observed the interference pattern in 1665, followed by the theoretical explanation published by Christiaan Huygens in his *Traité de la Lumière* in 1690, the wave theory of light was born. Later, in 1803, Thomas Young proved that light is a wave and demonstrated its key property: the ability to interfere. It brought a new perspective on how we can utilize light for measurement and thus study the surrounding world.

Significant progress in the field of interferometric measurement and sensors development came with the invention of the He-Ne laser in 1961. A further milestone was the emergence of semiconductor technology and optical fibers in the 1970s.

The research and development of fiber-optic technology were initially accelerated by the motivation to transfer the signal in telecommunications. Later, another utilization of the optical fiber started to arise, embodied by the fiber-optic sensors (FOS). Nowadays, there nearly does not exist a physical quantity we cannot measure with optical fibers.

In literature, we can encounter numerous advantages of the optical and the fiber-optic sensors, in general. The most cited ones include immunity to the electromagnetic interference, the possibility of contactless evaluation, and often featuring a unique performance, such as precision or speed [1, 2]. Deployment of the optical fibers has the potential to bring additional scalability, robustness, temperature and chemical resistivity, which is also connected to biological compatibility as well as dimensions and weight reduction [3, 4].

Optical sensing thus finds its application mainly in cases where the other principles cannot be used or their performance is limiting. These applications include movement and vibration sensing [1], distributed strain sensors [5], acoustic sensors such as hydrophones [6], inertial sensors including gyroscopes [7], electric current sensors [8], and many others [2, 9]. The importance of optical sensors in various disciplines is also supported by the fact that their global market value was estimated at around 2.3 Billion USD in 2022 [10], with a foreseen growth ranging from 11 % (till 2028) [11] to nearly 14 % (till 2030) [10].

From the metrology point of view, the optical sensor consists of the source, the optical trace, and the detector. The purpose of the optical source is to originate the carrier medium in the form of the light wave of desired parameters, which are determined by the source type. The light then passes through the optical path, where its exposition to the measured physical quantity affects some of its parameters. The parameters are mostly referred to as amplitude (intensity), wavelength, phase, or

polarization [3, 12], defining the corresponding types of optical sensors.

Nevertheless, most of the wave parameters cannot be measured directly. First, they need to be transferred to the intensity using an evaluation method, which is usually a part of the optical trace. These methods usually involve interferometry in the case of the phase and wavelength-sensitive sensors or polarimetry in the case of the polarization-sensitive sensors. Finally, the detector (photodiode, photomultiplier) converts the light intensity to the electrical signal, often requiring further processing.

Looking back at the leading metrology applications of the optical sensors, we can find that the evaluation principle adopted by the vast majority is interference. The reason is obvious – the light phase or wavelength is an extremely fine measurement tool, allowing the interferometric sensors to reach an exceptional sensitivity. The most innate to the interferometric sensors are the measurements of the mechanical quantities, such as displacement, strain, etc., directly affecting the light's phase or wavelength. In other cases, we need to exploit some physical phenomenon, such as the Sagnac effect (gyroscopes), the Faraday effect (current sensors), fiber gratings, thermal expansion, chemical reactions, the Raman or the Brillouin scattering, etc., to transduce the sensed quantity to a change of phase or frequency of the light wave [2, 7, 13, 14].

Although the fundamental evaluation principle of such sensors is still the interference, the setup of the optical path and the subsequent signal processing techniques may differ significantly based on the specific sensing task and approach. Along with the commercially successful designs of optical interferometric sensors, there is a vast amount of concepts that are still in the development stage, with new designs emerging incessantly.

This thesis centers around the examination of the measurement of the light wave phase shift induced by a mechanical movement. For these applications, four elemental interferometer structures can be distinguished: Sagnac, Michelson, Mach-Zehnder, and Fabry-Pérot [15]. While the individual structures are each mostly suitable for different applications, an ample amount of similarities in terms of the modulation or the signal processing techniques can be identified – especially considering the first three structures. This is mostly determined by the fact that these structures are based on the interference of two light beams, whereas the Fabry-Pérot interferometer utilizes a multiple-beam interference, requiring slightly different processing methods. We will further deal solely with the two-beam interferometers. In this case, usually, one beam is exposed to the measured physical quantity, and the other one acts as a reference. By combining them through interference, even a very small effect of the measured quantity can be distinguished. As an example, the interferometers are reported to achieve accuracy by about 4–5 orders higher compared to

conventional principles when measuring displacement [3].

Nevertheless, the immense sensing potential also brings in some drawbacks. The first problem lies in the high sensitivity to the surrounding parasitic effects, which can affect the light phase in the same manner as the measured quantity. Therefore, we need to find an effective tool or method to separate the desired signal from the unwanted component or, at the very least, to suppress it. Secondly, the interference is inherently a nonlinear function; thus, the detected output signal must be handled appropriately to obtain the measured quantity. To overcome these issues and also other problems discussed later, various modulation and closed-loop compensation methods have been adopted by the most advanced interferometric sensors and measurement systems [13, 16, 17].

Up to this point, the discussion regarding optical sensors has been of a general nature; while the problems, as well as the methods used in the two-beam interferometers, are similar in many aspects, the specific approach for an accurate signal detection must always be adapted to the specific application. The applications studied in this thesis are the fiber optic gyroscope and the thin film displacement vibrometer. Even though they embody the typical representatives of two distinct optical sensor groups – the fiber-optic sensors and the free-space optical sensors – many similarities are shared in terms of the detection methods employed and signal processing.

The fiber-optic gyroscopes (FOG) constitute probably the most widely spread application of the Sagnac interferometer. Due to their extreme accuracy, they have become the leading principle in measuring the angular velocity [18]. Consequently, FOGs became essential for inertial navigation within a broad spectrum of applications, ranging from space, the aviation industry, and marine vehicles to ground applications. As the use cases continually expand, new and new requirements on the FOG sensors are emerging, such as miniaturization and cost reduction [19, 20]. The motivation is thus to examine the possibilities of applying new modulation methods, which have the potential for cost-efficiency improvement of FOGs.

On the other hand, free-space laser interferometry is primarily beneficial for metrology applications, such as dimensional measurements and mechanical parts or material characterization [1, 21]. In this case, the target application is the measurement of the vibrations of the thin piezoelectric films. The need to characterize such materials arises from their vital role in MEMS devices, either serving as sensors or microactuators [22]. The most adopted interferometer arrangements for this application are based on the Mach-Zehnder or the Michelson interferometer [23]. Although this task might not appear directly related to the issues intertwined with the angular velocity measurement by FOGs, quite similar challenges regarding the phase modulation and compensation techniques can be identified. Compared to the goals

set for gyroscopes, the potential for the improvement of the vibrations measurement interferometer lies in the application of similar methods to target its major issues: the susceptibility to external noise and inherent parasitic effects.

For both use cases of the novel modulation methods, it is first necessary to examine the core principles of the interferometric sensors and to map the progress in the techniques and approaches explored to date (Chapter 1). After such insight, a clearer view of the research focus and its goals may be outlined (Chapter 2). Because the modulation and processing methods reflect distinct areas of performance improvement in either of the shown use cases, they are described separately for better clarity (Chapters 3 and 4). In both cases, the methods are successively introduced to reflect particular issues and then are discussed in a general manner. Afterward, the theoretical premises and findings are supported by the experimental results, accompanied by the detailed description and specification of the testbenches. The theoretical design and practical verification can subsequently provide a rigorous foundation to draw conclusions and evaluate the potential of the developed methods in general terms (Chapter 5).

1 State of the art

As already discussed, the range of physical quantities covered by the interferometric sensors is immense. Amongst them, we can quite often encounter multiple different approaches to sense the same phenomenon. Over time, new and new concepts are arising, while some of the past are still being developed and modified. Despite the diversity we can nowadays observe in the interferometric sensors field, they all have one common basis – the employment of the light wave summation, i.e., the interference.

Nevertheless, it is important to realize that the interference poses solely a physical phenomenon behind these sensors, and its evaluation and an exact transformation of the phase change to the measured optical power must be explored first to understand the basic principles and requirements of the two beam interferometers. Thereafter, the discussion will further turn towards the means of extracting the measured phase information from the acquired optical signal, with the aid of various modulation techniques and physical principles, providing a necessary background for their detailed study in the selected applications of the angular velocity (Sagnac interferometer) and vibrations measurement (Mach-Zehnder interferometer).

1.1 Laser Interferometry

The essentiality of the interferometric sensors is the wave property of light, which allows multiple beams to be combined and determine the resulting beam's properties. The light can thus be described as an electromagnetic wave. A spatially coherent monochromatic electromagnetic wave propagating in z direction, which vector $\mathbf{E}$ oscillates in xy plane, can be described as [24]:

$$\mathbf{E}(t,z) = \mathbf{E_0} \mathrm{e}^{j(kz-\omega t)}, \tag{1.1}$$

where $\mathbf{E_0}$ is the wave amplitude, k is the wave number, z represents the distance in the direction of propagation, ω stands for the light angular frequency, and t for time. In general, the amplitude can be expressed in the form of the Jones vector:

$$\mathbf{E_0} = \begin{bmatrix} E_{0x}\mathrm{e}^{j\phi_x} \\ E_{0y}\mathrm{e}^{j\phi_y} \end{bmatrix}, \tag{1.2}$$

which decomposes the electromagnetic field into two orthogonal components, the amplitudes E_{0x}, E_{0y} and phases ϕ_x,ϕ_y of which determine the input wave polarization.

The photodetected signal is proportional to the optical intensity, expressing the power influence of the electromagnetic wave [15]:

$$I = \frac{1}{2} n \epsilon_0 \mathrm{c} \left\langle \mathbf{E} \cdot \mathbf{E}^* \right\rangle, \tag{1.3}$$

where n represents the medium refractive index, c is the speed of light in vacuum, and ϵ_0 stands for vacuum permittivity. The brackets $\langle\rangle$ embody the time averaging, representing the integration property of the detector of the electromagnetic field.

Let us assume the interference of two waves with the same frequency, the fields of which are described as follows:

$$\mathbf{E_1}(t, z_1) = \mathbf{E_{01}} \mathrm{e}^{j(kz_1 - \omega t)}, \tag{1.4}$$

$$\mathbf{E_2}(t, z_2) = \mathbf{E_{02}} \mathrm{e}^{j(kz_2 - \omega t)}. \tag{1.5}$$

The sum of the individual interfering fields gives the resulting electric field:

$$\mathbf{E} = \mathbf{E_1} + \mathbf{E_2} \tag{1.6}$$

The intensity is then:

$$I = \frac{1}{2} n \epsilon_0 \mathrm{c} \left\langle (\mathbf{E_1} + \mathbf{E_2}) \cdot (\mathbf{E_1}^* + \mathbf{E_2}^*) \right\rangle. \tag{1.7}$$

In a general case, by combining Eqs. 1.1, 1.2, 1.3, the Eq. 1.7 can be rewritten as follows:

$$\begin{aligned} I = I_1 + I_2 + n\epsilon_0 \mathrm{c} \Big\{ & E_{0x1} E_{0x2} \cos\left[(\phi_{x1} - \phi_{x2}) + k(z_1 - z_2)\right] + \\ & + E_{0y1} E_{0y2} \cos\left[(\phi_{y1} - \phi_{y2}) + k(z_1 - z_2)\right] \Big\} \end{aligned} \tag{1.8}$$

In the case the waves originate from the same source, and assuming the polarization state is not affected, the Eq. 1.8 can be simplified to:

$$I = I_1 + I_2 + 2\sqrt{I_1 I_2} \cos\left[k(z_2 - z_1)\right]. \tag{1.9}$$

The path difference $\Delta z = z_2 - z_1$ can be then conveniently expressed by means of a phase difference $\Delta\phi = k\Delta z$. In the general case, the interference equation is thus written in the form:

$$I = I_n + I_i \cos(\Delta\phi), \tag{1.10}$$

where $I_i = 2\sqrt{I_1 I_2}$ denotes the interference and $I_n = I_1 + I_2$ stands for the non-interference intensity portion. A special case exists when the source beam is split equally, and the intensities are balanced, i.e., $I_1 = I_2 = I_0/2$, so that:

$$I = I_0 \left[1 + \cos\left(\Delta\phi\right)\right] \tag{1.11}$$

which is the most fundamental equation of the two-beam interferometry [16], valid for Sagnac, Michelson, and Mach-Zehnder interferometer structure.

As the phase difference $\Delta\phi$ is usually proportional to the physical quantity measured by the interferometric sensor, we can note the inconvenience in the dependency on the cosine function. The major disadvantages are the phase detection ambiguity

and also the insensitivity in the integer multiples of π. In specific cases, it is possible to benefit from the periodicity by counting the signal minima and maxima [25], which can be useful for the phase tracking, e.g., for large displacement measurement, but the accuracy is then limited to about few micrometers. However, in most cases, the phase change is evaluated within one period of the $I(\Delta\phi)$ dependency, where the output is unambiguous. Nevertheless, this delivers further complications, including nonlinearity and limited sensing range.

Another frequently discussed issue is the impact of the light source. The major light source parameters include intensity, wavelength, spectrum shape, and polarization. Limitations of their stability thus impact the interferometer's output signal and manifest as an additional noise of the phase or amplitude [3, 18, 26].

Furthermore, the high sensitivity of the interferometric sensors also entails susceptibility to parasitic effects. Their influence on the measured optical phase can even exceed the measured quantity. These effects and their overall impact are highly dependent on the specific interferometer structure and the measurement setup. In the case of the free-space interferometers, the most significant are the mechanical and acoustic vibrations, air flow, and temperature fluctuations, all impacting the paths elongation and the refractive index. In contrast, the fiber-optic interferometers are thus considered to be more robust; however, there exist a variety of other phenomena related to the guiding medium, such as scattering, loss, modes crosstalks, the Faraday and the Kerr effect, or the inhomogeneities caused by the temperature or bending [15, 24, 27].

The following section focuses on the commonly used approaches to overcome some of the above-outlined problems, namely the intensity signal undesired dependencies, and also its susceptibility to the ambient effects, both with emphasis on the target sensing applications.

1.2 Detection techniques

In general, the phase detection techniques adopted by the two-beam interferometers are divided into homodyne and heterodyne [13, 16]. In the case of the heterodyne techniques, the interfering beams differ in their optical frequency, causing beats in the resulting intensity signal. The beating frequency is equal to the beams' optical frequency difference Δf. This method is frequently adopted for the velocity measurement (e.g., vibrations) [28]. In this case, the movement of the measured object leads to the Doppler shift of the probing beam. The frequency shift is then proportional to the object's velocity. Another well-established utilization of the heterodyne principle is ring laser gyroscope (RLG), employing the Sagnac effect to

shift the counterpropagating laser beams in the active medium due to the angular velocity [29].

In the case of the homodyne techniques, on the other hand, the interfering beams have an equal frequency, yet they differ in the phase shift $\Delta\phi$. Considering that $\Delta\phi = 2\pi\Delta f t$, then $\frac{\partial\Delta\phi}{\partial t} = 2\pi\Delta f$. Hence, just as the heterodyne techniques are well suited for measuring velocity, the homodyne ones, on the other hand, naturally detect the displacement as far as the mechanical quantities are concerned. The simplified response of the homodyne interferometer, described by Eq. 1.11, is shown in Fig. 1.1. The previously discussed issue of the response ambiguity and sensitivity

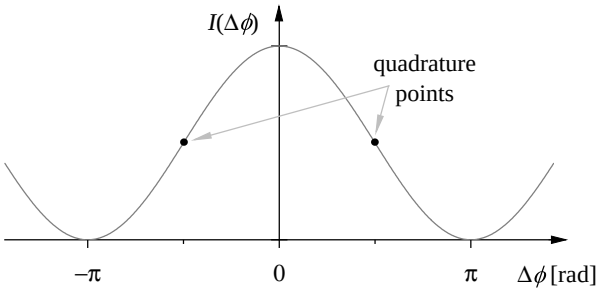


Fig. 1.1: Ideal response of the two-beam interferometer.

can be resolved by shifting the operating point to one of the derivative extremes. This can be performed by introducing a phase difference bias of $\frac{\pi}{2}(2K+1)$, where K is an integer. This point is referred to as quadrature [16]. Near these points, the response $I(\Delta\phi)$ can be regarded as linear, so for $|\Delta\phi| \ll \pi$, $I(\Delta\phi) \propto \Delta\phi$. To linearize the sensor output in a broader range and also to eliminate the dependency on the source intensity, a closed-loop method is commonly adopted (see Fig. 1.2). In this scenario, another phase shift $\Delta\phi_c$ is introduced, acting against the sensed phase shift $\Delta\phi_s$, so that their sum $\Delta\phi_{err}$ is equal to zero. The new sensor output is then the compensation phase shift $\Delta\phi_c = \Delta\phi_s$, assuming $\Delta\phi_{err} \to 0$. The compesation phase shift $\Delta\phi_c$ is thus referred to as a closed-loop signal, whereas the error $\Delta\phi_{err}$ is an open-loop signal [18].

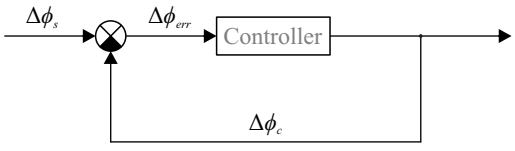


Fig. 1.2: Closed-loop phase shift detection: $\Delta\phi_s$ – phase shift induced by the measured quantity, $\Delta\phi_c$ – compensation phase shift (closed-loop signal), $\Delta\phi_{err}$ – error (open-loop signal).

One of the first implementations of the closed-loop compensation of the measured phase shift was reported in 1980 in the fiber-optic Mach-Zehnder interferometer [30], where the quadrature point was maintained via phase shifting in the reference branch. In that case, the deviation from the quadrature point was maintained by a simple comparison of the output intensity to the known intensity at that point. Nevertheless, due to susceptibility to the source intensity, such an approach tends to be less robust and thus having a lower accuracy, and it is also unusable for certain interferometric structures, such as Sagnac. Therefore, the detection of the quadrature point is mostly performed by introducing phase modulation techniques of various kinds, followed by a demodulation of the output electric signal [3, 17].

Before discussing the specific approaches to the phase modulation and the closed-loop compensation in the case of the selected interferometric sensors, the commonly employed principles of introducing a phase shift will be briefly described.

1.3 Phase modulation principles

The phase modulators, or shifters, are optical elements that introduce a controlled phase delay to the beam propagating through an optical path. The choice of a specific principle is highly dependent on the desired parameters, such as frequency, amplitude, or signal shape, and whether the optical beam is free-space or propagating through a waveguide, such as optical fiber. The most adopted principles by the interferometric sensors are the electro-optical and the piezoelectric.

1.3.1 Electro-optical phase modulators

The electro-optical modulator (EOM) is based on the Pockels effect, consisting in a refractive index change Δn of the optical material due to the application of an electric field [24]. The introduced phase shift is thus $\phi = \frac{2\pi}{\lambda} l \Delta n$, where l is the effective length of the modulated path. Typically used material is lithium-niobate ($LiNbO_3$), which is a crystalline material, with a large electro-optic coefficient and high trasparency within a wide range of wavelengths [17]. Due to its birefringence, the light must be linearly polarized before passing the EOM; otherwise the polarization is rotated by the modulation. Although the Pockels effect is present in both birefringent axes, their electro-optic coefficients are different and only the extraordinary mode is usually used [18]. An advantage of EOM, in general, is a high linearity of the introduced phase shift ϕ with applied voltage in a broad frequency range, theoretically achieving GHz or even THz orders, depending on the dimensions. Practically, the usable frequency range is limited by the bandwidth of the

driving circuits. From the electrical point of view, the EOM represents a capacitive load with small serial resistivity, which is often difficult to drive at high voltages.

The EOMs exist as free-space optical elements as well as components compatible with the optical fibers, most often as integrated waveguides. The integrated waveguides are created by microlitography by Ti atoms doping to increase the refractive index [27]. Due to the birefringence, the integrated waveguides support propagation of both transverse electric (TE) and transverse magnetic (TM) modes. The integrated EOMs exist in the in-line form, but also as Y-structures, serving further as beamsplitters, operating as push-pull, and are often used in the fiber-optic gyroscopes as multi-functional integrated optical circuits (MIOC). Nevertheless, due to the uneven phase shift for each mode, it is not fully compatible with a common single-mode (SM) fiber, and a polarization-maintaining (PM) fiber is typically used instead, enabling guiding a single polarization mode. Further, an alignment of the PM fiber polarization axes to the MIOC is necessary [18].

The key parameter of the EOM is its U_λ voltage, which induces the phase shift corresponding to λ. In the commonly used wavelength range (400 nm - 2 µm), the U_λ voltage of the free-space EOMs is normally in orders of 10^2 – 10^3 V. The integrated EOMs have the advantage of a much smaller profile, so their U_λ can be decreased to orders of 1 – 10 V. Therefore, this type of EOM can be utilized in the fiber-optic interferometers conveniently.

1.3.2 Piezoelectric phase modulators

The piezoelectric modulator (PEM) is based on the elongation Δl of the optical path, usually by mechanical stretching of the optical fiber. A phase shift $\phi = \frac{2\pi}{\lambda} n \Delta l$ is thus produced, where the produced elongation is proportional to the applied voltage. The most widely used material is poled zirconate-titanate (PZT), a ceramic material exhibiting a high piezoelectric coefficient [31]. The typical structure is formed by a poled ceramic tube, onto which an optical fiber is wrapped in several turns. Hence, the fiber is stretched by the radial displacement of the tube. Since the fiber is deformed by the tube, a parasitic change of the fiber refractive index and the birefringence can also be present, especially for a higher stretching ratio. Therefore, an approach based on an oval-like shape with straight sections was proposed, where the fiber is stretched only along the straight portions [32].

A general issue of PEM is the mechanical resonances. The resonant frequencies are inversely proportional to the particular dimensions of the PEM. This fact poses a significant limitation to the modulation bandwidth, which is usually up to several tens of kHz. In some cases, it is possible to take advantage of the resonance to drive the PEM at this frequency to achieve a higher modulation depth. However, it can

be then challenging to control the amplitude precisely, since the resonances of the PEM may drift due to temperature [33]. Therefore, to design a high-bandwidth PEM, a common approach is minimizing its dimensions and avoiding more complex structures to move the resonant frequencies beyond the operating range. Another parasitic effect of PEM is the limited linearity of the transfer from voltage to displacement, and its further conversion to the fiber elongation. The major factors distorting the linearity are the PZT hysteresis, the elastomechanical properties of the actuator, the fiber, and its attachment, which are all subjected to temperature dependency and also an aging phenomenon [34]. On the other hand, a strong advantage of PEM lies in its manufacturing simplicity and inherent compatibility with the optical fibers, and without the necessity of coupling to any other special components. Both SM as well as PM fibers can be used. With SM fibers, care has to be taken to the parasitic polarization modulation, which can occur with small PEM diameter [35].

Next to the common structures with a ceramic actuator, other approaches have been presented as well, such as piezoelectric fiber coating, acting as a fiber stretcher [36]. The phase shifting by the piezoelectric actuator is also used in the free-space optics [37]. The phase shift is usually introduced by a longitudinal displacement of the mirror.

1.3.3 Other principles of phase modulation

While the above-mentioned principles are used to modulate the phase directly, it is also possible to affect it by modulating the optical frequency since $f = \frac{1}{2\pi}\frac{\partial\phi}{\partial t}$. Therefore, the third principle used to introduce a phase shift is an acousto-optical modulator (AOM). This type of modulation employs an acoustic wave propagating through an optical material (usually lithium-niobate [24]) to shift the frequency of the incident optical wave using the Doppler shift. The AOMs, also referred to as Bragg cells, are often used as a part of heterodyne interferometers [38]. However, they also used to be implemented in homodynes, where the two consecutive modulators shifted the frequency in an opposite manner [39].

For completeness, it is also worth mentioning the thermo-optic phase modulators, which are due to their lower bandwidth more suitable for the quasi-static phase control and for the integrated optical devices [40].

1.4 Detection methods in fiber-optic gyroscopes

From a sensoric point of view, the gyroscopes are devices facilitating angular velocity measurement with respect to the inertial frame. As already outlined, this kind

of sensor is essential for the applications like inertial navigation and attitude and heading reference systems. Accompanied by accelerometers, the gyroscopes play a key role in the inertial measurement units, used for precise positioning without any need for an external reference. Such systems then find their application in aerospace, spacecraft and satellites, maritime, including submarines, drilling and mining [41, 42]. Gradually, the need for the accurate determination of the position and attitude is spreading to more common applications, such as autonomous vehicles, robotics, medical or manufacturing industry [43].

The first gyroscopes were mechanical with a rotating mass [29] and they are still used for specific use cases. The gyroscopes based on the Coriolis force form the largest group, in terms of their total numbers, thanks to MEMS technology, which allows them to be currently the smallest and cheapest angular velocity sensors. Nevertheless, their performance limitations, in terms of accuracy, stability, and bandwidth, leave a wide space for the optical gyroscopes [20]. Currently, there are two well-established technologies: the ring laser gyroscope (RLG) and the fiber-optic gyroscope (FOG).

The RLG appeared shortly after the introduction of a HeNe laser, when W. M. Macek and D. T. M. Davis demonstrated a square laser tube to sense the angular rate [44]. The RLG became a leading principle for the high-demand applications for many years [45], and they are still being used due to their superior parameters, especially the scale-factor stability, dropping down to 1 ppm [46]. Nonetheless, RLGs are known for their fundamental limitations, such as a limited lifetime and reliability, a need for frequency dithering, and complex manufacturing [19, 47, 48]. These factors also served as one of the primary motivations to find an alternative solution, in the form of a FOG.

The FOG was firsly introduced by V. Vali and R. W. Shorthill in 1976, where the sensitivity to the Saganc effect was magnified by guiding the light with the optical fiber in multiple turns [49]. Since that time, extensive effort has been made to develop the FOG technology and to turn it into the leading one, and the only one satisfying the strategic grade with bias stability dropping down to 0.0001 °/h [48,50]. The most widely spread FOGs share the original idea of the passive two-beams interferometer [49], improved by Ulrich [51] to comply with the reciprocity condition, and are thus referred to as interferometric fiber-optic gyroscopes (IFOG) [18]. Nowadays, the IFOGs are considered as one of the most advanced fiber-optic sensors in general, and are produced by many manufacturers (KVH Industries, EMCORE, Honeywell, NEDAERO, Northrop Grumman, iXBlue, Fizoptika, etc.) in various grades and performance levels [52–54].

Currently, most of the research related to FOGs is focused on miniaturization and price reduction, reflecting the high commercial potential in the range between

the Coriolis force gyroscopes (MEMS) and the IFOGs. Consequently, not only the optimization of the IFOG structure is performed, but also different approaches are developed [19,41]. Here, the highest attention is paid to the structures based on the optical resonator utilizing multiple-beam interference, and thus enabling reaching high sensitivity with relatively small dimensions. Various structures based on the resonant fiber-optic gyroscopes (RFOG) using an optical fiber as a resonator, or the resonant micro-optic gyroscopes (RMOG) employing an integrated waveguide instead, have been studied [43,55,56]. The devices are either active or passive. The active principle is similar to RLG, alas carrying similar challenges. The passive one operates with an external source and employs some type of light modulation to control the resonance. Currently, the passive devices seem to pose as a more promising approach [55]. Note that the integration is not strictly limited to the resonant structures, but also the waveguide-based IFOG has been reported [57].

Although the resonant optical gyroscopes exhibit a notable potential for the relatively cheap and compact sensors in the future, currently, the only commercially matured technology is represented by the RLG and IFOG. The following part focuses solely on methods surrounding IFOGs, representing the most widespread and technically advanced two-beam interferometers. From the perspective of the modulation methods and signal processing, the IFOGs are divided into the open-loop, where the angular rate is read directly from the optical signal, and the closed-loop, where the angular rate is optically compensated [18,19]. Before diving into the approaches adopted for both processing schemes, it is necessary to briefly explore the basic principle of the optical angular rate measurement, which is the Sagnac effect.

1.4.1 Sagnac effect in the fiber-optic gyroscopes

The Sagnac effect, sometimes also referred to as the Sagnac-Laue effect [18], is a consequence of the relativistic postulate about the constant velocity of the electromagnetic wave propagating in a vacuum. Assuming a planar closed path of any shape, the time needed for the wave to recirculate the path is a linear function of the whole system rotation within the plane [58]. The scenario of two waves propagating along the same path in the opposite directions is shown in Fig. 1.3. In a presence of an angular rate Ω, the waves traveling in clockwise (CW) and counterclockwise (CCW) direction undergo an opposite path shift due to shifting of the point of origin. The waves thus reach the point again with a phase difference $\Delta\phi = \phi_{ccw} - \phi_{cw}$. In the case of employing an optical fiber as an optical waveguide wound in N circular turns, the total phase difference induced by the angular velocity Ω is determined by the well-known equation of the IFOG:

$$\Delta\phi_s = \frac{4\pi RL\Omega}{\lambda \mathrm{c}}, \tag{1.12}$$

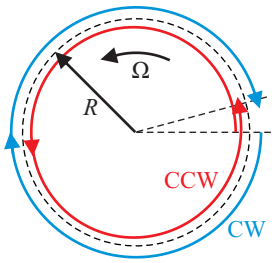


Fig. 1.3: Path difference between the counterpropagating waves in the rotating system.

where R is the fiber coil radius, $L = 2\pi RN$ represents the total fiber length. The Sagnac effect thus translates the measured physical quantity, which is the angular rate, into a phase difference of the optical beams, which can be measured interferometrically. Note that the relation is independent of the fiber refractive index, which results from the Fresnel-Fizeau effect [59]. The equation 1.12 is also often written in the short form $\Delta\phi_s = K_{IFOG}\Omega$, expressing the relation is considered to be linear. The K_{IFOG} then stands for the IFOG constant, even though its individual terms may be subjected to the influence by the surrounding parasitic effects.

1.4.2 Open-loop detection methods

For optimally aligned polarizations, the output IFOG intensity is described by the two-beam interferometer equation (Eq. 1.11). The IFOGs are commonly based on a so-called minimal configuration, satisfying the principle of reciprocity, consisting in an identical phase delay for both directions, and firstly demonstrated in [51]. In such setup, shown in Fig. 1.4, the input and output of the sensing coil share the same fiber, and the CW and CCW beams thus propagate through exactly the same path. The problem of cosine dependency of the angular velocity is normally

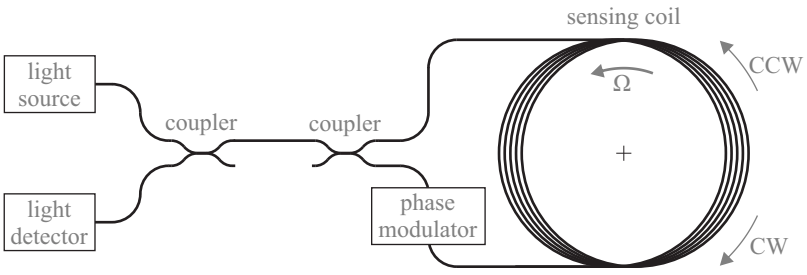


Fig. 1.4: The minimal configuration of the IFOG satisfying the principle of reciprocity.

overcome by the modulation-demodulation process, as firstly shown in [60]. Due to the asymmetrical placement of the modulator, the CW and CCW beams are phase-shifted with a delay of τ, given by the light propagation time along the sensing coil. Thus, a time-varying phase bias can be introduced, without violating the principle of reciprocity. Hence, the modulation is referred to as biasing. The total phase difference $\Delta\phi$ is then a sum of the Sagnac phase shift $\Delta\phi_s$ and the phase difference $\Delta\phi_b(t)$ induced by the modulation, so that the interferometer output can be described as:

$$I(t) = I_0 \left[1 + \cos(\Delta\phi_s + \Delta\phi_b(t))\right]. \tag{1.13}$$

Various biasing modulation schemes have been proposed, mostly with symmetrical sine or square-wave signals [18]. The modulation is mostly performed at the sensing coil eigenfrequency (or so-called proper frequency) $f_e = \frac{1}{2\tau}$, as it yields the highest efficiency, and also eliminates the negative effect of back reflections and Rayleigh scattering [61].

The basic scheme of the square-wave and the sinusoidal biasing modulation and their effect on the resulting intensity signal is shown in Fig. 1.5 and 1.6, respectively.

The square-wave biasing modulation can be expressed as:

$$\Delta\phi_b(t) = \begin{cases} \Delta\Phi_b, & \text{if } 0 < t < T/2, \\ -\Delta\Phi_b, & \text{if } T/2 < t < T, \end{cases} \tag{1.14}$$

where $\Delta\Phi_b$ stands for the modulation depth and T is the modulation period. In the case $\Delta\Phi_b$ is set to $\frac{\pi}{2}$, the output intensity signal can be described as:

$$I(t) = \begin{cases} I_0 \left[1 + \cos(\Delta\phi_s + \frac{\pi}{2})\right] = I_0 \left[1 + \sin(\Delta\phi_s)\right], & \text{if } 0 < t < T/2, \\ I_0 \left[1 + \cos(\Delta\phi_s - \frac{\pi}{2})\right] = I_0 \left[1 - \sin(\Delta\phi_s)\right], & \text{if } T/2 < t < T. \end{cases} \tag{1.15}$$

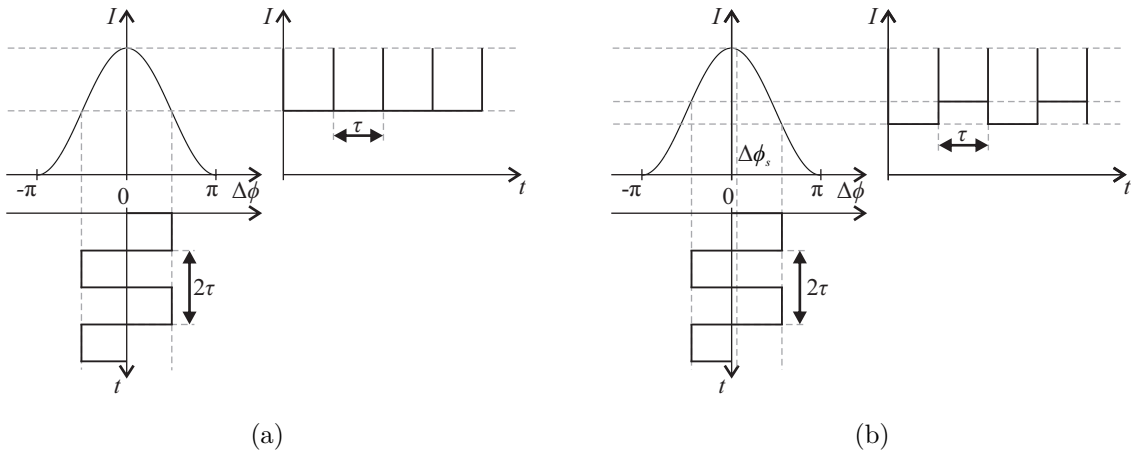


Fig. 1.5: Square-wave biasing modulation scheme: (a) $\Delta\phi_s = 0$, (b) $\Delta\phi_s \neq 0$.

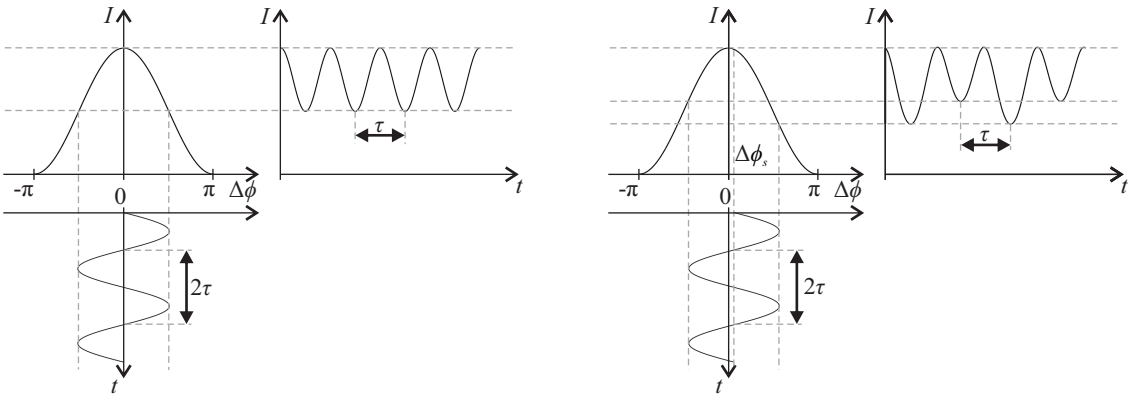


Fig. 1.6: Sinusoidal biasing modulation scheme: (a) $\Delta\phi_s = 0$, (b) $\Delta\phi_s \neq 0$.

The output signal S_{OL} is usually obtained by taking the difference between the successive levels so that:

$$S_{OL} \propto 2I_0 \sin(\Delta\phi_s). \tag{1.16}$$

As the square-wave modulation requires a broadband modulator, it can only be applied with EOM. On the other hand, the sinusoidal modulation, comprising a single harmonic component, is also compatible with a narrowband PEM, utilized in the all-fiber IFOGs [62]. The sinusoidal biasing modulation is described by:

$$\Delta\phi_b(t) = \Delta\Phi_b \sin(\omega_b t), \tag{1.17}$$

where $\Delta\Phi_b$ is the modulation depth and ω_b the angular frequency. The output intensity is then:

$$I(t) = I_0 \left[1 + \cos(\Delta\phi_s + \Delta\Phi_b \sin(\omega_b t))\right], \tag{1.18}$$

which can be rewritten as:

$$\begin{aligned} I(t) = I_0 \Bigg[1 + \sum_{k=0}^{\infty} \mathrm{J}_{2k}(\Delta\Phi_b) \cdot 2\cos(2k\omega_b t) \cdot \cos(\Delta\phi_s) + \\ + \sum_{k=0}^{\infty} \mathrm{J}_{2k+1}(\Delta\Phi_b) \cdot 2\sin((2k+1)\omega_b t) \cdot \sin(\Delta\phi_s) \Bigg], \end{aligned} \tag{1.19}$$

where J_k stands for the k-th order Bessel functions. It can be noted that by taking any odd harmonic component of ω_b, the relation described by Eq. 1.16 is obtained, which is referred to as an open-loop signal. Usually, the first harmonic is used with an amplitude $\Delta\Phi_b \approx 1.8$ rad to maximize the sensitivity [18].

Various demodulation methods have been presented to acquire the open-loop signal, focusing either on the performance improvement [63–65] or the process simplification [66–68]. In the case of the square-wave modulation, the demodulation is,

at the simplest, performed by synchronous sampling with a period of τ [60]. Concerning the sine modulation, which is much more common for the open-loop IFOG, the most widely reported method is based on the lock-in detection [62,64–66], though the sampling methods are also used [68–70]. The employment of the lock-in amplifier to demodulate the intensity signal from the all-fiber IFOG was firstly proposed by [62]. Later solutions focused on reducing the complexity of the lock-in amplifier circuits, such as using an active high Q-factor band-pass filter followed by a simple analog lock-in detector [64] or adopting a single analog IC to perform the demodulation as well as further signal processing [66]. The limitations of analog signal processing were overcome by semi-digital processing presented in [65], where the analog output of the lock-in circuit was sampled with an analog-digital converter (ADC) and processed digitally. Since the analog lock-in detection circuit is considered the most complex and critical part of the signal processing chain, there was an effort to replace it with an alternative and simpler mechanism. The solution described in [67] relied on the time measurement between the zero crossing instants of the AC-coupled output intensity signal. Another analog method was presented in [71], where the mean values of negative half-cycles are calculated, and the difference between the neighboring values is shown to correspond to the open-loop signal. Omitting the lock-in amplifier was also allowed by the synchronous sampling of the output intensity signal, as presented in [72] or [68]. In [73], a modification was proposed, using a higher sampling rate with subsequent undersampling, leading to an improvement of the noise performance. Another techniques utilize sampling at particular phase values, such as using 5 points per period with subsequent arithmetics [70], or employing 36 points and their sum computation [69]. Some approaches also address the common problem of the excess bias caused by the crosstalks between the modulation signal paths and the intensity output. It was shown that the main bias component is independent of the modulation polarity, so it can be solved by periodical reversing of both the biasing modulation and the output signal sign [74]. A similar method is presented in [75], where instead of reversing the biasing modulation, the half-periods of the demodulator input signal are swapped before further processing.

So far, the most common methods to obtain a sine-shaped open-loop signal, according to Eq. 1.16 were reviewed. Various processing schemes have also been adopted to obtain a linear response in a wide dynamic range with a good scale-factor stability. The simplest approach consists in an inverse sine function performed by an analytical model or a look-up table with interpolation [68]. Next to the limited dynamic range, the method has the disadvantage of a susceptibility to the source intensity I_0 variations under different conditions. Therefore, most of the open-loop IFOGs adopt the method presented in [76], employing a ratio of the first and the second harmonic component to obtain the phase shift independent of the intensity

and the electronics gain:

$$\Delta\phi_s = \tan^{-1}\left[\frac{\mathrm{J}_2(\Delta\Phi_b)S_1}{\mathrm{J}_1(\Delta\Phi_b)S_2}\right], \tag{1.20}$$

where $S_1 = \mathrm{J}_1(\Delta\Phi_b)\cdot 2\sin(\Delta\phi_s)$ is the first and $S_2 = \mathrm{J}_2(\Delta\Phi_b)\cdot 2\cos(\Delta\phi_s)$ the second harmonic component of the ω_b within the $I(t)$ signal according to Eq. 1.19.

Since the stability of the scale factor is further determined by the biasing modulation depth $\Delta\Phi_b$, its control must be performed by maintaining the constant ratio of the second and the fourth harmonic component (S_2/S_4). Alternatively, the ratio of the first and the third harmonic component (S_1/S_3) can also be used, as it has a lower noise in certain intervals of $\Delta\phi_s$ [77]. The inverse tangent function calculation can be solved by a look-up table and a linear or polynomial interpolation [65,73]. However, this poses a disadvantage in limiting the dynamic range of the measurable Sagnac phase shift from $-\pi/2$ to $\pi/2$. This problem has been addressed by a tracking method [78], where the quadrants of the $\tan^{-1}$ function are switched based on the previous $\Delta\phi_s$ value. Further modification of the tracking method was presented in [79], where the difference between the current and previous value of $\Delta\phi_s$ is obtained by arithmetic operations on the S_1 and S_2 components, which also avoids the need of $\tan^{-1}$ function calculation.

A different approach to obtaining a linear response of the open-loop IFOG, as presented in [80], is based on modulating the amplitudes of the S_1 and S_2 components by other harmonic signals shifted by $\pi/2$ and their summing. It was shown that by a proper adjustment of the phase modulation depth $\Delta\Phi_b$, the produced signal is phase-shifted by $\Delta\phi_s$, thus avoiding the $\tan^{-1}$ function calculation.

The possibility of a direct translation of the Sagnac phase shift into a phase shift of the derived electric signal was the motivation for the phase-reading methods developed to linearize the output of the early open-loop IFOGs. The phase-reading method, first introduced in [81], employed an all-fiber structure and a sinusoidal phase modulation with $f_m < f_e$. The output intensity signal (formally similar to Eq. 1.18) was then amplitude-modulated by two synchronized and mutually complementary square-wave signals, which is also referred to as gating. The modulated signals were then subjected to band-pass filtering. It was shown that if specific conditions are met, such as certain modulation depth, two harmonic signals, S_a and S_b, are obtained, which phase shifts are $-\Delta\phi_s$ and $+\Delta\phi_s$, respectively. Therefore, the Sagnac phase shift can be determined directly as their phase difference. The method was also realized using digital signal processing, avoiding the need for an analog phasemeter or an exact matching of the bandpass filters [82]. Nevertheless, there was reported a necessity for a high sampling rate of the modulated, or gated, signals to reach a sufficient phase resolution in the Sagnac shift detection.

A slightly modified method was presented in [83], employing a symmetrical triangular phase modulation instead, with a base frequency of f_e. Similar processing as in [81] was then applied to the detected intensity signal, where the gating was synchronized with the positive and negative modulation signal slopes to obtain S_a and S_b signals, respectively. Contrary to the previous method, here, the base frequency of S_a and S_b was determined by a triangular modulation slope, so it could be adjusted to be much lower, enabling an easier and more precise detection of the Sagnac phase shift. As the triangular modulation requires a broadband modulator, it is no longer compatible with an all-fiber architecture. This could be overcome by the deep sine modulation, with the amplitude significantly exceeding π [84]. Selecting its quasi-linear portions by a proper adjustment of the gating signal enables reaching the equivalent output as with the triangular modulation.

In general, although the phase-reading methods represented a prospective and simple approach to open-loop IFOG signal processing, they have not been adopted by further solutions, primarily due to the inherent intensity noise, limiting the performance of the precise phase detection in the electric signal [73]. Another alternative approach to the open-loop IFOG output linearization was presented by the electronic closed-loop. Even though this is not a genuine optical closed-loop with a phase shift compensation, the phase shift is compensated in the electrical output signal obtained by specific processing. In one of the first proposed methods, the intensity signal is multiplied by a pulse train, the spacing of which is adjusted in a closed-loop to compensate the Sagnac shift in the output signal [85]. A similar technique was demonstrated in [86] using a digital integrating processor, leading to a notable decrease of the linearity error compared to the previous solutions. Both methods employ a PEM and a sinusoidal phase modulation. A different approach to the electronic closed-loop, presented in [87], is based on multiplying the intensity signal with another phase-modulated signal, which phase shift is adjusted by the electronic closed-loop to null the Sagnac phase shift in the signal obtained by the low-pass filtration.

Despite the diversity of the proposed modulation and signal processing methods in the open-loop IFOGs, none of the solutions became widely accepted as being able to replace the closed-loop processing, especially as the scale factor stability and linearity are concerned. The major drawback of the alternative methods is that they usually require a specific modulation depth, but lack a sufficiently efficient mechanism for its control. Further, many of these methods are based on a precise time synchronization of the reference and the intensity signal, burdened by white noise, what may limit their performance for higher-grade applications. Therefore, the method based on a harmonic component detection remained the one adopted by later open-loop approaches [63, 64, 68]. Although the all-fiber architectures are

still attractive due to their simplicity and manufacturing costs, their major limitations lie in the PEM properties [35, 88], especially limited linearity and temperature dependence. Not only the eigenfrequency condition $\omega_b = 2\pi f_e$ must be satisfied, but also some control mechanism of the modulation depth and spectrum would be favorable, such as, e.g., error modeling based on the neural networks [63].

1.4.3 Closed-loop detection methods

In the closed-loop detection methods, instead of a direct measurement, the Sagnac phase shift is actively compensated (nulled) within the optical path. As the Sagnac shift is inherently non-reciprocal, another non-reciprocal shift $\Delta\phi_c$ must be introduced; however, without disrupting the optical reciprocity ensured by the minimal configuration (Fig. 1.4) [51]. The early solutions employed AOM to shift the frequency of the CW and CCW beam with the delay of τ and thus introduce a controlled phase shift $\Delta\phi_c$ [89, 90]. However, due to the different frequencies of the counter-propagating beams, such configuration is optically non-reciprocal. The first reciprocal solution to the closed-loop detection was proposed by [91], using a sawtooth (or ramp) modulation, shown in Fig. 1.7. The sawtooth phase signal, resetting at 2π level, is introduced with a delay of τ, causing a differential phase shift:

$$\Delta\phi_c = \frac{2\pi\tau}{T}, \tag{1.21}$$

where T is the sawtooth phase signal period. The open-loop signal:

$$S_{OL} \propto 2I_0 \sin(\Delta\phi_s - \Delta\phi_c) \tag{1.22}$$

is thus maintained at zero by T adjustment, usually using an integration or a proportional-integration controller [92]. To detect the open-loop signal, sinusouidal

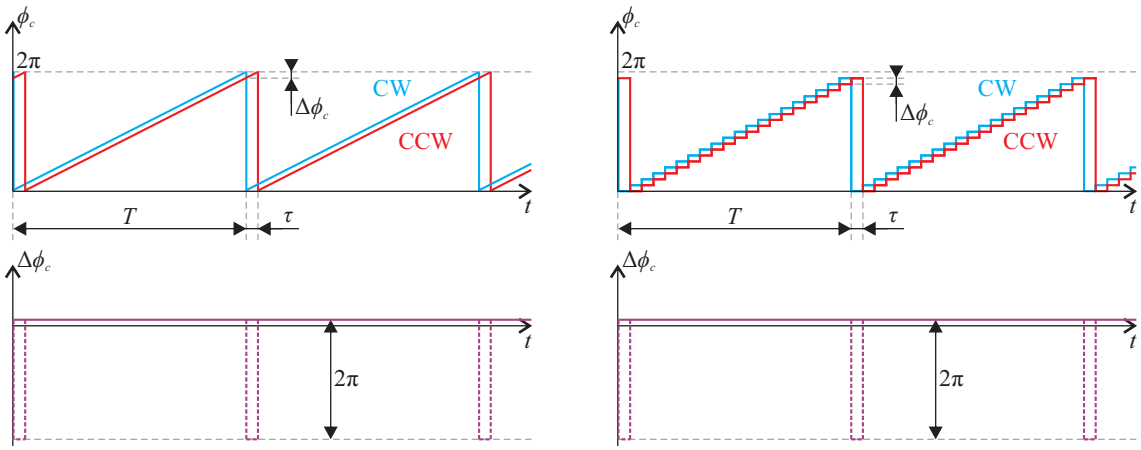


Fig. 1.7: Analog (a) and digital (b) sawtooth compensation modulation scheme.

or square-wave biasing modulation is normally used in addition to the compensation [18, 93]. The problem of the original analog sawtooth modulation was the finite reset flyback time, causing a spurious effect in the output intensity signal and disrupting the closed-loop output linearity [94]. This issue was surpassed by a digital sawtooth modulation introduced in [95], with discrete sampling, which is now adopted by most high-grade IFOGs. Next to it, the digital signal processing also led to elimination of the electronic bias drift [96].

Although the closed-loop processing scheme completely avoids the dependence on the source intensity I_0 as well as biasing modulation depth $\Delta\Phi_b$, the stability of the scale factor is directly determined by the stability of the modulator and electronics gain, which was shown to drift with temperature [97]. As a solution, a four-state modulation has been proposed [98,99], replacing a standard square-wave modulation for the open-loop signal detection. The four-state modulation, schematically shown in Fig. 1.8, is defined as follows:

$$\Delta\phi_b(t) = \begin{cases} \Delta\Phi_b, & \text{if } 0 < t < T/4, \\ a\Delta\Phi_b, & \text{if } T/4 < t < T/2, \\ -\Delta\Phi_b, & \text{if } T/2 < t < 3T/4, \\ -a\Delta\Phi_b, & \text{if } 3T/4 < t < T, \end{cases} \tag{1.23}$$

where a is a constant satisfying $\cos\Delta\Phi_b = \cos a\Delta\Phi_b$. The error of the modulation gain chain δ_{FS} is calculated by comparing the levels with and without multiplication by factor a, i.e., $\delta_{FS} \propto (x_1 + x_3) - (x_2 + x_4)$ (see Fig. 1.8), and another loop-back is established to maintain this error zero by modulation gain correction. The common open-loop signal is then determined as $S_{OL} \propto (x_1 + x_4) - (x_2 + x_3)$. As a side effect, the four-state modulation can also be used to monitor the IFOG temperature since

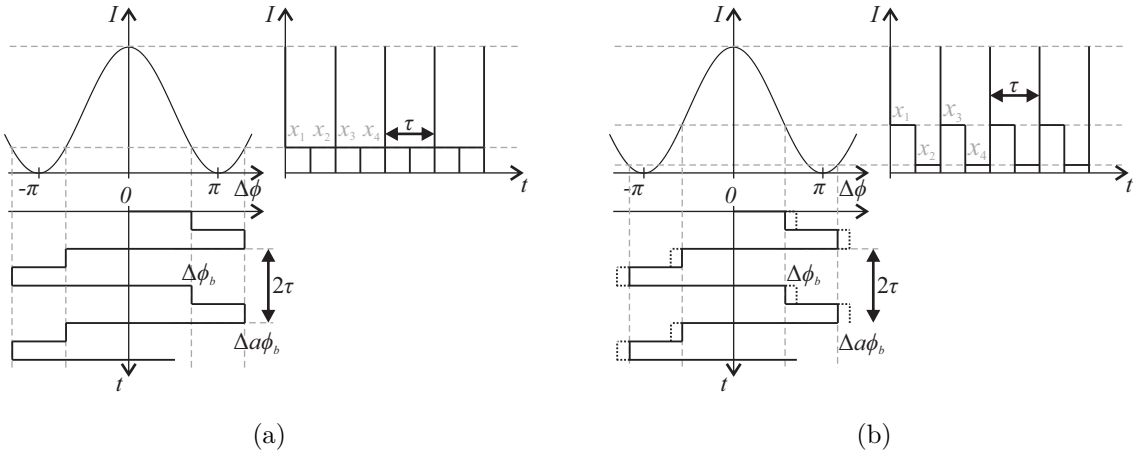


Fig. 1.8: Four-state biasing modulation scheme: (a) $\Delta\phi_s = 0$, (b) $\Delta\phi_s \neq 0$.

it is the major factor affecting the EOM gain [100]. Besides, the modulation brings improved noise performance [101] due to the possibility to control the resets at 2π precisely. The drawback of the four-state modulation can be found in the necessity to double the sampling frequency compared to the square-wave modulation. A simple alternative to the four-state modulation, firstly proposed by [95] and described in detail in [102], is based on the square-wave modulation, the amplitude of which is periodically multiplied by 1 or a factor a. The δ_{FS} signal is thus obtained with the periodicity of this switching.

Next to the scale-factor stability, another reported issue related to the closed-loop processing is a dead zone at small angular velocities, caused mainly by the electric cross-coupling, i.e., the interference between the modulation voltage and the photodetector signal, and the phase modulation drift [103]. Therefore, a common practice in closed-loop processing is the employment of phase dithering [104]. In high-grade IFOGs, another problem may also lie in the quantization error, caused by a limited resolution of the sawtooth modulation generation. A solution proposed by [105] utilizes EOM with a second pair of electrodes, enabling finer steps of the compensation modulation. Nevertheless, given that two modulators are actually used, a modified four-state biasing modulation based on waveform decomposition and time division is required to control the gain of each compensation modulation chain [105].

Both analog as well as digital sawtooth modulations require a broadband modulator and are thus compatible solely with EOM. Nevertheless, due to the attraction of an all-fiber architecture, there has also been a substantial effort to realize a closed-loop processing with PEM. One of the first attempts used a sinusoidal biasing modulation with a frequency of $f_b = f_e/2$ accompanied by a sinusoidal compensation modulation of frequency $f_c = f_e$ to null the effect of the Sagnac phase shift at this frequency in the output signal [106]. The relationship between the compensation modulation amplitude and the Sagnac phase shift was obviously nonlinear and dependent on the biasing modulation depth. Other alternative solutions were based on a technique of gating [107–110]. The key idea here is to use a much slower modulation ($f_c \ll f_e$), composed of one [107] or two [108, 109] harmonic components, which can compensate the Sagnac phase shift within a certain portion of its period T_c. The output signal is then acquired only within these intervals, but is gated out otherwise. The open-loop signal detection is performed by the standard sinusoidal biasing modulation satisfying $f_b = f_e$. Whereas with only single harmonic component in the compensation modulation the closed-loop response was far from linear, adding the second harmonic aided in flattening the portion within the intervals when the Sagnac shift is compensated, yielding an improved linearity (0.5 % in [109]) and a possibility to extend these intervals. Nevertheless, the scale-factor

stability is limited by the stability of the PEM transfer coefficient and its linearity. Therefore, a modification has been proposed by [110], using a fixed amplitude of the compensation modulation, and the gating phase is shifted instead. A different approach to the closed-loop processing with PEM was also shown in [111], employing a series of harmonic signals to approximate the sawtooth or triangular modulation. However, there is still the limitation posed by the need for modulation depth control of the utilized harmonic components. Moreover, since all of these methods use a slow compensation modulation with period $T_c \gg \tau$, the modulation depth must be sufficiently large compared to the resulting phase difference. This fact not only puts higher demands on the PEM driving circuits, but can also lead to a further decrease of the linearity due to the inherent PEM nonlinearity with the driving voltage [35]. Therefore, the alternative methods are yet to successfully replace the approach with EOM and the sawtooth modulation, especially in the high-grade IFOGs.

Nevertheless, concerning the closed-loop detection methods, attention was also paid to the compensation of thermal effects impacting the scale-factor and the bias stability. Although the bias drift due to the thermal transient effects (Shupe effect) is typically overcome optically, by adopting a proper winding method [112], further elimination of the residual thermal error is possible with additional signal processing, as shown in [113] with a voltage controlled loop. A more complex solution integrated an adaptive forward linear prediction and modeling with the least squares polynomial fit [114] or a finite elements analysis [115], allowing the error computation and an effective output correction. The second problem is associated with the thermal dilatation of the sensing coil having a direct impact on the scale factor, according to the Eq. 1.12. A common technique to measure the optical length change is to measure the transit time $\tau = \frac{1}{f_e}$, which can be accomplished by applying a periodic phase modulation. It can be shown that if the base frequency f_τ of the modulation $\phi_\tau(t) = \Phi_\tau \sin(2\pi f_\tau t)$ equals $f_\tau = N f_e$, where N is an integer, the total phase shift becomes $\Delta\phi_\tau(t) = \phi(t) - \phi(t-\tau) = 0$. In such a way, the transit time τ can be detected. A sinusoidal [116], square-wave [117, 118] as well as sawtooth [119] $\phi_\tau(t)$ modulation have been used to detect the τ change with temperature, revealing a highly linear temperature dependence [116, 119]. Based on the scale-factor temperature model, the scale-factor error can be established and effectively compensated. Another approach is a real-time tracking of τ, where $\Delta\phi_\tau(t)$ is used as another modulation, along with the biasing and compensation, to control the τ in the closed-loop [120]. Such an approach allows more precise detection of the coil dimensions change; however, it puts higher demands on the sampling frequency [121].

To conclude, despite the higher complexity, the closed-loop processing is advantageous for a number of reasons. Not only can it provide intrinsically linear output,

which is insensitive to the source intensity [111], but as the system is kept operating at the quadrature point, the stability of bias and scale factor can be enhanced significantly [93,103]. This is also evidenced by the fact that the closed-loop processing is adopted by the highest-grade IFOGs, relying on the digital sawtooth modulation to compensate the Sagnac phase shift and an appropriate mechanism to control the modulation gain, such as four-state biasing modulation.

1.5 Detection methods in vibrations measurement homodyne interferometers

As previously discussed, optical methods based on laser interferometry are extremely useful for accurate dimension measurements, e.g., distance or profile and surface measurement, as well as measurements of linear mechanical movement, such as displacement or velocity [1, 21]. In this context, mechanical vibrations constitute a special type of movement that is periodic and limited in amplitude. Therefore, laser interferometry is essential in this field, especially if high resolution is needed.

Currently, the broad scope of the precise interferometric vibration measurement facilitates tasks regarding materials characterization, such as piezoelectric and electrostrictive properties measurements. Such parameters are essential for the microelectromechanical structures (MEMS) development, typically used as microactuators or various kinds of sensors [22]. In recent years, of particular interest is not only the material characterization of bulk PZT ceramics, but also the measurement of composite samples comprising thin as well as thick films, such as AlN, ZnO, or ferroelectrics, constituting a key part of the MEMS devices [122]. Regarding the piezoelectric materials, the piezoelectric coefficient must be determined precisely for their proper design. Their characterization by means of interferometry is based on the inverse piezoelectric effect, where the material dimensions change is sensed as a function of applied voltage [123]. Due to the very small displacements, dropping down to the orders of several picometers, rather than a step-induced static distance change, the measurement of sample vibrations induced by AC voltage is usually preferred to suppress the surrounding noise. Furthermore, in many cases, it is required to characterize the sample within a broad frequency range, or to focus on its behavior in resonances.

As mentioned earlier, vibrations can be characterized either by displacement or velocity measurement. Accordingly, the heterodyne or the homodyne principle can be employed. The advantage of the heterodyne principle mainly consists in a direct conversion of the measured velocity into the frequency of the output intensity signal, which can be detected easily. The velocity measurement is insensitive to the surface

reflectivity, which is useful for scanning the vibrations along the sample surface [124, 125], as a widely accepted method for the MEMS devices characterization [22, 126]. On the other hand, when studying the piezoelectric parameters of materials, a frequently mentioned disadvantage is the limited resolution of the piezoelectric coefficient measurement. Moreover, the resolution is frequency-dependent [23, 127, 128]. Therefore, for a highly precise characterization in a broad frequency range, the displacement measurement by the homodyne principle is a more suitable approach. The following discussion is thus solely focused on the homodyne interferometer, the output signal of which can be described by Eq. 1.11 of the two-beam interferometer.

Finally, a special approach to the vibrations measurement can be represented by self-mixing interferometers based on laser feedback interacting with the measured sample [129]. Their advantage consists in a high displacement range, comparable to the fringe counting method [13,130]. However, due to its relatively rough resolution, its use for piezoelectric materials characterization is limited.

1.5.1 Interferometer arrangements for piezoelectric materials characterization

The most adopted types of interferometers used in the displacement measurement for the material characterization are the Michelson and the Mach-Zehnder. Unlike in the Sagnac interferometer, the output signal is here obtained by the interference of two beams propagating through different paths. The beams can be referred to as a probing beam, which phase is shifted by the sample displacement, and a reference beam.

The first type, the Michelson, is usually used for a single-side measurement [127]. The simplified structure of the single-beam Michelson interferometer (SBMI) is shown in Fig. 1.9(a). Concerning the piezoelectric materials characterization, the measured quantity is the effective piezoelectric coefficient, usually d_{33e}, which is

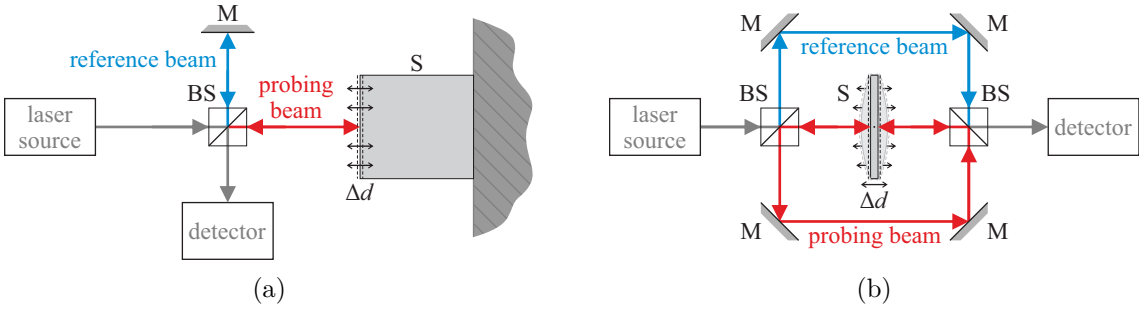


Fig. 1.9: Schematic of the SBMI (a) and the DBMZI (b) (M – mirror, BS – beam-splitter, S – measured sample).

converted to the displacement Δd through the inverse piezoelectric effect [131, 132]. The sensed phase change can be thus expressed as:

$$\Delta\phi_s = \frac{4\pi\Delta d}{\lambda}. \tag{1.24}$$

The effective piezoelectric coefficient can be thus determined as:

$$d_{33e} = \frac{\Delta d}{U_s}, \tag{1.25}$$

where U_s stands for the voltage applied to the measured sample. The single-beam measurement is mostly suitable for the bulk samples measurement, the thickness of which is comparable to their other dimensions. In the case of the piezoelectric films, which are usually clamped to the substrate, the common problem is the sample bending [22, 125, 133] caused by the mass center oscillation. In the case of the single-side measurement, the bending effect can exceed the total thickness change even by an order of magnitude, already at frequencies of several kHz [37]. This problem can be successfully overcome by a two-side sample measurement, as shown by experiments [37, 134–137] as well as simulations [138], employing a special arrangement of the Mach-Zehnder interferometer. The double-beam method is thus considered the most reliable and accurate approach as far as measuring the thickness displacement of piezoelectric or ferroelectric films is concerned [23, 123]. The simplified structure of the double-beam Mach-Zehnder interferometer (DBMZI) is shown in Fig. 1.9(b). The induced phase shift is defined by Eq. 1.24, as for the single-beam measurement. However, the Δd now stands for a real thickness displacement, regardless of the sample or substrate bending.

Note that also the heterodyne interferometer has been proposed in the double-beam arrangement [38, 139], which was arranged as two systems sensing the sample vibrations from both sides separately and subtracting the signals in post-processing. Although the bending effect can be supressed, it still manifests as a high common mode component in both signals, deteriorating the noise performance and accuracy. Conversely, the DBMZI inherently compensates the bending by optically differential measurement.

1.5.2 Quadrature point closed-loop stabilization

Unlike the Sagnanc interferometer, the optical reciprocity of the SBMI and the DBMZI is not inherently ensured by their structure, since the phase difference $\Delta\phi$ between the reference and the probing beam can be arbitrary. Nevertheless, the quadrature point can be conveniently reached by simply adjusting one of the interferometer arms. Recall that the output intensity is given by the Eq. 1.11. With no additional modulation, the relative phase difference $\Delta\phi$ between the beams is given

by the sum of the sample-induced phase change $\Delta\phi_s(t)$, and the phase random drift $\Delta\phi_{drift}$, caused by ambient factors, mostly the air flow, temperature fluctuations, and external acoustic and mechanical noise [133, 137]. To suppress most of the high-frequency noise, appropriate operating conditions with a quiet environment and vibration shielding are typically required [23,125]. The target of the closed-loop quadrature point control is thus the suppression of the low-frequency drift.

The common method to stabilize the quadrature point uses a mirror driven by a piezoelectric actuator in the closed-loop. This technique was first presented for the SBMI [140] and later adopted in the DBMZI [37,134,136,141]. In the case of SBMI, this task can be accomplished with the basic structure shown in Fig. 1.9(a). For DBMZI, the first proposed arrangement used an additional mirror in the reference branch [141]. The disadvantage of the beam deflection caused by a mirror movement was overcome by the solution presented in [134], replacing one of the mirrors with a beamsplitter. A simplified structure was then introduced in [135] with the common path arrangement, where the partial overlap of the probing and reference beam trace led not only to their balanced lengths, but also to reducing the number of needed optical components. Even more significant component reduction has been achieved with a triangular arrangement [142]; however, it has limited possibilities for the quadrature point control.

In all of the mentioned cases, the quadrature point, corresponding to the relative phase difference of $\pm\left(n+\frac{1}{2}\right)\pi$, was maintained by referencing the low-frequency component of the output intensity signal to the fixed value. This value was obtained as a medium value between the minimum and the maximum of the interference fringe (see Fig. 1.1). Therefore, before a measurement, a calibration is required, which can be performed by a triangular phase sweep.

With the stable quadrature point, the cosine interference equation (Eq. 1.11) is converted into sine, similarly as with an open-loop signal in the IFOG. For small sample-induced phase shift amplitudes $\Delta\Phi_s \ll \pi$, which is the predominant case with the thin samples, the sine function can be neglected, so the displacement and the corresponding effective piezoelectric coefficient can be determined directly from the intensity signal. For effective noise suppression, a lock-in technique is usually adopted to determine the amplitude as well as phase of the d_{33e} value [133,136,140].

1.5.3 Phase modulation

The major drawback of the quadrature point control based on the fixed intensity level referencing is the susceptibility to the total intensity variations. These can be caused by a laser source intensity drift [133], but especially by the reflectivity variations along the sample surface, in case of measurement in multiple points. It has been

shown that the characterization of the vibrations profile along the sample is essential for the study of MEMS devices [124, 128], requiring a calibration in each new point with the previously described method. This problem can be solved by introducing a phase modulation method, proposed for the DBMZI [137] as well as SBMI [127].

Instead of maintaining the quadrature point, the modulation method relies on periodically passing the quadrature point without closed-loop control. In [137], the phase modulator, represented by the actuated mirror, is driven by the triangular or sinusoidal signal of sufficient peak-to-peak value (i.e., larger than π) to obtain an amplitude-modulated intensity signal. After high-pass filtering, the sample displacement can be determined from the maximal amplitude, which corresponds to the quadrature point. The low-frequency component peak-to-peak value then corresponds to the $\frac{\lambda}{2}$ path difference, so the actual displacement can be calculated by taking their ratio. The invariance of this ratio with the total intensity change thus allows this technique to be used for scanning the displacement along the sample surface.

As for the limitations of such approach, the phase modulation introduced to sweep the phase difference must be significantly below the frequency of the sample driving signal, at which the sample is characterized. The second drawback lies in the amplitude detection from the modulated signal. In the case of employing a more sensitive lock-in technique, the magnitude of the detected component depends on the modulation signal depth, which may reduce accuracy unless the modulator gain is exactly known or controlled. Nevertheless, the modulation provides robustness enhancements, combining the high resolution needed for the characterization of piezoelectric films with the possibility of rapid scanning.

2 Aims and objectives

The major goal of the thesis is the development of novel methods of phase modulation and signal processing facilitating the closed-loop phase compensation for the selected interferometric sensors setups. A number of research reports pointed out that the compensation of the measured quantity by the closed-loop operation can introduce substantial advantages. These include not only overcoming their inherently nonlinear response, but especially suppressing a range of parasitic effects deteriorating their performance.

Even though the closed-loop methods are already well-established in the field of FOGs, the commercial devices rely nearly exclusively on the sawtooth modulation scheme with EOM-based architecture and PM fiber, leading to the added complexity and manufacturing costs. As suggested, cost reduction is one of the crucial challenges in the field of FOGs, which could be achieved either with new optical structures, or by utilization of a cost-efficient setup, such as a PEM-based all-fiber architecture with an ordinary SM fiber. Therefore, the subject of the research presented here is this type of IFOG structure, based on the minimal architecture, and with the possibility of the closed-loop phase compensation methods. Although several approaches to address similar goals have already been proposed in the past, none became widely employed as an alternative to the established closed-loop IFOGs, mostly due to a lack of significant performance improvement and an increased complexity. Furthermore, the prior approaches employed analog signal processing, for the most part, and were also limited in the stability induced by the SM coil polarization non-reciprocities. Nevertheless, it was demonstrated that with the advance in the manufacturing process and a careful design, a significant improvement can be achieved in the all-SM fiber-based IFOG, making it a candidate for a medium-grade gyroscope; however, with a dramatic decrease in costs [143–145]. Therefore, a challenge arises to develop a mechanism enabling its closed-loop operation to reduce some of the parasitic effects, and improve its performance in terms of the linearity error, the temperature sensitivity, or the scale-factor stability. The primary aim, in relation to the IFOG sensors, is thus the development of the all-SM-fiber compatible closed-loop method, as well as its implementation and verification. As the optical part is generally considered to be the defining factor in the IFOG price, it is desirable to avoid adding further complexity to the optical architecture in favor of closed-loop processing. Instead, a more powerful processing unit based on COTS electronics should accommodate the newly developed algorithms and the software-based method for the aforementioned errors mitigation.

In contrast, the homodyne interferometers for the vibrations measurement are far less mature regarding the modulation techniques. Furthermore, a truly closed-

loop method of vibrations measurement has not been reported so far, neither for double-beam nor single-beam interferometers. In the prior solutions, the closed-loop control was employed to stabilize the quadrature point, but not to nullify the effect of the measured quantity, represented by the vibrations-induced phase shift. The objective is thus to develop a closed-loop processing method, capable of inherently overcoming issues like interference response nonlinearity or sensitivity to the intensity fluctuations. As the setup is purposed to measure the dynamic displacement up to 10^5 or even 10^6 Hz, the phase changes can not be nullified by a commonly used piezoelectric actuator to a reliable extent, so an EOM must be utilized instead. As the additional drawback of the interferometric measurement reported is a high susceptibility to environmental disturbances, another target of the processing scheme design is to enhance the robustness and mitigate the effect of the outer vibrations coupling to the measured signal.

To summarize, the goal of the research reported within this thesis is the development of closed-loop processing methods for two types of homodyne interferometric sensors. Generally, the interferometric sensors with a closed-loop compensation are considered one of the most advanced and accurate. Yet, regarding the configurations addressed in this work, such an approach has been so far reported either very rarely and with significant limitations (in the case of the IFOG with PEM) or has not been reported at all (in the case of DBMZI), despite potentially offering a number of advantages, as already suggested. The impact of this work, among others, should also lie in exploring these new approaches and demonstrating their pros and cons over the state-of-the-art (SOTA) solutions.

2.1 Aims summary

- Design and development of a closed-loop processing method for the all-fiber IFOG.
- Identification of the parasitic effects induced by PEM and development of an efficient error compensation method.
- Implementation and verification of the methods with the emphasis on overall cost reduction of the IFOG sensor.
- Design and development of a closed-loop processing method for the DBMZI.
- Implementation and verification of the method for vibration scanning of thin samples.

3 Closed-loop fiber optic gyroscope with piezoelectric modulator

The target application for the closed-loop phase modulation method design is an IFOG structure based on the minimal configuration (Fig. 1.4), utilizing all-fiber components and an SM fiber coil. It has been shown that using a polarized light may yield significant reciprocity errors in the case of an SM fiber coil, so a depolarized light must be used in this case [144,146–148]. The PEM meets the requirements posed by the depolarized light well due to its inherent insensitivity to the polarization state, assuming its proper design [35]. In most cases, the default minimal configuration is further modified with additional optical elements for polarization handling to minimize the polarization-induced non-reciprocities [18]. Nevertheless, for the signal processing and phase modulation methods design, the main issue is defined solely by the employed modulation principle.

The simplified schematic of the IFOG testbench is shown in Fig. 3.1. All of the techniques proposed herein are based on digital signal processing. The optical intensity signal $I(t)$ is thus converted into a signal $I(k)$, which is processed by the control unit. The unit then composes the phase modulation signal, which is fed into the PEM, introducing the time-varying non-reciprocal phase shift.

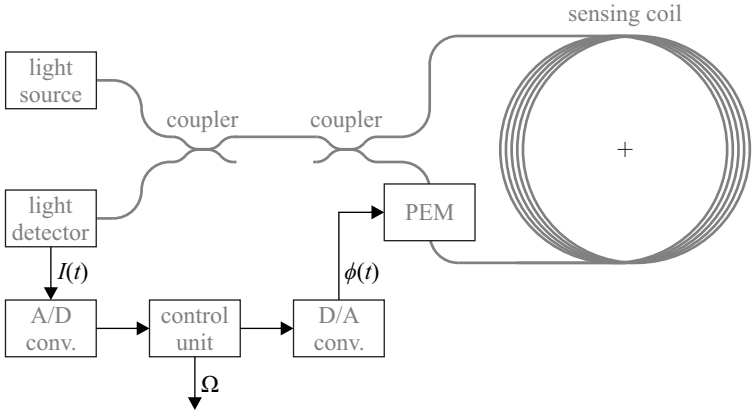


Fig. 3.1: Schematic of the IFOG testbench for the closed-loop modulation methods design.

The proposed methods were later tested using the developed IFOG testbench. Two IFOG prototypes have been developed. The purpose of the prototype 1 (P1) was mainly to test the designed processing methods and an optical architecture optimization. The prototype 2 (P2) was then a result of a miniaturization with the emphasis on cost reduction, implementing the newly developed methods into a fully integrated control unit.

3.1 Closed-loop modulation methods

3.1.1 Double-sine modulation

Prior to dealing with the approach to the Sagnac shift compensation, it is useful to recall the critical property of PEM, which is an uneven frequency response containing the resonances, making it impossible to introduce a broadband signal modulation reliably. The sinusoidal biasing modulation, as per Eq. 1.17, is thus used to facilitate the open-loop signal detection, further serving as an error signal for the closed-loop compensation. Instead of an analog demodulation by the lock-in amplifier, the open-loop signal is obtained by synchronous sampling, as in common digital closed-loop IFOGs. By setting the biasing modulation amplitude to $\Phi_b = \frac{\pi}{4}$ (i.e., $\Delta\Phi_b = \frac{\pi}{2}$), the intensity signal has a form similar to Eq. 1.15, assuming no further modulation. It can be shown that the same discrete intensity signal $I(k)$ can be obtained if the sampling period satisfies $T_{sa} = (2N_b - 1)\frac{\pi}{\omega_b}$, where N_b is a natural number. By calculating the difference between odd and even $I(k)$ samples, the open-loop signal is obtained, as described by the following equation:

$$S_{OL}(k) = [I(k) - I(k-1)]\,(-1)^k. \tag{3.1}$$

The discrete form can then be advantageously used to design an efficient compensation scheme. Similarly to the sawtooth compensation modulation, introducing a continuous non-reciprocal phase shift, in the case of the discrete signal, a DC-like compensation can be obtained by spectral flipping of the sinusoidal signal with the frequency of:

$$f_c = \frac{2N_c - 1}{T_{sa}}, \tag{3.2}$$

where N_c is a natural number. In other words, the sinusoidal modulation can effectively compensate the Saganc phase shift at the sampling moments. Based on this theory, the biasing modulation is optimal at the eigenfrequency, i.e., $\omega_b = \frac{\pi}{\tau}$, defining the sampling frequency:

$$T_{sa} = (2N_b - 1)\tau. \tag{3.3}$$

Assume the sinusoidal compensation modulation:

$$\phi_c(t) = \Phi_c \sin(\omega_c t), \tag{3.4}$$

where $\omega_c = 2\pi f_c$. With a total sensing coil delay of τ, the induced phase difference is:

$$\Delta\phi_c(t) = \phi_c(t) - \phi_c(t - \tau). \tag{3.5}$$

Assuming $N_b = 1$, the Eq. 3.3 implicates $T_{sa} = \tau$, and with the use of Eq. 3.2, the introduced phase difference is:

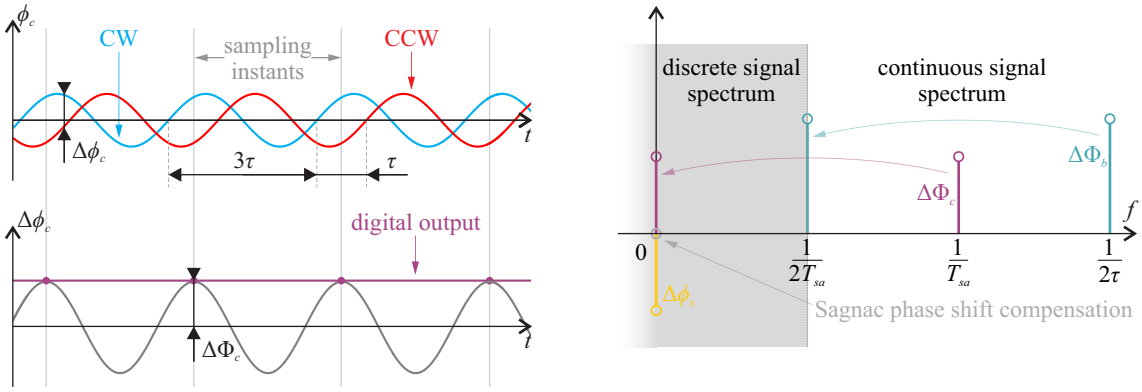
$$\begin{aligned}\Delta\phi_c(t) &= \Phi_c\left[\sin(2\pi f_c t) - \sin(2\pi f_c t - 2\pi f_c \tau)\right] = \\ &= \Phi_c\left[\sin\left(2\pi\frac{2N_c-1}{\tau}t\right) - \sin\left(2\pi\frac{2N_c-1}{\tau}t - 4\pi N_c - 2\pi\right)\right] = 0.\end{aligned} \tag{3.6}$$

Therefore, $N_b = 1$ can not be used. Nevertheless, it can be shown in a similar manner that for any $N_b > 1$, an equal nonzero discrete signal compensation is achieved. As it is required to maximize the data rate, the most convenient is the next possible sampling rate, i.e., $T_{sa} = 3\tau$. On the other hand, the compensation modulation frequency should be kept low, so $N_c = 1$ is optimal. Therefore, the compensation modulation frequency is defined to be:

$$f_c = \frac{1}{3}\tau = \frac{2}{3}f_b. \tag{3.7}$$

The effect of the compensation modulation on the CW and CCW beam phase and their difference is shown in Fig. 3.2(a). It can be seen that at the sampling moments, the phase shift of $\Delta\Phi_c$ is introduced, which manifests as non-reciprocal in the discrete signal. Therefore, the Sagnac phase shift can be directly compensated by adjusting the compensation modulation amplitude. This fact can also be viewed in the frequency domain in Fig. 3.2(b), where the sampling leads to the spectrum lines flipping, yielding a non-reciprocal phase shift at zero frequency in the discrete signal. The intensity signal with the double-sine (biasing and compensation) modulation is then expressed as:

$$I(t) = I_0\left[1 + \cos\left(\Delta\phi_s + \Delta\phi_b(t) + \Delta\phi_c(t)\right)\right], \tag{3.8}$$



(a) (b)

Fig. 3.2: Sinusoidal compensation modulation: (a) phase shift introduced to the CW and CCW beams, and resulting phase difference [149] (b) Sagnac phase shift compensation in the frequency domain [150].

where the individual modulation components are defined as:

$$\Delta\phi_b(t) = \Delta\Phi_b \sin(\omega_b t), \tag{3.9}$$

$$\Delta\phi_c(t) = \Delta\Phi_c \sin(\omega_c t + \varphi). \tag{3.10}$$

The $I(t)$ signal is then sampled with the period of $T_{sa} = 3\tau$. The sampling occurs in the maxima and minima of the $\phi_b(t)$ modulation, corresponding to the time shift of $\frac{\tau}{2}$. Using the substitution $t \to \left(3k\tau - \frac{\tau}{2}\right)$, and considering $\omega_b = \frac{\pi}{\tau}$, the discrete intensity is obtained:

$$I(k) = I_0\left\{1+\cos\left[\Delta\phi_s+\Delta\Phi_b \sin\left(3k\pi - \frac{\pi}{2}\right)+\Delta\Phi_c \sin\left(2k\pi - \frac{\pi}{3} + \varphi\right)\right]\right\}. \tag{3.11}$$

The compensation modulation component is maximized in the discrete signal if $\varphi = -\frac{\pi}{6}$; Eq. 3.11 can be then rewritten to:

$$I(k) = I_0\left\{1 + \cos\left[\Delta\phi_s - \Delta\Phi_b(-1)^k - \Delta\Phi_c\right]\right\}. \tag{3.12}$$

Consequently, Eq. 3.12 can be rewritten to:

$$I(k) = I_0\Big[1+A_0(\Delta\Phi_b)\cos(\Delta\phi_s-\Delta\Phi_c)-(-1)^k A_1(\Delta\Phi_b)\sin(\Delta\phi_s-\Delta\Phi_c)\Big], \tag{3.13}$$

where the coefficients $A_0(\Delta\Phi_b)$ and $A_1(\Delta\Phi_b)$ can be expressed as:

$$A_0(\Delta\Phi_b) = \cos(\Delta\Phi_b), \tag{3.14}$$

$$A_1(\Delta\Phi_b) = \sin(\Delta\Phi_b). \tag{3.15}$$

The open-loop signal is obtained according to Eq. 3.1, resulting in:

$$S_{OL} = 2I_0 A_1(\Delta\Phi_b) \cdot \sin(\Delta\phi_s - \Delta\Phi_c), \tag{3.16}$$

proving the Sagnac phase shift $\Delta\phi_s$ can be compensated by controlling the compensation modulation amplitude $\Delta\Phi_c$.

Compared to the traditional approach based on the ramp compensation modulation signal with a constant amplitude and a varying frequency, the proposed modulation method employs a fixed-frequency harmonic signal with a variable amplitude instead. The resulting modulation contains only two harmonic components, and it is thus easily applicable to the PEM. The only constraint is posed by the PEM resonances; they should not coincide with the modulation frequencies due to the possible amplitude instability induced by the resonances drift. The PEM geometry, as well as the material, has to be matched to the sensing coil, determining the transit time τ, and thus also the modulation frequencies ω_b and ω_c.

3.1.2 Quadruple-sine modulation

Compared to the sawtooth modulation, the disadvantage of the abovementioned method lies in the need for a perfect sampling synchronization and an infinitesimally short sample acquisition time. The problem of frequency synchronization can be possibly solved by an appropriate hardware, yet, the risk of PEM latency still remains. Furthermore, this latency can vary over time and due to different conditions. Nevertheless, the demand for close to infinitesimally short sample acquisition time increases the requirements for the hardware used. Furhthermore, the short acquisition time allows the propagation of higher noise level to the measured signal. Note that the intensity signal bandwidth can not be filtered according to the Nyquist theorem prior to sampling.

To overcome this issue, we can modify the double-sine modulation by adding higher harmonic components to the base biasing and compensation ones to broaden the intervals during which the Sagnac shift is compensated. Neglecting the bandwidth limitations, an infinite row of odd harmonic components can produce a square-wave signal. Nevertheless, as the density of the PEM resonances increases with frequency, in practical cases, using multiple higher harmonics rapidly increases the risk of coincidence with the resonance. A combination of the base component with only one further odd harmonic multiple will be thus examined. Assuming the biasing modulation at the eigenfrequency, i.e., $f_b = \frac{1}{2\tau}$, and the compensation modulation frequency according to Eq. 3.7, the properties of the first five odd harmonic multiples are shown in Tab. 3.1. As can be noted, whereas the biasing modulation harmonic multiples all exhibit equal performance, in the case of the compensation modulation, only some of them are usable. This results from the fact that the modulation at $\frac{1}{\tau}$ multiple frequency is nulled when the CW and CCW beam are combined. The peak portions of the base harmonic can be flattened by adding the k-th harmonic component, assuming the second derivative reaches zero. It can be shown that this is achieved when the ratio of their amplitudes is $1 : k^2$. Therefore, the phase difference introduced by the biasing and the compensation modulation, respectively, can be expressed as:

$$\Delta\phi_b(t) = \frac{k_b^2}{k_b^2 - 1}\Delta\Phi_b \sin(\omega_b t) + \frac{1}{k_b^2 - 1}\Delta\Phi_b \sin(k_b\omega_b t), \tag{3.17}$$

$$\Delta\phi_c(t) = \frac{k_c^2}{k_c^2 - 1}\Delta\Phi_c \sin\left(\omega_c t - \frac{\pi}{2}\right) + \frac{1}{k_c^2 - 1}\Delta\Phi_c \sin\left(k_c\omega_c t + \frac{\pi}{2}\right), \tag{3.18}$$

preserving the modulations depth $\Delta\Phi_b$ and $\Delta\Phi_c$. With the phase difference signal peaks flattening, the error caused by non-infinitesimally short sample acquisition time can be reduced significantly. The impact of the ratio between the sample

Tab. 3.1: Comparison of the higher harmonics components of the biasing and compensation modulation.

Modulation component	Phase delay between CW and CCW direction φ_τ	Modulation efficiency $\eta_* = \frac{\Delta\Phi_*}{\Phi_*}$	Applicable for modulation
$\phi_{b1}(t)$	π	2	yes
$\phi_{b3}(t)$	3π	2	yes
$\phi_{b5}(t)$	5π	2	yes
$\phi_{b7}(t)$	7π	2	yes
$\phi_{b9}(t)$	9π	2	yes
$\phi_{c1}(t)$	$\frac{2}{3}\pi$	$\sqrt{3}$	yes
$\phi_{c3}(t)$	2π	0	no
$\phi_{c5}(t)$	$\frac{10}{3}\pi$	$\sqrt{3}$	yes
$\phi_{c7}(t)$	$\frac{14}{3}\pi$	$\sqrt{3}$	yes
$\phi_{c9}(t)$	6π	0	no

acquisition time T_{acq} and τ on the error of the measured Sagnac phase shift $\Delta\phi_s$ for various harmonic components combinations is displayed in Fig. 3.3. For $\Delta\phi_s$ values in the order of radians, the relative error value remains approximately constant. Moreover, a negligible difference is observed between combinations where only the biasing modulation component order k_b is changed, so the curves for $k_b = 3 \ldots 9$ are plotted as a single curve in Fig. 3.3. Nevertheless, it can be seen that adding the harmonic components can significantly decrease the $\Delta\phi_s$ detection error. Further, assuming the intensity signal is burdened by white noise, prolonging the sample

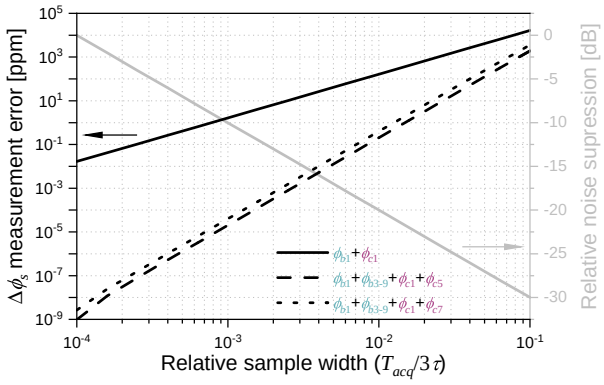


Fig. 3.3: Simulated dependency of $\Delta\phi_s$ detection error caused by the non-zero length of sample acquisition for different modulation harmonic components combinations and a relative white noise level suppression.

acquisition time has a positive effect on its mitigation in the resulting discrete signal.

Assuming the sampling frequency $f_{sa} = \frac{1}{T_{sa}} = 100$ kHz and the acquisition time $T_{acq} = 100$ ns, the error is reduced by nearly three orders if components $\phi_{b3}(t)$ and $\phi_{c5}(t)$ are added. The lowest components also constitute an optimum from the bandwidth perspective, as the probability of avoiding the PEM resonances is the largest. The comparison of the double-sine and the quadruple-sine modulation scheme, comprising the components according to Eq. 3.17 and 3.18 with $k_b = 3$ and $k_c = 5$ is shown in Fig. 3.4. However, adding further harmonic components imposes even more stringent requirements on PEM performance over the frequency. The suitability of the PEM for selected modulation harmonic components should thus always be verified. An example can be seen in Fig. 3.5 for a hard-ceramics PEM (NCE40, outer diameter of 25.4 mm, height 12.7 mm, and wall thickness 3.15 mm)

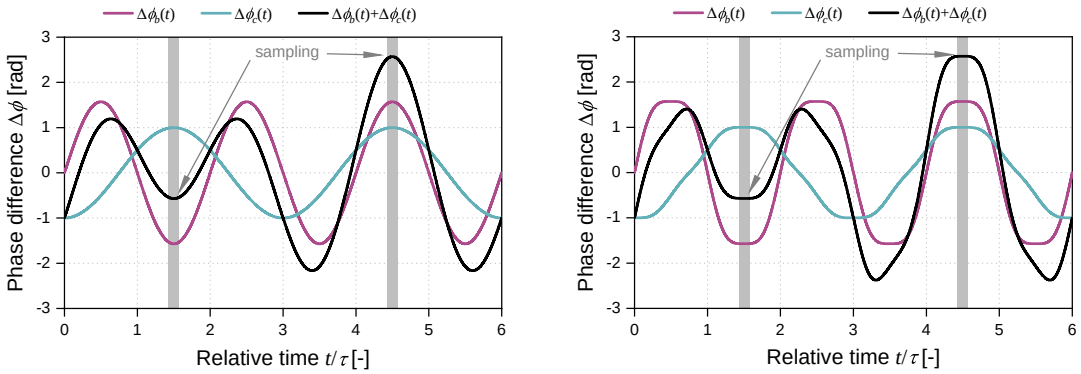


Fig. 3.4: Biasing and compensation modulation waveforms with the double-sine (a) and the quadruple-sine (b) modulation (for $\Delta\Phi_c = 1$ rad) [150].

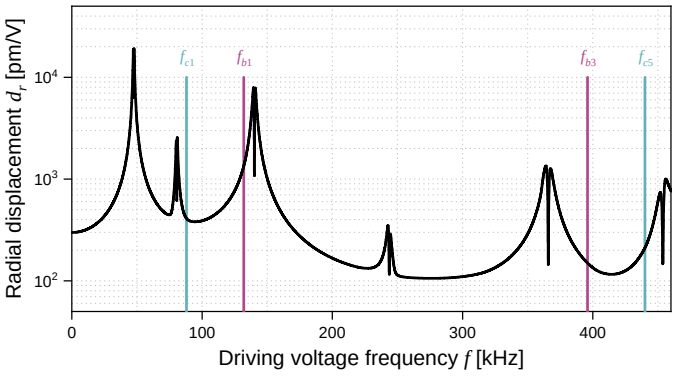


Fig. 3.5: Sample PEM radial displacement frequency spectrum and the harmonic components distribution for the quadruple-sine modulation scheme (simulated with finite elements method) [150].

and a sensing coil having $\tau = 3.78$ µs.

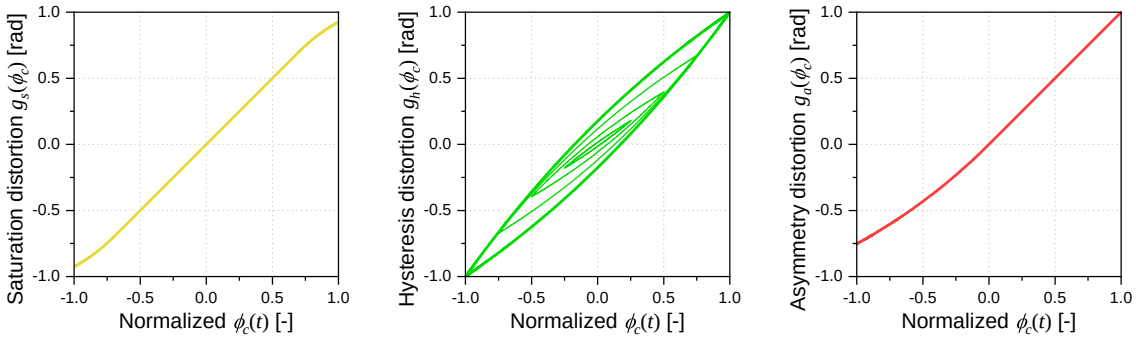
3.1.3 Modulation parasitic effects

The compensation of the Sagnac phase shift through the amplitude $\Delta\Phi_c$ is based on an assumption of the linear transfer function of the PEM as well as the corresponding driving circuits. However, as previously discussed with PEM, there are several factors affecting the voltage-to-phase shift transfer. These include especially hysteresis, asymmetry between the positive and negative fiber stretch, temperature dependency, and aging. Further nonlinearity can be attributed to the driving circuits, limited by the slew rate, saturation, and harmonic distortion.

As for the biasing modulation, it has been demonstrated that using the eigenfrequency suppresses the asymmetry of PEM response, as well as a possible parasitic intensity modulation [151, 152]. This can be achieved by ensuring that the sampling occurs at the maxima (or minima) of $\phi_b(t)$ signal. Conversely, this is not true for the $\phi_c(t)$ signal, even though the resulting difference $\Delta\phi_c(t)$ satisfies the condition. As shown in Fig. 3.2(a), at the sampling instants in both CW and CCW directions, the ϕ_c is ascending for the given $\Delta\phi_s$ polarity. Assuming the asymmetry between positive and negative half-periods is the only present effect, the corresponding nonlinearity between the effective compensation modulation depth Φ_c and the voltage U_c applied to PEM is induced. Furthermore, the inclusion of hysteresis causes an inequality between the ascending and descending portions in $\phi_c(t)$. Therefore, the closed-loop compensation response becomes different for positive and negative angular rates. Finally, although the PEM driving voltage is usually far below its saturation level, we need to consider the saturation posed by the analog driving circuits, which can manifest itself as we approach the voltage limits.

These three phenomena were considered while creating the PEM distortion model, comprising saturation g_s, hysteresis g_h, and asymmetry g_a. All these effects were modeled as piecewise exponential functions, which sample transfer functions are shown in Fig. 3.6. Whereas g_s and g_a can be described by a simple analytical form, g_h operates with the internal dynamics, requiring knowledge of the previous states to correctly reflect the input derivative sign switching. By adjusting the distortion model parameters, a good approximation of the PEM induced closed-loop IFOG nonlinearity can be obtained, as shown in Fig. 3.7[1]. For the purpose of further analysis, let us assume normalized parasitic effects distortion level coefficients γ_a, γ_h, and γ_s equal to 1 for the measured data distortion approximation in Fig. 3.7.

[1]The experimental test was performed with P1 IFOG using the double-sine modulation. The simulation was done with a numeric closed-loop IFOG model with a piecewise exponential PEM distortion approximation.



(a) (b) (c)

Fig. 3.6: Components of closed-loop IFOG linear distortion approximation: saturation g_s (a), hysteresis g_h (b), and asymmetry g_a (c).

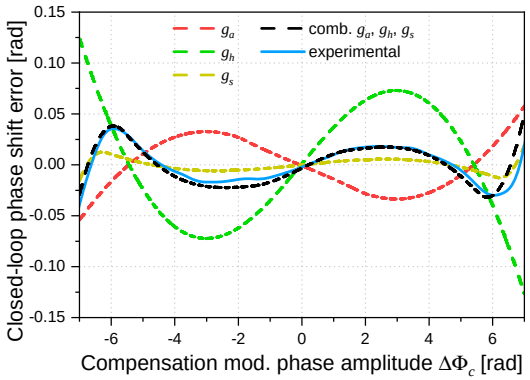


Fig. 3.7: Closed-loop IFOG linearity error - comparison of experimental (P1) and simulated response including PEM linearity distortion model with separate effects of individual components.

As soon as the model of the closed-loop IFOG parasitic effects is known, there is a possibility to compensate the errors by the corresponding correction of the direct output. Nevertheless, a further effect that needs to be taken into account is temperature. In such a scenario, the distortion model parameters have to be identified as functions of temperature, and the correction should be made according to the actual temperature of PEM, which must be measured simultaneously with the angular velocity. A similar approach was presented in [63] to correct the output of an open-loop IFOG. However, instead of an analytical model, the nonlinear distortion is defined by the neural network trained with the calibration data.

The general drawback of the model-based correction methods lies in including only a limited range of selected parasitic effects, which have to be a priori known for specific conditions, such as temperature, and detection of these conditions at the same time. A problem may arise outside the operational conditions or angular

rate ranges covered by the calibration. Additionally, the model approximation in between the calibration points can be less accurate. This is especially risky with a NN model, which may tend to over- or under-fitting if an inappropriate structure is chosen. Further, reflecting some other effects, like aging, can be challenging. Also, the temperature hysteresis of the PEM can play a significant role, as demonstrated in [150]. This concerns not only the determining parameters, such as the charge coefficient, but in the case of the model-based correction approach, also the γ_* coefficients of the three-component PEM distortion model. Though, it can be assumed that the model complexity could increase dramatically with an explicit involvement of this phenomenon.

3.1.4 Modulation depth control

Although the model-based correction approach may suit lower- or medium-grade applications, it lacks the robustness and the reliability provided by the traditional closed-loop methods based on the sawtooth modulation utilizing EOM. As discussed before, the monitoring of the modulation depth is performed by the four-state modulation scheme, enabling a direct and real-time detection of the actual phase modulation depth and a corresponding output correction. Although such an approach can not be directly transferred to the proposed modulation scheme, the PEM modulation monitoring can be performed externally by measuring its actual movement.

One of the possible approaches consists in a measurement by means of an external non-optical sensor, such as a strain gauge or a piezoelectric sensor. The strain gauge is capable of providing reasonable data when monitoring the piezoelectric actuators. In this case, the limiting factor can be the modulation frequency, reaching up to the orders of 10^5 Hz, which, considering the sensor's bandwidth, can be a critical restriction. Also, the typical tube shape of the PEM and its supra-resonant operation for distinct sinusoidal modulation components make it difficult to find an optimal sensor placement for a reliable modulation depth measurement. While the piezoelectric sensor may seem better suited due to its larger bandwidth, it can suffer from the already discussed parasitic effects, which, in the worst-case scenario, can be in correlation with the PEM. The tight connection between the direct and the indirect piezoelectric effect thus can make the sensor output data unusable for the actual PEM movement monitoring.

Most of the mentioned issues can be solved by measuring the fiber stretching effect directly by utilizing an additional optical fiber wrapped on the PEM alongside the IFOG trace fiber. If both fibers are bonded identically, the mechanical coupling effect between the actuator and the fiber itself can also be suppressed. Nevertheless, the optical sensing brings another difficulty in the fiber stretch evaluation. The Fiber

Bragg gratings or the long period gratings, typically used to sense strain, suffer from lower bandwidth as well as high complexity of their interrogation. Therefore, a viable solution can be an interferometric measurement employing, e.g., the Mach-Zehnder setup. This solution still represents a significant increase in complexity, as it requires not only the input light branch but also a separate light detector and corresponding processing.

The obstacles discussed above present crucial limitations on the performance of an actual PEM, particularly in terms of compensation modulation depth. The ultimate solution lies then in an assumption that the desired information is already involved in the resulting intensity signal $I(t)$. Yet, it can not be resolved from the discrete signal $I(k)$ as defined by Eq. 3.11 since, by principle, the phase difference is fully compensated at those moments. Detection of $I(t)$ signal level in other points is thus required.

Assume the conversion function f_{PEM}, describing a relationship between the modulation voltage $u(t)$ and resulting phase shift, has a simple form of:

$$\phi(t) = f_{PEM}(u(t)) = K_{PEM}(\omega)u(t), \tag{3.19}$$

where $K_{PEM}(\omega)$ is a frequency-depended voltage-to-phase gain, comprising the PEM and its driving circuits. For the quadruple-sine modulation, the PEM driving voltage is composed of the components as follows:

$$u(t) = u_{b1}(t) + u_{bk_b}(t) + u_{c1}(t) + u_{ck_c}(t). \tag{3.20}$$

Considering $\Delta\Phi_* = \eta\Phi_*$, as specified by Tab. 3.1, the biasing and the compensation modulation can be then described as:

$$\Delta\phi_b(t) = \frac{2K_{PEM}(\omega_b)k_b^2}{k_b^2 - 1}U_{b1}\sin(\omega_b t) + \frac{2K_{PEM}(k_b\omega_b)}{k_b^2 - 1}U_{bk_b}\sin(k_b\omega_b t), \tag{3.21}$$

$$\begin{aligned}\Delta\phi_c(t) = &\frac{\sqrt{3}K_{PEM}(\omega_c)k_c^2}{k_c^2 - 1}U_{c1}\sin\left(\omega_c t - \frac{\pi}{2}\right) + \\ &+\frac{\sqrt{3}K_{PEM}(k_c\omega_c)}{k_c^2 - 1}U_{ck_c}\sin\left(k_c\omega_c t + \frac{\pi}{2}\right),\end{aligned} \tag{3.22}$$

where U_* stands for the corresponding amplitudes of the driving voltage components. By comparing the Eq. 3.22 to the Eq. 3.18, the depth of the compensation $\Delta\Phi_c$, corresponding to the measured Sagnac phase shift $\Delta\phi_s$, is:

$$\Delta\Phi_c = \sqrt{3}K_{PEM}(\omega_c)U_{c1}, \tag{3.23}$$

$$\Delta\Phi_c = \sqrt{3}K_{PEM}(k_c\omega_c)U_{ck_c}. \tag{3.24}$$

Assuming the $K_{PEM}(\omega_c)$ and $K_{PEM}(k_c\omega_c)$ terms can be, to a certain extent, considered to be correlated at given operating conditions, it is possible to introduce a proportional coefficient:

$$G_c = \frac{K_{PEM}(\omega_c)}{K_{PEM}(k_c\omega_c)}. \tag{3.25}$$

A similar form can be derived for the biasing modulation:

$$G_b = \frac{K_{PEM}(\omega_b)}{K_{PEM}(k_b\omega_b)}. \tag{3.26}$$

The goal of the modulation depth control is thus an estimation of the $K_{PEM}(\omega_c)$ only. As a result, the actual value of the compensation modulation depth is obtained, according to Eq. 3.23.

As suggested above, we assume that $K_{PEM}(\omega_c)$ can be measured from the $I(t)$ with a certain accuracy. In accordance with Eq. 3.23, an estimation of $\Delta\Phi_c$ from $I(t)$ is required. This may appear to lead to the origins of the defined problem with $\Delta\Phi_c$ detection. However, it is important to remark that the rate of the $\Delta\Phi_c$ computation (as per Eq. 3.23) and the inverse operation of $K_{PEM}(\omega_c)$ calculation differ by several orders of magnitude. Whereas the $\Delta\Phi_c$, corresponding to the angular velocity, is assumed to be a large-bandwidth signal, the $K_{PEM}(\omega_c)$ depends on the surroundings conditions, which changes much more slowly, and can be thus considered as constant for the purpose of the calculation described by Eq. 3.23. The procedure of the compensation modulation depth control is shown in Fig 3.8.

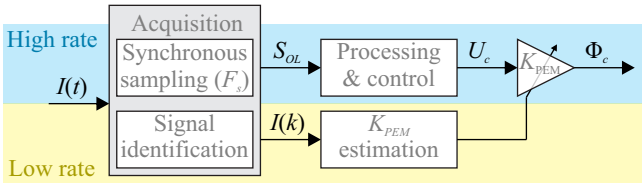


Fig. 3.8: Schematic of the compensation modulation depth control in the PEM-based closed-loop IFOG.

For both the double-sine as well as the quadruple-sine modulation, the intensity is described by Eq. 3.8. Nevertheless, as described in [150], retrieving the compensation modulation depth analytically by calculating an inverse cosine of $I(t)$ leads to several difficulties. Firstly, neither the gain nor the offset of the real acquired intensity signal is precisely known and can not be considered constant. Secondly, the periodicity of the interference function does not allow a reliable phase decoding beyond the unambiguous region. Therefore, the method adopted further relies on a reverse approach based on the numerical modeling of the intensity signal denoted as $\hat{I}(t)$ and comparing it to the actual intensity by means of an error function

$E\left(\hat{I}(t), I(t)\right)$, which is minimized in terms of the compensation modulation depth estimation $\Delta\hat{\Phi}_c \rightarrow \Delta\Phi_c$. The estimation obtained in this way can then be used to update the $K_{PEM}(\omega_c)$ value, valid for current conditions.

The minimization of $E\left(\hat{I}(t), I(t)\right)$ is a nonlinear problem, and several numerical approaches can be considered. For the purpose of processing, assume the discrete form of both signals $I(k)$, $\hat{I}(k)$, obtained by sampling with a period of $T_{sf} \ll T_{sa}$. Further, assuming a steady state, when $\Delta\phi_s$ is constant and fully compensated ($S_{OL} \rightarrow 0$), $I(k)$ and $\hat{I}(k)$ can be interpreted as vectors corresponding to one signal period, so that $k = \langle 0; K_f - 1\rangle$, where $K_f = \frac{3\tau}{T_{sf}}$. As a next step, an error function has to be defined. The optimal criterion of $\Delta\hat{\Phi}_c \rightarrow \Delta\Phi_c$ requires $\Delta\Phi_c$ measurement, which can be only attained by calibration with the exact knowledge of Ω and the IFOG scale factor according to Eq. 1.12. However, this can be problematic when reaching the desired precision since further errors may be introduced, e.g., by λ or L stability. A more viable approach is thus posed by a direct comparison of $I(k)$ and $\hat{I}(k)$ vectors in a simple quadratic form, defined as:

$$E\left(\hat{I}(k), I(k)\right) = \sum_{0}^{K_f-1} \left(\hat{I}(k) - I(k)\right)^2. \tag{3.27}$$

By involving the parasitic effects linearity distortion model, where the normalized distortion coefficients $\gamma_* = \gamma = 1$, the Sagnac phase shift detection error when the quadratic form error criterion is employed is shown in Fig. 3.9. Note the error is due to the modeled parasitic effects, causing a linearity distortion, which impact is increasing with the modulation depth. Compared to the original distortion (Fig. 3.7), the detection error with the estimation is lower by about one order, making such approach viable. Next to it, the major benefit is the resilience against

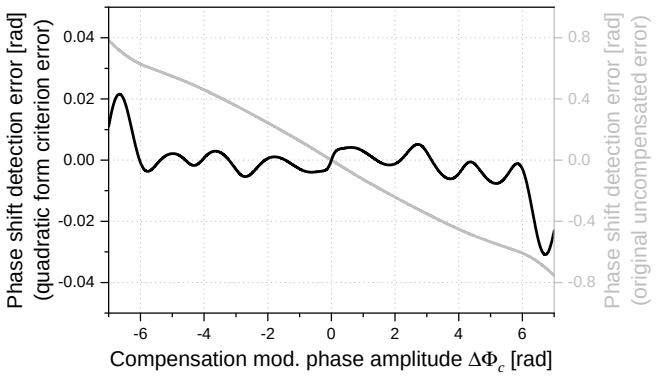


Fig. 3.9: Residual phase shift detection error of the quadratic criterion error function with the linearity distortion model ($\gamma = 1$) and the original uncompensated absolute error.

$K_{PEM}(\omega_c)$ fluctuations due to temperature and time, and thus an increased stability of the depth estimation $\Delta\hat{\Phi}_c$.

Once the assessment of the $\hat{I}(t)$ signal can be performed, it is possible to design an estimator of the vector of parameters $\hat{\theta}$, which is then fed to the $\hat{I}(t)$ model, and thus closes the depth control loop, as schematically shown in Fig. 3.10. So far, the only parameter assumed was the compensation modulation depth, i.e., $\hat{\theta} = \Delta\hat{\Phi}_c$. However, a closer approximation of $I(t)$, distorted by the parasitic effects, may, in general, require more parameters.

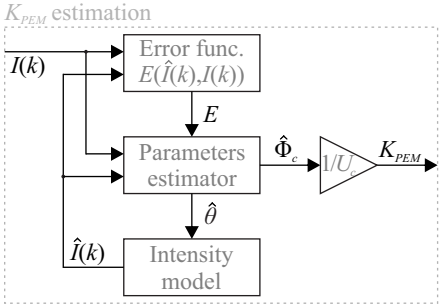


Fig. 3.10: Iterative procedure of the K_{PEM} estimation.

Taking a closer look at the $\hat{\theta}$ estimator, its task is to adjust the individual elements to minimize the error E. Performing such a task in a single step is obviously rather challenging since there is a broad range of parameters and errors that may affect the $I(k)$ and $\hat{I}(k)$ vector combinations for specific angular rates. These include noise, amplitude and phase errors of all harmonic components, and especially the distortion due to the parasitic effects, which can not be reliably approximated over the whole range of conditions with a simple model. Instead, an iterative minimization of the error E in multiple steps provides a better stability of the optimal $\hat{I}(k)$ searching, despite requiring a longer computation time. The assumption is made on the fact that the $\hat{\theta}$ estimation precision increases with decreasing error E. Herein, two approaches of the $\hat{\theta}$ estimation are proposed and compared: the Neural network closed-loop estimation (NNCLE) and the Least-square curve fitting estimation (LSCFE).

The first approach is a function-based relation between the deviation of $I(k)$ and $\hat{I}(k)$ vectors and the optimal parameters vector $\hat{\theta}$. Based on the previous discussion, an exact analytic description could be challenging due to its complexity and a possible instability caused by the random factors. The problem can be simplified by employing an approximation of this function using a neural network (NN) regression. The NN can serve as an iterative estimator, providing a correction $\Delta\hat{\theta}$ of parameters vector $\hat{\theta}$ for the next iteration. Either a simple form, such as:

$$\hat{\theta}(n+1) = \hat{\theta}(n) + \Delta\hat{\theta}(n) \tag{3.28}$$

can be used, or, more conveniently, we can use a proportional-integration (PI) controller form:

$$\hat{\theta}(n+1) = I_{\hat{\theta}} \sum_{\nu=0}^{n} \Delta\hat{\theta}(\nu) + P_{\hat{\theta}} \Delta\hat{\theta}(n), \tag{3.29}$$

where $I_{\hat{\theta}}$ and $P_{\hat{\theta}}$ stand for its constants. This form is less susceptible to the $\Delta\hat{\theta}(n)$ estimation inaccuracy. As for the NN input data, it is convenient to compress the $\hat{I}(k)$, $I(k)$ to obtain a deviation vector:

$$D(k) = f\left(\hat{I}(k), I(k)\right), \tag{3.30}$$

where $\dim(D(k)) < \dim\left(\hat{I}(k)\right) + \dim(I(k))$. Such a function should contain mutual normalization and comparing operations between $\hat{I}(k)$ and $I(k)$, such as a simple difference in time or frequency domain. The dimension can then be further reduced by filtering or the principal components analysis (PCA) method. Furthermore, the NN uses an auxiliary input U_{c1}, providing an approximate delimitation of the $\hat{\theta}$ estimate. The proposed NNCLE method is schematically shown in Fig. 3.11. Note that the error E is not included when NN is used for the estimation. However, it must be present during its training, as it is the decisive criterion for the identification of the $\Delta\hat{\theta}$ target values.

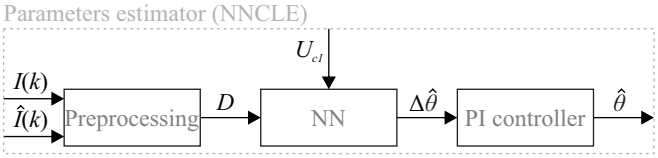


Fig. 3.11: Parameters estimator employing the NNCLE method.

The LSCFE, on the other hand, is a heuristic approach, where the relation between the $\hat{I}(k)$ and $I(k)$ is unknown. In general, this method may employ various algorithms (such as Levenberg-Marquardt or trust region reflective algorithm) differing in speed or robustness, and the selection can be performed depending on the specific problem. The block of the Parameters estimator in Fig. 3.10 is thus represented by an appropriate algorithm minimizing the $E\left(\hat{I}(t), I(t)\right)$. Similarly to the NNCLE method, multiple iterations are needed to obtain a final vector $\hat{\theta}$, satisfying a termination condition. Note that even when the E is minimized, its final value will be nonzero, reflecting that the vectors $\hat{I}(k)$ and $I(k)$ are never equal, which results from the nonlinear distortion in $I(k)$. This is not a problem of the previous method, where the NN output may converge to the actual parameters θ even after a single iteration. Moreover, since we deal with a highly nonlinear problem, the convergence is highly dependent on the initial estimate $\hat{\theta}_0$. This may also determine which parameters will form this vector, as they can be measured or estimated approximately

prior to the error function minimization. Also, the convergence speed may vary for different methods.

Although both proposed methods are equivalent in their overall functionality (as shown in Fig. 3.10), they differ significantly in their implementation and data preparation. The NNCLE, once established by terms of its structure as well as the parameters, defined in the NN training process, can be very efficient in computation since only simple numerical operations are used, the number of which is known beforehand. Furthermore, assuming appropriate NN regression model is used, a rapid convergence after a single iteration can be achieved, as discussed before. On the other hand, the NNCLE method is burdened by the need for training, including also the data acquisition and preparation. The training data set, including the input vector ($D(k)$, U_{c1}) and the target values of $\Delta\hat{\theta}$, must cover a sufficient sub-space of all possible combinations of $I(k)$ and $\hat{I}(k)$ in combination with U_{c1}. The $I(k)$ can either be acquired by a measurement, carried out for different angular velocities and operational conditions, or obtained by simulations if the nonlinear distortion model can cover the real system behavior sufficiently well. The training procedure has thus a significant impact on the stability of $\hat{\theta}$ estimation, and therefore also on the modulation depth control, under different set of operational conditions. Similarly, convergence of the LSCFE method depends on the initial estimate and the specific algorithm employed. From this point of view, both methods are non-deterministic.

The testing and verification of the discussed methods were performed by simulation, where the real $I(t)$ signal was emulated by the nonlinear distortion model with added white noise. As discussed before, the intensity signal model $\hat{I}(k)$ can approximate the real signal to the extent determined by its parameters $\hat{\theta}$. In an optimal case, the $\hat{I}(k)$ model can even cover the distortion, such as asymmetry, hysteresis, and saturation, if they are parametrized by $\hat{\theta}$. Nevertheless, such an approach would bring excess computational expenses, especially in the case of the LSCFE method, and possibly degrade the overall stability of the estimation procedure. For the purpose of verification, a simple parametrization $\hat{\theta} = (\Delta\hat{\Phi}_c, \Delta\hat{\Phi}_b)$ is thus chosen, reflecting the depth control of the major modulation components. The Figs. 3.12 and 3.13 show the results of the NNCLE and LSCFE method for different parasitic effects distortion levels.[2]

The training data were generated for the given range of $\Delta\phi_s$ and with a sweep of $\hat{\theta}$. The parameters error vector $\Delta\hat{\theta}$ was obtained by zero offsetting, corresponding to the minimum of the quadratic error function (Eq. 3.27). Further, a preprocessing

[2]As the NN weight initialization during the training is a pseudo-random process, the resulting shape of the phase shift detection error with the NNCLE is different each time, especially for larger $|\Delta\Phi_c|$ values. The Fig. 3.12 thus demonstrates the error bounds, which were similar also for further trials of the NN training, rather than a specific curve shape

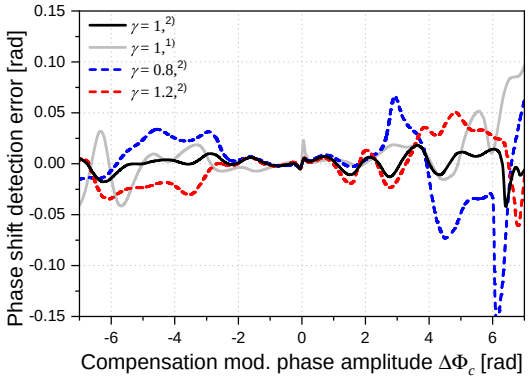


Fig. 3.12: Phase shift detection error with the NNCLE correction method for different NN size (HLS – hidden layer size) and relative parasitic effects distortion levels γ ([1)]HLS = [100, 10], medium training length, [2)] HLS = [300, 30], large training length).

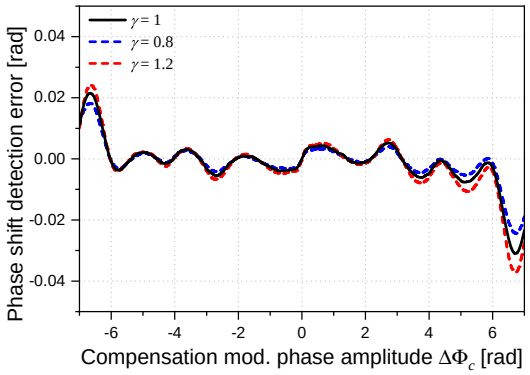


Fig. 3.13: Phase shift detection error with the LSCFE correction method for different relative parasitic effects distortion levels γ.

in the form of a simple difference $D(k) = \hat{I}(k) - I(k)$ was used. Such data were then used to train the NN with the scaled conjugate gradient backpropagation method in the Matlab environment employing a Simulink model of the IFOG system. Similar testing was also performed using the LSCFE method. This method does not require either the training dataset generation or the training process itself, and it is thus easier to test assuming the same conditions. The emulated intensity signal was burdened by the equal amount of distortion and noise, and also the equal intensity model $\hat{I}(k)$ and parameters vector $\Delta\hat{\theta}$ were employed. The initial estimate $\hat{\theta}_0$ was based upon the simulation parameters without a distortion. In a real system, these can be obtained by calibration, when the $K_{PEM}(\omega_b)$ and $K_{PEM}(\omega_c)$ gain is approximately measured. The resulting error with the LSCFE method, obtained by simulation in the Matlab environment, almost overlaps with the residual error

limiting case, displayed in Fig. 3.9.

When comparing the methods by simulations with equal conditions (noise level, power level, γ level), it can be clearly seen that the performance of the NNCLE method is notably worse, even though its original training data and the LSCFE output data are equivalent. This can be explained by the fact that the NN approximation introduces an additional error. The root of this error lies in a complex relation between the $D(k)$ vector and the actual $\Delta\Phi_c$ value. On the other hand, although the NN was trained with the voltage U_{c1} derived from an actual value of $\Delta\phi_s$, in the NN implementation, the convergence of $\Delta\hat{\Phi}_c$ to its best estimation (as shown in Fig. 3.9) is equally attained if a slightly different U_{c1} voltage is used as an initial value instead. An analysis of various NN structures in terms of the hidden layers size as well as the training methods was performed. It was shown that by using suitable preprocessing, such as PCA or filtration with decimation, the $D(k)$ dimensionality can be conveniently reduced if K_f is higher, making the computation more efficient. Nonetheless, using such methods did not significantly improve the error bounds in Fig. 3.12, which also applies to the different NN sizes and training methods.

Nevertheless, although the NNCLE can not diminish the distortion effect on the linearity of the output data, it can stabilize the static change of the scale factor, assuming the distortion does not vary significantly. However, even a 20% change in γ coefficients leads to a noticeable deterioration of the linearity, especially for the higher compensation modulation depth. The LSCFE method is less susceptible to the distortion level, as it is not coupled with its specific level due to the specific training data. On the other hand, the drawback of the LSCFE method lies in the requirement of more computational resources, as the multidimensional function minimization of the given task is relatively complex compared to the NN single data pass.

However, despite the capability to suppress the parasitic effects induced nonlinearity varies, both methods are able to supress the $\Delta\hat{\Phi}_c$ detection susceptibility to K_{PEM} fluctuations, as demonstrated by the uncompensated characteristics in Fig. 3.9. Therefore, they were proven to principally pose as an equivalent to the four-state modulation depth control in the established square-wave modulation scheme. The parasitic effects-induced nonlinearity, which is inherent to the PEM, represents thus an additional issue that the prior methods have not addressed. From this point of view, the LSCFE method appears as a better candidate, since it provides additional robustness with the nonlinearity shape change, caused by the nonlinear distortion parameters drift. This can not be reflected by the NNCLE method since it is strictly bound to the nonlinearity shape contained within the training data.

3.1.5 Stabilization of the modulation signal parameters

The modulation parasitic effects, represented by the linearity distortion model, may manifest themselves as an instability of $K_{PEM}(\omega)$, especially when they vary with the operation conditions and time. Such an issue can be addressed with the proposed modulation depth control methods. So far, it was assumed that the modeled intensity vector $\hat{I}(k)$ fits the measured data $I(k)$ with a small residual error, and the compensation modulation depth thus can be determined accurately, so that $\Delta\hat{\Phi}_c \rightarrow \Delta\phi_s$. However, as the parasitic effects also lead to a nonlinear distortion, the minimal residual error $E\left(\hat{I}(k), I(k)\right)\Big|_{\min}$ is hence increased, and the depth estimate $\Delta\hat{\Phi}_c$ becomes less accurate. This can be seen from Fig. 3.14, showing the minimum of the error function $E\left(\hat{I}(k), I(k)\right)$ and the corresponding $\Delta\hat{\Phi}_c$ in dependence on the relative proportion of the parasitic effects γ, as demonstrated in Fig. 3.15, where the $I(k)$ and the approximation $\hat{I}(k)$ according to Eq. 3.25 is portrayed.

The key parameters of $I(t)$ signal, the proper setting of which has a crucial impact on the modulation depth control performance due to the parasitic effects, include the phase of the individual harmonic components and, in the case of the quadruple-sine modulation scheme, also the relative magnitude levels of the higher harmonic components (k_b, k_c). Consequently, their individual relative ratios can deviate from the ideal ratio, as stated in Eqs. 3.17 and 3.18. Additionally, as the phase and amplitude of the $\Delta\phi(t)$ signal components deviate from their optimal values, the performance of the quadruple-sine modulation is further degraded, as also seen in Fig. 3.15. Consequently, the open-loop signal (S_{OL}) detection is less

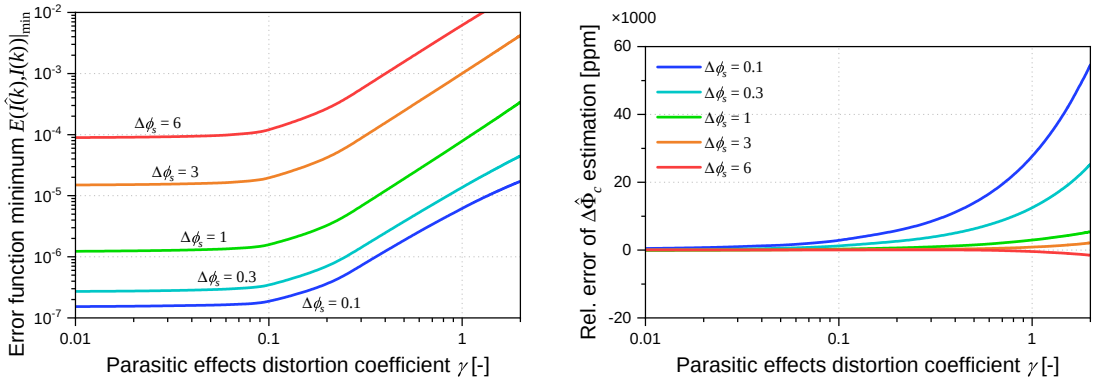


Fig. 3.14: Error function minimum $E\left(\hat{I}(k), I(k)\right)$ (a) and the corresponding error of the modulation depth estimate $\Delta\hat{\Phi}_c$ (b) in dependence on the γ coefficient level.

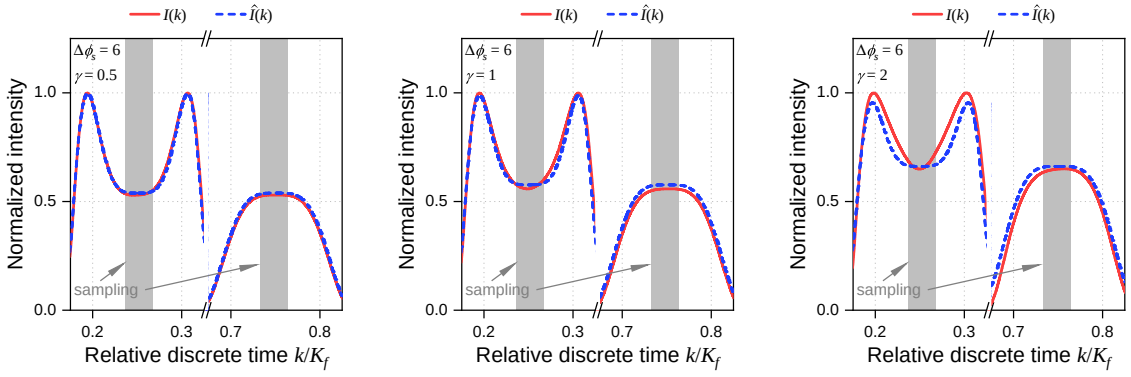


Fig. 3.15: The intensity signal with the parasitic effects model and its model-based estimate.

accurate due to the non-infinitesimal duration of sample acquisition time T_{acq}, and the $\Delta\phi_s$ detection error may thus notably exceed the theoretical limits valid for the optimum case (Fig. 3.3).

Rather than including these deviations into the modeled intensity signal $\hat{I}(k)$ as the $\hat{\phi}(t)$ phase difference errors, it is more convenient to compensate these error components directly in the real $\phi(t)$ signal. For the purpose of error detection of the individual frequency components in the phase difference signal $\Delta\phi(t) = \Delta\phi_b(t) + \Delta\phi_c(t)$, where the ideal biasing and compensation modulations are described by Eq. 3.17 and Eq. 3.18, the acquired discrete intensity signal $I(k)$ and its model without the errors $\hat{I}(k)$ can be fittingly used.

Assuming the quadruple-sine modulation with $k_b = 3$ and $k_c = 5$, the phase error of the four modulation components can be denoted as ψ_{b1}, ψ_{b3}, ψ_{c1}, and ψ_{c5} correspondingly. Although the phase shift of the individual signal components can be generally determined easily by frequency analysis, the problem here is more complex. This results not only from the interference function nonlinearity, but also from the parasitic effects distortion, introducing further harmonic components. Therefore, the ψ_* errors should be determined in the time domain by utilizing a suitable criterion reflecting the main target of the proposed methods – accurate detection of the open-loop signal S_{OL}. Regardless of the presence of the distortion in the $I(t)$ signal or the distortion level, the ψ_* should be ideally diminished, especially in and near the sampling points, marked in Fig. 3.4. The $I(t)$ signal thus has to be examined within these portions. Assuming $I(k)$ is the discrete representation of $I(t)$, i.e., it satisfies the sampling theorem, four subsections I_{s*} can be defined in a single

$I(k)$ period:

$$\begin{aligned} I_{s1}(k) =& I\left(\tfrac{1}{4}K_f + 1 + k\right), \\ I_{s2}(k) =& I\left(\tfrac{1}{4}K_f - 1 - k\right), \\ I_{s3}(k) =& I\left(\tfrac{3}{4}K_f + 1 + k\right), \\ I_{s4}(k) =& I\left(\tfrac{3}{4}K_f - 1 - k\right), \end{aligned} \tag{3.31}$$

where $k = \left\langle 0; \frac{K_f}{4} \right)$, and $K_f = \frac{3\tau}{T_{sf}}$ stands for the discrete period of the $I(k)$. It can be shown that the error functions exhibiting a minimal cross-correlation between the biasing and the compensation modulation phase errors can be obtained with a simple arithmetic operation:

$$\begin{aligned} E_{\psi b}(k) =& (I_{s1} - I_{s2}) - (I_{s3} - I_{s4}), \\ E_{\psi c}(k) =& \left[(I_{s1} - I_{s2}) + (I_{s3} - I_{s4})\right] g_{\psi c}(\Delta\Phi_c), \end{aligned} \tag{3.32}$$

where $g_{\psi c}(\Delta\Phi_c)$ is a correction inversely proportional to $\Delta\Phi_c$, or $\Delta\hat{\Phi}_c$, making the $E_{\psi c}(k)$ invariable with $\Delta\phi_s$. The error functions are shown in Fig. 3.16 for the

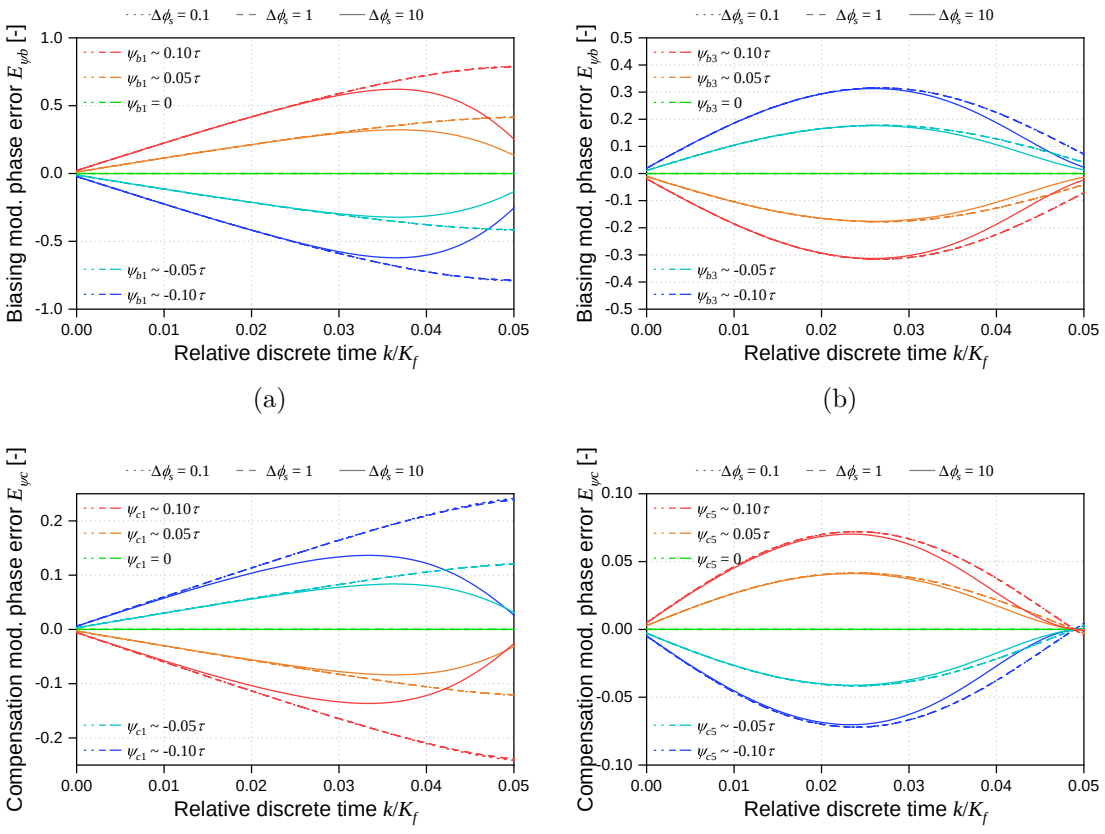


Fig. 3.16: Error functions for different $\Delta\phi_s$: $E_{\psi b}$ under the effect of ψ_{b1} (a) and ψ_{b3} (b), $E_{\psi c}$ under the effect of ψ_{c1} (c) and ψ_{c5} (d).

different values of $\Delta\phi_s$ and individual modulation components phase error ψ_*. The functions are shown for small values of $\frac{k}{K_f}$, as it is obvious that their courses diverge rapidly beyond this region. Assuming that k is limited to a certain level ($\approx 0.03K_f$), the functions $E_{\psi*}$ decrease monotonously with ψ_* errors and are similar in their shape, where the scale parameter is proportional to the corresponding error. To determine the portion of ψ_{b1} and ψ_{b3} in the E_{ψ_b}, and similarly ψ_{c1} and ψ_{c5} in E_{ψ_c}, it is necessary to compare the overall shapes within the defined interval, i.e., the function values for multiple k must be evaluated. This can be done either analytically or with the help of a suitable numeric method. One of the simplest approaches is the NN regression model, directly determining the individual values of ψ_*. Although $E_{\psi*}$ are only loosely dependent on $\Delta\phi_s$ for $k < 0.03K_f$, the $E_{\psi*}$ is proportional to the $I(k)$ gain and the interference contrast, which may generally drift over time. Therefore, the compensation based on the NN estimates, denoted as $\hat{\psi}_*$, can not be used directly as corrections of the modulation signal components phases, and a closed-loop error nulling control should be used instead. With such an approach, the estimates $\hat{\psi}_*$ are integrated, and the actual phase shift error ψ_* within the $\Delta\phi(t)$ signal is iteratively controlled to zero, as schematically shown in Fig. 3.17. In a practical case, it can be useful to employ filtering of $E_{\psi*}$ before it is passed to



Fig. 3.17: Compensation of the modulation components phase error.

NN regression to supress the noise carried by $I(k)$ signal, followed by decimation to reduce the dimensionality of the NN input vector, which helps to prevent overfitting and improves the stability of $\hat{\psi}_*$ estimation.

The second kind of error is the relative magnitude of the k_b, k_c components, and it is thus relevant solely to the quadruple-sine scheme. In the aforementioned scenario, the gain G_b and G_c of the modulation voltage components $u_{b3}(t)$, $u_{c5}(t)$ are not a priori known and should be thus controlled to reach an optimal flatness of the $I(t)$ signal portions where the S_{OL} signal acquisition occurs, to follow the assumptions made in Sec. 3.1.4. To obtain the error, the difference vector $D(k) = \hat{I}(k) - I(k)$ can be conveniently used, to avoid a correlation with the components phase error

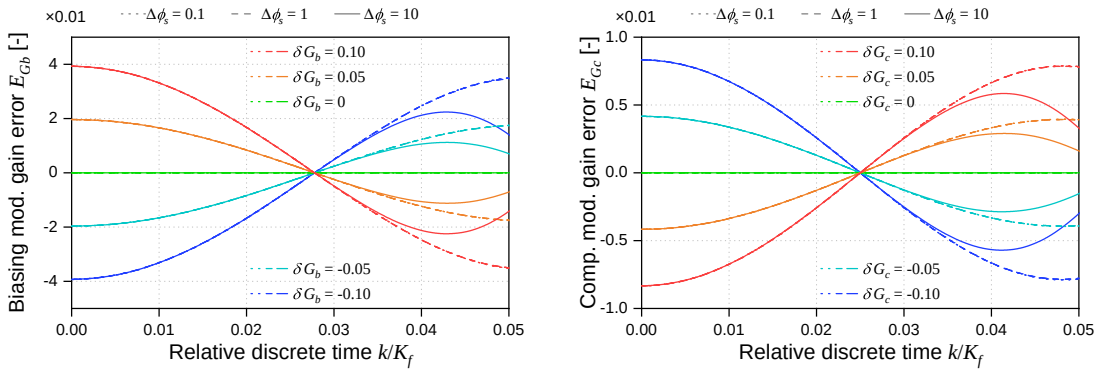
estimation. Similarly to the previous case, four subsections D_{s*} can be defined:

$$\begin{aligned} D_{s1}(k) =& D\left(\tfrac{1}{4}K_f + 1 + k\right), \\ D_{s2}(k) =& D\left(\tfrac{1}{4}K_f - 1 - k\right), \\ D_{s3}(k) =& D\left(\tfrac{3}{4}K_f + 1 + k\right), \\ D_{s4}(k) =& D\left(\tfrac{3}{4}K_f - 1 - k\right), \end{aligned} \tag{3.33}$$

where $k = \left\langle 0; \frac{K_f}{4}\right)$. Based on the relation between the errors and the modulation components' polarity, the following error vectors can be likewise defined, with a minimized cross-dependency between G_b and G_c errors:

$$\begin{aligned} E_{Gb}(k) =& (D_{s1} + D_{s2}) + (D_{s3} + D_{s4}), \\ E_{Gc}(k) =& \left[(D_{s1} + D_{s2}) - (D_{s3} + D_{s4})\right] g_{Gc}(\Delta\Phi_c), \end{aligned} \tag{3.34}$$

where $g_{Gc}(\Delta\Phi_c)$ stands for the normalizing function according to the current value of $\Delta\phi_s$, and thus also $\Delta\hat{\Phi}_c$ value, similarly as for the compensation phase error. The error functions $E_{Gb}(k)$ and $E_{Gc}(k)$ are shown in Fig. 3.18 for different values of $\Delta\phi_s$



(a) (b)

Fig. 3.18: Error functions for different $\Delta\phi_s$: E_{Gb} in dependency on δG_b (a), E_{Gc} in dependency on δG_c (b).

and the relative gain error values δG_* of the corresponding modulation components. It can be seen that the estimated gain error $\delta\hat{G}_*$ can be determined based on the E_{G*} functions as a scale parameter of the shape within a suitable interval (such as $k < 0.03K_f$, as noted above). Similar to the phase errors, the specific E_{G*} depends on $I(k)$ signal gain and contrast, and a closed-loop error nulling must be thus employed as well. The procedure of the $\Delta\phi_{b3}(t)$ and $\Delta\phi_{c5}(t)$ components gain error compensation is shown in Fig. 3.19.

The control of the modulation signal parameters requires that the error of one parameter does not influence the estimated errors of other parameters. In the optimal case, the cross-coupling between the estimated and the real error values should

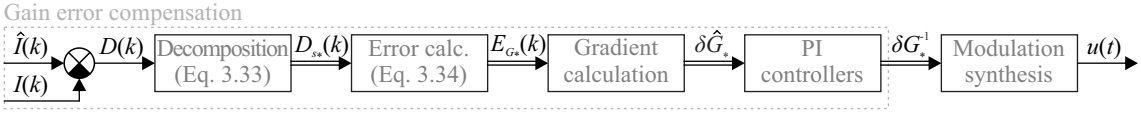


Fig. 3.19: Compensation of the modulation components gain error.

be zero. If this can not be satisfied, the problem can be solved by the closed-loop parameters stabilization, assuming two conditions are fullfilled. Firstly, if an error of the parameter x is coupled to another parameter error estimate $\hat{y}$, then the following must apply: $x \to 0 \Rightarrow \hat{y} \to 0$. Secondly, the coupling of x to $\hat{y}$ can be solved by different dynamics of x and y control; however, it must be ensured that the reverse coupling of y to $\hat{x}$ is below a certain threshold. This threshold is proportional to the ratio between the x to $\hat{x}$ and x to $\hat{y}$ coupling. The matrix of the corresponding cross-coupling functions shapes for the above-described methods of the modulation parameters error estimation is shown in Fig. 3.20. As normalizing functions make

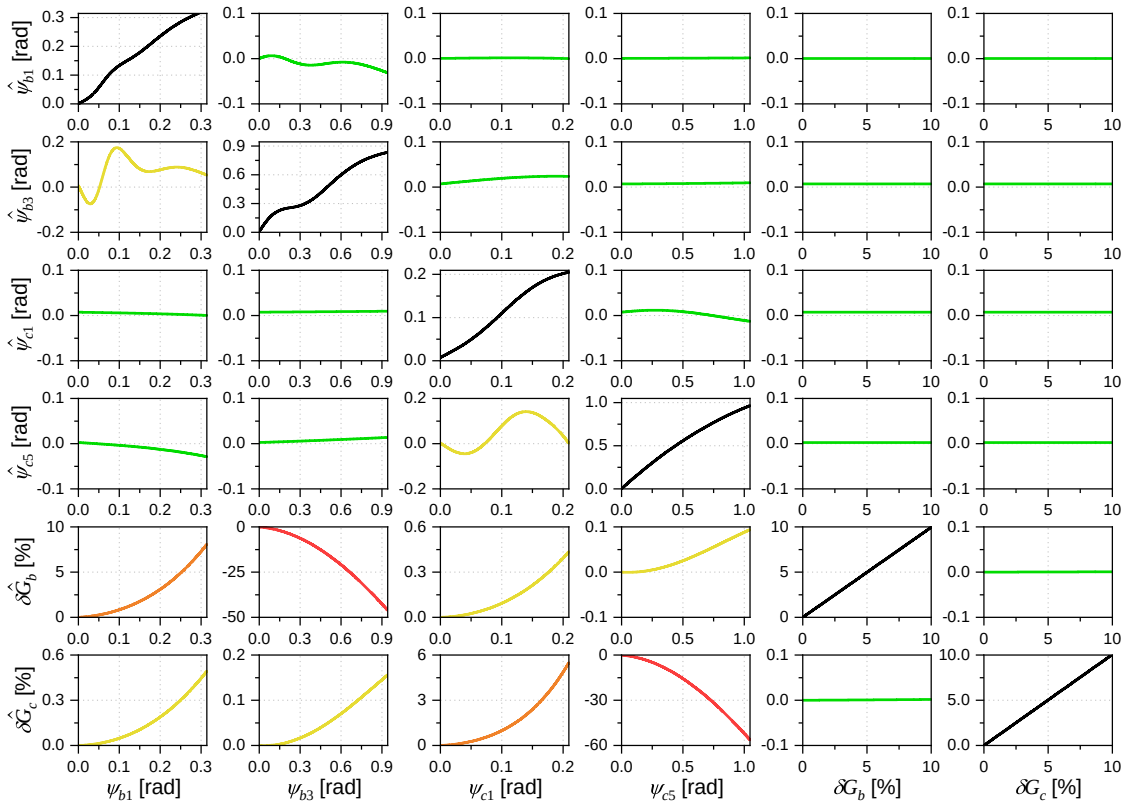


Fig. 3.20: The cross-coupling functions between the parameters errors and their estimated values illustrating a direct coupling (black) as well as a cross-coupling with weak (green), medium (yellow), strong (orange), and very strong (red) level.

the parameters error estimation to be nearly invariable with $\Delta\phi_s$, the cross-coupling functions are calculated as an average for the range $\Delta\phi_s \in \langle -7, 7\rangle$ rad, as considered in the prior analyses. It can be clearly seen that the most problematic is $\delta\hat{G}_*$ estimation whenever any component of the phase error ψ_* is present as well, as the cross-coupling of ψ_* to $\delta\hat{G}_*$ even exceeds the direct coupling of ψ_* to $\hat{\psi}_*$. Consequently, the ψ_* control must have much higher dynamics compared to δG_* to assure a stable operation of the entire parameters stabilization mechanism. This ensures that the phase error components ψ_* are driven to near-zero values, where the cross-coupling decreases, facilitating the δG_* parameters control.

The parameters stabilization process can be incorporated into an overall closed-loop IFOG processing alongside the K_{PEM} estimation, as shown in Fig. 3.21. The $\hat{I}(k)$ signal calculated by the intensity model for the K_{PEM} estimation can

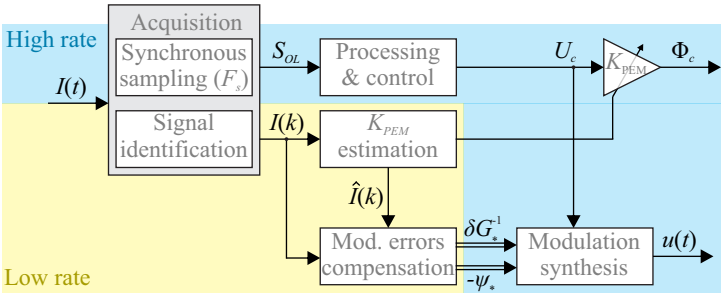


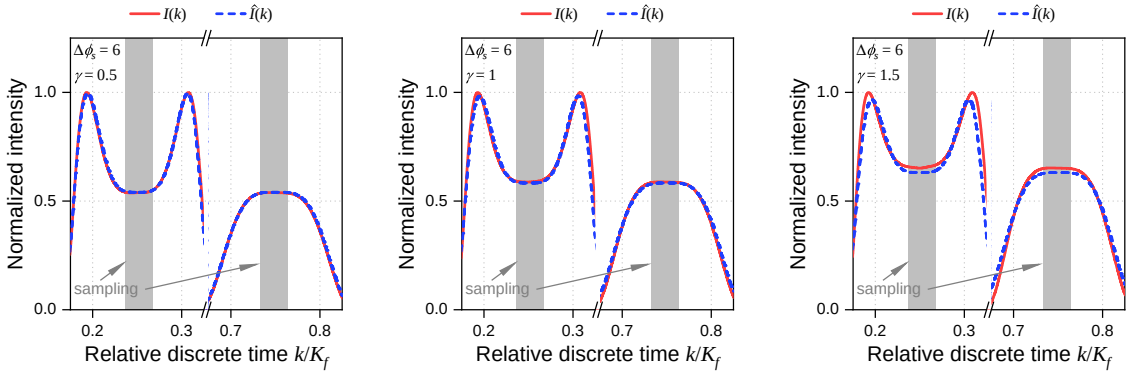
Fig. 3.21: Schematic of the PEM-based closed-loop IFOG signal processing with the compensation modulation depth control and modulation errors compensation.

thus be also used for the modulation errors compensation. Note that the original closed-loop compensation can still operate in the high-rate processing section, reflecting the high bandwidth of the angular velocity measurement. The compensation modulation depth control as well as the errors compensation, on the other hand, can be implemented as slow-rate processes, as they correspond to, in principle, much slower drift of parameters, influenced mainly by the temperature. The modulation voltage $u(t)$ is synthesized according to Eq. 3.20, where the individual components for $k_b = 3$, $k_c = 5$ are defined as:

$$\begin{aligned} u_{b1}(t) &= U_{b1} \sin\left(\omega_b t - \psi_{b1}\right), \\ u_{b3}(t) &= \delta G_3^{-1} G_b U_{b1} \sin\left(3\omega_b t - \psi_{b3}\right), \\ u_{c1}(t) &= U_{c1} \sin\left(\omega_c t - \tfrac{\pi}{2} - \psi_{c1}\right), \\ u_{c5}(t) &= \delta G_5^{-1} G_c U_{c1} \sin\left(5\omega_c t + \tfrac{\pi}{2} - \psi_{c5}\right), \end{aligned} \tag{3.35}$$

where U_{b1} is a at set value, and U_{c1} is controlled to satisfy the equality defined by Eq. 3.23.

The intensity signal with the parasitic effects and simultaneous parameters stabilization is displayed in Fig. 3.22, showing that the homogeneity of compensation during the S_{OL} signal acquisition time is notably improved. Nevertheless, the performance of the stabilization decreases with γ, which stems from the fact that the model $\hat{I}(k)$ becomes less accurate with increasing parasitic effects distortion, deteriorating the modulation parameters estimate.



(a) (b) (c)

Fig. 3.22: The intensity signal with the parasitic effects model and its model-based estimate.

3.2 Test setup

The primary objective of the described methods is to enable the all-fiber PEM-based IFOG configuration to operate in a closed loop, thereby realizing the advantages discussed above and reducing associated errors and parasitic effects. For the purpose of verification and testing, two IFOG prototypes (P1, P2) have been developed.

The P1 was mainly designed to demonstrate the double-sine and the quadruple-sine modulation methods within the all-fiber IFOG and compare them to a standard open-loop operation. Additionally, this setup also aided in the identification and definition of the major errors and parasitic effects discussed above, which are related to the PEM-based phase modulation. Therefore, optimal techniques for their mitigation could be developed. Finally, P1 was also subjected to several optimization steps of the optical architecture with respect to the SOTA, enhancing the overall performance of the low-cost SM fiber-based IFOG.

A large number of the tests were performed with an external signal processing unit. For this purpose, the NI PXI system was used. In the following stages, the processing was optimized and transferred to an embedded system based on the Xilinx Zynq platform, which was integrated into the P1 setup.

Further integration was performed with the P2 setup, developed from scratch as a compact device, with the aim of demonstrating the feasibility of integrating the designed methods. The whole IFOG setup, along with the signal processing, was packed into a device that can be considered close to a production unit. The P2 was subjected to the next set of testing, particularly focused on the stability error mitigation techniques, which pose a major challenge when employing PEM-based modulation.

3.2.1 Optical setup

Both P1 and P2 share similar optical architecture, schematically shown in Fig. 3.23. For the most part, the employed architecture is based on a commonly used arrangement [144,145,148], where the polarization reciprocity is attained through the polarization handling components. In this case, this is accomplished by the polarizer and the depolarizer. Utilization of the SM fiber coil has posed an attractive alternative for decades, as it has the capability of reducing the overall price. Various studies have been performed, analyzing and reducing the polarization-induced non-reciprocity [61,147,148,153]. The proposed approaches included the integration of a polarizer in between the fiber couplers [51,62,64], placing the Lyot depolarizer in the sensing coil [146,154], a combination of the polarizer and depolarizer [155], or even multiple depolarizers [144]. However, as each approach represents a slightly different manner of the errors mitigation, the optimal method has to be chosen based on the given setup, including the employed optical components, the desired sensing performance, i.e., a residual non-reciprocity, and also the setup complexity, related to the total costs.

In the case of the P1 and P2 IFOG setups, a broadband depolarized light source

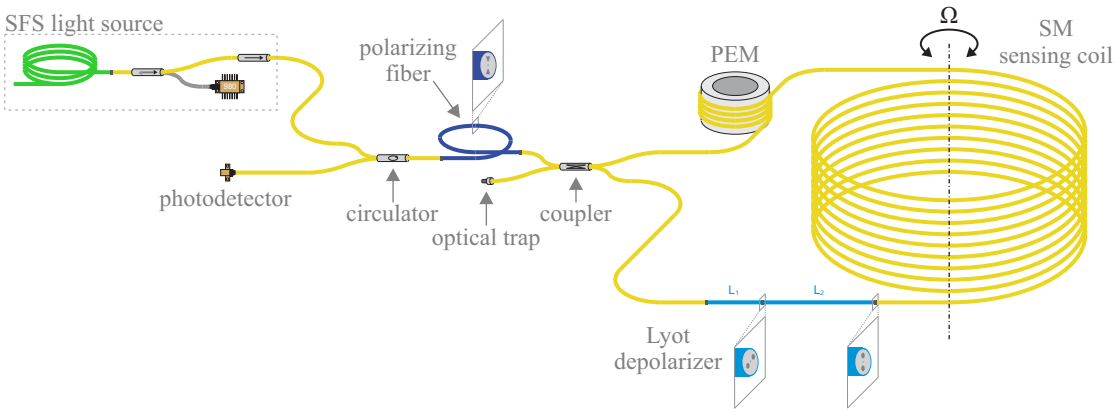


Fig. 3.23: The optical architecture of the P1 and the P2 IFOG testing prototypes [149].

is used. The experiments proved that a satisfactory level of polarization reciprocity can be reached with a single depolarizer placed in the sensing coil. The fiber Lyot depolarizer consists of two PM fiber segments with a nangle twist of 45° between their principal axis. The design of the depolarizer should thus be performed carefully, considering the source spectrum width and profile. Experimental testing showed that, in our setup, adding the polarizer between the couplers can further reduce the residual bias sensitivity with temperature caused by the polarization errors by about 14 times (tested with the P2). A fully reciprocal fiber polarizer is utilized in both prototypes, represented by a polarizing fiber segment (HB1550Z, Fibercore).

The PEM was manufactured by winding an SM fiber onto a piezoelectric tube actuator. In both P1 and P2 prototypes, a hard piezoceramic tube (NCE40, Noliac) was used with an outer diameter of 25.4 mm, a height of 12.7 mm, and a wall thickness of 3.15 mm. In the optimized manufacturing procedure (used for P2), the fiber was wound with a homogenous pre-tension of 2320 $\mu\epsilon$ to suppress the stretching asymmetry, which had been identified during previous tests (P1). To prevent parasitic amplitude and polarization modulation, a bend-resistive SM fiber (G657 B3, YOFC) was wound in 42 turns.

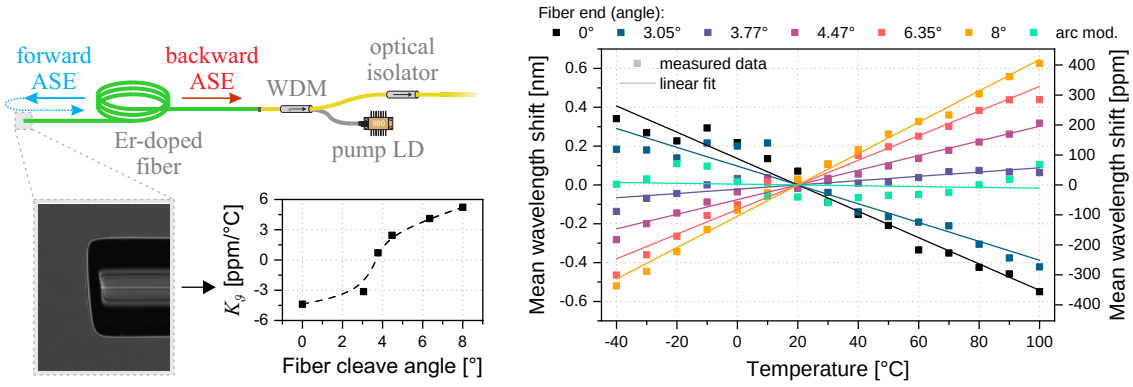
Special attention was dedicated to the input light source design. In the IFOGs, the use of a broadband source is required to suppress many of the parasitic optical effects [18,19,61]. Therefore, in the vast majority, the sources employed by the SOTA solutions comprise a superfluorescent fiber source (SFS) with an Er-doped fiber, or a superluminescent diode (SLD). In some cases, frequency-swept laser diodes are also used. However, in the case of depolarized IFOG, only the first two candidates are suitable, as they feature a sufficient spectral width. Considering a closed-loop operation, it can be shown via Eq. 1.12 that the wavelength stability directly impacts the measured angular velocity. In comparison to the SLDs, the SFSs exhibit by about 2–3 orders better stability of the central wavelength with temperature, making them more suitable for the IFOGs. As their inherent stability is typically in orders of units of ppm/°C, additional optimization is necessary in case of the navigation-grade and better IFOGs, where stability of at least 1 ppm is required [156].

For that purpose, many different techniques have been proposed, such as fiber grating stabilization, including a long period grating [157] or Bragg grating [158,159]. Other approaches employed filtering the spectrum by the photonic bandgap filter [160], thin film filter [161, 162], Er-doped fiber filter [163–166], or photonic crystal Er-doped fiber [167]. Further, stabilization methods with the Faraday rotator mirror [168–170] or variable parameters control have also been proposed [171]. Nevertheless, most of these methods have the disadvantage of narrowing the spectrum width as well as the power drop, reducing the SFS conversion efficiency. Moreover, the additional optical components and functional elements further contribute to the

increased complexity, also resulting in a higher total cost.

These limitations can be conveniently overcome by the weak-feedback backward-pump double-pass (WF-DPB) SFS, which has been proposed in [172]. It is based on a standard backward-pump setup, where the reflectivity of the free (unpumped) fiber end is adjusted to produce feedback with an opposite mean wavelength temperature behavior, as shown in Fig. 3.24(a). The reflectivity was adjusted through an angled fiber cleave and a fusion arc. Consequently, a balance can be found between the backward and the forward amplified spontaneous emission (ASE), reaching minimized mean wavelength temperature gradient $K_\vartheta = \frac{\partial \bar{\lambda}}{\partial \vartheta}$, as shown in Fig. 3.24(b). Compared to other published methods, no additional filtration components are required, making this solution cost-effective and well-suited for the designed IFOG setup. Further, the absence of filtration preserves its inherent spectral width and ensures high power efficiency.

The last critical part of the IFOG optical setup is the sensing coil. In both cases, it was formed by a standard telecom fiber (SMF-28 in P1, G657 B3 in P2) in quadrupole winding and mean winding radius R of 77.8 (P1) and 34.5 mm (P2), respectively. In both cases, the total fiber length is $L = 770$ m, producing a transit time $\tau = 3.78$ µs for the whole trace, including the PEM and the Lyot depolarizer. With a central wavelength of 1532 (P1) and 1544 nm (P2), the IFOG constant $K_{IFOG} = \frac{\Delta\phi_s}{\Omega}$ of the tested prototypes was equal to 1.6389 and 0.7212 s, respectively. Further details related to the optical setup of the tested prototypes are given in [149,173] (P1) and [150,172] (P2). The supplementary materials detailing the optical



(a) (b)

Fig. 3.24: Designed WF-DPB SFS configuration (WDM – wavelength division multiplexer) with optimal cleave and fusion arc modified fiber end and pure angle cleave temperature gradient characteristics (a) and the SFS mean wavelength temperature dependency (normalized to a lin. wavelength at 20 °C) for different fiber endings (b) [172], (modified).

setup can be found in Sec. A.1.

3.2.2 Control unit and data processing

To implement the methods described in Sec. 3.1, it is necessary to consider their specific demands on computational resources and time synchronization. The closed-loop processing and modulation methods require both synchronous sampling with the generation of the modulation signal and also continuous maintaining of the S_{OL} signal at zero. To maximize the measurement bandwidth, high-rate processing is required for this task, best fulfilled by an FPGA, a solution typically adopted by the SOTA closed-loop IFOGs. On the other side, the modulation depth control and the parameters stabilization require more complex processing, implementation of which would cost a large amount of available FPGA resources, leading to dramatic cost increase. Since the major objective of this processing task is following the parameters drift, which is generally a slow process, real-time processing is not strictly required. Therefore, the outlined methods can be cost-efficiently accommodated by a hybrid architecture, combining an FPGA with a processing system (PS).

For the purpose of closed-loop methods verification and also the modulation depth control as well as the parameters stabilization methods development, the data processing was implemented within a testbench, comprising a NI PXI (PXIe-1062Q) equipped with an FPGA module (PXI-7854R) for the high rate part of signal processing. In the first stage of the system development, the synchronous sampling of the optical signal $I(t)$ with a frequency of $f_{sa} = \frac{1}{3\tau} = 88$ kHz was performed by a 16-bit SAR ADC. In this setup, referred to as a P1a, no depth control or stabilization was present.

Implementation of the modulation depth control requires an additional sampling with a period of T_{sf} for a full $I(t)$ signal identification, as suggested in Sec. 3.1.4. Assume a 16-bit resolution, corresponding to a -96dB signal level in case of the ADC full scale coverage by the $I(t)$ signal, and a phase shift $\Delta\phi_s = 10$ rad being compensated by the $\Delta\phi_c(t)$. Then, the bandwidth of the $I(t)$ signal spectral components above this level is approximately $f_{BW}\left(I(t)\right) = \frac{10.4}{\tau}$, which is about 2.75 MHz, in the described case. Therefore, the minimal sampling frequency for full $I(t)$ signal identification is $f_{sf} = \frac{20.8}{\tau} = 5.5$ MHz. In a real setup, a 40 MS/s 16-bit pipelined ADC was utilized, yielding a discrete signal $I(k)$ period $K_f = 912$ samples. Such sampling frequency was considered suitable, as it avoids the double sampling of the $I(t)$ signal (with a frequency of f_{sa} and f_{sf}), which would bring an additional complexity. The synchronous sampling at the frequency f_{sa} and the sample acquisition time T_{acq} can be replaced by an appropriate decimation of the $I(k)$ signal with a sampling frequency of f_{sf}. Moreover, it was proven by the experiment that with

the integration of N_{acq} samples of $I(k)$, where $N_{acq} = \frac{T_{acq}}{T_{sf}}$, it is possible to reach an equal noise level in the S_{OL} signal. Hence, the slower $I(t)$ signal acquisition can be omitted, preserving only the fast sampling at f_{sf}. These modifications were implemented by the P1b setup, enabling testing of modulation depth control and parameter stabilization techniques. The layout of the P1b test setup is shown in Fig. 3.25.

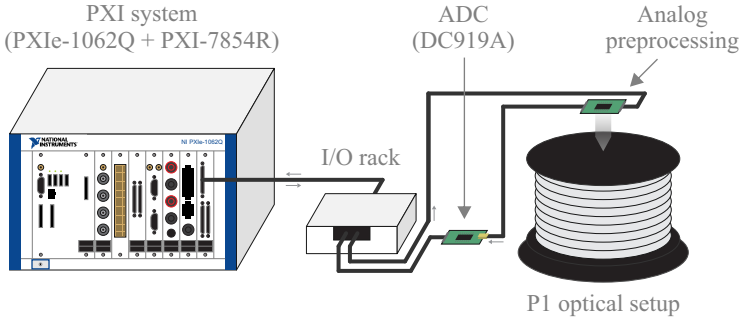


Fig. 3.25: Layout of the P1b test setup.

Further test setup modifications were made to integrate data processing and corresponding algorithms into an embedded platform, replacing the PXI system with an external ADC. For this purpose, a Xilinx Zynq family SoC was selected, combining an FPGA with a PS within a single chip. In the P1 IFOG prototype, a low-cost development board Cora Z7-10 (Digilent) was employed as a control unit (CU1), incorporating all of the designed processing methods. The unit was connected to the IFOG optical setup through an interface unit (IU1), serving for the $I(k)$ signal acquisition and the PEM driving voltage $u(t)$ generation. The layout of the integrated P1c setup is shown in Fig. 3.26. For the IFOG data acquisition, an embedded Ethernet and UART interface was used. The Ethernet interface also serves for a data processing control in real-time, selected variables and auxiliary data monitoring, and parameters setting. Further details on the implemented functionality of the control unit may be found in Sec. A.1.

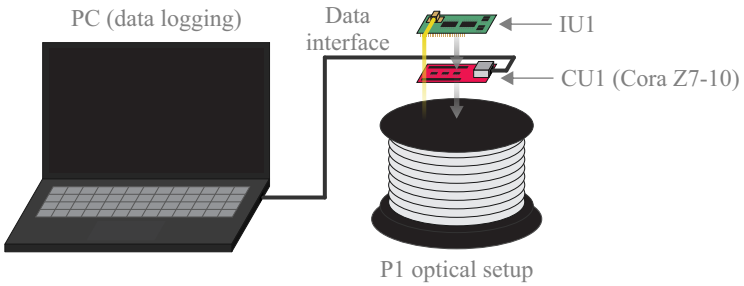


Fig. 3.26: Layout of the P1c test setup.

Finally, the processing was embedded into the P2, demonstrating the integrability of the whole IFOG setup into a compact package, including the designed modulation and processing methods. For this purpose, a compact platform TE0720 (Trenz Electronic) was employed as a control unit (CU2) with a newly developed interface unit (IU2). Apart from the functionality of the IU1, the IU2 also accommodates the interface for the output data transfer and control, including Ethernet, UART, CAN, and analog output. The P2 setup with the data processing is shown in Fig. 3.27. Further details of the control and an interface unit implementation are also provided in Sec. A.1.

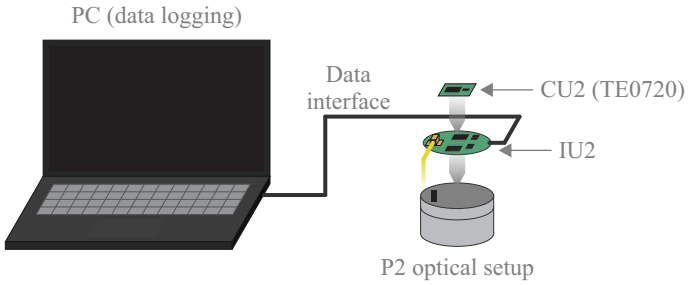


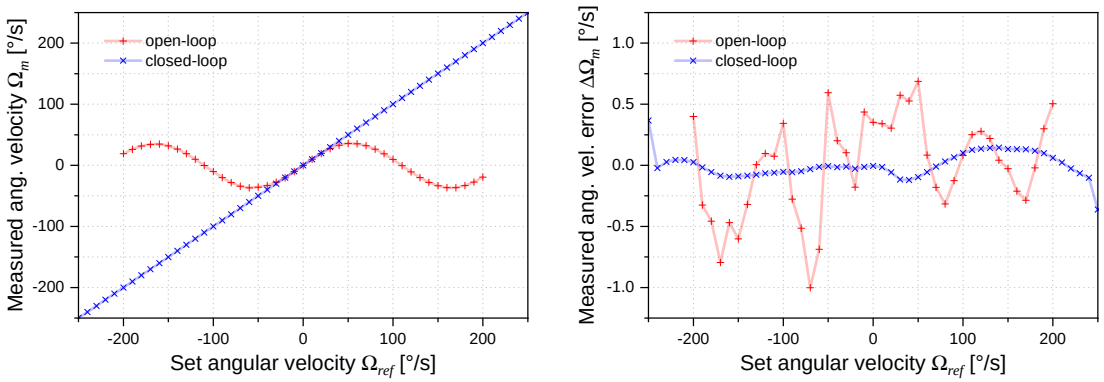
Fig. 3.27: Layout of the P2 test setup.

3.3 Verification and results

To verify the designed methods, the prototypes were subjected to a thorough testing. The test results then served not only to demonstrate the methods' capabilities to improve specific measurement parameters but also to facilitate further system optimization, including the identification of the parasitic effects during the P1 testing stage. Numerous tests were also performed solely for the purpose of the optical setup development and optimization, the signal processing design, and the parametrization. The following discussion will focus solely on the results directly related to the verification of the proposed processing and modulation methods. For this purpose, both static and dynamic tests were performed, with the use of the calibration rotary table SDL1401 (RMS GmbH & Co.) and the temperature chamber T-65/50 (CTS GmbH).

3.3.1 Closed-loop phase shift compensation

The main contribution of the proposed compensation method lies in the capability to null the Sagnac phase shift during the sampling moments, with the period of T_{sa}, by an additional phase shift modulation. The method was demonstrated and compared



(a) (b)

Fig. 3.28: Comparison of the designed closed-loop and the open-loop P1a setup response: normalized output characteristics (a) and the corresponding error from their ideal approximation (b) (measured with $\vartheta = 25$ °C) [149], (modified).

to the standard SOTA approach to the depolarized all-fiber IFOG, relying on open-loop processing. The P1a setup was employed, featuring the capability to operate also in the open loop, by switching off the compensation control and observing the S_{OL} signal. The response of the closed-loop method compared to the open-loop operation with the same setup is demonstrated in Fig. 3.28(a). In both cases, the IFOG output signal was rescaled to the angular velocity, corresponding to the reference angular rate Ω_{ref}, applied by the rotation table. It can be seen that in the open-loop operation, the output signal can be used directly only within a small range, where it is approximately linear and unambiguous. For a larger angular rate, further processing must be applied, as discussed in Sec. 1.4.2. The Fig. 3.28(b) then depicts the characteristics' errors, as a deviation from a linear or a sine fit, for the closed-loop or the open-loop case, respectively. It can be seen that the variance of the closed-loop error is significantly below the open-loop one. This can be partially explained by the fact that, in the case of the closed-loop processing, the output signal is filtered by the PI controller. Similarly, in the open-loop signal error, the random component could be suppressed by filtering. Nevertheless, we can see another component present, representing the true open-loop error. This error is likely caused by the residual nonlinearity of the optical detection and the processing electronics. Other possible causes may include the broadband light source coherence, leading to the interference pattern fading with increasing $\Delta\phi$. On the contrary, the advantage of the closed-loop processing lies in the operation in a single point of the intensity characteristics, (see Fig. 1.1), and it is thus resistant to the detection chain nonlinearities.

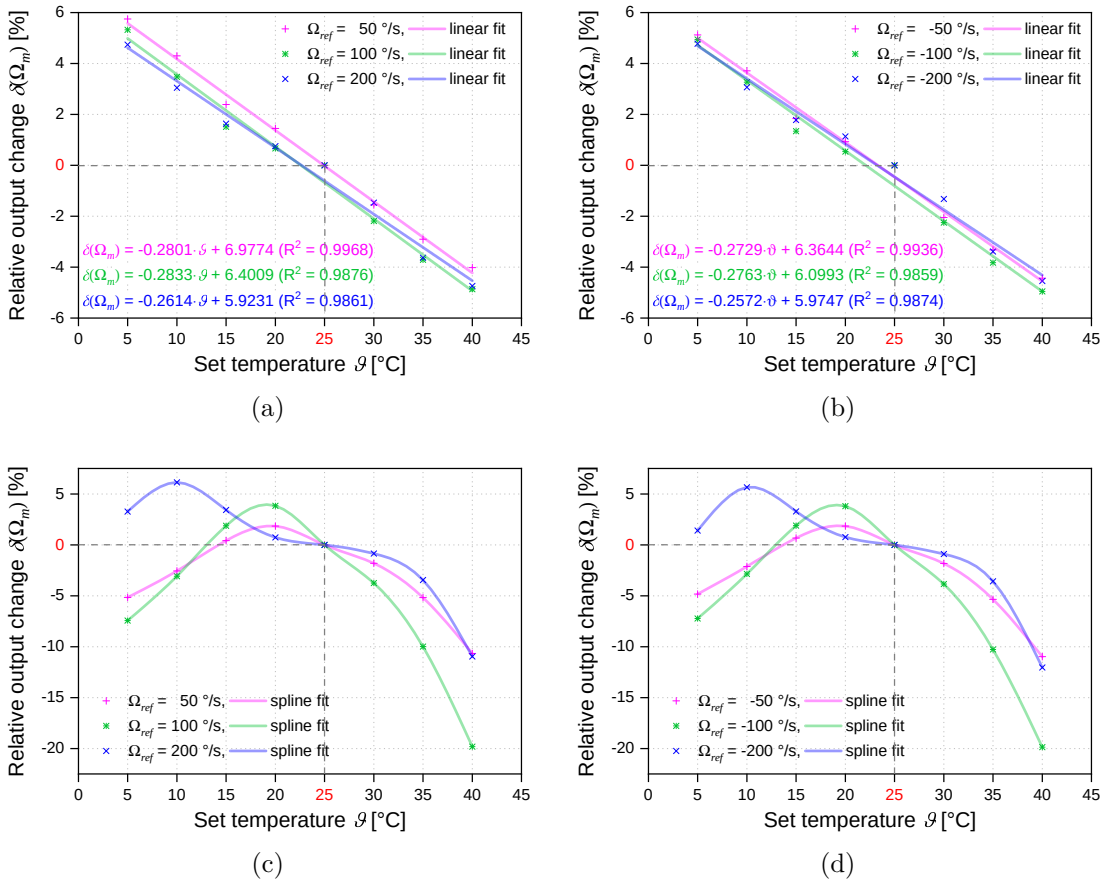


Fig. 3.29: Relative change of the closed-loop (a,b) and the open-loop (c,d) IFOG (P1a) output with temperature ($\vartheta_{ref} = 25$ °C) [149].

Further analysis was focused on the temperature dependency of the closed-loop phase shift compensation, in comparison to the standard open-loop scheme. Taking the temperature $\vartheta_{ref} = 25$ °C as a reference point, the relative changes of the output signal rescaled to the angular velocity for the closed-loop and open-loop processing are compared in Fig. 3.29. The comparison is performed for various angular velocities in both directions. Each point was acquired as an average over one minute, and >4 h settling time was applied at each temperature. For the closed-loop processing, an almost linear trend can be observed, with a slope of -0.27 %/°C. This behavior can be explained well by the inherent PEM material temperature dependencies [34]. Therefore, even though the testing was performed within the 5 – 40 °C temperature range, it can be assumed that this behavior will follow the trend dictated by the material also beyond the tested region.[3] The open-loop processing, on the other hand, exhibits a significant nonlinearity, with a more considerable variance and also

[3]The PEM is usually characterized by $K_{PEM}(\omega_c)$. Due to the closed-loop operation, the IFOG temperature dependency follows the $\frac{1}{K_{PEM}(\omega_c)}$ trend.

a dependency on the applied angular rate. This can be explained by the manifestation of the PEM temperature dependency through the biasing modulation, which is nonlinear due to the moving operation point. The open-loop processing is also more susceptible to the source spectrum variation with temperature, causing an interference pattern drift. Note that this effect has an approximately linear (see Fig. 3.24) behavior in the case of the closed-loop processing due to the stable operation point. Consequently, this can be conveniently employed to passively compensate the PEM temperature dependency, and thus improve the overall IFOG temperature stability without any further processing methods.

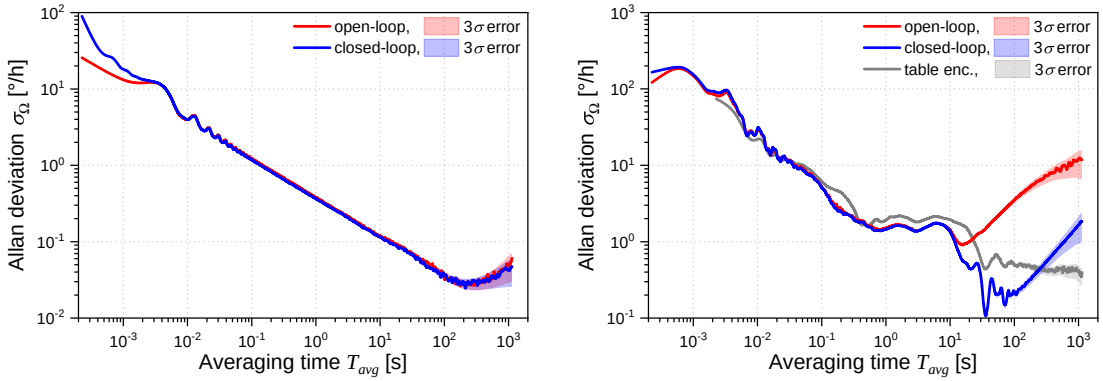
Further tests were devoted to exploring a possible impact of the closed-loop method on the parameters' stability. The stability of the bias is mostly determined by the optical design, whereas the scale-factor stability is also influenced by other factors, such as the stability of the light source parameters, the sensing coil, or the modulation chain. The stability and the noise are most often characterized by an Allan variance or deviation, obtained by computing an average of the output signal over different periods, described in detail by the IEEE standard [174].

The Allan deviation σ of the IFOG (P1a) output in the closed-loop and the open-loop operation at zero angular velocity, expressing their bias, is shown in Fig. 3.30(a)[4]. In accordance with the theoretical expectations, both operation modes behave similarly in terms of bias since they both operate close to the quadrature point with very small action by the compensation modulation in the closed-loop mode. Moreover, the data show that the compensation modulation and the closed-loop control do not impair the IFOG's inherent noise and stability. Note that even though the 16-bit ADC and DAC provide a sample resolution of 0.012 °/s in the P1a setup, the presence of white noise dithering led to a decrease of the detection threshold down to about 0.03 °/h, expressing the bias stability level [149].

The scale factor was tested at the reference angular velocity $\Omega_{ref} = 10$ °/s, inducing a phase shift of $\Delta\phi_s \approx 0.286$ rad. The corresponding Allan deviation for the closed-loop and the open-loop setup is depicted in Fig. 3.30(b). In the case of the shorter averaging times, it can be seen that both curves follow the noise introduced by the rotation table, the angular rate of which was measured by an internal encoder, serving as a reference. The longer averaging times then reveal the open-loop processing limitations posed by the moving operational point and the dependency on the light source stability. This is effectively overcome in the closed-loop processing, as it attained by about one order better absolute stability compared to the open-loop operation.

As the closed-loop signal processing brings additional complexity in terms of the

[4]Both the Allan deviation and the 3σ-error reliability were calculated according to [174]



(a) (b)

Fig. 3.30: The Allan deviation of the closed-loop and the open-loop IFOG operation for zero angular velocity (a) and the angular velocity $\Omega_{ref} = 10$ °/s, with table encoder data as a reference (b) [149].

controller and the compensation modulation, there is a potential risk of decreasing the bandwidth of the sensed angular velocity because of the closed-loop delay. Therefore, one of the major requirements on the compensation method design was to enable a high-bandwidth measurement. Unlike the previously designed harmonic compensation methods, operating with a long period between the compensation intervals, the proposed method gives the possibility to utilize each S_{OL} sample, obtained with frequency $f_{sa} = \frac{1}{3\tau}$. By forwarding each sample to the controller, the compensantion up to the same rate is possible. Assuming the modulation frequencies are optimally tied to the sensing coil fiber length L, the theoretical bandwidth limitations posed by the designed closed-loop method follow the equation:

$$f_{bw} = \frac{f_{sa}}{2} = \frac{\mathrm{c}}{6Ln}, \tag{3.36}$$

where n is the fiber group refractive index. The actual bandwidth can be verified by the rotation table by applying sine torsion vibrations. The IFOG housing tangential movement was sensed by a laser vibrometer OFV-505 (Polytec), providing reference data. The measured angular velocity normalized to the set reference over the frequency range up to 1 kHz is shown in Fig. 3.31. With the sine profile of the applied angular velocity (Ω_{ref}), the system was producing a sine angular velocity signal with the same amplitude up to about 100 Hz, which coincides with the limits of the commercial IFOGs. Beyond this frequency, accurate measurement was not possible due to the inertial mass of the sensor and the table, causing a delay in the table control loop, and also by the mechanical stiffness and resonances of the system, preventing an equal transfer of the applied angular velocity to all components of the sensor.

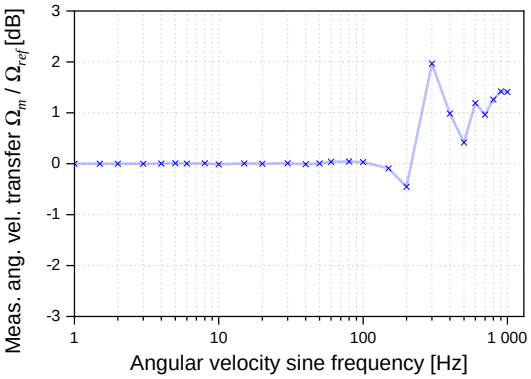


Fig. 3.31: The frequency transfer characteristics of the angular velocity measurement with the P1a IFOG setup and the designed closed-loop processing method [149].

3.3.2 Scale-factor stability control

Based on the discussion in Sec. 3.1.4 providing the NNCLE and the LSCFE methods comparison, a conclusion was drawn that the LSCFE method provides a better theoretical performance in terms of the compensation modulation depth control and associated stability and it is resistant to the modulation distortion induced by the parasitic effects. Thus, it has been selected for the implementation. Even though the theoretical number of computational resources required by the LSCFE method is larger than by the NNCLE method, it was shown by an experimental verification that this issue can be effectively solved by selecting a suitable hardware platform with an optimized algorithms implementation and computation rate constraints. The method was implemented and tested mainly with the use of the P1b and P1c setups. Within this set of testing, the Sagnac phase shift was always compensated at the sampling intervals by the compensation modulation. The quadruple-sine scheme was employed for the biasing and the compensation modulations.

As shown by the previous results (Sec. 3.3.1), the IFOG scale factor is varying with the temperature. Even if the dependency is close to a linear in the case of the closed-loop method, its compensation by a fixed linear correction does not provide a general solution with the sufficient output parameters stability and reliability. Firstly, the parameters of the phase compensation chain, including their own temperature sensitivity, may be subject to a drift over longer period of time, or under the influence of other affecting quantities, such as magnetic field or radiation. Secondly, the possibility of linear approximation within the given range (5–40 °C) is solely built upon the corresponding PEM material characteristics. However, from a general perspective, a different trend is obtained if the key influencing parameters, such as PEM material, the operational frequency f_c, or the temperature range

change. Finally, such correction requires PEM temperature measurement, which then serves as an additional processing input. Yet, since the fiber stretching by the piezoelectric actuator is a distributed process and its temperature can be different over distinct points, multiple temperature sensors should be employed to achieve sufficient accuracy. Moreover, assuming a contact measurement, the temperature sensors' mass can influence the PEM oscillations and introduce additional resonances into its frequency response.

The discussed negatives are overcome by the technique of scale-factor stability control, providing a universal solution to the correction of the direct closed-loop IFOG output. To verify the performance of the proposed stability control mechanism, implementing the LSCFE method, the IFOG output data were acquired at the reference angular velocity of $\Omega_{ref} = \frac{\pi}{2}$ rad/s = 90 °/s at different temperatures, impacting the modulation chain gain and the scale factor, accordingly. In the first case, the compensation modulation voltage U_c was transferred with the fixed K_{PEM}, resulting in the $\Delta\Phi_c$, which was normalized to Ω_{ref} at the reference temperature $\vartheta_{ref} = 25$ °C. In the second case, an estimated value $\Delta\hat{\Phi}_c$ was used instead, obtained with the LSCFE method (Fig. 3.10). The testing was performed with the P1b setup. At each temperature, a settling time of 4 hours was employed. The results shown in Fig. 3.32 demonstrate that the detection of an angular velocity with a use of the estimation method is by about one order less susceptible to the temperature changes, compared to the direct output with a fixed K_{PEM} factor. A residual error of the model-based output may be caused by the drift of parameters which are not part of the closed-loop phase shift compensation chain, and thus can not be compensated by the proposed method. These factors may include, e.g., the source wavelength temperature drift, which remains nonzero even with the optimized WF-DPB SFS configuration (Fig. 3.24). Next to that, it is obvious that

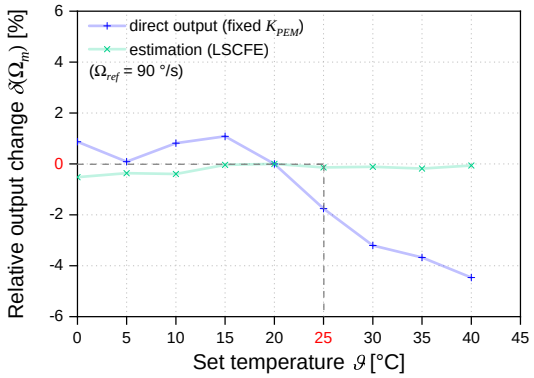


Fig. 3.32: Comparison of the direct closed-loop output and the LSCFE method output temperature dependency (tested with IFOG P1b, $\vartheta_{ref} = 25$ °C).

the direct output (with a fixed K_{PEM}) error is not linear with temperature anymore. This may be a consequence of employing a more complex modulation scheme (quadruple-sine instead of double-sine), i.e., the temperature drift of both components $K_{PEM}(\omega_c)$ and $K_{PEM}(k_c\omega_c)$ has to be taken into account. Note that with the proposed technique, only the $K_{PEM}(\omega_c)$ component is estimated and controlled, whereas the $K_{PEM}(k_c\omega_c)$ term is maintained at the optimal value by the δG_c control loop, described in Sec. 3.1.5.

The stability of the scale factor is often expressed in terms of the Allan deviation. The comparison of the direct output (fixed K_{PEM}) and the output obtained with the LSCFE method can be seen in Fig. 3.33 for different reference angular velocities and temperature profiles. In the first case (Fig. 3.33(a,b)), when the temperature was maintained stable at $\vartheta_{ref} = 25$ °C, a notable difference in the performance improvement by the LSCFE method can be seen at distinct angular velocities. This arises from higher proportion of the PEM parasitic effects as the $\Delta\Phi_c$ increases, and thus affecting the higher angular velocities more, in the case of the direct output. Whereas at $\Omega_{ref} = 45$ °/s both outputs are comparable, for 90 °/s, the long-term stability of the LSCFE output is significantly better. During the following tests, the temperature was swept with a sawtooth profile between 20 and 40 °C, with a period of 10 (Fig. 3.33(c,d)) and 40 minutes (Fig. 3.33(e,f)). The resulting Allan deviation curves indicate a notable temperature dependency of the direct output signal with a peak proportional to the temperature sweep period. Conversely, the data provided by the LSCFE method exhibit a significantly lower susceptibility. Similarly as with the previous case, the difference becomes more apparent with an increase of the reference angular velocity Ω_{ref}. An even more apparent difference between the direct and the model-based output was observed if the temperature period was prolonged to 40 minutes, which is most probably caused by the PEM thermal isolation in the P1. As an actual IFOG temperature does not exactly follow the ambient temperature, when the 10-minute sweep period is used, it does not reach the set minimum and maximum values. However, with the longer sweep period, facilitating better temperature settling, it was revealed that for both reference angular velocities, almost equal improvement is achieved with the LSCFE method, which amounts to about one order of magnitude better temperature stability compared to the direct output. This conclusion is also closely aligned with the static characteristics in Fig. 3.32.

Even though the LSCFE method was verified to provide a stable output, significantly less susceptible to the temperature fluctuations, its fundamental purpose is to provide a correction to the direct output, as was explained in Sec. 3.1.4. As can be noticed from Fig. 3.33(a–f), the data rate, corresponding to the minimal averaging time T_{avg}, is different for both curves. Whereas the direct closed-loop data rate can

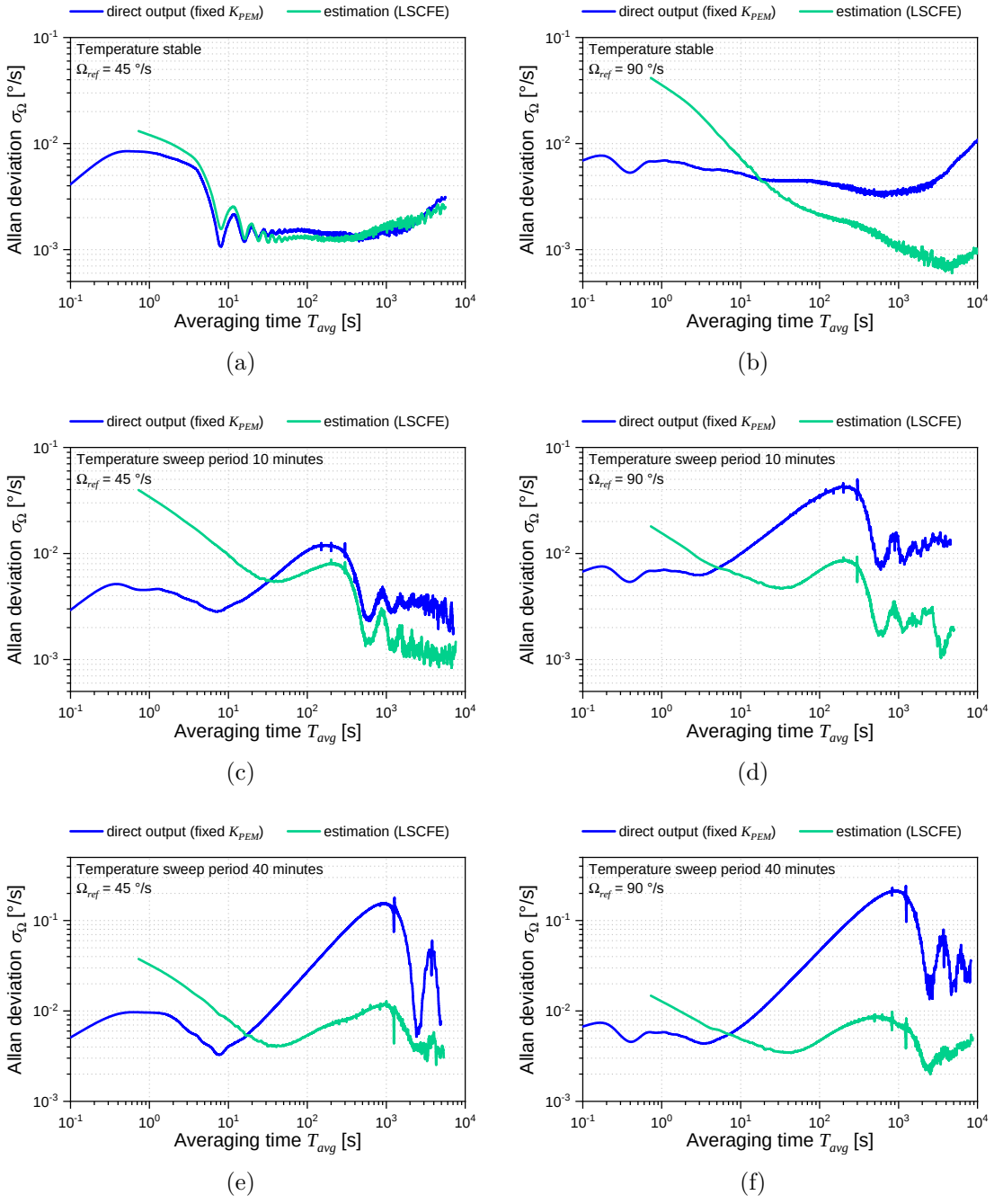
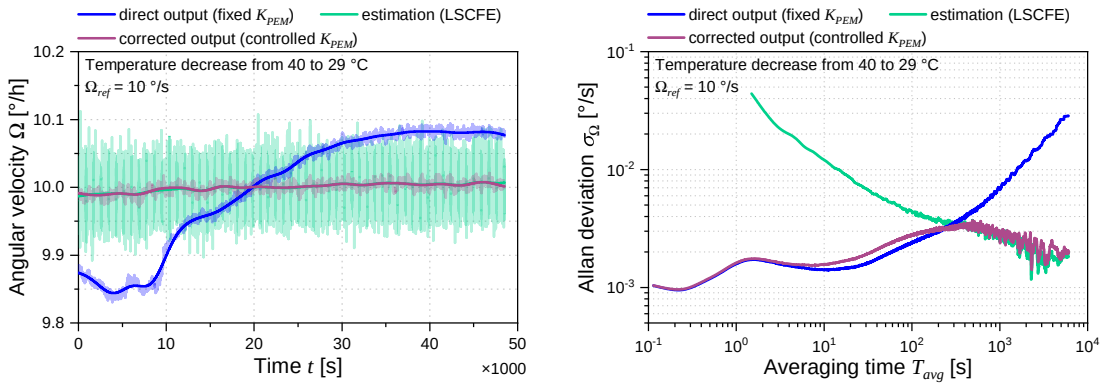


Fig. 3.33: Allan deviation of the direct closed-loop output and the LSCFE method output, measured at stable temperature ϑ_{ref} = 25 °C (a,b), and ramp-sweep temperature between 20 – 40 °C within the periods of 10 (c,d) and 40 minutes (e,f), (tested with IFOG P1b) [150], (modified).

reach up to f_{sa}, which amounts to 88 kHz in the tested setup, the output provided by the estimation is significantly slower. Although both NNCLE and LSCFE methods use a single $I(k)$ signal period, corresponding to 3τ = 11.34 µs, to estimate

the modulation depth $\hat{\Phi}_c$, the computational time is much longer, ranging in tens or even in hundreds of milliseconds, depending on the utilized hardware platform. Therefore, an averaging of multiple $I(k)$ periods was employed for each estimation cycle, leading to the K_{PEM} correction calculation with an equal rate (see Fig. 3.8).

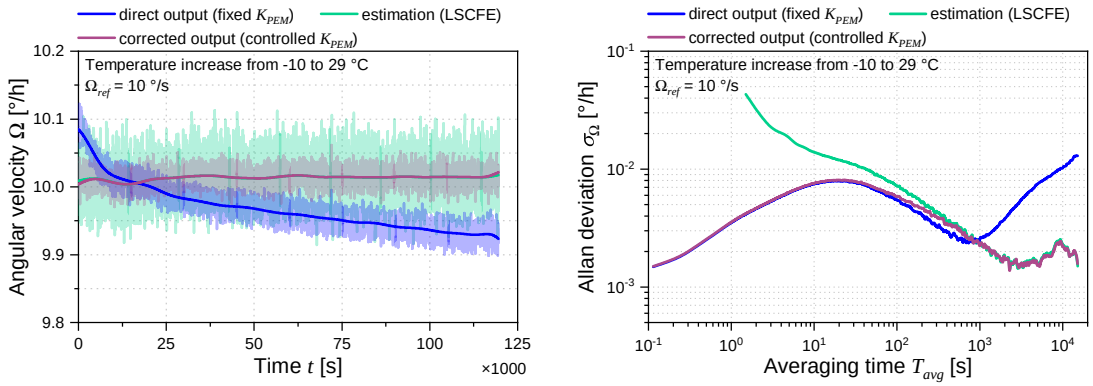
This procedure was implemented and tested with the P1c setup. In this scenario, the direct output data were corrected by the results obtained by the estimation, resulting in the corrected data. Those data thus have the same rate as the direct output data. Additionally, in the P1c setup, the correction was implemented as a function of the compensation modulation depth $\Delta\Phi_c$, meaning the $K_{PEM}(\Delta\Phi_c)$ factor is estimated for a certain value of $\Delta\Phi_c$. That allows the compensation of the direct output linearity error as well, induced by the discussed parasitic effects linearity error. A detailed description of the $K_{PEM}(\Delta\Phi_c)$ function calculation is provided in Sec. A.1. The verification of the direct data correction was performed at the angular velocity $\Omega_{ref} = 10$ °/s for different temperature profiles. The first two tests were performed for the temperature transient without active control by the temperature chamber. In this scenario, the possible parasitic effects caused by the temperature chamber, such as temperature fluctuations caused by internal control switching or mechanical vibrations, are completely eliminated. The transient was performed from an initial temperature of $\vartheta_1 = 40$ °C to a steady state temperature of the IFOG inside the chamber $\vartheta_2 = 29$ °C. The acquired signal of the direct data, data corrected with $K_{PEM}(\Delta\Phi_c)$, and the estimated data with slow rate are shown in Fig. 3.34(a) as a time series and in Fig. 3.34(b) in the form of the Allan deviation. It can be seen that the corrected data follow the trend determined by the estimation and demonstrate the stability improvement by about one order for



(a) (b)

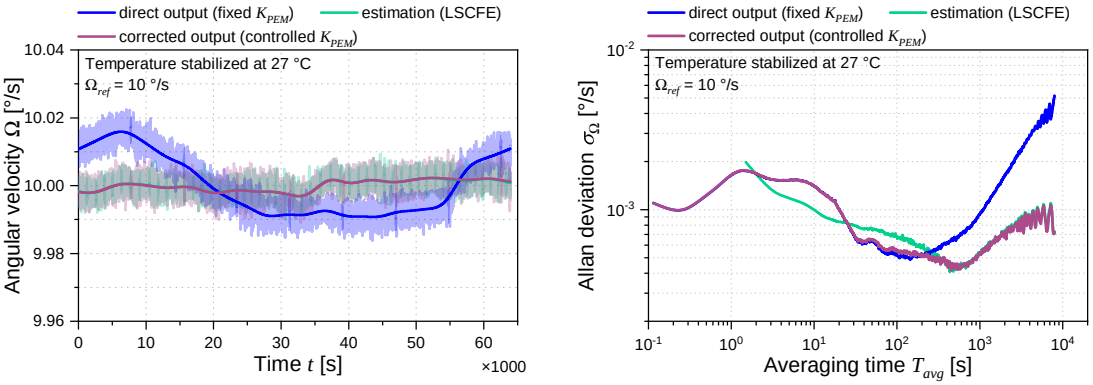
Fig. 3.34: Comparison of the direct data, corrected data, and the estimated data in the time domain (a) and as an Allan deviation (b) for the temperature drop from 40 to 29 °C (tested with IFOG P1c).

the longest averaging time, in a good agreement with the estimation data. On the other hand, from the short averaging time perspective, the noise level as well as the data rate of the corrected signal are equal to the corresponding parameters of the direct signal, so the advantages of the fast closed-loop phase shift compensation are preserved. The same conclusion can be drawn from an inverse temperature settling, where the initial temperature of $\vartheta_1 = -10$ °C was used, with the results displayed in Fig. 3.35. Although a different output filtering was used, resulting in higher noise, it can be equally seen that the corrected output follows the direct output in the short-term region. On the other hand, its long-term stability is determined by the estimation, which was shown to be independent from the modulation chain gain



(a) (b)

Fig. 3.35: Comparison of the direct data, corrected data, and the estimated data in the time domain (a) and as an Allan deviation (b) for the temperature rise from -10 to 29 °C (tested with IFOG P1c).



(a) (b)

Fig. 3.36: Comparison of the direct data, corrected data, and the estimated data in the time domain (a) and as an Allan deviation (b) for stabilized temperature at 27 °C (tested with IFOG P1c).

and thus much less susceptible to the impacting effects.

Despite the fact that temperature is the most significant factor influencing the K_{PEM}, it is not the only one, as already discussed. This was demonstrated by the test at a stable temperature of $\vartheta_{ref} = 27$ °C with the results shown in Fig. 3.36. The residual drift of the K_{PEM}, which is probably due to random effects and time varying fluctuations of the modulation chain parameters, can not be fully eliminated just by the temperature sensing. Therefore, the long-term scale-factor stability can only be attained with a suitable estimation technique, embodied by the LSCFE method in this testbench.

4 Scanning double-beam laser interferometer with closed-loop compensation and phase stabilization

The second use case of the optical phase shift compensation within the interferometric measurements studied in this thesis constitutes the DBMZI. It has been shown that employment of the phase modulation provides a useful technique to marginalize the output signal amplitude dependency on the sample reflectivity and the intensity fluctuations, facilitating the utilization of both the SBMI and DBMZI for sample vibrations scanning without a necessity of repeated recalibrations. Nevertheless, such a technique requires a precise knowledge of the modulation depth, which may pose an accuracy limitation, especially in the case of the commonly employed PEM due to its hysteresis, linearity, and the material parameters drift. Next to that, a relatively low bandwidth of such modulation principle renders it impossible to employ a closed-loop compensation of the measured vibrations, overcoming the residual nonlinearity caused by the interference transfer function and the optical signal detection chain.

To overcome the outlined issues, the employment of a broadband EOM is required. Compared to the cost-sensitive IFOG market, in the case of the DBMZI, the replacement of PEM by EOM does not introduce a notable price or complexity increase. On the contrary, the utilization of EOM leads to a simplification of the optical structure, since it does not require an additional beamsplitter to direct the beam to the PEM-driven mirror. Instead, the EOM can be placed into the reference beam path as a pass-through element to introduce a desired phase difference. The basic structure of the newly designed EOM-based DBMZI is schematically shown in Fig. 4.1. Both the EOM as well as the sample are controlled here, as the sample peizoelectric coefficient is a passive quantity and requires a driving voltage and a displacement measurement to be determined. Therefore, the lock-in detection is used to separate distinct frequency components within the intensity signal $I(t)$, as with the published SOTA DBMZI approaches.

The proposed closed-loop modulation methods have been tested using a DBMZI prototype, which also provides a possibility to operate as SBMI. Since such devices are usually used in the form of laboratory instruments, their miniaturization or integrability is not considered a critical requirement. However, since similar systems also exist as commercial devices, their competitiveness in terms of price and overall complexity should also be considered during the development. Hence, a notable effort has also been devoted to optimizing the measurement performance

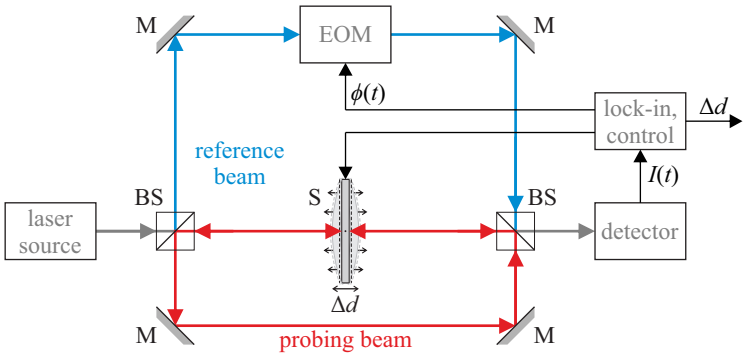


Fig. 4.1: Schematic of the DBMZI setup with a phase difference modulation by EOM (M – mirror, BS – beam-splitter, S – measured sample).

while concurrently minimizing the needed hardware and optical elements number through the design of the optical setup as well as the implementation of modulation and processing methods.

4.1 Closed-loop modulation methods

4.1.1 Quadrature point stabilization

In order to compensate the phase shift induced by the measured physical quantity, which, in this case, is displacement, obtaining a reliable open-loop signal is necessary. Since the Michelson and Mach-Zehnder interferometer topologies do not hold an inherent optical paths' reciprocity, both the probing as well as the reference beam optical phase may be subjected to a non-reciprocal random drift. To attain an operation near the quadrature point (see Fig. 1.1), a highly-stable environment is normally required.

The first task addressed by the proposed methods constitutes the active control of the quadrature operational point, which overcomes the aforementioned problem. The random drift $\Delta\phi_{drift}$ between the reference and the probing beam phase is compensated by a stabilization phase shift $\Delta\phi_{stab}$ introduced to the reference beam by the EOM, so that the operational point is held in quadrature point $\Delta\phi_q$:

$$\Delta\phi_q = \Delta\phi_{drift} + \Delta\phi_{stab} = \left(2n \pm \frac{1}{2}\right)\pi. \tag{4.1}$$

Recall that in the previously published solutions, the deviation from the quadrature point was detected through the intensity signal comparison to the fixed value obtained by the previous calibration. To avoid recalibration for each measurement point, i.e., to compensate the intensity fluctuations during the measurement, the

deviation from the quadrature point must be done independently from the detected intensity level. For this purpose, a modulation $\Delta\phi_m(t)$ of a phase difference is introduced by a sinusoidal signal of an angular frequency $\omega_m = 2\pi f_m$:

$$\Delta\phi_m(t) = \Delta\Phi_m \sin(\omega_m t). \tag{4.2}$$

The output intensity signal can be then expressed as:

$$\begin{aligned} I(t) &= I_n + I_i \cos\left[\Delta\phi_q + \Delta\phi_m(t)\right] = \\ &= I_n + I_i \left[\cos(\Delta\phi_q) A_0\left(\Delta\phi_m(t)\right) - \sin(\Delta\phi_q) A_1\left(\Delta\phi_m(t)\right)\right], \end{aligned} \tag{4.3}$$

where:

$$A_0\left(\Delta\phi_m(t)\right) = \mathrm{J}_0(\Delta\Phi_m) + \sum_{k=1}^{\infty} 2\mathrm{J}_{2k}(\Delta\Phi_m) \cdot \cos\left(2k\omega_m t\right), \tag{4.4}$$

$$A_1\left(\Delta\phi_m(t)\right) = \sum_{k=1}^{\infty} 2\mathrm{J}_{2k-1}(\Delta\Phi_m) \cdot \sin\left[(2k-1)\omega_m t\right]. \tag{4.5}$$

By the synchronous demodulation of $I(t)$ at even higher harmonics of ω_m, the qadrature point error signal can be obtained:

$$e_q(k) = 2I_i \mathrm{J}_{2k}(\Delta\Phi_m) \cos(\Delta\phi_q). \tag{4.6}$$

This signal approaches zero if the condition defined by Eq. 4.1 is satisfied. Best efficiency is reached for $k = 1$, reaching the highest maximum of $\mathrm{J}_2(\Delta\Phi_m)$ and also requiring the lowest modulation depth $\Delta\Phi_m$. This signal is then forwarded to the I or PI controller, driving the $\Delta\phi_{stab}$ phase shift. Due to the periodicity of the error function, the nearest positive or negative slope quadrature point can be controlled, depending on the feedback sign. The procedure is schematically shown in Fig. 4.2.

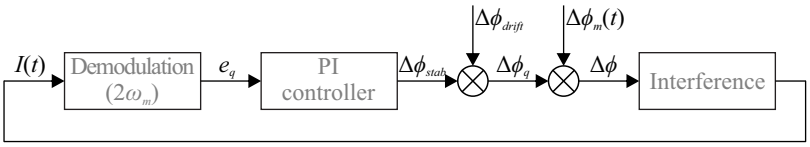


Fig. 4.2: Schematic of the quadrature point stabilization in the DBMZI.

As for the DC phase component, this procedure ensures an operation in the stable quadrature point, where the highest sensitivity is reached. A frequency component added by the modulation $\Delta\phi_m(t)$ can be separated by lock-in detection, which is a commonly adopted technique in the DBMZI for the sample vibrations detection. Limitations of the method may be posed by its frequency coincidence with $k\omega_m$, and also the dependency of the sensitivity on $\Delta\Phi_m$. To some extent, similar drawbacks have been discussed in connection with an open-loop phase modulation method in Sec. 1.5.3. Nevertheless, the major difference consists in a complete avoidance of the problem with the operation point drift, facilitating a sensitive lock-in detection of both magnitute and phase, without sensitivity fading.

4.1.2 Sample vibrations closed-loop compensation

The second task addressed is the measurement of the sample thickness displacement by the closed-loop compensation of the induced phase shift. With the compesation approach, any optical intensity variations during the measurement are completely suppressed, which allows the system to be used for multiple points measurement, i.e., the scanning vibrometry. Assume a sinusoidal driving voltage $u_s(t) = U_s \sin(\omega_s t)$ is applied to the sample. The resulting optical phase difference is expressed as:

$$\Delta\phi_s(t) = \Delta\Phi_s \sin(\omega_s t + \varphi_s), \tag{4.7}$$

where $\Delta\Phi_s = \frac{4\pi}{\lambda} U_s d_{33}$ and φ_s stands for the phase delay between the voltage and the displacement, caused by sample piezoelectric dynamics, hysteresis and the driving circuits delay. The closed-loop measurement approach consists in nulling the phase shift $\Delta\phi_s(t)$ by a compensation modulation $\Delta\phi_c(t)$, introduced by the EOM, so that:

$$\Delta\phi_s(t) + \Delta\phi_c(t) = 0. \tag{4.8}$$

Note that it is necessary to null not only the amplitude but also the phase of the $\Delta\phi_s(t)$. This can be achieved by complex $\Delta\phi_c(t)$ having an inphase and a quadrature component, i.e.:

$$\Delta\phi_c(t) = \Delta\phi_{c\langle i\rangle}(t) + \Delta\phi_{c\langle q\rangle} = \Delta\Phi_{c\langle i\rangle} \sin(\omega_s t) + \Delta\Phi_{c\langle q\rangle} \cos(\omega_s t). \tag{4.9}$$

Assuming the condition defined by Eq. 4.1 is attained by the quadrature point stabilization, the output intensity can be defined as:

$$I(t) = I_n \mp I_i \sin\Big[\Delta\Phi_m \sin(\omega_m t) + (\Delta\Phi_{\Delta s\langle i\rangle}) \sin(\omega_s t) + (\Delta\Phi_{\Delta s\langle q\rangle}) \cos(\omega_s t)\Big], \tag{4.10}$$

where $\Delta\Phi_{\Delta s\langle i\rangle} = \Delta\Phi_s \sin\varphi_s + \Delta\Phi_{c\langle i\rangle}$ and $\Delta\Phi_{\Delta s\langle q\rangle} = \Delta\Phi_s \cos\varphi_s + \Delta\Phi_{c\langle q\rangle}$ stand for the uncompensated, or residual error. An error signal of the sample-induced phase shift compensation can be then conveniently obtained by employing a synchronous demodulation of $I(t)$ at odd harmonics of ω_s. The inphase and quadrature error components are thus defined as:

$$e_{s\langle i\rangle}(k) = \mp 2 I_i \mathrm{J}_0(\Delta\Phi_m) \mathrm{J}_{2k-1}(\Delta\Phi_{\Delta s\langle i\rangle}), \tag{4.11}$$

$$e_{s\langle q\rangle}(k) = \mp 2 I_i \mathrm{J}_0(\Delta\Phi_m) \mathrm{J}_{2k-1}(\Delta\Phi_{\Delta s\langle q\rangle}). \tag{4.12}$$

Consequently, an I or PI controller can be used to control the amplitude of the inphase and quadrature compensation modulation components so that the condition defined by Eq. 4.8 is met.

As the odd-order Bessel functions are odd functions, the convergence can be reached for any k, assuming both $\Delta\Phi_{\Delta s\langle i\rangle}$ and $\Delta\Phi_{\Delta s\langle q\rangle}$ are in between the first J_{2k-1} function minimum and maximum. Nevertheless, since $\mathrm{J}'_{2k-1}(0) = 0$ for $k > 0$, only $k = 1$ is usable for a reliable phase shift nulling. The maximal error in both orthogonal error components can thus reach $\left|\Delta\Phi_{\Delta s\langle i\rangle}\right|, \left|\Delta\Phi_{\Delta s\langle q\rangle}\right| < 1.8412$, corresponding to the maximal sample displacement of $\Delta d|_{\max} = 0.146\lambda$. Larger displacements can be measured either with an amplitude ramp of the driving voltage $u_s(t)$, or by switching between $k > 1$ components, which reaches a broader monotonous region.

The schematic of the closed-loop measurement process by the sample-induced phase shift compensation is shown in Fig. 4.3. The desired piezoelectric coefficient then can be determined as follows:

$$d_{33} = \frac{\lambda}{4\pi U_s}\sqrt{\Delta\Phi^2_{c\langle i\rangle} + \Delta\Phi^2_{c\langle q\rangle}}, \tag{4.13}$$

and the phase delay as:

$$\varphi_s = \pi + \tan^{-1}\left(\frac{\Delta\Phi_{c\langle q\rangle}}{\Delta\Phi_{c\langle i\rangle}}\right). \tag{4.14}$$

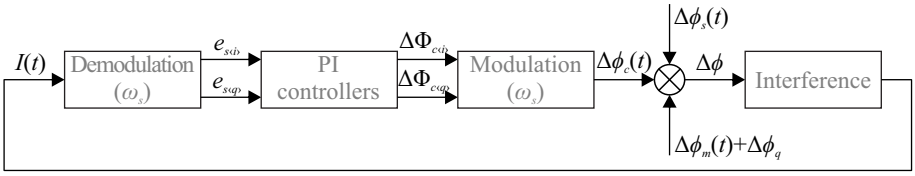


Fig. 4.3: Schematic of the sample-induced phase shift compensation.

Recall that the relations above are fully valid only when the condition defined by Eq. 4.1 is satisfied and maintained by the first control loop. In practical case, a deviation in the control can affect the $e_{s\langle i\rangle}$ and $e_{s\langle q\rangle}$ detection. Moreover, the inphase and the quadrature components can affect each other, as they are handled by separate control loops. Including the other components' error dependencies, the Eqs. 4.11 and 4.12 for $k = 1$ can be rewritten to a general form:

$$e_{s\langle i\rangle} = -2I_i \sin(\Delta\phi_q)\mathrm{J}_0(\Delta\Phi_m)\mathrm{J}_1(\Delta\Phi_{\Delta s\langle i\rangle})\mathrm{J}_0(\Delta\Phi_{\Delta s\langle q\rangle}), \tag{4.15}$$

$$e_{s\langle q\rangle} = -2I_i \sin(\Delta\phi_q)\mathrm{J}_0(\Delta\Phi_m)\mathrm{J}_1(\Delta\Phi_{\Delta s\langle q\rangle})\mathrm{J}_0(\Delta\Phi_{\Delta s\langle i\rangle}), \tag{4.16}$$

The sensitivity to the quadrature point stabilization error $\Delta\phi_q$ can be expressed by means of the partial derivative, which is proportional to $-\cos(\Delta\phi_q)$. Consequently, the sensitivity in the operational points defined by Eq. 4.1 approaches zero, so the $e_{s\langle i\rangle}$, $e_{s\langle q\rangle}$ detection is merely dependent on the imperfections in the $\Delta\phi_q$ control. Moreover, as an advantage of the closed-loop method of the $\Delta\Phi_s$ measurement, the

noise in the $\Delta\phi_q$ control propagates only as the error signal gain drift. Therefore, it will neither affect the stability of the $\Delta\Phi_s$ compensation, nor the noise in the compensation amplitudes $\Delta\Phi_{c\langle i\rangle}$, $\Delta\Phi_{c\langle q\rangle}$, as it drops to zero when $\Delta\Phi_s$ is fully compensated. This could not be attained in the open-loop approach, where an error in the $\Delta\phi_q$ control can directly propagate to the measured signal.

Another matter to consider is the mutual influence of $\Delta\Phi_{c\langle i\rangle}$ and $\Delta\Phi_{c\langle q\rangle}$, as they are handled by separate control loops. Firstly, a minimal cross-coupling must be ensured, i.e., each error component $e_{s\langle i\rangle}$, $e_{s\langle q\rangle}$ must be in phase with the sensed effect of $\Delta\phi_{c\langle i\rangle}(t)$ and $\Delta\phi_{c\langle q\rangle}(t)$ components within the $I(t)$ signal. This can be ensured by a proper phase adjustment of the inphase and quadrature error detection, corresponding to the modulation and signal detection chain delay. Secondly, even with an orthogonal detection, the error component $e_{s\langle i\rangle}$ is sensitive to the uncompensated phase shift $\Delta\Phi_{\Delta s\langle q\rangle}$ and, analogously, the $e_{s\langle q\rangle}$ depends on the $\Delta\Phi_{\Delta s\langle i\rangle}$, as expressed by the following equation:

$$\frac{\partial e_{s\langle i\rangle}}{\partial\Delta\Phi_{\Delta s\langle q\rangle}} = \frac{\partial e_{s\langle q\rangle}}{\partial\Delta\Phi_{\Delta s\langle i\rangle}} = 2I_i \sin(\Delta\phi_q)\mathrm{J}_0(\Delta\Phi_m)\mathrm{J}_1(\Delta\Phi_{\Delta s\langle i\rangle})\mathrm{J}_1(\Delta\Phi_{\Delta s\langle q\rangle}). \quad (4.17)$$

Similarly to the previous case, the cross-sensitivity drops to zero when the other component is fully compensated. In this case, only the magnitude of the error is affected by the other component, but not its sign. The additional limit for both $e_{s\langle i\rangle}$ and $e_{s\langle q\rangle}$ error components is thus posed by the J_0 function sign inversion, i.e., $\left|\Delta\Phi_{\Delta s\langle i\rangle}\right|, \left|\Delta\Phi_{\Delta s\langle q\rangle}\right| < 2.4048$, which is always fulfilled, as it is well within the operating range outlined before.

4.1.3 Modulation gain detection

As with any compensation measurement method, the output signal is proportional to the closed-loop compensation chain gain. In general, each component of the compensation chain can be described by its transfer function, which has to be known to perform a precise measurement. In the case of the scanning DBMZI, these components comprise an EOM and its driving electronics. Compared to PEM, EOM is known to provide a uniform frequency transfer up to several GHz. However, in the free-space EOM, a voltage of several tens or hundreds of volts is required to provide a shift of several radians due to the relatively weak Pockels effect. Therefore, a high-voltage amplifier is usually required to magnify the input voltage $u_c(t)$, outputting the EOM driving voltage, which causes a corresponding phase shift $\Delta\Phi_c = K_{EOM} \cdot u_c$, where K_{EOM} refers to the voltage-to-phase gain. In general, the gain is always frequency-dependent, where the limiting component is typically the amplifier. Further, the EOMs are known to have a temperature dependency, based on the employed cut type, unless a temperature-balanced EOM is utilized. Additionally, as EOM works

on the principle of the refractive index change, the introduced phase shift is also wavelength-dependent. However, this phenomenon can be neglected in this case, as purely monochromatic light is employed.

Unlike the IFOG, where the K_{PEM} coefficient should be controlled and corrected continuously due to varying operating conditions and the level of the measured quantity, the DBMZI is assumed to operate in a stable environment and for sensing the steady vibrations. Therefore, the calibration of K_{EOM}, which represents also the compensation modulation gain, may be performed as a separate procedure before the measurement itself. There are multiple ways to detect the $K_{EOM}(\omega_s)$ in the DBMZI. Assuming a stabilized laser is employed as a light source, its wavelength can be utilized as a highly accurate reference.

The first method proposed herein is based on canceling the first harmonic component and employs a similar principle to that used for detecting the compensation modulation error components. To maximize the sensitivity, it can also be useful to employ a $\Delta\phi_m(t)$ modulation and the quadrature point stabilization. The compensation modulation $\Delta\phi_c(t) = \Delta\Phi_c \sin(\omega_s t)$ is then applied to the EOM, but without driving the sample. The magnitude of the component obtained by the demodulation at ω_s is then likewise expressed as:

$$S_{\omega_s} = \mp 2 I_i \mathrm{J}_0(\Delta\Phi_m)\mathrm{J}_1(\Delta\Phi_c), \tag{4.18}$$

reaching zero for $\Delta\Phi_c = \mp 3.8317$, which is the first zero-crossing of the J_1 function. From the corresponding voltage amplitude U_c, the K_{EOM} can be directly determined as:

$$K_{EOM} = \frac{3.8317}{U_s}. \tag{4.19}$$

This simple method can only be applied if the compensation chain provides a sufficient range of modulation depth. However, both the DBMZIs and SBMIs are usually purposed for an accurate measurement of very small displacements, so a calibration method requiring a depth larger by several orders of magnitude may not be convenient in this case. It can be overcome by the multiple harmonics detection method, avoiding a need for large compensation modulation depth. Assume the quadrature point is stabilized with the use of $\Delta\phi_m(t)$ modulation. When a small modulation $\Delta\phi_c(t)$ is further applied, apart from the S_{ω_s} signal detection, other components can be obtained from $I(t)$ signal by the demodulation at $(\omega_s \pm 2\omega_m)$ and $(2\omega_s \pm \omega_m)$:

$$S_{\omega_s \pm 2\omega_m} = \mp 4 I_i \mathrm{J}_2(\Delta\Phi_m)\mathrm{J}_1(\Delta\Phi_c), \tag{4.20}$$

$$S_{2\omega_s \pm \omega_m} = \mp 4 I_i \mathrm{J}_1(\Delta\Phi_m)\mathrm{J}_2(\Delta\Phi_c). \tag{4.21}$$

By adding Eq. 4.18, we obtain a set of equations that yield an unambigous solution if $|\Delta\Phi_m|$ and $|\Delta\Phi_c|$ are both less than 5.135. This condition must be met for both modulations. Additionally, the I_i level is also determined by the multiple harmonics method. However, as the demodulation occurs at distinct frequencies, a disadvantage of this method can be posed by an uneven gain $K_{det}(\omega)$ of the detection chain. Hence, practical constraints regarding the utilized modulation frequencies should be taken into account. As the DBMZIs are targeted especially at high-frequency samples' characterization, it is convenient to choose $\omega_m \ll \omega_s$. Consequently, the $K_{det}(\omega_s) \cong K_{det}(\omega_s \pm 2\omega_m)$. Though, $K_{det}(2\omega_s \pm \omega_m)$ may differ due to the limited detection chain bandwidth and thus lead to an error in $\Delta\Phi_c$ detection. The detector bandwidth should be thus known before the K_{EOM} calibration.

As an alternative, a half frequency $\omega_s' = \frac{\omega_s}{2}$ can be used with the detection of the $S_{2\omega_s' \pm \omega_m}$ component instead of $S_{2\omega_s \pm \omega_m}$. Since $K_{det}(2\omega_s' \pm \omega_m) \cong K_{det}(\omega_s \pm 2\omega_m)$, the calibration procedure is virtually independent on the detection gain. On the other hand, it must be ensured that $K_{EOM}(\omega_s) = K_{EOM}(\omega_s')$. Therefore, this modification should only be considered if the optical signal detection chain is the major limiting factor.

4.2 Implementation

The outlined methods were implemented and tested in a designed DBMZI setup utilizing the EOM. Compared to the so-far published solutions with PEM, the configuration proposed herein reduces the number of required optical components. Consequently, besides the total costs, the errors caused by the parasitic reflections and the optical beam misalignments are also decreased. As already outlined, the experimental setup was developed not only to demonstrate the novel modulation and the closed-loop compensation methods, but also as a tool for practical characterization of the specific piezoelectric materials and samples, purposed for further research and the sensors development.

Even though the outlined stabilization method can compensate both the long-term drift as well as sudden parameters change, the system is still susceptible to the high-bandwidth noise represented dominantly by external acoustic and mechanical vibrations. Therefore, the optical setup is isolated from the vibrations by an air-damped optical table. It was observed that the damping is necessary, especially for the measurement at lower frequencies ω_s, where exists a high risk of the coincidence with the external vibrations bandwidth. Additionally, the setup is placed into a simple enclosure, serving as dust and air flow protection. With such equipment, it was possible to operate the DBMZI in normal laboratory conditions, without requiring a separate room or an additional temperature stabilization.

It is worth mentioning that the DBMZI setup underwent several modifications during its development and testing. The changes performed, nevertheless, primarily focused on enhancing scalability and the automation of the measurement procedure, without affecting key parameters, such as resolution or displacement measurement range. Therefore, only the final evolution of the system will be described in this section, with a separate view on its optical part and the processing and control part.

4.2.1 Optical setup

As for the optical part of the designed DBMZI, its topology is schematically outlined in Fig. 4.4. A frequency-stabilized HeNe laser is used as a source, providing a wavelength $\lambda = 632.991$ nm and a power of 1.2 mW. The light beam passes through the isolator (IS), preventing the laser destabilization by backreflection, and the half-wave (HWP) plate, changing the polarization from vertical to diagonal. To avoid power loss, polarization beam splitters (PBS) are employed to split and combine the probing and the reference beams. Similarly to the common DBMZI, the probing beam is directed to the front and then to the back side of the measured sample. The quarter-wave (QWP) plates are employed to transform the polarization from horizontal to circular in one direction, and from circular to vertical in the opposite direction, or vice versa, to ensure that the light passes through the PBS in a desired manner. The focusing of the beam to the single point on the sample surface is then ensured by the lenses (L1, L2). The reference beam is directed by the mirrors (M3, M4) to the PBS2. In the EOM-based setup, it is possible to place the modulator anywhere in the reference beam path, or even the probing beam trace if the

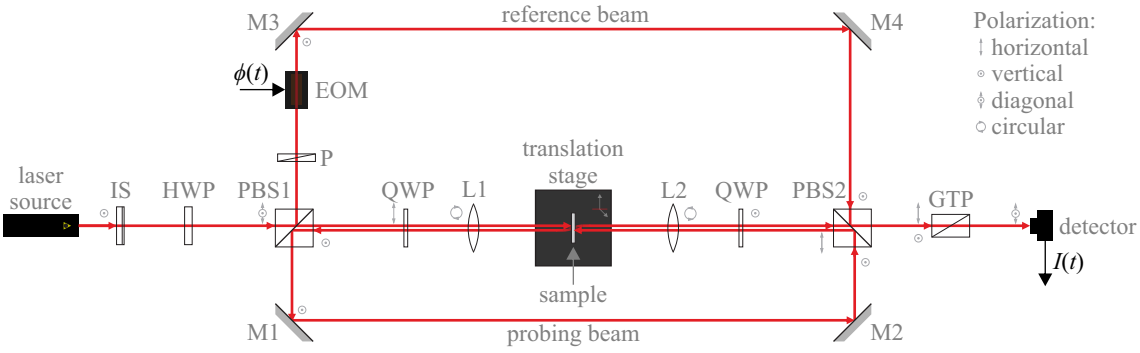


Fig. 4.4: The optical architecture of the DBMZI testing setup (IS – isolator, M – mirror, PBS – polarization beam splitter, L – lens, P – polarizer, GTP – Glan-Thompson polarizer, QWP – quarter-wave plate, HWP – half-wave plate) [175], (modified).

polarity is reversed. To be able to adjust the direction of both beams independently, the most convenient location of the EOM is shown in Fig. 4.4. To diminish a residual horizontal component, a polarizer (P) is placed before the EOM, ensuring that solely its extraordinary mode is affected. The interference between the probing and the reference beams is ensured by the Glan-Thompson polarizer (GTP), combining both orthogonal polarizations to a diagonal, which is then directed to the detector. As shown by Eq. 1.10, the interference contrast, or visibility, is maximized if both beams are balanced in power. This can be additionally achieved by rotating the HWP plate located behind the IS. The loss due to a limited sample reflectivity can thus easily be compensated by increasing the initial power of the probing beam over the reference one. Scanning of the sample vibrations is facilitated by the motorized sample translation stage, allowing a sample movement in its surface plane relative to the fixed probing beam, further referred to as X and Y coordinates.

One of the most critical parts of the DBMZI optical setup is a proper beam direction on the sample surfaces. Most of the DBMZI systems thus employ lenses to focus the beam onto the sample surface to measure in a single point. The longer their focal length, the deeper the field of view is, as well as the tolerance to the focal plane and the sample surface mismatch. On the other hand, with the increase of the focal length, the overall dimensions of the system also increase. The distance can be shortened using a lens or a system of multiple lenses. It can be shown that by placing a concave lens with a focal length f_2 after the normally employed convex lens with a focal length f_1 in a distance d_l, a virtual focal length of:

$$f = \frac{f_1 \cdot f_2}{f_1 + f_2 + d_l} \tag{4.22}$$

is obtained, enabling a large depth of field with reasonably small dimensions.

On the other hand, some cases require a short depth of field or defocusing the beam. This concerns samples with a poor reflection. DBMZI systems described by the research literature require an application of a reflective coating on the sample surface to ensure a large and uniform reflection. Thanks to the compensation methods, this step is not necessary with the proposed system. The measurement of uncoated and even non-flat samples was successfully demonstrated, requiring just a simple surface polishing to reduce the speckle noise. Due to double reflection, the speckle noise is multiplied and can constitute a significant problem for the precise sample measurement. In some cases, this problem may be overcome by an unlensed system, where the beam covers a larger area of the sample surface. Nevertheless, apart from worse spatial resolution for scanning, such configuration exhibits significant susceptibility to the sample deflection. A geometric analysis of the designed optical setup revealed that a deflection of 0.1° leads to a beam misalignment of 4.2 mm on the back side of the sample. Therefore, the second purpose of the lenses

is to compensate the sample deflection, which can also occur as a parasitic motion during its driving.

In the case of thin samples, for which the system is primarily intended, the sample deflection can cause another problem if the front and the back side points of measurements are misaligned. The measurement of the AlN layer on the Si substrate demonstrated that the substrate deflection reaches the displacement an order of magnitude larger compared to the thickness change of the piezoelectric layer itself. Therefore, the misalignment can introduce a significant error in the characterization of such samples. Thus, a novel method was developed for the back and the front side probing beams alignment. In the traditional alignment approach, before inserting the sample into its position, two pinholes are placed between its intended position and PBS2, aligned with the beam incident from PBS1. Then, the sample is inserted, and the mirrors M1 and M2 are adjusted so that the beam coming from PBS2 is aligned with both pinholes. Due to using the beam reflected from the sample, this procedure can be challenging in the case of nonperfectly reflective samples. Secondly, the precision of the beam alignment is determined not only by the laser spot and the pinhole size, but also by the arm length. The larger the length the beam can travel between the pinhole and the adjusting element, the more precise the alignment generally is. The same applies also to the distance between the pinholes. Both of these factors are quite limiting in the traditional method. The proposed method based on multiple beam recirculations overcomes both problems. The method allows placing the pinholes behind the PBS2, allowing the path to be virtually unlimited by the setup dimension. The method is based on the reciprocal property of the beam propagation and operates without the need for sample insertion. By adding the second HWP plate between the PBS2 and neighboring QWP, the beam coming from the QWP to the PBS2 then passes straight through the PBS2 but, due to a different polarization, is partially reflected to the M2 and is thus subsequently recirculated through the whole path of the probing arm. Hence, by adjusting this second HWP plate, an infinite number of rounds can be theoretically attained, producing an array of beam spots on the pinhole. By tuning the M1 and M2 mirrors, a precise alignment of the spots of the front and the back side of the sample can be achieved. Further details related to the DBMZI optical setup are given in [175]. The supplementary materials can also be found in Sec. B.1.

4.2.2 Control unit and data processing

Employing the lock-in detection in the DBMZI is considered the most common technique to separate the desired frequency components. Unlike with the other reported solutions, where solely the ω_s component is extracted, the proposed method

exploits further the $2\omega_m$ component and, for the purpose of a calibration, also their combinations.

The demodulation is accomplished by a lock-in amplifier (Zurich Instruments HF2LI), which also fulfills the function of modulation signal generation and control. The electronic part of the DBMZI setup is shown in 4.5. The top-level control is then ensured by a PC, running a LabVIEW application, enabling full measurement settings, monitoring, control, and automation. The implemented functions include automatic frequency sweep, position scanning, quadrature point switching, automatic K_{EOM} calibration procedure, measured data validity check, data logging, etc. The application thus controls not only the lock-in amplifier, but also the sample translation stage and the laser switch to save its wear hours after finishing the measurement.

For the quadrature point stabilization as well as the sample vibrations compensation, three proportional-integration (PI) controllers are utilized (see Figs. 4.2 and 4.3). The first task is ensured by an inbuilt controller in the lock-in amplifier. On the other hand, the vibrations compensation task can be performed either with inbuilt controllers, or externally, via the PC application. The benefit of the external controller is a broader numerical resolution of the integrator in comparison to the inbuilt integrator, which can be insufficient for very small $\Delta\Phi_c$ adjustments, and thus limiting the resolution of the closed-loop measurements.

The components of the phase modulation signal are generated within the lock-in amplifier and serve also as reference signals for the consequent intensity signal

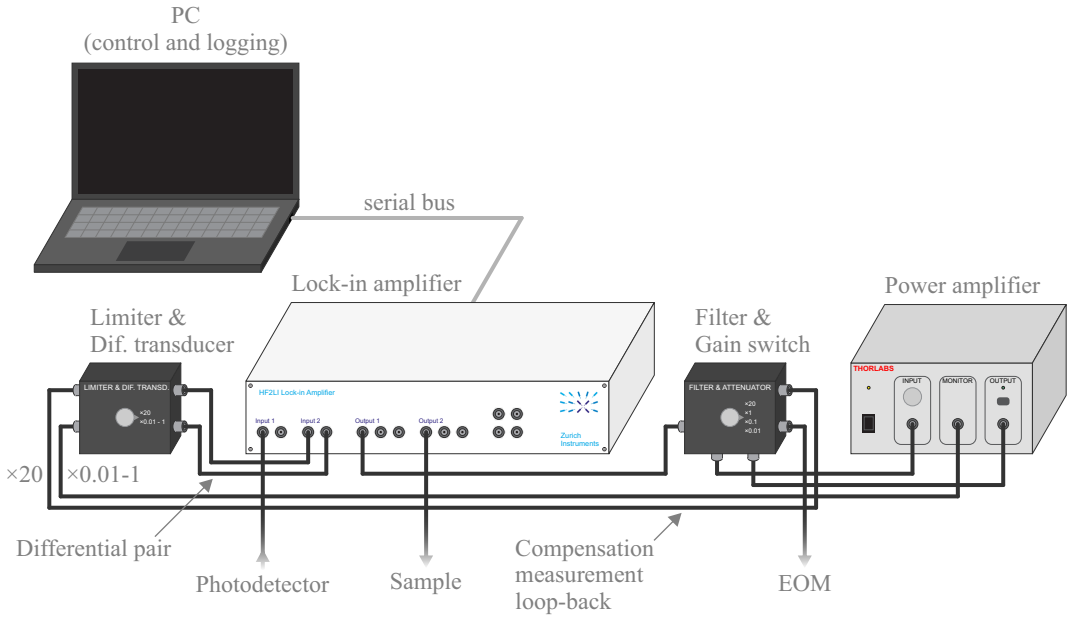


Fig. 4.5: Layout of the DBMZI control and processing setup.

demodulation. The amplifier provides two outputs: one for driving the sample by the voltage $u_s(t)$, and the other for the EOM, having the components $u_{stab}+u_m(t)+u_c(t)$, representing the quadrature point stabilization, the corresponding modulation, and the sample vibrations compensation, respectively.

Although the amplitude of the $u_m(t)$ component is fixed, the other two components are regulated by the PI controllers, requiring additional over-range monitoring. Especially the u_{stab} can easily exceed the range in case of the large phase drift. Therefore, a quadrature point switching technique is employed, taking advantage of the interference periodicity, as expressed by Eq. 4.1. The u_{stab} is thus controlled towards reaching the nearest quadrature point. As both positive and negative slope sections of the interference fringe can be used (see Fig. 1.1), the range of $\left\langle -\frac{\pi}{2}; \frac{\pi}{2} \right\rangle$ is sufficient for the stabilization. Nevertheless, in practical cases, it is convenient to slightly extend this range to introduce hysteresis, which prevents instability caused by the operational point switching. In the referred setup, the range is extended to about $\left\langle -\frac{1.4\pi}{2}; \frac{1.4\pi}{2} \right\rangle$.

Due to the relatively weak Pockels effect of the EOM (Thorlabs EO-PM-NR-C1), the modulation voltage is directed to the power amplifier (Thorlabs HVA200), providing a fixed gain of a factor 20. Nevertheless, as the $u_c(t)$ voltage resolution is also limited, such amplification may not be suitable for very small $\Delta\Phi_s$ measurement, requiring fine adjustment of the compensation voltage $u_c(t)$. This is solved by additional switchable filters and attenuators, facilitating the $u_c(t)$ component driving the EOM directly, or, instead, with up to 100-fold attenuation, for finer compensation of even very small displacements. The filters are set to have a cutoff frequency of 80 Hz for the low-pass and 300 Hz for the high-pass filter, separating the slower modulation $\Delta\phi_m(t)$ and the compensation modulation $\Delta\phi_c(t)$, respectively. Both signals are then electrically combined by driving the EOM electrodes differentially. With such extension, an overall achieved dynamic range of the compensation depth $\Delta\Phi_c$ amounts to 136 dB, facilitating the measurement of the thickness vibrations from 1.4 fm up to 9 nm.

As already discussed with the compensation phase shift $\Delta\Phi_c$ and the detected error e_s, it is crucial to minimize the cross-coupling between the inphase and the quadrature components. Such an issue is resolved by a phase correction between the outputting compensation modulation phase shift and the detected error. The correction function was obtained by means of calibration at distinct frequencies and polynomial approximation, performed separately for each compensation voltage range. As the residual cross-coupling can potentially destabilize the compensation of inphase and quadrature components, it is advisable to select different dynamics for the controllers. This can be achieved by adjusting their time constants to prevent matching.

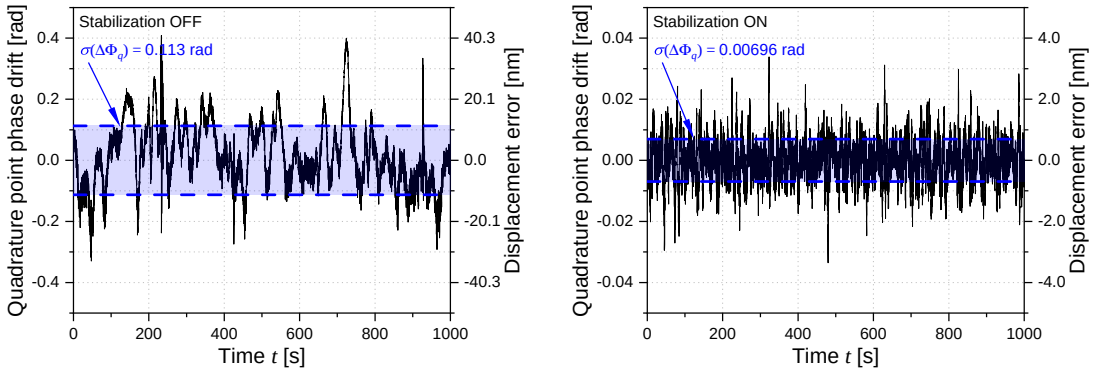
The measured sample thickness displacement, proportional to the thickness piezoelectric coefficient, is determined through Eq. 4.13, where the phase amplitudes are computed from the voltage amplitudes $U_{c\langle i\rangle}$, $U_{c\langle q\rangle}$ employing the K_{EOM} obtained by the gain detection method. The voltage can be calculated directly by multiplying the PI controllers' output values and the selected compensation range gain. As the gain may also be subjected to drift, the proposed implementation provides a loop-back measurement of an actual compensation voltage, which is then detected through the lock-in technique accurately. Such detection is not only highly resistant to the gain instability but also provides additional filtering of the undesired frequency components present in the direct PI output signals.

4.3 Verification and results

The testing and verification of the DBMZI system using the designed methods was performed through an inherent response measurement as well as the real piezoelectric samples characterization. Both thin piezoelectric films and bulk PZT samples were employed. Firstly, the benefits of the closed-loop stabilization of the quadrature point were demonstrated, revealing also its impact on the sample vibrations error detection. Subsequently, measuring the thickness vibrations of several sample demonstrated the capabilities of the closed-loop measurement method, showing not only its achievable performance, but also the advantages of the closed-loop compensation approach over the direct open-loop vibrations sensing.

4.3.1 Quadrature point stabilization

A benefit of the closed-loop quadrature point stabilization can be straightforwardly demonstrated by observing the quadrature point error over a longer period of time. The stabilized measurement was thus compared to the non-stabilized, where the $\Delta\phi_{stab}$ component was fixed. The testing was conducted with $f_m = 80$ Hz, corresponding to the settings used for the subsequent measurements as well. For both of the mentioned cases, the phase drift of the quadrature point acquired over a 1000 s interval can be seen in Fig. 4.6. The mean error of the non-stabilized error was normalized to zero, equalling an optimal $\Delta\phi_{stab}$ setting. Despite that, it can be clearly seen in Fig. 4.6(a) that the quadrature point is subjected to a random drift with a standard deviation of 0.113 rad. Remember that the noise corresponds to the discussed acoustic and vibration shielding and standard laboratory conditions. On the other hand, by employing the stabilization method, it is possible to detect and compensate the drift in real time. The phase error is thus reduced by about

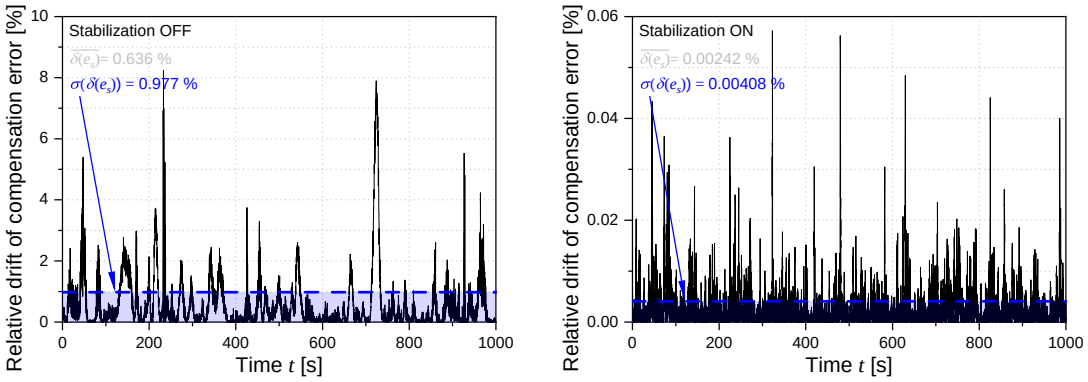


(a) (b)

Fig. 4.6: Comparison of the quadrature point phase drift when it is set to an optimal fixed $\Delta\phi_{stab}$ value (a) and when it is stabilized by the closed-loop method (b).

one order, as its standard deviation drops to only 0.00696 rad, representing an improvement of about 16 times compared to the non-stabilized case. Further, a zero phase error mean value over a longer period of time is attained by the principle of operation and does not have to be tuned manually before the measurement.

The most important benefit of the quadrature point stabilization technique can be seen in the detection of the sample vibrations error signal $e_{s\langle i\rangle}$ and $e_{s\langle q\rangle}$. As shown by the Eqs. 4.15 and 4.16, an operational point affects their gain through the $\sin(\Delta\phi_q)$ factor. Therefore, the stability of the operational point is much more important than maintaining the exact quadrature point. The reason is that any noise in $\Delta\phi_q$ propagates also to the $e_{s\langle i\rangle}$ and $e_{s\langle q\rangle}$ error components and thus has an impact on the $\Delta\Phi_c$ as well. Based on the observed drift of $\Delta\phi_q$ displayed in Fig. 4.6, a relative drift of the sample vibrations error signal $\delta(e_s)$ can be derived as $1 - \sin(\Delta\phi_q)$, as demonstrated in Fig. 4.7. From this point of view, the benefit of the quadrature stabilization is even more significant. Whereas the fixed setting of $\Delta\phi_{stab}$ produces the oscillations of the e_s signal components up to several percent, the stabilization method reduces the noise by about two orders of magnitude. Specifically, its standard deviation is reduced from 9770 ppm to 41 ppm, constituting a 238-fold improvement. Its mean value is then reduced 262 times, from 6360 to 24 ppm. Compared to the static quadrature point setting, a proposed stabilization technique represents a vital enhancement, regardless of the method employed for the consequent sample vibrations detection.



(a) (b)

Fig. 4.7: Comparison of the relative drift of the sample vibrations compensation error signal for the case when the $\Delta\phi_{stab}$ is set to an optimal fixed value (a) and when it is stabilized by the closed-loop method (b).

4.3.2 Sample vibrations closed-loop compensation

A verification of the closed-loop compensation method was performed through a measurement of both piezoelectric film as well as bulk PZT samples. As stated above, one of the key advantages of the closed-loop phase shift compensation is the independence on the detected optical intensity, which is directly proportional to the reflectivity of both sample surfaces. In the case of the d_{33} profile scanning, the traditional methods thus require performing an intensity level calibration at every single measurement point of the sample surface. The importance of this step can be demonstrated by the results of the open-loop sample vibrations measurement, i.e., without the compensation modulation. A bulk PZT sample (cylinder, NCE41) with polished Ag electrodes was employed, driven by $U_s = 1$ V and $f_s = 2$ kHz, where a uniform vibration profile is expected. The open-loop signal e_s was then directly measured and normalized to the mean value of the actual sample thickness displacement. The resulting profile in Fig. 4.8(a) clearly demonstrates the significant effect of the sample reflectivity and thus the related displacement misinterpretation with the open-loop measurement unless the recalibration is performed at each point. This issue is completely eliminated with the closed-loop method, allowing fluent point-to-point scanning without any errors induced by the sample reflectivity, as shown in Fig. 4.8(b). The residual non-uniformity is most likely caused by the sample clamping, which leads to parasitic damping of the vibrations, and thus corresponding to an actual displacement in sample thickness.

Further verification of the closed-loop compensation method was carried out by one-axis vibrations scanning, demonstrating the capability of fluent point-to-point vibrations scanning. With the finest measurement range (100-fold $u_c(t)$ attenuation)

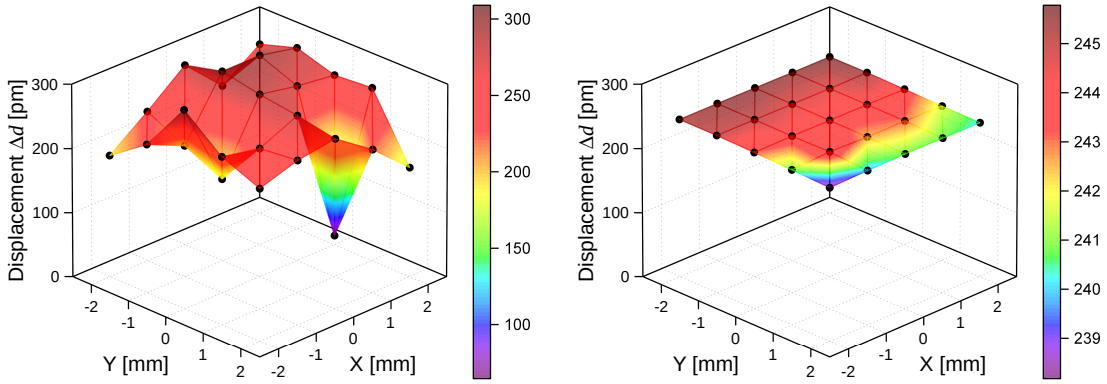


Fig. 4.8: Scanning of the thickness displacement of the PZT sample (cylinder, NCE41) demonstrating the reflectivity-induced error of the measured displacement determined from the open-loop demodulated output (a) and through the closed-loop compensation method (b) (measured for $U_s = 1$ V and $f_s = 2$ kHz) [175].

and employing a thin piezoelectric sample (AlN film on a Si substrate), a capability of a highly sensitive scanning was demonstrated, as shown in Fig. 4.9. The thickness vibration profile corresponded well to the electrode position and showed thus also the actual movement of its edge. Furthermore, a single-side measurement, carried out by placing a mirror between the sample and the left QWP plate (resulting in a SBMI, as mentioned previously), exhibited vibrations approximately one order of magnitude larger, confirming the effect of the parasitic substrate bending. The experiment thus also confirmed the necessity of employing the DBMZI for the thin piezoelectric films characterization. It is also worth mentioning that unlike the previously published experiments, all of which required an additional reflective coating of the sample, the

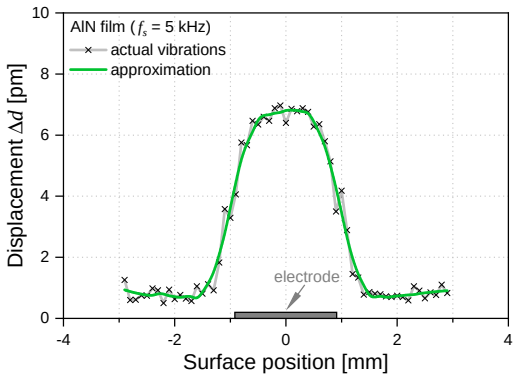


Fig. 4.9: Scanning the thickness vibrations profile of the AlN film on a Si substrate [175].

probing beam was pointing directly onto the Si substrate in this case. Despite its limited reflectivity, which led to increased noise in the intensity signal, it was still possible to recognize the vibration profile with high accuracy.

As a further advantage of the closed-loop compensation method, an invariance to an intensity detection chain gain was demonstrated. Nevertheless, it has been discussed before that with the closed-loop approach, the measured value only depends on the modulation chain gain K_{EOM}, obtained by the described gain detection procedure (Sec. 4.1.3). Fig. 4.10 compares the sample vibrations measurement with the standard open-loop and the designed closed-loop method in a wide frequency range. The measurement was performed with a thin AlN film on a Si substrate. The open-loop measurement was performed by detecting the open-loop error signal e_s, normalized by a fixed factor, corresponding to the detection chain gain K_{det}. The results demonstrate that the open-loop measurement is limited by the detector bandwidth, which is $f_{BW} = 260$ kHz with the used detection gain, resulting in a signal fading beyond this frequency. The bandwidth constraints posed by $K_{det}(\omega)$, which, from certain ω_{BW}, is no longer uniform, are especially limiting if the total sample reflectivity is low, and a high detection gain has to be used. In contrast, the $K_{EOM}(\omega)$ is not related to the reflectivity, and the closed-loop method is thus immune to the $K_{det}(\omega)$ fading. Therefore, the limitation of the closed-loop method only consists in an increased signal-to-noise ratio within the e_s signal, as the $K_{det}(\omega)$ decreases with ω. Note also that the total closed-loop measurement background noise level was measured when zero voltage was applied to the sample (see Fig. 4.10). In accordance with the expectations, the background noise is higher at lower frequencies, as its level corresponds to the ambient acoustic noise and mechanical vibrations.

It is worth remarking that the parasitic ambient noise propagates to the open-loop error signal components $e_{s\langle i\rangle}$, $e_{s\langle q\rangle}$ not only through the phase shift $\Delta\phi_s(t)$

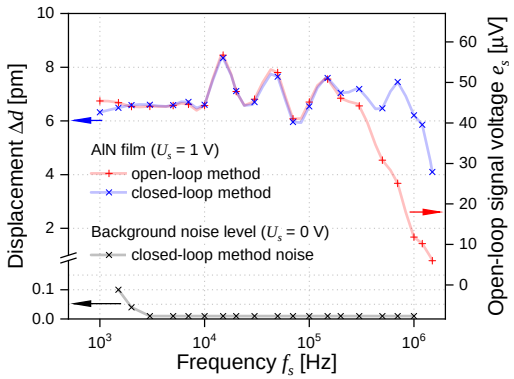


Fig. 4.10: The frequency response (thin AlN film) measured with the open-loop and the closed-loop method and the closed-loop method noise level [175].

and the intensity, but also via the $\Delta\phi_q$ drift, as discussed in Sec. 4.3.1. Thanks to the closed-loop measurement, a significant portion of the noise is suppressed within the $\Delta\Phi_c$. The degree of its suppression is determined by the PI controllers nulling the inphase and the quadrature phase shift components. Nevertheless, as a consequence of the background noise, there is always a nonzero signal level of $e_{s\langle i\rangle}$, $e_{s\langle q\rangle}$ components in a real case, even if the sample vibrations are perfectly compensated by the $\Delta\phi_c(t)$ modulation.

Although the DBMZI system is primarily purposed for high-frequency measurements, and thus focusing especially on the samples for the MEMS application, it is capable to cover also the low-frequency region, as demonstrated by the bulk PZT sample (disc, NCE51) frequency response measurement displayed in Fig. 4.11. The maximum measurement range (20-fold $u_c(t)$ gain) was used, enabling $\omega_s < \omega_m$ setting. The results reflect the sample sub-resonant behavior, exhibiting a uniform $\Delta d(f)$ dependency.

A further subject of testing involved verifying the method's linearity, resolution, and dynamic range. The closed-loop vibrations compensation has been implemented to cover the range from several femtometers up to several nanometers to satisfy the requirements of both thin films, having lower piezoelectric coefficients, and also of the bulk samples, producing much greater displacement. Note also that a damage voltage threshold of the thin samples is typically much lower, so the displacement can not be simply magnified by increasing the driving voltage. Two thin film samples and one bulk PZT sample were tested over a nearly full voltage range. All samples were measured at their central position and at the driving voltage frequency $f_s = 2$ kHz. The frequency was chosen to avoid a coincidence with any resonant frequencies of neither of the samples and, simultaneously, to provide a satisfactory low noise level, according to its measurement in Fig. 4.10. The results in Fig. 4.12(a) then denote

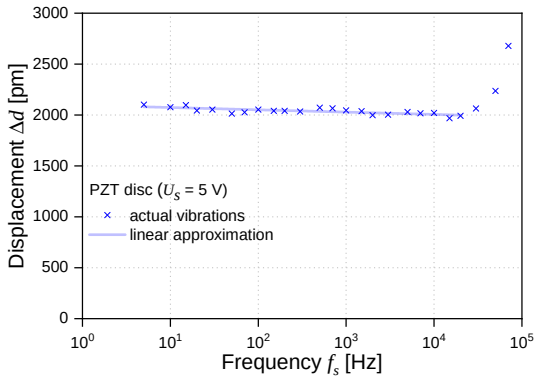


Fig. 4.11: The frequency response (bulk PZT disc) measured with the closed-loop method within a low-frequency region [175].

a high reliability for the covered range of measured displacements. Moreover, the smallest detectable displacement, regarded as the DBMZI system resolution, was observed to be only several tens of femtometers, which is by about one order better value compared to the other scanning DBMZIs reported in the literature to date. The measurement linearity error is then displayed in Fig. 4.12(b,c). The absolute error is not exceeding 0.1 pm for the finest ranges (below several picometers), indicating the measurement is highly reliable even with very small displacement. With the PZT cylinder sample, additionally, high linearity across a broad range (0.5 to 2453 pm) was demonstrated, with $\delta_{lin}(\Delta d) = 0.76$ %, even when multiple measurement ranges set by the gain switch (according to Sec. 4.2.2) were covered.

Finally, as already discussed, the detected displacement of the closed-loop DBMZI is only proportional to the modulation chain gain K_{EOM}. Hence, a compatibility test was performed, comparing the values measured with the DBMZI to the other methods to verify the validity of the measurement. Three types of samples

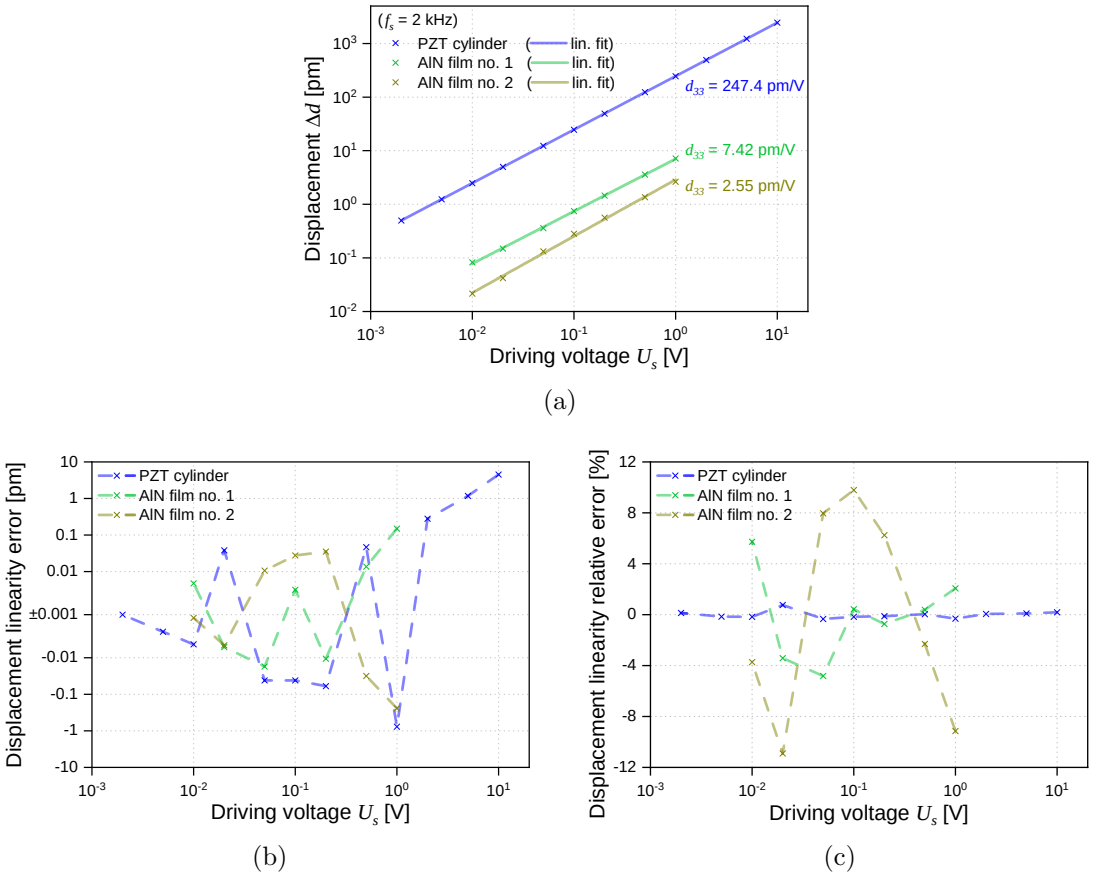
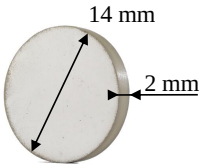
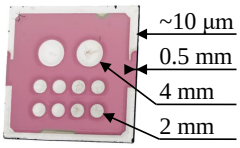


Fig. 4.12: Measured displacement with the driving voltage of the thin films and the PZT samples (a) [175] and the corresponding linearity error in absolute (b) and relative scales (c).

were used, comprising a PZT cylinder and disc, representing both hard as well as soft ceramic materials, and a thin AlN film. As the first comparative method, the samples were measured with the quasistatic method, based on the direct piezoelectric effect. The method is based on measuring the induced charge when the samples are exposed to a static force [33]. The second comparison was made with a frequency method, also referred to as the resonance method. Due to its principal restriction regarding sample dimensions [176], the method is applicable solely to the cylinder sample out of the tested samples. The resulting values of the piezoelectric coefficient acquired with individual methods are listed in Tab. 4.1. It can be seen that the results of both the quasistatic as well as the resonance method (in the case of the PZT cylinder) are in close agreement with the values measured with the DBMZI, proving a high fidelity of both the modulation gain setting and the detection itself.

Tab. 4.1: Comparison of results measured with DBMZI to the reference results measured with the direct (quasistatic) and the frequency (resonance) method.

cylinder	disc	thin film
PZT (NCE41)	PZT (NCE51)	AlN on Si substrate
		
d_{33} [pm · V^{-1}] – Measured (DBMZI)		
247.4	411	6.5
d_{33} [pC · N^{-1}] – Reference (quasistatic method)		
243 (± 1–2 %)	413 (± 1–2 %)	6.4 (± 1–2 %)
d_{33} [pC · N^{-1}] – Reference (resonance method)		
250 (± 1–2 %)	—	—

5 Conclusions and future perspectives

This thesis deals with modulation and closed-loop phase shift compensation methods in the homodyne interferometric sensors. It was demonstrated that the closed-loop processing brings notable benefits to the interferometric measurement, namely overcoming the inherent nonlinearity and ambiguity of the interference response, and suppressing the susceptibility to the detected power and its fluctuations. This work studies new approaches to the closed-loop processing and demonstrates its application in two diverse areas of mechanical quantities measurement, embodied by the IFOG and the DBMZI.

The methods for the IFOG were designed to target an all-fiber architecture with a PEM, typically used for cost-efficient applications of angular velocity measurement. As these types of IFOGs typically operate as open-loop, a novel method was developed for the Sagnac phase shift compensation, based on digital signal processing. A similar situation was with the DBMZI, where a completely new approach utilizing an EOM was presented, facilitating sample-induced phase shift compensation. Unlike with inherently reciprocal IFOG, the DBMZI method further requires a quadrature point stabilization, which the proposed techniques also solved. In both use cases of the proposed methods, the closed-loop compensation is performed through a sinusoidal modulation signal, the amplitude of which is proportional to the measured quantity. In the IFOG, the measured signal corresponds to the DC-like angular velocity, and the compensation is thus achieved only in the digital signal through synchronous sampling. In contrast, the stationary sample vibrations are compensated continually in the DBMZI. Furthermore, both applications of the proposed methods involve an additional harmonic modulation, facilitating the phase detection in a quadrature point. Nevertheless, a different structure and requirements on both interferometers give a slightly different function to this modulation. While it introduces only a phase bias in the Sagnac structure, in the Mach-Zehnder structure, this modulation represents a sweep for detecting the optimal operation point, which is actively controlled.

A general requirement of the closed-loop measurement method is an accurate knowledge of the control gain, giving the proportion between the direct output signal and the measured physical quantity. Therefore, as the second result of the thesis, the methods for the gain identification and its drift compensation were developed. For the IFOG, two approaches to the compensation modulation depth control were presented and analyzed, both employing an actual modulation depth estimation based on the ideal model of the interference signal composition. The approaches were compared theoretically and through simulations, revealing their capabilities not only for the precise gain control, but also to mitigate the residual errors caused by

the parasitic effects related to PEM inherent properties. Moreover, an optimization of the closed-loop compensation method was proposed in the form of a quadruple-sine modulation scheme. As the closed-loop processing method in IFOG is subject to the proper synchronization of the modulation generation and the output signal acquisition, the techniques of the modulation signal parameters stabilization were also developed. In the case of DBMZI, the lack of optical reciprocity condition does not limit the modulation methods to a single frequency, and it thus provides the possibility of large bandwidth measurement. On the other hand, the modulation gain cannot be controlled during the measurement; therefore, a calibration detection technique is proposed instead.

The proposed methods were then implemented and verified through practical testing. In the case of the IFOG, multiple test setups and their evolutions were developed. The major advantages of the closed-loop processing technique stemming from the results comprise output linearization, temperature dependency improvement, and enhancement of the scale-factor stability. Further improvement of the scale-factor stability, especially during varying operation conditions, was achieved through the modulation depth control implementing the LSCFE method based on a virtual sensor approach. In the case of the DBMZI, the major benefits brought by the closed-loop methods entail the insensitivity to the sample reflectivity as well as the source and the detection gain, facilitating scanning of the sample vibrations profile along its entire surface. Further, an extension of the frequency range and also the superior linearity were observed with the implementation of the proposed method. Moreover, the quadrature point stabilization by the second closed loop enabled a notable noise decrease in the sample vibrations signal. The active stabilization also loosened the stringent requirements concerning the environmental sensitivity and facilitated the system operation even in standard laboratory conditions.

As a further result of the thesis, progress has also been made in the optical structure design and optimization of both test setups. In the IFOG setup, a novel and efficient SFS source temperature stability technique has been developed. In the DBMZI, employing the EOM simplified the optical architecture compared to the previous solutions.

Based on the summary of the major achievements, the set aims and objectives have been met. Before concluding, it is also worth to mention the added value of the work, consisting in exploring unconventional modulation applications and principles. So far, there has not been proposed a commercial solution to the closed-loop IFOG operating with PEM. Similarly, the DBMZI implementing the EOM has not been published by other studies and, to the author's knowledge, it is proposed with the closed-loop compensation for the first time. In both cases, these combinations brought novel benefits when utilizing the proposed methods. The all-fiber IFOG

with PEM allows for the ultimate simplicity and cost-efficiency among the SOTA solutions, which are difficult to attain with EOM-based architectures. This work then shows that by employing suitable methods, many of the commonly cited drawbacks can be sufficiently addressed, facilitating the all-fiber IFOG attacking the performance of much more expensive devices. In the case of DBMZI, high-bandwidth EOM for a phase compensation showed a potential in a notable parameters enhancement, in line with the discussed advantages of the proposed methods.

Although the methods of closed-loop phase compensation and parasitic effects mitigation outlined herein targeted two specific applications, their diversity provides an opportunity to depict the versatility of the proposed approach. This is demonstrated by the fact that both fiber-optic as well as free-space interferometers, both reciprocal Sagnac and nonreciprocal Mach-Zehnder structures, both PEM versus EOM-based modulation principles, and both stationary and dynamic sensing can all take advantage of the closed-loop processing. We must consider not only its potential in the presented applications, which by themselves are surely worth of further exploration and optimization, but also contemplate their viability beyond them, encompassing a wide array of applications and physical quantities measurable by light interferometry. The closed-loop can, for instance, be particularly beneficial in the Fabry-Pérot interferometers as well, as they exhibit an extreme sensitivity, but suffer from a very small linearity region. One of the subjects of further research is thus a system for high-sensitivity vibration measurement utilizing a fiber-optic Fabry-Pérot sensor with closed-loop processing. Future research could also aim at areas where the interferometric principle plays a key role, such as optical accelerometers, hydrophones, seismometers, or microphones, and where the phase modulation methods with the closed-loop processing can pose a viable enhancement of the sensing capabilities.

Bibliography

[1] DE GROOT, Peter J. A review of selected topics in interferometric optical metrology. *Reports on Progress in Physics*. 2019, **82**(5), 56101. ISSN 0034-4885. DOI:10.1088/1361-6633/ab092d

[2] SABRI, Naseer, et al. Toward Optical Sensors: Review and Applications. *Journal of Physics: Conference Series*. 2013, **423**, 012064. ISSN 1742-6588. DOI:10.1088/1742-6596/423/1/012064

[3] KROHN, D. A. *Fiber optic sensors: fundamentals and applications*. Fourth edition. Washington, US: SPIE Press, 2014, 332 p. ISBN 978-1-6284-1180-5.

[4] LEE, Byeong Ha, et al. Interferometric Fiber Optic Sensors. *Sensors*. 2012, **12**(3), p. 2467–2486. ISSN 1424-8220. DOI:10.3390/s120302467

[5] YU, Francis T. S. and Shizhuo YIN. *Fiber optic sensors*. New York, US: Marcel Dekker, 2002. Optical engineering, 495 p. ISBN 082470732X.

[6] KIRKENDALL, Clay K and Anthony DANDRIDGE. Overview of high performance fibre-optic sensing. *Journal of Physics D: Applied Physics*. 2004, **37**(18), R197–R216. ISSN 0022-3727. DOI:10.1088/0022-3727/37/18/R01

[7] SONG, Ningfang, et al. Advanced Interferometric Fiber Optic Gyroscope for Inertial Sensing: A Review. *Journal of Lightwave Technology*. 2023, **41**(13), p. 4023–4034. ISSN 0733-8724. DOI:10.1109/JLT.2023.3260839

[8] BOHNERT, K., A. G. MIGNANI and H. C. LEFÈVRE. Temperature and vibration insensitive fiber-optic current sensor. *Journal of Lightwave Technology*. IEEE, 2002, **20**(2), p. 267–276. ISBN 9780819438485. DOI:10.1117/12.2302320

[9] LEE, Byoungho. Review of the present status of optical fiber sensors. *Optical Fiber Technology*. 2003, **9**(2), p. 57–79. ISSN 10685200. DOI:10.1016/S1068-5200(02)00527-8

[10] RESEARCH AND MARKETS. *Optical Sensors: Global Strategic Business Report*. GLOBAL INDUSTRY ANALYSTS, INC. 2024. Available at: https://www.researchandmarkets.com/report/optical-sensors#product–related-products

[11] EXPERT MARKET RESEARCH. *Global Optical Sensor Market Outlook*. 2023. Available at: https://www.expertmarketresearch.com/reports/optical-sensor-market

[12] FIDANBOYLU, K. and H. S. EFENDIOĞLU. Fiber optic sensors and their applications. In: *5 th International Advanced Technologies Symposium (IATS-09)*. Karabuk, Turkey, 2009, p. 1–6. ISBN 978-605-60681-0-2.

[13] BAHRAMPOUR, A. R., S. TOFIGHI, M. BATHAEE and F. FARMAN. Optical Fiber Interferometers and Their Applications. In: PADRONON, I., ed. *Interferometry: Research and Applications in Science and Technology*. InTech, 2012. ISBN 978-953-51-0403-2.

[14] CULSHAW, Brian and Alan KERSEY. Fiber-Optic Sensing: A Historical Perspective. *Journal of Lightwave Technology*. 2008, **26**(9), p. 1064–1078. ISSN 0733-8724. DOI:10.1109/JLT.0082.921915

[15] SHARMA, K. K. *Optics: principles and applications*. Elsevier, 2006, 639 p. ISBN 978-0-12-370611-9.

[16] LÓPEZ-HIGUERA, José Miguel. *Handbook of optical fibre sensing technology*. New York, US: Wiley, 2002, 810 p. ISBN 0471820539.

[17] UDD, Eric. and William B. SPILLMAN. *Fiber optic sensors: an introduction for engineers and scientists*. 2nd ed. Hoboken, N.J., US: John Wiley, 2011. ISBN 978-0-470-12684-4.

[18] LEFÈVRE, H. C. *The Fiber-Optic Gyroscope*. 2nd ed. London, GB: Artech House, 2014, 416 p. ISBN 1608076962.

[19] CIMINELLI, Caterina, Francesco DELL'OLIO, Carlo E. CAMPANELLA and Mario N. ARMENISE. Photonic technologies for angular velocity sensing. *Advances in Optics and Photonics*. 2010, **2**(3), p. 370–404. ISSN 1943-8206. DOI:10.1364/AOP.2.000370

[20] DEPPE, Olaf, et al. MEMS and FOG Technologies for Tactical and Navigation Grade Inertial Sensors-Recent Improvements and Comparison. *Sensors*. 2017, **17**(3), 567. ISSN 1424-8220. DOI:10.3390/s17030567

[21] YANG, Shuming and Guofeng ZHANG. A review of interferometry for geometric measurement. *Measurement Science and Technology*. 2018, **29**(10), 102001. ISSN 0957-0233. DOI:10.1088/1361-6501/aad732

[22] TROLIER-MCKINSTRY, S. and P. MURALT. Thin Film Piezoelectrics for MEMS. *Journal of Electroceramics*. 2004, **12**(1-2), p. 7–17. ISSN 1385-3449. DOI:10.1023/B:JECR.0000033998.72845.51

[23] HUANG, Z., et al. Comparative measurements of piezoelectric coefficient of PZT films by Berlincourt, interferometer, and vibrometer methods. *IEEE Transactions on Ultrasonics, Ferroelectrics and Frequency Control*. 2006, **53**(12), p. 2287–2293. ISSN 08853010. DOI:10.1109/TUFFC.2006.175

[24] SALEH, Bahaa E. A. and Malvin Carl TEICH. *Fundamentals of Photonics*. 2nd ed. New Jersey, US: Wiley, 2007, 966 p. ISBN 978-0-471-35831-9.

[25] DOWNS, M.J. a K.W. RAINE. An unmodulated bi-directional fringe-counting interferometer system for measuring displacement. *Precision Engineering* [online]. 1979, **1**(2), p. 85–88 [cit. 2024-03-28]. ISSN 01416359. DOI:10.1016/0141-6359(79)90138-7

[26] IIZUKA, Keigo. *Engineering optics*. 3rd ed. New York, US: Springer, 2008, 525 p. Optical Sciences. ISBN 978-0-387-75723-0.

[27] DECUSATIS, Casimer M. and Carolyn J. Sher DECUSATIS. *Fiber Optic Essentials*. Elsevier Academic Press, 2006, 271 p. ISBN 0-12-208431-4.

[28] STRAND, O. T., et al. Compact system for high-speed velocimetry using heterodyne techniques. *Review of Scientific Instruments*. 2006, **77**(8), 083108-2-8. ISSN 0034-6748. DOI:10.1063/1.2336749

[29] LAWRENCE, Anthony, LING, Frederick F., ed. *Modern Inertial Technology: Navigation, Guidance, and Control*. Mechanical Engineering Series. 2nd ed. New York, US: SpringerVerlag, 1998, 278 p. ISBN 0-387-98507-7.

[30] JACKSON, D. A., R. PRIEST, A. DANDRIDGE and A. B. TVETEN. Elimination of drift in a single-mode optical fiber interferometer using a piezoelectrically stretched coiled fiber. *Applied Optics*. 1980, **19**(17), p. 2926–2929. ISSN 0003-6935. DOI:10.1364/AO.19.002926

[31] FIALKA, Jiří a Petr BENEŠ. Comparison of Methods for the Measurement of Piezoelectric Coefficients. *IEEE Transactions on Instrumentation and Measurement*. 2013, **62**(5), p. 1047–1057. ISSN 0018-9456. DOI:10.1109/TIM.2012.2234576

[32] MEI, Haiping, Baosheng LI, Honglian HUANG and Ruizhong RAO. Piezoelectric optical fiber stretcher for application in an atmospheric optical turbulence sensor. *Applied Optics*. 2007, **46**(20), p. 4371–4375. ISSN 0003-6935. DOI:10.1364/AO.46.004371

[33] FIALKA, Jiří, et al. Measurement of thermal depolarization effects in piezoelectric coefficients of soft PZT ceramics via the frequency and direct methods. *Journal of the European Ceramic Society*. 2016, **36**(11), p. 2727–2738. ISSN 0955-2219. DOI:10.1016/j.jeurceramsoc.2016.03.036

[34] SABAT, Ribal Georges, Binu K. MUKHERJEE, Wei REN and Guomao YANG. Temperature dependence of the complete material coefficients matrix of soft and hard doped piezoelectric lead zirconate titanate ceramics. *Journal of Applied Physics*. 2007, **101**(6), p. 064111-1–7. ISSN 0021-8979. DOI:10.1063/1.2560441

[35] MALYKIN, G. B. and É. G. MALYKIN. On possibility of using the lowest odd harmonics of the phase modulation frequency in the output signal of the fiber-optic ring interferometer for detection of the sagnac effect. *Optics and Spectroscopy*. 2008, **105**(1), p. 3117–123. ISBN 10.1134/S0030400X08070187. DOI:10.1134/S0030400X08070187

[36] BARROW, D. A., O. LISBÔA, C. K. JEN and M. SAYER. In-line phase modulators using coaxial thick lead zirconate titanate coated optical fibers. *Journal of Applied Physics*. 1996, **79**(6), p. 3323–3329. ISSN 0021-8979. DOI:10.1063/1.362661

[37] KHOLKIN, A. L., Ch. WÜTCHRICH, D. V. TAYLOR and N. SETTER. Interferometric measurements of electric field-induced displacements in piezoelectric thin films. *Review of Scientific Instruments*. 1996, **67**(5), p. 1935–1941. ISSN 0034-6748. DOI:10.1063/1.1147000

[38] LEE, Bong Yeon and Takashi IIJIMA. High-frequency piezoelectric displacement of PZT films measured using twin-beam laser doppler vibrometer. *Journal of the Ceramic Society of Japan*. 2010, **118**(1381), p. 842–846. ISSN 1882-0743. DOI:10.2109/jcersj2.118.842

[39] PRENTISS, M. G., J. L. DAVIS. and S. EZEKIEL. Closed Loop, High Sensitivity Fiberoptic Gyroscope. In: EZEKIEL, S. and H. J. ARDITTY, ed. *Fiber-Optic Rotation Sensors and Related Technologies: Proceedings of the First International Conference MIT*. Cambridge, US: Springer-Verlag, 1982, p. 297–301. ISBN 978-3-662-13527-3. DOI:10.1007/978-3-540-39490-7

[40] PENTANGELO, Ciro, et al. Analytical modeling of the static and dynamic response of thermally actuated optical waveguide circuits. *Physical Review Research*. 2021, **3**(2), 023094. ISSN 2643-1564. DOI:10.1103/PhysRevResearch.3.023094

[41] PASSARO, Vittorio M. N., et al. Gyroscope Technology and Applications: A Review in the Industrial Perspective. *Sensors*. 2017, **17**(10), p. 2284-1–22. ISSN 1424-8220. DOI:10.3390/s17102284

[42] MERLO, S., M. NORGIA and S. DONATI. Fiber gyroscope principles. In: LÓPEZ-HIGUERA, J. M., ed. *Handbook of optical fibre sensing technology*. New York, US: Wiley, 2002, p. 331–348. ISBN 978-0-471-82053-6.

[43] DELL'OLIO, F., T. TATOLI, C. CIMINELLI and M. N. ARMENISE. Recent advances in miniaturized optical gyroscopes. *Journal of the European Optical Society: Rapid Publications*. 2014, **9**, 14013. ISSN 1990-2573. DOI:10.2971/jeos.2014.14013

[44] MACEK, W. M. and D. T. M. DAVIS. Rotation rate sensing with traveling-wave ring lasers. *Applied Physics Letters*. 1963, **2**(3), p. 67–68. ISSN 0003-6951. DOI:10.1063/1.1753778

[45] ARONOWITZ, F. Fundamentals of the Ring Laser Gyro. In: LOUKIANOV, D., et al., ed. *Optical Gyros and their Application*. NATO, Research and Technology Organization, 1999, p. 3-1–45. ISBN 92-837-1014-2.

[46] PATUREL, Y., J. HONTHAAS, H. LEFÈVRE and F. NAPOLITANO. One nautical mile per month fog-based strapdown inertial navigation system: A dream already within reach? *Gyroscopy and Navigation*. 2014, **5**(1), p. 1–8. ISSN 2075-1087. DOI:10.1134/S207510871401009X

[47] LEFÈVRE, H. C. The fiber-optic gyroscope: Achievement and perspective. *Gyroscopy and Navigation*. 2012, **3**(4), p. 223–226. ISSN 2075-1087. DOI:10.1134/S2075108712040062

[48] LEFÈVRE, Hervé C. The fiber-optic gyroscope: Challenges to become the ultimate rotation-sensing technology. *Optical Fiber Technology*. 2013, **19**(6), p. 828–832. ISSN 10685200. DOI:10.1016/j.yofte.2013.08.007

[49] VALI, V. and R. W. SHORTHILL. Fiber ring interferometer. *Applied Optics*. 1976, **15**(5), p. 1099–1100. ISSN 0003-6935. DOI:10.1364/AO.15.001099

[50] KORKISHKO, Yu. N., et al. Highest bias stability fiber-optic gyroscope SRS-5000. In: *2017 DGON Inertial Sensors and Systems (ISS)*. IEEE, 2017, p. 1–23. ISBN 978-1-5386-3962-7. DOI:10.1109/InertialSensors.2017.8171490

[51] ULRICH, R. Fiber-optic rotation sensing with low drift. *Optics Letters*. 1980, **5**(5), p. 173–175. ISSN 0146-9592. DOI:10.1364/OL.5.000173

[52] PAVLATH, George A. Fiber optic gyros from research to production. In: UDD, E., et al., ed. *Proceedings of SPIE, Fiber Optic Sensors and Applications XIII*. SPIE, 2016, p. 985205-1–7. ISBN 978-151060093-5. DOI:10.1117/12.2228562

[53] SANDERS, Glen A., et al. Fiber optic gyro development at Honeywell. In: UDD, E., et al., ed. *Proceedings of SPIE, Fiber Optic Sensors and Applications XIII*. SPIE, 2016, p. 985207-1–14. ISBN 978-151060093-5. DOI:10.1117/12.2228893

[54] YOLE DEVELOPPEMENT. *Gyroscopes and IMUs for Defense, Aerospace & Industrial*. Market Report. 2012, 18 p.

[55] VENEDIKTOV, V Yu, Yu V FILATOV and E V SHALYMOV. Passive ring resonator micro-optical gyroscopes. *Quantum Electronics*. 2016, **46**(5), p. 437–446. ISSN 1063-7818. DOI:10.1070/QEL15932

[56] FENG, Zuo, et al. Progress of Waveguide Ring Resonators Used in Micro-Optical Gyroscopes. *Photonics*. 2020, **7**(4), p. 96. ISSN 2304-6732. DOI:10.3390/photonics7040096

[57] WU, Beibei, Yu YU and Xinliang ZHANG. Mode-assisted Silicon Integrated Interferometric Optical Gyroscope. *Scientific Reports*. 2019, **9**(1), 12946. ISSN 2045-2322. DOI:10.1038/s41598-019-49380-x

[58] POST, E. J. Sagnac Effect. *Reviews of Modern Physics*. 1967, **39**(2), p. 475–493. ISSN 0034-6861. DOI:10.1103/RevModPhys.39.475

[59] ARDITTY, H. J. and H. C. LEFÈVRE. Sagnac effect in fiber gyroscopes. *Optics Letters*. 1981, **6**(8), p. 401–403. ISSN 0146-9592. DOI:10.1364/OL.6.000401

[60] MARTIN, J. M., J. T. WINKLER and Elsa M. GARMIRE. Fiber Optic Laser Gyro Signal Detection And Processing Technique. In: *Proceedings Volume 0139, Guided Wave Optical Systems and Devices I*. SPIE, 1978, p. 98–103. ISSN 0277786X. DOI:10.1117/12.956249

[61] ANDRONOVA, Irina A and Grigorii B MALYKIN. Physical problems of fiber gyroscopy based on the Sagnac effect. *Physics-Uspekhi*. 2002, **45**(8), p. 793–817. ISBN 10.1070/PU2002v045n08ABEH001073. DOI:10.1070/PU2002v045n08ABEH001073

[62] BERGH, R. A., H. C. LEFEVRE and H. J. SHAW. All-single-mode fiber-optic gyroscope with long-term stability. *Optics Letters*. 1981, **6**(10), p. 502–504. ISSN 0013-5194. DOI:10.1364/OL.6.000502

[63] ZHANG, Yanshun, et al. A New Open-Loop Fiber Optic Gyro Error Compensation Method Based on Angular Velocity Error Modeling. *Sensors*. 2015, **15**(3), p. 4899–4912. ISSN 1424-8220. DOI:10.3390/s150304899

[64] ÇELIKEL, Oğuz. Construction and characterization of interferometric fiber optic gyroscope (IFOG) with erbium doped fiber amplifier (EDFA). *Optical and Quantum Electronics*. 2007, **39**(2), p. 147–156. ISSN 0306-8919. DOI:10.1007/s11082-007-9070-z

[65] LI, Hua, et al. A novel realization of signal processing to improve the precision of the open-loop IFOG. In: *Proceedings Volume 5634, Advanced Sensor Systems and Applications II*. Beijing, China: SPIE, 2005, p. 323–329. ISSN 0277786X. DOI:10.1117/12.576001

[66] ZHOU, Kejiang, et al. An analog modulation and demodulation method employing LVDT signal conditioner for fiber-optic interferometric sensors. *Measurement Science and Technology*. 2017, **28**(9), 095102. ISSN 0957-0233. DOI:10.1088/1361-6501/aa7e56

[67] RODRIGUEZ, R.B.G. and E.C. FERREIRA. Zero-crossing demodulation for open loop fiber optic gyroscopes. In: *Proceedings of the 2001 SBMO/IEEE MTT-S International Microwave and Optoelectronics Conference. (Cat. No.01TH8568)*. IEEE, 2001, p. 149–152. ISBN 0-7803-7065-1. DOI:10.1109/SBMOMO.2001.1008739

[68] MEDJADBA, H. and L.M. SI MOHAMED. Low cost technique for improving open loop fiber optic gyroscope scale factor linearity. In: *Proc. of the 10th WSEAS International Conference on SYSTEMS*. Damascus, Syria: IEEE, 2006, p. 499–502. ISBN 10.1109/ICTTA.2006.1684718. DOI:10.1109/ICTTA.2006.1684718

[69] CHEN, Lin, et al. Digital Control and Demodulation Algorithm for Compact Open-Loop Fiber-Optic Gyroscope. *Sensors*. 2023, **23**(3), 1473. ISSN 1424-8220. DOI:10.3390/s23031473

[70] LU, Chengjie and Kejiang ZHOU. A low cost all-digital demodulation method for fiber-optic interferometric sensors. *Measurement Science and Technology*. 2018, **29**(10), 105103. ISSN 0957-0233.DOI:10.1088/1361-6501/aad9e4

[71] FERREIRA, E. C., F. F. DE MELO and J. A. Siqueira DIAS. Precision analog demodulation technique for open-loop Sagnac fiber optic gyroscopes. *Review of Scientific Instruments*. 2007, **78**(2), 024704. ISSN 0034-6748. DOI:10.1063/1.2536433

[72] BENNETT, Sidney M. and Richard B. DYOTT. *DSP signal processing for open loop fiber optic sensors*. U.S. Patent No 6,429,939, 2002.

[73] AHMAD, Irfan a A.I. BHATTI. A novel technique for spectral processing of a fiber optic gyroscope. *Kuwait Journal of Science and Engineering*. 2010, **37**(1), p. 49–68. ISSN 10248684.

[74] WANG, Xinyue, Changhong HE and Ziyu WANG. Method for suppressing the bias drift of interferometric all-fiber optic gyroscopes. *Optics Letters*. 2011, **36**(7), p. 1191–1193. ISSN 0146-9592. DOI:10.1364/OL.36.001191

[75] BACURAU, Rodrigo M., et al. Technique for suppressing the electronic offset drift of interferometric open-loop fiber optic gyroscopes. *Optics Letters*. 2016, **41**(22), p. 5186–5189. ISSN 0146-9592. DOI:10.1364/OL.41.005186

[76] BÖHM, K., P. MARTEN, E. WEIDEL and K. PETERMANN. Direct rotation-rate detection with a fibre-optic gyro by using digital data processing. *Electronics Letters*. 1983, **19**(23), p. 997–999. ISSN 00135194. DOI:10.1049/el:19830677

[77] GRONAU, Yuval and Moshe TUR. Digital signal processing for an open-loop fiber-optic gyroscope. *Applied Optics*. 1995, **34**(25), p. 5849–5853. ISBN 10.1364/AO.34.005849. DOI:10.1364/AO.34.005849

[78] WANG, Qin, Chuanchuan YANG, Xinyue WANG a Ziyu WANG. All-digital signal-processing open-loop fiber-optic gyroscope with enlarged dynamic range. *Optics Letters* 2013, **38**(24), p. 5422–5425. ISSN 0146-9592. DOI:10.1364/OL.38.005422

[79] XIE, Jun, et al. A low-complexity scheme for enlarging the dynamic range of the open-loop I-FOG. *Microwave and Optical Technology Letters*. 2016, **58**(3), p. 498–502. ISSN 0895-2477. DOI:10.1002/mop.29601

[80] ONO, Kimizo, Yozo NISHIURA and Mitsuru NISHIKAWA. Phase-modulated fiber optic gyroscope with wide dynamic range and linear scale factor. *Applied Optics*. 1991, **30**(9), p. 1070–1073. ISSN 0003-6935. DOI:10.1364/AO.30.001070

[81] KIM, B. Y. and H. J. SHAW. Phase-reading, all-fiber-optic gyroscope. *Optics Letters*. 1984, **9**(8), p. 378–380. ISSN 0146-9592. DOI:10.1364/OL.9.000378

[82] JODOR, Gabriel, et al. Digitally processed, phase-reading fibre gyroscope. *Optics & Laser Technology*. 2000, **32**(5), p. 343–346. ISSN 00303992. DOI:10.1016/S0030-3992(00)00078-5

[83] CHIEN, Pie-Yau, Ci-Ling PAN and Lih-Wuu CHANG. Triangular phase-modulation approach to an open-loop fiber-optic gyroscope. *Optics Letters*. 1991, **16**(21), p. 1701–1703. ISBN 10.1364/OL.16.001701. DOI:10.1364/OL.16.001701

[84] CHIEN, Pie-Yau and Ci-Ling PAN. Deep phase-modulation approach to an open-loop fiber optic gyroscope. *IEEE Photonics Technology Letters*. 1991, **3**(3), p. 284–286. ISSN 1041-1135. DOI:10.1109/68.79782

[85] TOYAMA, K., K. A. FESLER, B. Y. KIM and H. J. SHAW. Digital integrating fiber-optic gyroscope with electronic phase tracking. *Optics Letters*. 1991, **16**(15), p. 1207–1209. ISSN 0146-9592. DOI:10.1364/OL.16.001207

[86] YEH, Y., D.I. KIM and B.Y. KIM. New digital closed-loop processor for a fiber-optic gyroscope. *IEEE Photonics Technology Letters*. 1999, **11**(3), p. 361–363. ISSN 1041-1135. DOI:10.1109/68.748235

[87] KERSEY, Alan D., et al. Single-channel phase-tracker for the open-loop fiber optic gyroscope. In: *Proceedings Volume 1585, 15th Anniversary Conference on Fiber Optic Gyros*. Boston, US: SPIE, 1992, p. 198–202. ISSN 0277786X. DOI:10.1117/12.135048

[88] MALYKIN, G. B. Effect of nonsinusoidal phase modulation on the zero shift in a fiber ring interferometer. *Radiophysics and Quantum Electronics*. 1994, **37**(10), p. 870–872. ISSN 0033-8443. DOI:10.1007/BF01038062

[89] CAHILL, R. F. a E. UDD. Phase-nulling fiber-optic laser gyro. *Optics Letters*. 1979, **4**(3), p. 93–95. ISBN 10.1364/OL.4.000093. DOI:10.1364/OL.4.000093

[90] DAVIS, J. L. and S. EZEKIEL. Closed-loop, low-noise fiber-optic rotation sensor. *Optics Letters*. 1981, **6**(10), p. 505–507. ISSN 0146-9592. DOI:10.1364/OL.6.000505

[91] ARDITTY, Hervé J., Claude PUECH and Michel PAPUCHON. *Device for measuring a phase shift which is not reciprocal produced in a ring interferometer*. U.S. Patent No 5,056,919, 1991.

[92] YAN, Jingtao, et al. Research on the feedback control characteristics and parameter optimization of closed-loop fiber optic gyroscope. *Optik*. 2021, **229**, 166298. ISSN 00304026. DOI:10.1016/j.ijleo.2021.166298

[93] CELIKEL, Oguz and S. Eren SAN. Establishment of All Digital Closed-Loop Interferometric Fiber-Optic Gyroscope and Scale Factor Comparison for Open-Loop and All Digital Closed-Loop Configurations. *IEEE Sensors Journal*. 2009, **9**(2), p. 176–186. ISBN 10.1109/JSEN.2008.2011066. DOI:10.1109/JSEN.2008.2011066

[94] EBBERG, A. and G. SCHIFFNER. Closed-loop fiber-optic gyroscope with a sawtooth phase-modulated feedback. *Optics Letters*. 1985, **10**(6), p. 300–302. ISSN 0146-9592. DOI:10.1364/OL.10.000300

[95] GRAINDORGE, Philippe, Hervé ARDITTY and Hervé LEFEVRE. *Device for measuring a nonreciprocal phase shift produced in a closed-loop interferometer*. U.S. Patent No 4,705,399, 1987.

[96] PERLMUTTER, M.S. A tactical fiber optic gyro with all-digital signal processing. In: *IEEE Position, Location and Navigation Symposium (PLANS'94)*. Las Vegas, US: IEEE, 1994, p. 170-175. ISBN 0-7803-1435-2. DOI:10.1109/PLANS.1994.303311

[97] PAN, Xiong, et al. Novel Compensation Scheme for the Modulation Gain to Suppress the Quantization-Induced Bias in a Fiber Optic Gyroscope. *Sensors*. 2017, **17**(4), 823. ISSN 1424-8220. DOI:10.3390/s17040823

[98] LEFEVRE, Hervé and Philippe MARTIN. *Optical-fiber measuring device, gyrometer, central navigation and stabilizing system*. U.S. Patent No 5,141,316, 1992.

[99] LEFEVRE, Herve C., et al. Latest advances in fiber optic gyroscope technology at Photonetics. In: *Proceedings Volume 2292, Fiber Optic and Laser Sensors XII*. San Diego, US: SPIE, 1994, p. 156–165. DOI:10.1117/12.191830

[100] JIN, Jing, et al. A Reliable and Efficient Method for Temperature Sensing in Interferometric Fiber-Optic Gyro. *IEEE Sensors Journal*. 2016, **16**(11), p. 4192–4197. ISSN 1530-437X. DOI:10.1109/JSEN.2016.2542280

[101] XUYOU LI, Zhang YONG and Yu QIANG. Four-state modulation in fiber optic gyro. In: *IEEE International Conference on Mechatronics and Automation*. IEEE, 2008, p. 189–192. ISBN 978-1-4244-2631-7. DOI:10.1109/ICMA.2008.4798749

[102] BACURAU, Rodrigo M., et al. Two-level and two-period modulation for closed-loop interferometric fiber optic gyroscopes. *Optics Letters*. 2018, **43**(11), p. 2652–2655. ISSN 0146-9592. DOI:10.1364/OL.43.002652

[103] CHONG, Kyoung-Ho, Woo-Seok CHOI and Kil-To CHONG. Analysis of dead zone sources in a closed-loop fiber optic gyroscope. *Applied Optics*. 2016, **55**(1), p. 165–170. ISSN 0003-6935. DOI:10.1364/AO.55.000165

[104] LO, Pei-hwa and Robert A. KOVACS. *Fiber optic gyroscope with reduced nonlinearity at low angular rates*. U.S. Patent No 5,684,591, 1997.

[105] ZHENG, Yue, et al. Suppression of the quantization error in a fiber optic gyroscope using a double-electrode-pair multifunction integrated-optic circuit. *Optics Express*. 2019, **27**(19), p. 27028–27038. ISSN 1094-4087. DOI:10.1364/OE.27.027028

[106] KIM, B. Y., H. C. LEFEVRE, R. A. BERGH and H. J. SHAW. Response Of Fiber Gyros To Signals Introduced At The Second Harmonic Of The Bias Modulation Frequency. In: *Proceedings SPIE 0425, Single Mode Optical Fibers*. San Diego, US, 1983, p. 86–89. ISBN 10.1117/12.936218. DOI:10.1117/12.936218

[107] KIM, B.Y. and H.J. SHAW. Gated phase-modulation feedback approach to fiber-optic gyroscopes. *Optics Letters*. 1984, **9**(6), p. 263–265. ISSN 0146-9592. DOI:10.1364/OL.9.000263

[108] KIM, B. Y. and H. J. SHAW. Gated phase-modulation approach to fiber-optic gyroscope with linearized scale factor. *Optics Letters*. 1984, **9**(8), p. 375–377. ISBN 10.1364/OL.9.000375. DOI:10.1364/OL.9.000375

[109] OH, Moonsu, Yongduk KIM and Manho CHUNG. Effects of the second harmonic and the duty cycle on the scale factor of a fiber-optic gyroscope with gated two-harmonic phase modulation. *Optics Letters*. 1988, **13**(5), p. 410–412. ISBN 10.1364/OL.13.000410. DOI:10.1364/OL.13.000410

[110] ECKE, W., S. SCHROETER, G. SCHWOTZER and R. WILLSCH. All-fiber closed-loop gyroscope with zero rate and scale factor self-calibration. In: *Proceedings Volume 1585, 15th Anniversary Conference on Fiber Optic Gyros*. Boston, US: SPIE, 1992, p. 203–214. ISSN 0277786X. DOI:10.1117/12.135072

[111] MENÉNDEZ, Ramón J. P. Optical Phase-Modulation Techniques. In: DEKOULIS, G., ed. *Modulation in Electronics and Telecommunications*. IntechOpen, 2019, DOI:10.5772/intechopen.90343

[112] FRIGO, Nicholas J., Emery L. MOORE and O. G. RAMER. Compensation Of Linear Sources Of Non-Reciprocity In Sagnac Interferometers. In: *Proceedings Volume 0412, Fiber Optic and Laser Sensors I*. SPIE, 1983, p. 268–271. ISSN 0361-0748. DOI:10.1117/12.935827

[113] HANDRICH, Eberhard and Manfred KEMMLER. *Closed loop fiber optic gyro with shupe effect compensation*. U.S. Patent No 6,181,428, 2001.

[114] CHEN, Xiyuan and Chong SHEN. Study on error calibration of fiber optic gyroscope under intense ambient temperature variation. *Applied Optics*. 2012, **51**(17), p. 3755–3762. ISSN 1559-128X. DOI:10.1364/AO.51.003755

[115] RAMADASS, G. A., et al. Finite Element Analysis of the Influence of Ambient Temperature Variations on the Performance of Fiber Optic Gyroscope Sensing Coils. *Marine Technology Society Journal*. 2017, **51**(1), p. 16–22. ISSN 0025-3324. DOI:10.4031/MTSJ.51.1.2

[116] CHIEN, Pie-Yau, Yau-Sheng CHANG and Ming-Wen CHANG. Fiber sensor based on frequency tracking in a phase-modulated fiber-optic gyroscope. *Optics Communications*. 1995, **118**(3-4), p. 215–219. ISSN 00304018. DOI:10.1016/0030-4018(95)00190-J

[117] XI, Wang, Gao YAN-BIN and Huo LIANG. Low Cost Method for FOG Eigenfrequency Measurement. In: *2012 International Conference on Industrial Control and Electronics Engineering*. IEEE, 2012, p. 1003–1006. ISBN 978-1-4673-1450-3. DOI:10.1109/ICICEE.2012.266

[118] YANG, Mingwei and Yuanhong YANG. New measurement method for eigen frequency of a fiber optic gyroscope. *Optical Engineering*. 2013, **52**(2), p. 024401-1–7. ISSN 0091-3286. DOI:10.1117/1.OE.52.2.024401

[119] WANG, Xiaxiao, Xiang WANG, Jia YU and Yue ZHENG. Eigenfrequency detecting method with sawtooth wave modulation theory for navigation grade fiber optic gyroscopes. *Optical Engineering*. 2017, **56**(09), p. 094109-1–6. ISSN 0091-3286. DOI:10.1117/1.OE.56.9.094109

[120] STANDJORD, Lee K. and David A. DOHENY. *Eigen frequency detector for Sagnac interferometers*. U.S. Patent No 7,038,783, 2006.

[121] DENG, Bowen, Ningfang SONG and Xiaxiao WANG. The Even Frequency Doubled Sine Wave Modulation Used for Proper Frequency Measurement of IFOG: Apply Effect and Implementation Rules. (Preprint) *SSRN*. 2024, 4760518. DOI: 10.2139/ssrn.4760518

[122] SUN, Hongbin, et al. Laser Doppler vibrometry for piezoelectric coefficient (d_{33}) measurements in irradiated aluminum nitride. *Sensors and Actuators A: Physical*. 2022, **347**, 113886. ISSN 09244247. DOI:10.1016/j.sna.2022.113886

[123] LIU, J.-M., et al. Piezoelectric coefficient measurement of piezoelectric thin films: an overview. *Materials Chemistry and Physics*. 2002, **75**(1-3), p. 12–18. ISSN 02540584. DOI:10.1016/S0254-0584(02)00023-8

[124] YAO, Kui and F. E. H. TAY. Measurement of longitudinal piezoelectric coefficient of thin films by a laser-scanning vibrometer. *IEEE Transactions on Ultrasonics, Ferroelectrics and Frequency Control*. 2003, **50**(2), p. 113–116. ISSN 0885-3010. DOI:10.1109/TUFFC.2003.1182115

[125] LEIGHTON, Glenn J. T. and Zhaorong HUANG. Accurate measurement of the piezoelectric coefficient of thin films by eliminating the substrate bending effect using spatial scanning laser vibrometry. *Smart Materials and Structures*. 2010, **19**(6), 065011. ISSN 0964-1726. DOI:10.1088/0964-1726/19/6/065011

[126] WANG, Zhihong, et al. Characterization of composite piezoelectric thick film for MEMS application. *Surface and Coatings Technology*. 2005, **198**(1-3), p. 384–388. ISSN 02578972. DOI:10.1016/j.surfcoat.2004.10.104

[127] CHAO, Chen, Zhihong WANG, Weiguang ZHU and Ooikiang TAN. Scanning homodyne interferometer for characterization of piezoelectric films and microelectromechanical systems devices. *Review of Scientific Instruments*. 2005, **76**(6), 063906. ISSN 0034-6748. DOI:10.1063/1.1932308

[128] WANG, Zhihong, et al. Measurement of longitudinal piezoelectric coefficient of film with scanning-modulated interferometer. *Sensors and Actuators A: Physical*. 2006, **128**(2), p. 327–332. ISSN 09244247. DOI:10.1016/j.sna.2006.01.039

[129] LI, Jiyang, Haisha NIU a Yanxiong NIU. Laser feedback interferometry and applications: a review. *Optical Engineering*. 2017, **56**(5), 050901. ISSN 0091-3286. DOI:10.1117/1.OE.56.5.050901

[130] BOBROFF, N. Recent advances in displacement measuring interferometry. *Measurement Science and Technology* 1993, **4**(9), p. 907–926. ISSN 0957-0233. DOI:10.1088/0957-0233/4/9/001

[131] LEFKI, K. and G. J. M. DORMANS. Measurement of piezoelectric coefficients of ferroelectric thin films. *Journal of Applied Physics*. 1994, **76**(3), p. 1764–1767. ISSN 0021-8979. DOI:10.1063/1.357693

[132] POKORNY, Marek, et al. Measurement Methods for the d_{33} Coefficient of PZT Thin Films on Silicon Substrates: A Comparison of Double-Beam Laser Interferometer (DBI) and Single-Beam Laser Vibrometer (LDV) Techniques. *Ferroelectrics*. 2007, 2007-06-08, **351**(1), p. 122–130. ISSN 0015-0193. DOI:10.1080/00150190701354109

[133] ŠULC, Miroslav and Dagmar BAROŠOVÁ. Laser interferometry for piezoelectric material study-possibilities and limits. *Ferroelectrics*. 1999, **224**(1), p. 129–136. ISSN 0015-0193. DOI:10.1080/00150199908210559

[134] PAN, W. Y. and L. E. CROSS. A sensitive double beam laser interferometer for studying high-frequency piezoelectric and electrostrictive strains. *Review of Scientific Instruments*. 1989, **60**(8), p. 2701–2705. ISSN 0034-6748. DOI:10.1063/1.1140644

[135] HUANG, Z. and R. W. WHATMORE. A double-beam common path laser interferometer for the measurement of electric field-induced strains of piezoelectric thin films. *Review of Scientific Instruments*. 2005, **76**(12), 123906. ISSN 0034-6748. DOI:10.1063/1.2149002

[136] GERBER, P., et al. Short-time piezoelectric measurements in ferroelectric thin films using a double-beam laser interferometer. *Review of Scientific Instruments*. 2003, **74**(4), p. 2613–2615. ISSN 0034-6748. DOI:10.1063/1.1544415

[137] CHAO, Chen, Zhihong WANG and Weiguang ZHU. Modulated laser interferometer with picometer resolution for piezoelectric characterization. *Review of Scientific Instruments*. 2004, **75**(11), p. 4641–4645. ISSN 0034-6748. DOI:10.1063/1.1805010

[138] YAN, Xingwei, et al. Influence of substrate deformation on piezoelectric displacement measurement of piezoelectric film. *Ceramics International*. 2013, **39**(suppl. 1), p. S583–S586. ISSN 02728842. DOI:10.1016/j.ceramint.2012.10.140

[139] GUILLOT, François M., Jacek JARZYNSKI and Edward BALIZER. Electromechanical response of polymer films by laser Doppler vibrometry. *The Journal of the Acoustical Society of America*. 1998, **103**(3), p. 1421–1427. ISSN 0001-4966. DOI:10.1121/1.421282

[140] ZHANG, Q. M., W. Y. PAN and L. E. CROSS. Laser interferometer for the study of piezoelectric and electrostrictive strains. *Journal of Applied Physics*. 1988, **63**(8), p. 2492–2496. ISSN 0021-8979. DOI:10.1063/1.341027

[141] ZHANG, Q. M., S. J. JANG and L. E. CROSS. High-frequency strain response in ferroelectrics and its measurement using a modified Mach-Zehnder interferometer. *Journal of Applied Physics*. 1989, **65**(7), p. 2807–2813. ISSN 0021-8979. DOI:10.1063/1.342744

[142] NOSEK, J., et al. Nonlinear Properties of the ZnO Thin Films and Their Experimentally Verification by Laser Interferometry. *Ferroelectrics*. 2009, **389**(1), p. 63–74. ISSN 0015-0193. DOI:10.1080/00150190902987756

[143] LIU, Junhao, Yifan LIU and Tianhua XU. Bias error and its thermal drift due to fiber birefringence in interferometric fiber-optic gyroscopes. *Optical Fiber Technology*. 2020, **55**, 102138. ISSN 10685200. DOI: doi:10.1016/j.yofte.2020.102138

[144] WANG, Zinan, et al. All-Depolarized Interferometric Fiber-Optic Gyroscope Based on Optical Compensation. *IEEE Photonics Journal*. 2014, **6**(1), p. 1–8. ISSN 1943-0655. DOI:10.1109/JPHOT.2014.2299212

[145] YAHALOM, Ram, et al. Low-cost, compact Fiber-Optic Gyroscope for super-stable Line-of-Sight stabilization. In: *IEEE/ION Position, Location and Navigation Symposium*. Indian Wells, US: IEEE, 2010, p. 60–66. ISBN 10.1109/PLANS.2010.5507131. DOI:10.1109/PLANS.2010.5507131

[146] BURNS, W.K. and A.D. KERSEY. Fiber-optic gyroscopes with depolarized light. *Journal of Lightwave Technology*. 1992, **10**(7), p. 992–999. ISSN 07338724. DOI:10.1109/50.144925

[147] SANDERS, G.A. and B. SZAFRANIEC. Progress in Fiber-Optic Gyroscope Applications II with Emphasis on the Theory of Depolarized Gyros. In: LOUKIANOV, D., et al., ed. *Optical Gyros and their Application*. NATO, Research and Technology Organization, 1999, p. 11-1–42. ISBN 92-837-1014-2.

[148] PÉREZ, Ramón, Ignacio ÁLVAREZ and José ENGUITA. Theoretical Design of a Depolarized Interferometric Fiber-Optic Gyroscope (IFOG) on SMF-28 Single-Mode Standard Optical Fiber Based on Closed-Loop Sinusoidal Phase Modulation with Serrodyne Feedback Phase Modulation Using Simulation Tools for Tactical and Industrial Grade Applications. *Sensors*. 2016, **16**(5), 604. ISSN 1424-8220. DOI:10.3390/s16050604

[149] SKALSKÝ, Michal, Zdeněk HAVRÁNEK and Jiří FIALKA. Efficient Modulation and Processing Method for Closed-Loop Fiber Optic Gyroscope

with Piezoelectric Modulator. *Sensors*. 2019, **19**(7), 1710. ISSN 1424-8220. DOI:10.3390/s19071710

[150] SKALSKÝ, Michal, Jiří FIALKA, Ladislav KOPEČNÝ and Zdeněk HAVRÁNEK. Scale-Factor Stability Control Technique for Closed-Loop All-Fiber Interferometric Optical Gyroscope. In: *2021 IEEE International Symposium on Inertial Sensors and Systems (INERTIAL)*. IEEE, 2021, 9430458. ISBN 978-1-7281-5099-4. DOI:10.1109/INERTIAL51137.2021.9430458

[151] LEFÈVRE, Hervé C. Fundamentals of the interferometric fiber-optic gyroscope. *Optical Review*. 1997, **4**(1), p. 20–27 . ISSN 1340-6000. DOI:10.1007/BF02935984

[152] CULSHAW, B. The optical fibre Sagnac interferometer: an overview of its principles and applications. *Measurement Science and Technology*. 2006, **17**(1), R1–R16. ISSN 0957-0233. DOI:10.1088/0957-0233/17/1/R01

[153] SZAFRANIEC, B. and G.A. SANDERS. Theory of polarization evolution in interferometric fiber-optic depolarized gyros. *Journal of Lightwave Technology*. 1999, **17**(4), p. 579–590. ISBN 10.1109/50.754787. DOI:10.1109/50.754787

[154] PAVLATH, G. A. and H. J. SHAW. Birefringence and polarization effects in fiber gyroscopes. *Applied Optics*. 1982, **21**(10), p. 1752–1757. ISSN 0003-6935. DOI:10.1364/AO.21.001752

[155] FREDRICKS, R.J. and R. ULRICH. Phase error bounds of fibre gyro with imperfect polariser/depolariser. *Electronics Letters*. 1984, **20**(8), p. 330–332. ISSN 00135194. DOI:10.1049/el:19840224

[156] HALL, D.C., W.K. BURNS and R.P. MOELLER. High-stability Er^{3+}-doped superfluorescent fiber sources. *Journal of Lightwave Technology*. 1995, **13**(7), p. 1452–1460. ISSN 07338724. DOI:10.1109/50.400711

[157] PATRICK, H. J., A. D. KERSEY, W. K. BURNS a R. P. MOELLER. An Erbium-doped Superfluorescent Fiber Source with Long Period Fiber Grating Wavelength Stabilization. In: *12th International Conference on Optical Fiber Sensors*. Washington DC, US: OSA, 1997, p. 138–141. ISBN 1-55752-485-8. DOI:10.1364/OFS.1997.OWB6

[158] GAIFFE, Thierry P., et al. Wavelength stabilization of an erbium-doped fiber source with a fiber Bragg grating for high-accuracy FOG. In: *Proceedings Volume 2837, Fiber Optic Gyros: 20th Anniversary Conference: 20th Anniversary Conference*. SPIE, 1996, p. 375–380. ISSN 0277786X. DOI:10.1117/12.258200

[159] OU, P., et al. Er-doped superfluorescent fibre source with enhanced mean-wavelength stability using chirped fibre grating. *Electronics Letters*. 2008, **44**(3), p. 87–189. ISSN 00135194. DOI:10.1049/el:20082948

[160] WANG, A., et al. High-Stability Er-Doped Superfluorescent Fiber Source Incorporating Photonic Bandgap Fiber. *IEEE Photonics Technology Letters*. 2009, **21**(24), p. 1843–1845. ISSN 1041-1135. DOI:10.1109/LPT.2009.2034621

[161] YANG, Yuanhong, et al. Erbium-doped superfluorescent fiber source for fiber optic gyroscope. In: *Proceedings Volume 4920, Advanced Sensor Systems and Applications*. Shanghai, China: SPIE, 2002, p. 111–114. ISSN 0277786X. DOI:10.1117/12.481957

[162] GUILLAUMOND, D. and J.-P. MEUNIER. Comparison of two flattening techniques on a double-pass erbium-doped superfluorescent fiber source for fiber-optic gyroscope. *IEEE Journal of Selected Topics in Quantum Electronics*. 2001, **7**(1), p. 17–21. ISSN 1077260X. DOI:10.1109/2944.924004

[163] WAN, Hongdan, Desheng ZHANG and Xiaohan SUN. Stabilization of a superfluorescent fiber source with high performance erbium doped fibers. *Optical Fiber Technology*. 2013, **19**(3), p. 264–268. ISSN 10685200. DOI:10.1016/j.yofte.2013.02.006

[164] WANG, Xiulin. Stable L-band superfluorescent fiber source using one pump. *Optical Engineering*. 2009, **48**(7), 075002. ISSN 0091-3286. DOI:10.1117/1.3168643

[165] LI, Yan, Yanfeng SUN, Xu WANG, and Man JIANG. Er-doped superfluorescent fiber source with enhanced mean- wavelength stability incorporating a fiber filter. *Infrared and Laser Engineering*. 2015, **44**(1), p. 244–248. ISSN 10072276.

[166] LI, Yan, et al. High stability double-pass backward Er-doped superfluorescent fiber source incorporating an Er-doped fiber filter. In: *International Conference on Multisensor Fusion and Information Integration for Intelligent Systems (MFI)*. IEEE, 2014, 6997726. ISBN 978-147996732-2. DOI:10.1109/MFI.2014.6997726

[167] RUAN, Shuang-chen, Xu WU, Cheng-xiang LIU and Li ZHANG. High-stability double-pass backward erbium-doped superfluorescent photonic crystal fiber source. In: *Proceedings Volume 9157, 23rd International Conference on Optical Fibre Sensor*. SPIE, 2014, 9157AK. ISSN 0277786X. DOI:10.1117/12.2059007

[168] WANG, Aimin. High Stability Er-Doped Superfluorescent Fiber Source Improved by Incorporating Bandpass Filter. *IEEE Photonics Technology Letters*. 2011, **23**(4), p. 227–229. ISSN 1041-1135. DOI:10.1109/LPT.2010.2098436

[169] FALQUIER, D.G., M.J.F. DIGONNET and H.J. SHAW. A polarization-stable Er-doped superfluorescent fiber source including a Faraday rotator mirror. *IEEE Photonics Technology Letters*. 2000, **12**(11), p. 1465–1467. ISSN 1041-1135. DOI:10.1109/68.887672

[170] LI, Yan, Man JIANG, Chun Xi ZHANG and Hong Jie XU. High Stability Er-Doped Superfluorescent Fiber Source Incorporating an Er-Doped Fiber Filter and a Faraday Rotator Mirror. *IEEE Photonics Technology Letters*. 2013, **25**(8), p. 731–733. ISSN 1041-1135. DOI:10.1109/LPT.2013.2250948

[171] GUO, Jinjin, Tong SHEN, Guancheng ZHAO and Yuanhong YANG. Mean wavelength stable SFS with variable parameter control technology. In: *Proceedings Volume 6830, Advanced Sensor Systems and Applications III*. SPIE, 2007, p. 409–414. ISSN 0277786X. DOI:10.1117/12.757648

[172] SKALSKÝ, Michal, Jakub HNIDKA and Zdeněk HAVRÁNEK. Improvement of the Temperature Stability of the Erbium-Doped Superfluorescent Fiber Source by Tuning the Reflectivity of the Fiber End. *Journal of Lightwave Technology*. IEEE, 2023, **41**(6), p. 1843–1850. ISSN 0733-8724. DOI:10.1109/JLT.2022.3226206

[173] SKALSKÝ, Michal, Zdeněk HAVRÁNEK and Jiří FIALKA. Fibre optic gyroscope with single-mode fibre and loop-back phase shift compensation. In: *Proceedings Volume 10603, Photonics, Devices, and Systems VII*. Prague, CZ: SPIE, 2017, 1060309. ISBN 9781510617025. ISSN 1996-756X. DOI:10.1117/12.2292298

[174] IEEE. *IEEE Standard for Specifying and Testing Single-Axis Interferometric Fiber Optic Gyros (IEEE Std 952-2020)*. 2021, 93 p. ISBN 978-1-5044-6978-4. DOI:10.1109/IEEESTD.2021.9353434

[175] SKALSKÝ, Michal, Jiří FIALKA and Zdeněk HAVRÁNEK. Scanning Double-Beam Laser Interferometer with Loop-Back Compensation and Phase Stabilization. In: *2019 IEEE International Instrumentation and Measurement Technology Conference (I2MTC)*. Auckland, New Zealand: IEEE, 2019, 8826963. ISBN 978-1-5386-3460-8. DOI:10.1109/I2MTC.2019.8826963

[176] CENELEC. *Piezoelectric properties of ceramic materials and components – Part 1: Terms and definitions (The European Standard EN 50324-1:2002).* 2002, 16 p. ISBN 0-580-40539-7.

[177] IEEE. *IEEE Recommended Practice for Inertial Sensor Test Equipment, Instrumentation, Data Acquisition, and Analysis (IEEE Std 1554-2005).* 2005, 103 p. ISBN 0738147397. DOI: 10.1109/IEEESTD.2013.6673990

List of symbols, physical constants, and abbreviations

Abbreviations

ADC	Analog-to-digital converter
AOM	Acousto-optical modulator
ASE	Amplified spontaneous emission
CCW	Counterclockwise
COTS	Commercial off-the-shelf
CU	Control unit
CW	Clockwise
DAC	Digital-to-analog converter
DBMZI	Double-beam Mach-Zehnder interferometer
EDFA	Erbium-doped fiber amplifier
EOM	Electro-optical modulator
FOG	Fiber-optic gyroscope
FOS	Fiber-optic sensors
FPGA	Field programmable gate array
GTP	Glan-Thompson polarizer
HLS	Hidden layer size
HWP	Half-wave plate
IFOG	Interferometric fiber-optic gyroscope
IS	Optical isolator
IU	Interface unit
L	Lens
LD	Laser diode
LED	Light-emitting diode
LQCFE	Least-square curve fitting estimation
M	Mirror
MEMS	Micro electro-mechanical systems
MIOC	Multi-functional integrated optical circuit
MM	Multi-mode
NN	Neural network
NNCLE	Neural network closed-loop estimation
P	Polarizer
P1	Prototype 1 (IFOG)
P2	Prototype 2 (IFOG)

PBS	Polarization beam splitter
PCA	Principal components analysis
PEM	Piezoelectric modulator
PI	Proportional-integration (controller)
PM	Polarization maintaining
PS	Processing system
PZT	Poled zirconate-titanate
QWP	Quarter-wave plate
RFOG	Resonant fiber-optic gyroscope
RLG	Ring laser gyroscope
RMOG	Resonant micro-optic gyroscope
SBMI	Single-beam Michelson interferometer
SF	Scale factor
SFS	Superfluorescent fiber source
SM	Single-mode
SLD	Superluminiscent diode
SNR	Signal-to-noise ratio
SOTA	State of the art
SP	Single polarization
TE	Transverse electric (mode)
TM	Transverse magnetic (mode)
WDM	Wavelength division multiplexer
WF-DPB	Weak-feedback double-pass backward-pump (SFS)

Symbols

$*$	wildcard symbol for any corresponding designation
$\langle\rangle$	time averaging operation
c	speed of light in vacuum $[\mathrm{m} \cdot \mathrm{s}^{-1}]$
Δd	displacement (thickness) [m]
d_{33e}	effective piezoelectric thickness coefficient $[\mathrm{pm} \cdot \mathrm{V}^{-1}]$, $[\mathrm{pC} \cdot \mathrm{N}^{-1}]$
$D(k)$	deviation vector between $\hat{I}(k)$ and $I(k)$ for the modulation depth control
e_q	quadrature point stabilization error signal [-]
$e_{s\langle i\rangle}$	inphase component of the sample-induced phase difference compensation error signal [-]
$e_{s\langle q\rangle}$	quadrature component of the sample-induced phase difference compensation error signal [-]
E	intensity error function
$E_{\psi b}$	error function for the biasing modulation components phase error [-]

$E_{\psi c}$	error function for the compensation modulation components phase error [-]
E_{Gc}	error function for the k_c-th harmonic component of the compensation modulation gain error [-]
E_{Gb}	error function for the k_b-th harmonic component of the biasing modulation gain error [-]
$\mathbf{E}(t, z)$	electric field [$\mathrm{V} \cdot \mathrm{m}^{-1}$]
$\mathbf{E_0}$	electric field amplitude [$\mathrm{V} \cdot \mathrm{m}^{-1}$]
f	frequency [Hz]
Δf	frequency difference [Hz]
f_b	biasing modulation frequency [Hz]
f_{BW}	frequency bandwidth [Hz]
f_c	compensation modulation frequency [Hz]
f_e	sensing coil eigenfrequency [Hz]
f_m	sweep modulation frequency [Hz]
f_s	sample driving frequency [Hz]
f_{sa}	sampling frequency [Hz]
f_{sf}	sampling frequency of $I(t)$ signal for the modulation depth control [Hz]
g_a	asymmetry distortion function [-]
g_h	hysteresis distortion function [-]
g_s	saturation distortion function [rad]
G_b	gain of the $u_{bk_b}(t)$ modulation voltage component [-]
δG_b	relative gain error of the $u_{bk_b}(t)$ modulation voltage component [-]
$\delta \hat{G}_b$	relative gain error estimate of the $u_{bk_b}(t)$ modulation voltage component [-]
G_c	gain of the $u_{ck_c}(t)$ modulation voltage component [-]
δG_c	relative gain error of the $u_{ck_c}(t)$ modulation voltage component [-]
$\delta \hat{G}_c$	relative gain error estimate of the $u_{ck_c}(t)$ modulation voltage component [-]
I	optical wave intensity [$\mathrm{W} \cdot \mathrm{m}^{-2}$]
$\hat{I}$	intensity signal estimate/model [$\mathrm{W} \cdot \mathrm{m}^{-2}$]
I_0	original optical wave intensity (intensity without interference) [$\mathrm{W} \cdot \mathrm{m}^{-2}$]
I_i	interference optical wave intensity portion [$\mathrm{W} \cdot \mathrm{m}^{-2}$]
I_n	non-interference optical wave intensity portion [$\mathrm{W} \cdot \mathrm{m}^{-2}$]
$\mathrm{J}_k()$	Bessel function of the k-th order
k	wave number [m^{-1}]
k_b	order of higher harmonic component of the biasing modulation [-]
k_c	order of higher harmonic component of the compensation modulation

	[-]
K_{det}	intensity signal detection chain gain [$\mathrm{V} \cdot \mathrm{m}^2 \cdot \mathrm{W}^{-1}$]
K_f	discrete period of $I(k)$ signal for the modulation depth control [s]
K_{EOM}	voltage-to-phase gain with EOM [$\mathrm{rad} \cdot \mathrm{V}^{-1}$]
K_{IFOG}	IFOG constant (proportional coefficient) [s]
K_{PEM}	voltage-to-phase gain with PEM [$\mathrm{rad} \cdot \mathrm{V}^{-1}$]
K_ϑ	mean wavelength temperature gradient [$\mathrm{m} \cdot {}^\circ\mathrm{C}^{-1}$]
l	length/optical path [m]
Δl	length/optical path elongation [m]
L	IFOG sensing coil length [m]
L_{dp}	depolarizing length [m]
L_{dc}	decoherence length [m]
n	medium refractive index [-]
N_b	biasing modulation frequency factor [-]
N_c	compensation modulation frequency factor [-]
R	IFOG fiber coil radius [m]
S_{OL}	open-loop signal [-]
S_{ω_*}	signal component obtained by demodulation at ω_* [-]
t	time [s]
T_{acq}	sample acquisition time [s]
T_{avg}	averaging time [s]
T_{sa}	sampling period [s]
T_{sf}	sampling period of $I(t)$ signal for the modulation depth control [s]
u_*	driving voltage for the corresponding modulation component [V]
u_s	voltage applied to the measured sample [V]
U_*	amplitude of the driving voltage for the corresponding modulation component [V]
U_s	amplitude of the voltage applied to the measured sample [V]
U_λ	voltage induces a light path shift of λ [V]
γ	normalized parasitic effects distortion level coefficient [-]
γ_a	normalized parasitic effects asymmetry distortion level coefficient [-]
γ_h	normalized parasitic effects hysteresis distortion level coefficient [-]
γ_s	normalized parasitic effects saturation distortion level coefficient [-]
$\delta(*)$	relative error/change of the corresponding quantity [%], [-]
$\delta_{lin}(*)$	relative linearity error of the corresponding quantity dependency [%], [-]
ϵ_0	permittivity of vacuum [$\mathrm{F} \cdot \mathrm{m}^{-1}$]
θ	parameters vector of the $\hat{I}(t)$ model for the modulation depth control
ϑ	temperature [°C]

$\hat{\theta}$	estimated parameters vector of the $\hat{I}(t)$ model for the modulation depth control
$\Delta\hat{\theta}$	correction of the estimated parameters vector $\hat{\theta}$ for the next iteration
λ	wavelength [m]
$\Delta\lambda_\Gamma$	spectral width [m]
Λ	optical beat length [m]
$\sigma(*)$	standard deviation of the corresponding quantity [*]
σ_Ω	Allan deviation of the angular velocity [$\mathrm{rad}\cdot\mathrm{s}^{-1}$], [$^\circ\cdot\mathrm{s}^{-1}$]
τ	light propagation time along the sensing coil [s]
ϕ	phase [rad]
$\Delta\phi$	phase difference [rad]
ϕ_b	biasing modulation phase [rad]
$\Delta\phi_b$	biasing modulation phase difference [rad]
ϕ_c	compensation modulation phase [rad]
$\Delta\phi_c$	compensation modulation phase difference [rad]
$\Delta\phi_{c\langle i\rangle}$	inphase component of the compensation modulation phase difference [rad]
$\Delta\phi_{c\langle q\rangle}$	quadrature component of the compensation modulation phase difference [rad]
$\Delta\phi_{drift}$	phase difference random drift [rad]
$\Delta\phi_{err}$	phase difference/shift error [rad]
ϕ_m	sweep modulation phase [rad]
$\Delta\phi_m$	sweep modulation phase difference [rad]
$\Delta\phi_q$	quadrature point phase difference [rad]
$\Delta\phi_s$	sensed (IFOG – Sagnac, DBMZI – sample vibrations-induced) phase difference/shift [rad]
$\Delta\phi_{stab}$	stabilization phase difference [rad]
Φ_b	depth of biasing modulation phase [rad]
$\Delta\Phi_b$	depth of biasing modulation phase difference [rad]
Φ_c	depth of compensation modulation phase [rad]
$\hat{\Phi}_c$	estimated depth of compensation modulation phase [rad]
$\Delta\Phi_c$	depth of compensation modulation phase difference [rad]
$\Delta\hat{\Phi}_c$	estimated depth of compensation modulation phase difference [rad]
$\Delta\Phi_{c\langle i\rangle}$	inphase component of the depth of compensation modulation phase difference [rad]
$\Delta\Phi_{c\langle q\rangle}$	quadrature component of the depth of compensation modulation phase difference [rad]
$\Delta\Phi_m$	depth of sweep modulation phase difference [rad]
$\Delta\Phi_s$	depth of sample-induced modulation phase difference [rad]

$\Delta\Phi_{\Delta s\langle i\rangle}$	inphase component of the uncompensated sample-induced phase difference error [rad]
$\Delta\Phi_{\Delta s\langle q\rangle}$	quadrature component of the uncompensated sample-induced phase difference error [rad]
φ	phase shift of the phase modulation [rad]
φ_s	phase delay between the sample displacement and the applied voltage [rad]
ψ_*	phase error of the corresponding modulation components [rad]
$\hat{\psi}_*$	phase error estimate of the corresponding modulation components [rad]
ω	angular frequency [$\mathrm{rad}\cdot\mathrm{s}^{-1}$]
ω_b	biasing modulation angular frequency [$\mathrm{rad}\cdot\mathrm{s}^{-1}$]
ω_c	compensation modulation angular frequency [$\mathrm{rad}\cdot\mathrm{s}^{-1}$]
ω_m	sweep modulation angular frequency [$\mathrm{rad}\cdot\mathrm{s}^{-1}$]
ω_s	sample driving angular frequency [$\mathrm{rad}\cdot\mathrm{s}^{-1}$]
ω_s'	half of the sample driving angular frequency [$\mathrm{rad}\cdot\mathrm{s}^{-1}$]
Ω	angular velocity [$\mathrm{rad}\cdot\mathrm{s}^{-1}$], [$^\circ\cdot\mathrm{s}^{-1}$]
Ω_m	measured angular velocity [$\mathrm{rad}\cdot\mathrm{s}^{-1}$], [$^\circ\cdot\mathrm{s}^{-1}$]
Ω_{ref}	reference angular velocity [$\mathrm{rad}\cdot\mathrm{s}^{-1}$], [$^\circ\cdot\mathrm{s}^{-1}$]

List of appendices

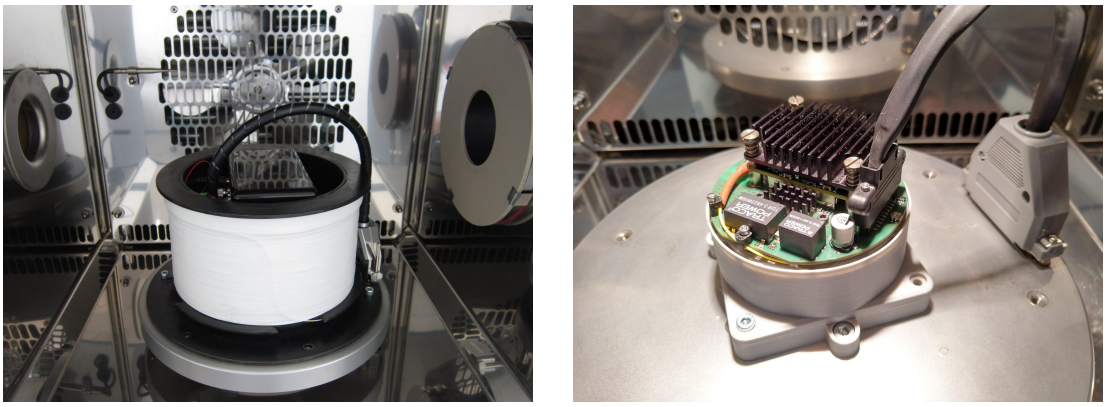
A Supplementary materials on the closed-loop IFOG prototypes 138

B Supplementary materials on the closed-loop DBMZI setup 158

A Supplementary materials on the closed-loop IFOG prototypes

The purpose of the following materials is to deliver additional technical details and specifications of the IFOG test setups. From this perspective, it serves also as an expansion of the description provided within Sec. 3.2. Finally, the additional measurement results demonstrating the prototype functionality are provided.

The gradual evolution of the test setup development is demonstrated in Fig. A.1, depicting the P1a optical setup and the final P2 setup (uncovered), including both optical as well as electronic parts. Their overall dimensions, for comparison, are then summarized in Tab. A.1. Considering the total volume, it was decreased by a factor of 15 in the P2. Note that the P2 additionally integrates all of the processing. As the P2 was developed as an evolution of the P1, with an emphasis on processing optimization, miniaturization, cost reduction, and integration, the further description is focused solely on the P2 design.



(a) (b)

Fig. A.1: The P1a (a) and uncovered P2 (b) IFOG setups on the rotary table inside the temperature chamber.

Tab. A.1: Overall IFOG prototypes dimensions

Parameter	P1	P2
outer diameter [mm]	224	82.5
height [mm]	118	58
sensing coil fiber length L [m]	770	770
mean coil radius R [mm]	77.8	34.5

A.1 Optical setup development

From a general perspective, both the P1 and the P2 prototypes follow the architecture in Fig. 3.23. The specific components utilized in the P2 are listed in Tab. A.2.

Tab. A.2: List of the P2 optical setup's components and their key parameters.

Component	Type	Key parameters
pump LD	Lumentum T13-7402-050	50 mW, $\lambda = 975.6$ nm
Er-doped fiber	Fibercore I-6(980/125)	length 20 m
WDM	WDMC-1x2-9815-0-4-0.8	dim. 2.4 × 30 mm
optical isolator	IS-S-1550-0-1-1	dim. 3.0 × 21 mm
circulator	CIR-3-P-1550-0-1-1	dim. 3.8 × 30 mm
coupler	CP-W-P-1x2-50/50-1550-0-1-1	dim. 2.4 × 30 mm
polarizing fiber	Fibercore HB1550Z(11/125)	PER $\approx$ 28 dB[1], 3 m
Lyot depolarizer	custom-made	DOP = 1.08 %[2], 5 m
sensing coil	Luna FCQ-60-20-760-250-15-SM-0	insertion loss 0.225 dB
PEM	custom-made	0.43 rad/V[3], DOP $<$ 1 %[2]
photodetector	Ushio PDINCF070500D-A-0-01	0.85 A/W, 5 GHz

[1] polarization extinction ratio, measured with SFS

[2] degree of polarization, measured with SFS

[3] pure PEM gain, a component of K_{PEM}, measured at $f_{c1} = 88$ kHz, $\lambda = 1544$ nm

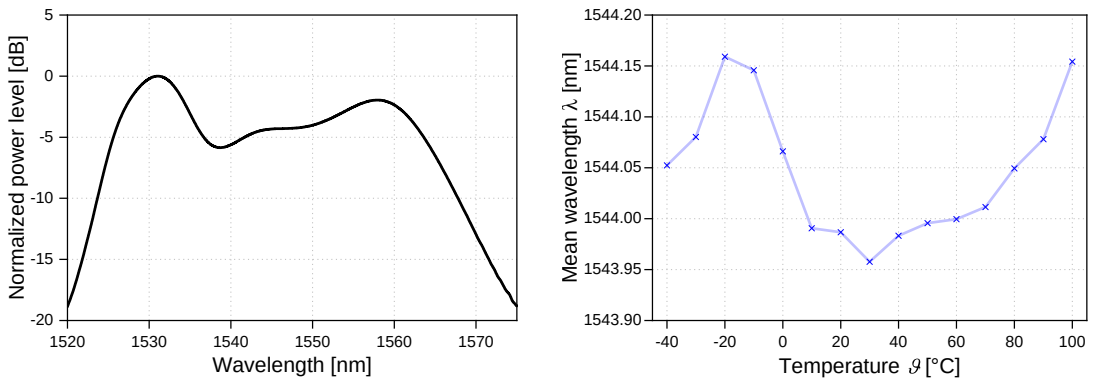
The components were selected or designed with an emphasis to maximize the ratio between the price and their performance regarding the IFOG requirements. Further critical features comprised also the dimensions, as the device was intended for an easy integration into a superior inertial navigation system. Therefore, although a commercial form of the standard optical components (WDM, coupler, etc.) was employed, the most compact packages possible were specifically selected. In commercial IFOG devices, such components are usually integrated directly into the device package or made as MIOC, in the case of the single-polarization architecture, which further optimizes both cost and dimensions. The special-purpose components, including the SFS, the PEM, and the Lyot depolarizer, were developed as a part of our own research.

A.1.1 Superfluorescent fiber source

The design of the SFS has been discussed broadly in Sec. 3.2.1, and a deeper background may be also found in [172]. The output SFS spectrum is shown in

Fig. A.2(a). Two distinct peaks can be distinguished at 1531 and 1558 nm, with a slight ripple at 1545 nm. An optimal reflectivity of the free (unpumped) fiber end results in a balanced power redistribution among the peaks with temperature, which is accompanied by their wavelength shift as well. The achieved balance means that those processes mutually compensate each other in their effect on an overall SFS mean wavelength so that it remains quasi-stable with the temperature, as evidenced by Fig. A.2(b).

Despite the number of optical components required by the SFS structure, their appropriate selection and a proper design allowed an assembly into a compact form and a subsequent integration into the P2, as shown in Fig. A.3. As the temperature stability of the mean wavelength is ensured by design, it is not necessary to utilize any active control of the pump LD. Thereafter, a compact and inexpensive LD can be employed, driven by the constant current of 36 mA via a simple step-down converter with a high efficiency. As the Er-doped fiber serves as a low-pass filter,



(a) (b)

Fig. A.2: Optimized SFS output spectrum (a) and its mean wavelength temperature drift (b) [172].

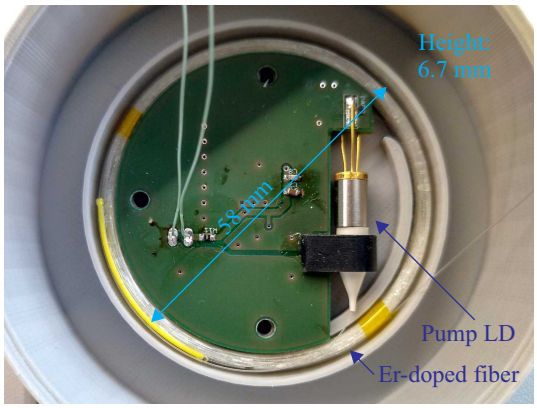


Fig. A.3: Assembly and integration of the SFS in the P2 case.

the high-frequency switching is not propagating to the IFOG, as was also confirmed by the Allan deviation method. The SFS is producing an output power of 9.4 mW. Among other SFSs employing any other form of temperature stabilization, both a superior power efficiency of up to 22 % and a spectral width of 38 nm is achieved.

A.1.2 Piezoelectric modulator

An additional custom-made component is the PEM, which constitutes a crucial part for an all-fiber IFOG. For both the double-sine as well as the quadruple-sine modulation schemes the piezoelectric actuator has to be selected carefully with regard to its behavior at the biasing and the compensation modulation frequencies under the given set of conditions. Special care has to be taken to avoid its eigen resonances. Before employing the selected actuator (PZT tube, NCE40, outer diameter of 25.4 mm, height 12.7 mm, and wall thickness of 3.15 mm), its properties were verified through an impedance measurement within a temperature range from -10 to 120 °C. It can be seen that the impedance characteristics in Fig. A.4 (obtained for 20 °C) are in close agreement with the displacement response in Fig. 3.5, acquired by the simulation. The impedance was then studied especially at the frequencies corresponding to the modulation frequencies within the set temperature range, with the results shown in Fig. A.5. A fluent transition of the impedance curves through the temperatures can be noticed, suggesting only moderate changes in the PEM behavior at the given frequencies. More importantly, there are no resonance-like features that could lead to the instability of the modulation depth control, except a residual ripple for f_{b1}. The actuator is thus compatible with the employed frequencies and is suitable for the PEM construction.

The fiber was then wound using a 3D-printed winding system, allowing a variable pre-tension by weight loading, and a microscope camera for a precise and tight fiber

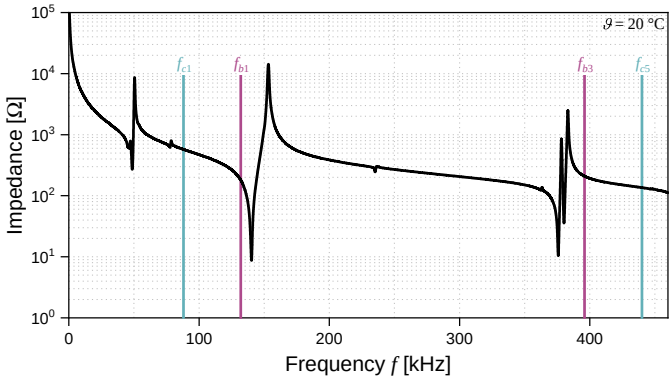


Fig. A.4: Impedance characteristics of the PZT tube actuator used for the PEM (at 20 °C).

alignment, as shown in Fig. A.6. Due to the utilization of a bend-resistive fiber (G657 B3) an insertion loss of <27 dB was measured, including the connecting pigtails (SMF-28).

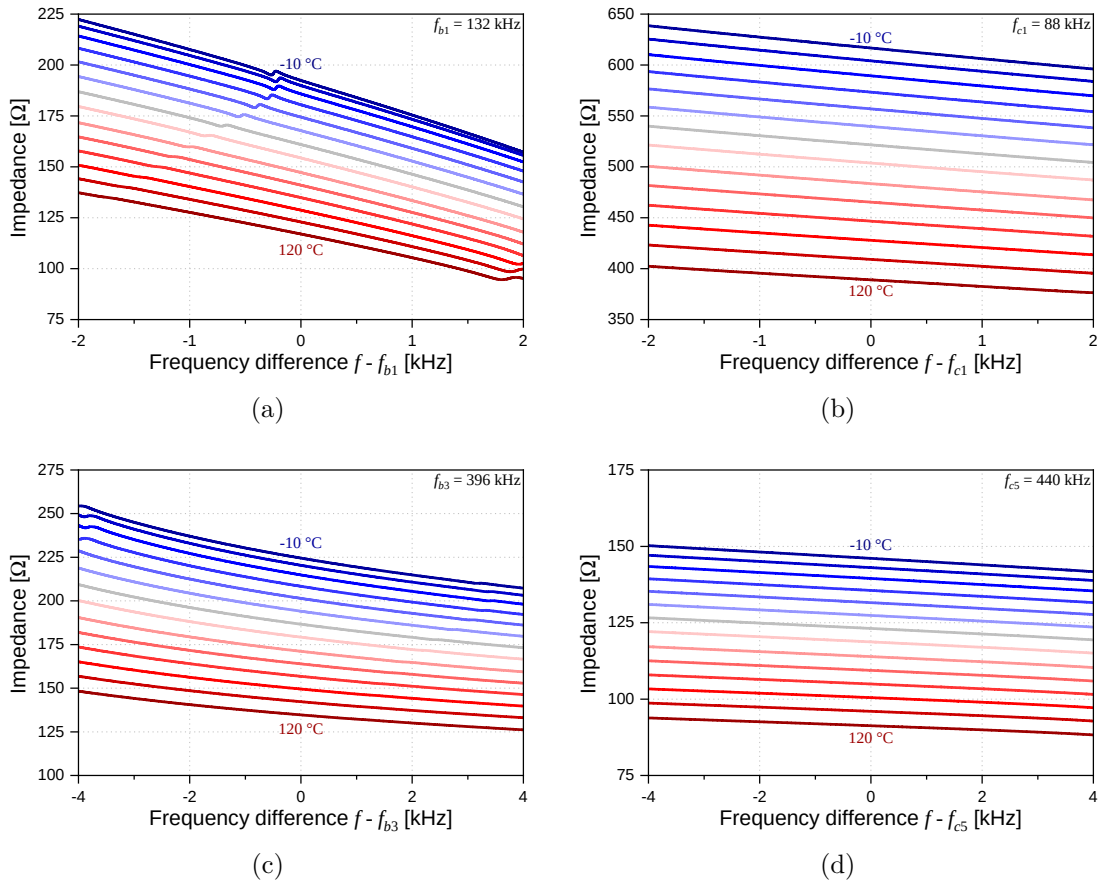


Fig. A.5: Impedance characteristics of the PZT tube actuator used for the PEM around the employed biasing and compensation modulation frequency components at different temperatures.

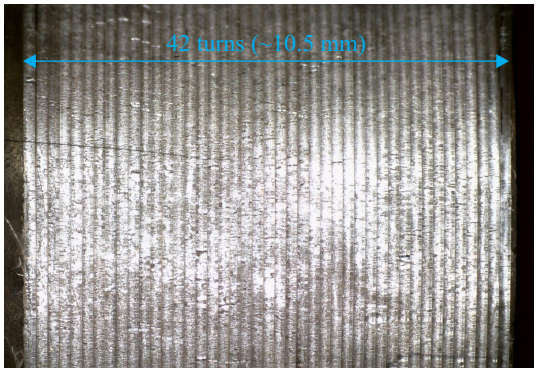


Fig. A.6: Detail of the fiber winding on the PZT actuator.

A.1.3 Lyot depolarizer

Finally, the Lyot depolarizer was composed of two segments of the PM fiber with a length ratio of $L_1 : L_2 = 1 : 2$. A well-known panda-type fiber (PM1550-XP) with a beat length of $\Lambda = 5$ mm (at $\lambda \approx 1550$ nm) was employed. For an efficient depolarization of a typical source with a Gaussian spectrum, the minimum length of the short segment must be greater than the so-called depolarizing length L_{dp}, defined as:

$$L_{dp} = \frac{L_{dc}\Lambda}{\lambda}, \tag{A.1}$$

where L_{dc} stands for the decoherence length expressed as:

$$L_{dc} = \frac{\lambda^2}{\Delta\lambda_\Gamma}. \tag{A.2}$$

The $\Delta\lambda_\Gamma$ denotes the light spectral width. Although the designed SFS integral spectral width reaches 37.8 nm (at $\vartheta = 20$ °C), the fact that the spectrum is not Gaussian must be taken into account. Thus, a narrower effective width must be considered for the depolarizing purpose. It was shown in [172] that the designed SFS spectrum can be closely approximated by a sum of three Gaussian functions corresponding to the above-discussed spectrum peaks, with the narrowest component at $\lambda = 1531$ nm having $\Delta\lambda_\Gamma = 8$ nm (at $\vartheta = 20$ °C). Therefore, the minimum length for the depolarization of this component can be calculated to be $L_{dp} = 0.957$ m. The segments of lengths 1.678 and 3.356 m were used, adding a 75% margin to cover ambient conditions change and a possible splice misalignment. The 45° splice, constituting the most critical step in the depolarizer manufacturing, was performed with an end-view alignment method (Fujikura FSM 100P+), with its detail shown in Fig. A.7. The resulting component insertion loss was measured to be 0.424 dB, including the SM fiber pigtails (SMF-28).

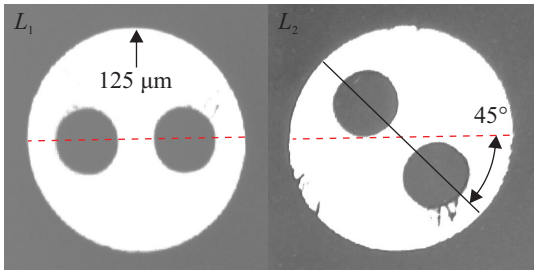


Fig. A.7: Detail of PM fiber segments (L_1, L_2) alignment during the Lyot depolarizer manufacturing.

A.2 Mechanical assembly

The optical setup of the P2 was assembled together in a 3D-printed case made of highly resistive ASA (acrylonitrile styrene acrylate) material. The case design was tailored to fit the optical components with an emphasis on the maximal compactness. Its structure can be seen in Fig. A.8.

The components were fixed by bonding (coupler, circulator) and mechanical coupling (PEM, sensing coil). The PEM was fixed through elastic elements allowing an undamped movement. The fiber components (polarizing fiber, Lyot depolarizer, Er-doped fiber) were fixed by a UV-cured glue to form a self-supported coil, that can be inserted into the case grooves. The guiding fibers management was assured

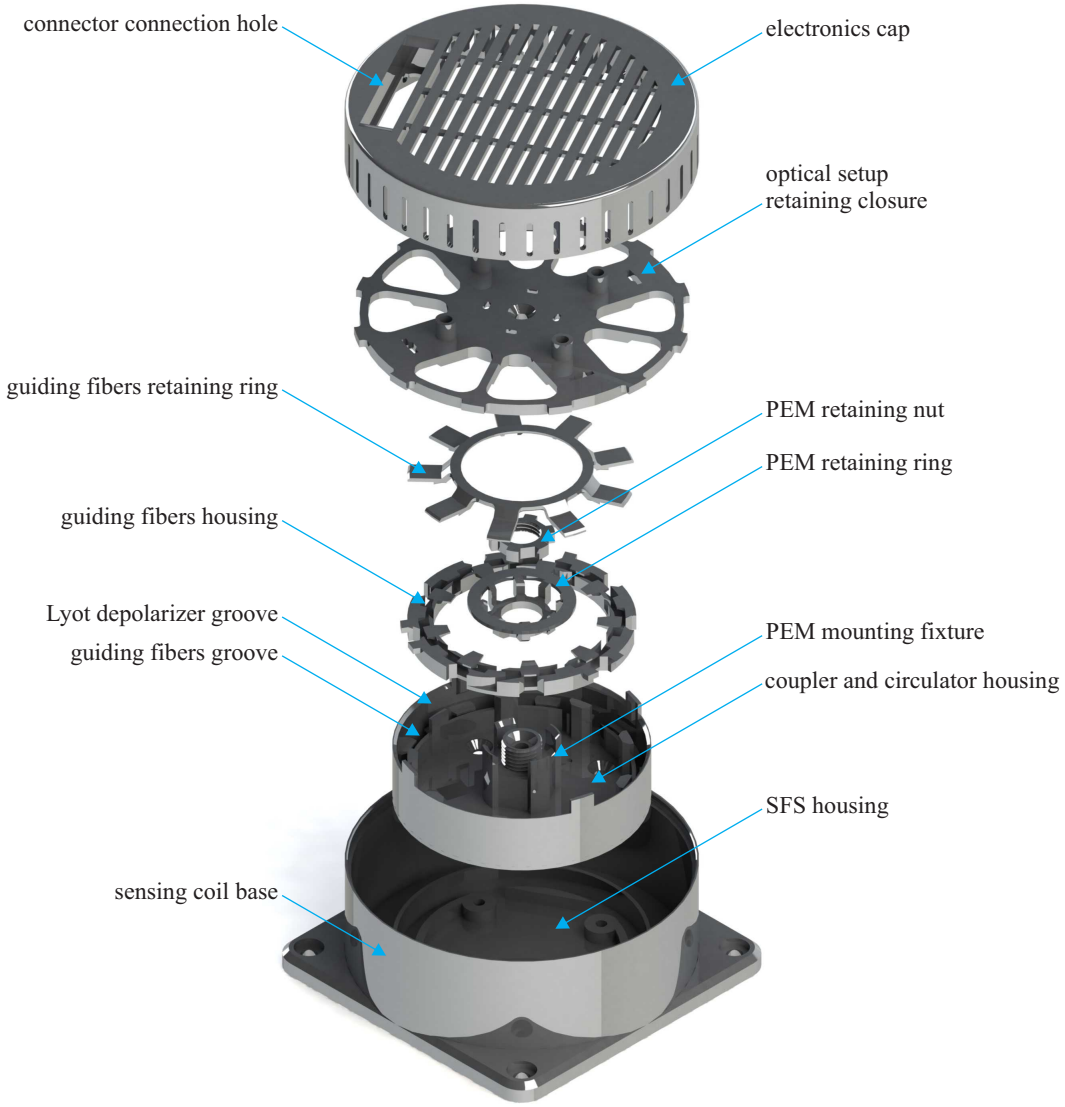
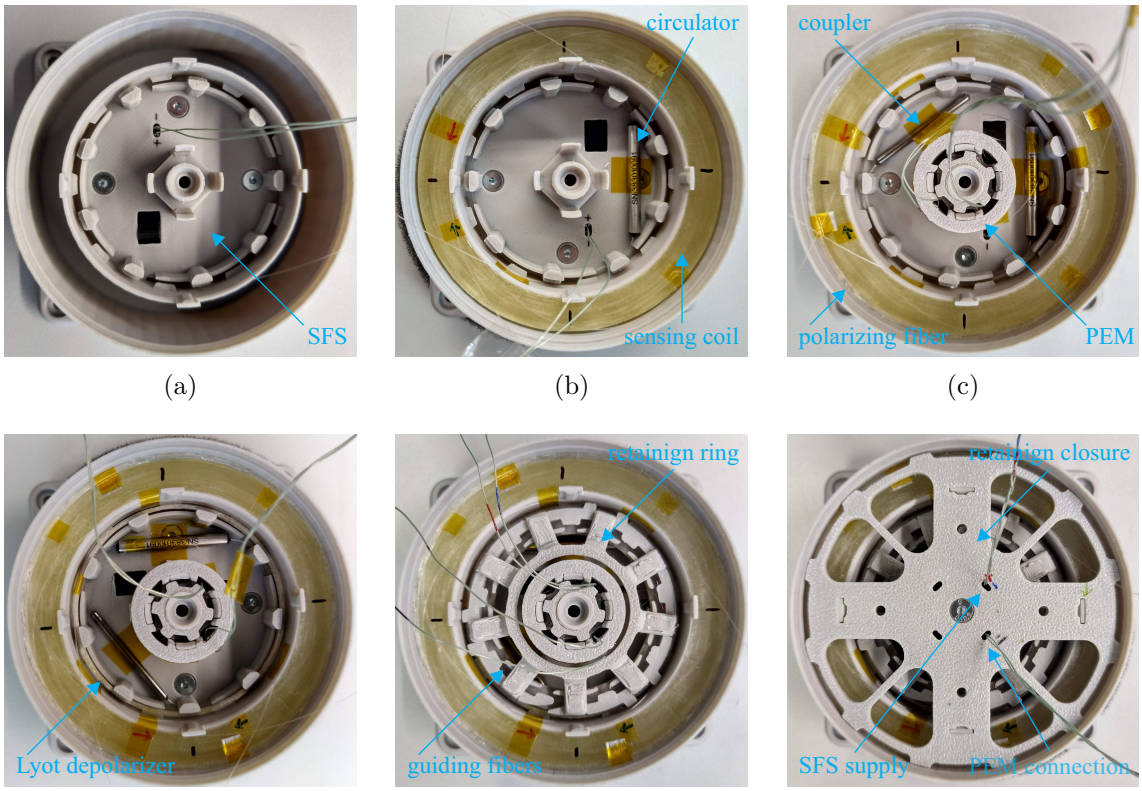


Fig. A.8: Exploded view of the P2 IFOG prototype case design structure.

by the grooves and housing with mechanical retainers. The individual stages of components integration are shown in Fig. A.9.



(a) (b) (c)

(d) (e) (f)

Fig. A.9: Stages of the optical components integration in the P2 IFOG prototype: SFS packaging into the case base (a), placement and fixing of the sensing coil and the circulator (b), the coupler, the PEM and the polarizing fiber (c), the Lyot depolarizer (d), the guiding fibers housing and the retaining ring (e), and closing of the optical assembly (f).

A.3 Electronics and control software development

A.3.1 Hardware design

The electronic module of the P2 IFOG is composed of the control unit CU2 and the interface unit IU2, as shown in Fig. 3.27. The module was developed on the basis of the requirements defined by the previous evolution composed of the CU1 and IU1 in the P1c setup. Whereas the prior design was based on an evaluation board Cora Z7-10 (CU1), the new module in the P2 was specifically designed from scratch to fulfill the requirements of maximal integrability, noise performance, high communication

interface compatibility, and power efficiency. The schematic of the P2 electronic module are shown in Fig. A.10. As a CU2, an off-the-shelf board TE0720 (Trenz Electronic) was used, embedded with a Zynq family XC7Z020 (Xilinx) SoC. The main benefit of the Zynq family SoCs is a combination of an FPGA with a dual-core ARM Cortex-A9 processor. Such combination allows a full compatibility with the proposed modulation and compensation method.

The CU2 was integrated into the self-developed IU2 board, functioning as an expansion or a carrier board, with a functionality specifically purposed for the IFOG requirements. Its major blocks can be seen in Fig. A.10. The board with the

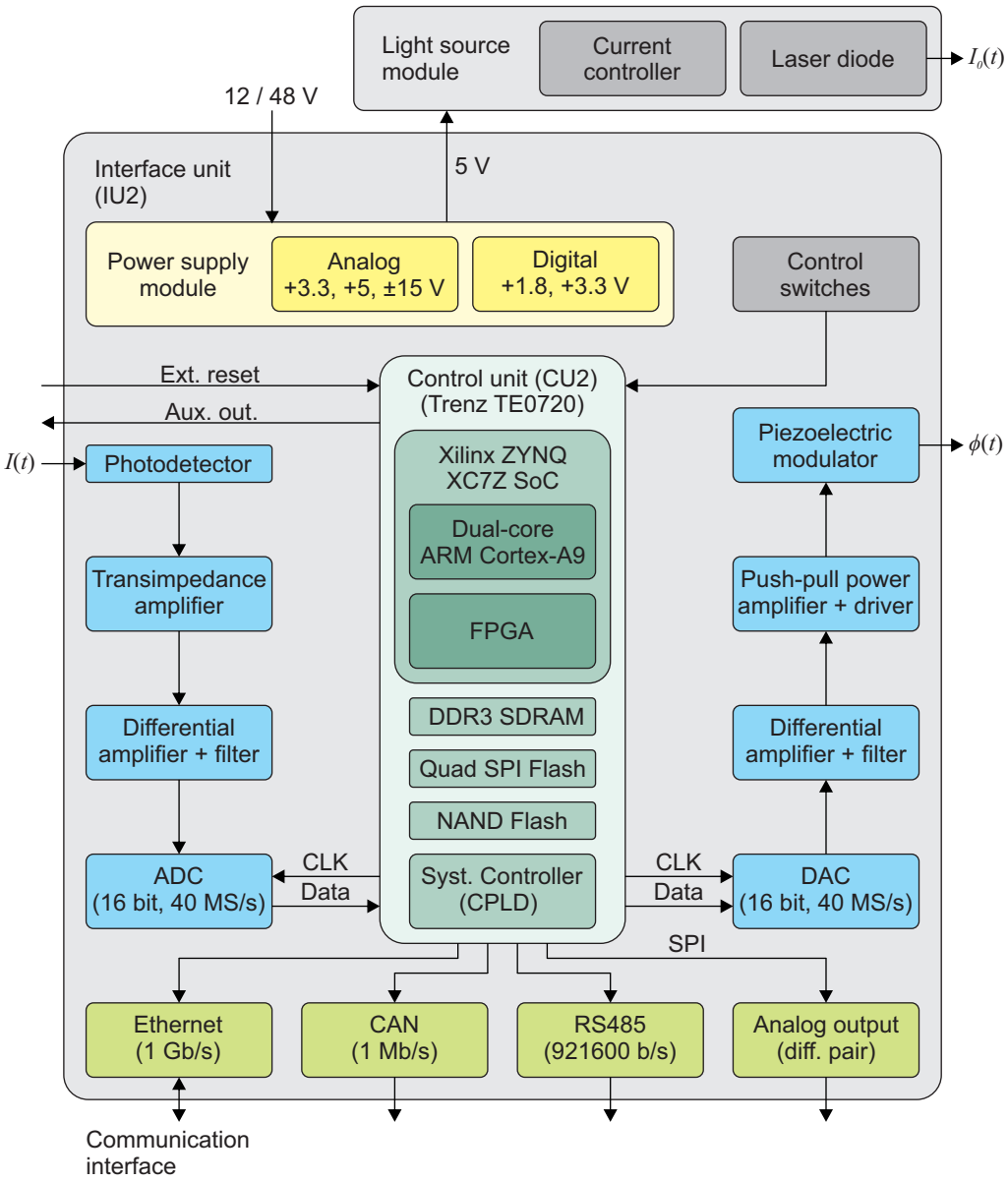


Fig. A.10: Schematic of the electronic module comprising the IU2 and CU2.

function blocks placement is then shown in Fig. A.11.

The power supply is ensured by a pair of isolated DC-DC convertors, distributing a voltage of 5 V, used for the majority of blocks within IU2 and the light source, and ±15 V, used for PEM driving. Two versions of the power supply were developed, accepting either 12 or 48 V as the input supply voltage. The internal 5 V voltage is further turned into 3.3 and 1.8 V digital voltage levels, supplying the digital circuits, and a 3.3 V analog voltage, which is produced separately by two linear regulators to supply analog circuits of the photodetector and the PEM interfaces.

The photodetector interface is implemented by an ADC and its front-end circuits. A high-speed fiber-coupled InGaAs photodiode and a transimpedance amplifier (OPA380) are used to convert the optical signal into the electric one. Its conversion to a fully differential signal and preprocessing is then ensured by a differential amplifier (LTC6404), and it is further sampled by a 16-bit ADC (LTC2204) with a parallel interface, clocked at 40 MHz by the CU2. The digital signal is then transferred directly to the CU2 by a 16-bit parallel bus.

Analogously, the PEM interface, represented by the DAC and its front-end circuits, converts the digital PEM driving signal, distributed through a 16-bit parallel bus from the CU2, to an analog PEM driving voltage. The conversion is ensured by a 16-bit DAC (MAX5885) with a differential output, clocked at 40 MHz by the CU2. The analog signal is then filtered (LT6600) and routed to the pair of high-speed power amplifiers (THS3120) supplied by ±15 V in a push-pull configuration, generating a differential modulation voltage of 54 V_{pp}.

The further part introduces communication circuits, implementing physical layers of the IFOG data interfaces (Ethernet, CAN, RS485) and a differential analog output controlled from CU2 via SPI. The board is also equipped with a hardware reset initiated by a button or through a software function from the CU2 itself. All the interfaces and the power supply are then routed to the I/O 20-pin interface connector (M80, Harwin). Additionally, the board further allows direct programming

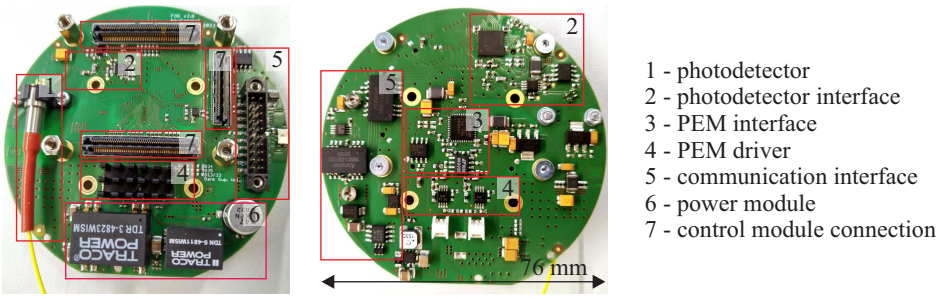


Fig. A.11: Interface unit (IU2) board of the P2 (shown without the CU2) and its major blocks.

mode connection for CU2 program flashing or debugging.

A.3.2 Software design

The CU2 accommodates the Zynq SoC (XC7Z020) and other digital circuits, such as the corresponding peripherals, the communication interface, or the system controller. The Zynq SoC is a core part, implementing all the compensation and processing methods, including the data distribution and configuration. Its functionality is conveniently distributed among the programmable logic (PL) part in the form of the FPGA, and the processing system (PS), represented by the CPU0 and CPU1 cores. The block diagram of the implemented functionality distribution among the individual entities is shown in Fig. A.12. The PL includes the blocks necessary for a fast acquisition of the $I(t)$ signal, S_{OL} signal computing, closed-loop $\Delta\phi_s$ compensation, and generation of the compound modulation signal $u(t) \propto \phi(t)$ for PEM driving, according to Sec. 3.1.2. All these processes are clocked at 40 MHz, except the data transfer to PS, which is clocked at 200 MHz. The PS then implements the compensation methods and the communication functions.

Namely, the CPU0 is responsible for a distribution of the configuration parameters and for streaming the output data, represented by the measured $\Delta\phi_s \propto \Omega$. The CPU0 also performs a control of the actual modulation depth. The correction is implemented as a transfer function $K_{PEM}(\Delta\Phi_c)$, conversing the directly obtained phase shift $\Delta\Phi_c \propto U_c$ to the corrected phase shift. This is performed using a so-called transfer table, containing a history of pairs of estimated values of the compensation modulation depth $\Delta\hat{\Phi}_c$ and the corresponding direct value $\Delta\Phi_c$, which are both obtained simultaneously. Each pair is assigned its reliability weight – a value calculated as a function of several parameters, including LSCFE fit error, modulation components gain and phase errors, stability of acquired $I(k)$ vector, etc. The change in the ambient conditions, and thus $K_{PEM}(\Delta\Phi_c)$, is reflected by the weights decrease over time. Based on the transfer table data, the actual $K_{PEM}(\Delta\Phi_c)$ is determined separately for each measured $\Delta\Phi_c$ value using the transfer function. The transfer function performs a weighted polynomial fit within the region near the current $\Delta\Phi_c$ value. This helps to achieve a high computation rate, even if the $K_{PEM}(\Delta\Phi_c)$ is nonlinear and varying over time.

The major task of CPU1 is an estimation of the $\Delta\hat{\Phi}_c$ values based on $\hat{I}(k)$ computed from the multiple $I(k)$ periods average by the LSCFE method. The CPU1 thus provides the input data for the transfer table. Its second task is then the modulation components gain and phase error computation and compensation through the six separate control functions, as outlined in Sec. 3.1.5. The CPU1 is also responsible for the transfer table management, consisting in weights updating

and replacing the least valuable pair with a new one. Several factors are taken into account to evaluate the pairs, including the density of the pairs in a distinct $\Delta\Phi_c$ region, their proximity to the currently measured $\Delta\Phi_c$, and the mentioned weight decrease with time.

Outlined functionality distribution between the CPUs ensures the processing reliability and the system integrity, as the tasks of the closed-loop data distribution as well as the correction and depth control methods both require an independent and real-time operation, controlled by the data flowing from the PL part.

Two types of communication interfaces can be distinguished, one for the system configuration, the other for the output data distribution. Both are provided

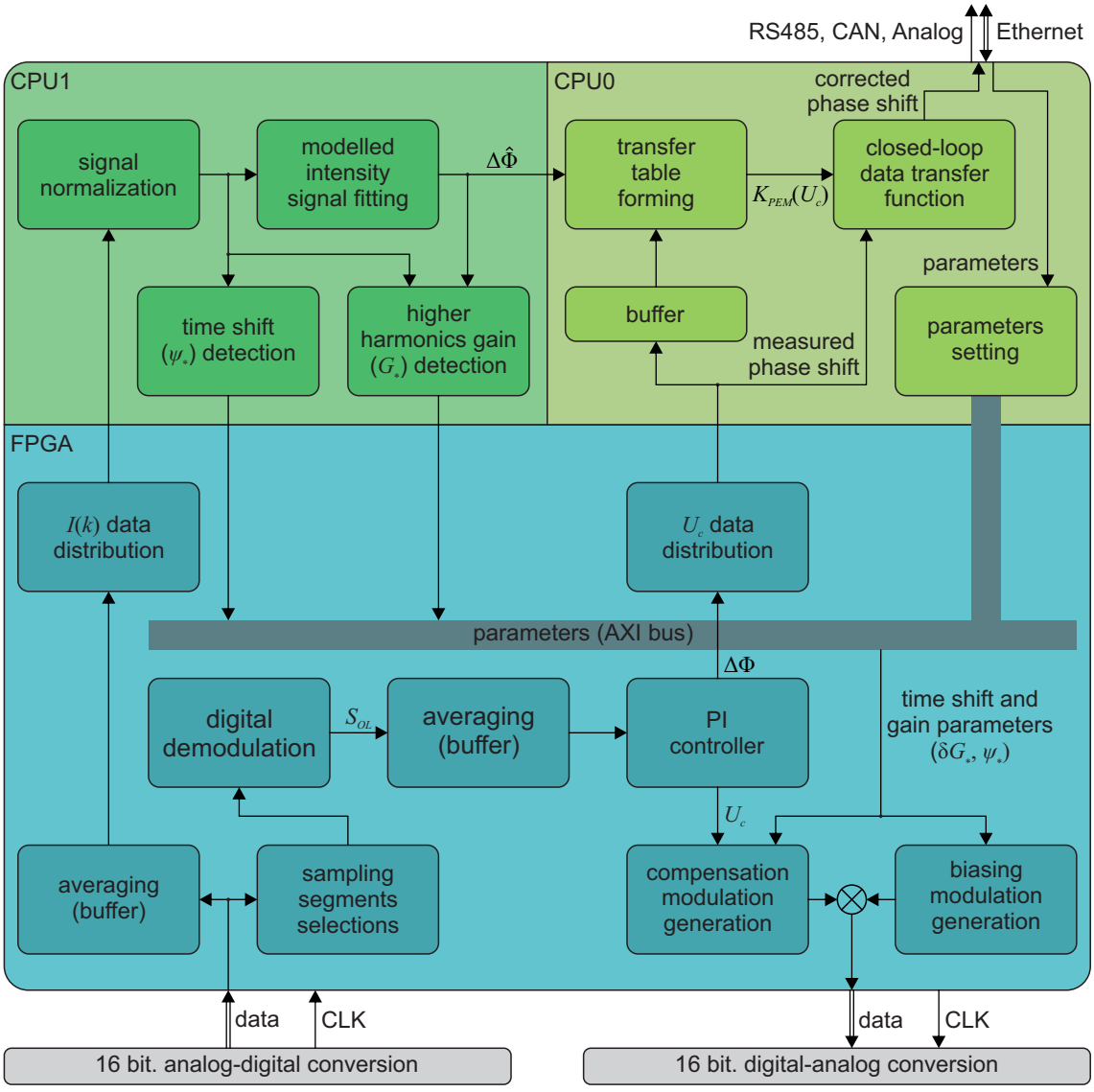


Fig. A.12: Block diagram of the methods implementation and functions distribution within the CU2.

by the CPU0 functionality. The output data distribution is performed as a fixed-rate stream, the rate of which is strictly determined by the rate of close-loop $\Delta\phi_s$ compensation and subsequent decimation within PL and PS. The output data can be distributed via Ethernet, RS485, and CAN, all with optional formats and auxiliary metadata, or via a differential analog interface. These data thus represent the IFOG sensor output, providing angular velocity data to the superior navigation system during the normal operation. On the other hand, the configuration interface is purposed for the initial setting of the parameters, their tuning and optimization for the specific task, which allows full control over multiple parameters of the PL and PS implemented functions, not only related to the described methods, but also to the output data communication protocols. The configuration is possible via the Ethernet interface. For this purpose, a LabVIEW PC application was developed, enabling data visualization and parameters settings in real time. The control panel of the application can be seen in Fig. A.13. On the left side, there are settings related to the modulation signal generation, the output signal acquisition and the closed-loop $\Delta\phi_s$ compensation, and angular velocity measurements. The middle part serves to display the vector data, such as the measured and modeled signals, transfer table with the transfer function and the time course of the direct and corrected $\Delta\Phi_c$ value. The right-hand part contains settings for the modulations gain and the phase error compensation, the model-based output signal fitting, the transfer table management settings, and the weighting and transfer function settings. The interface thus allows monitoring of a proper functionality of all of the implemented methods with given settings, and also the data rates control among individual functions and their adjustment to assure a reliable and real-time data distribution and integrity.

A.4 Supplementary measurement results

A.4.1 Laboratory testing

The IFOG P2 was subjected to laboratory as well as practical testing to evaluate its key parameters and overall performance. The laboratory tests were performed with the precise rotation table (RMS SDL1401). The temperature stability of the operating environment during specific tests was ensured by a temperature chamber (CTS T-60-50). The IFOG output data were transferred through the table slip-ring connection via the Ethernet interface to the PC. The tests performed include the bias and the scale factor measurement and the stability analysis.

The scale factor gives a proportion between the set angular velocity and the IFOG output, in terms of the compensation modulation depth. The scale factor measurement was performed for the reference angular velocities ranging from -300

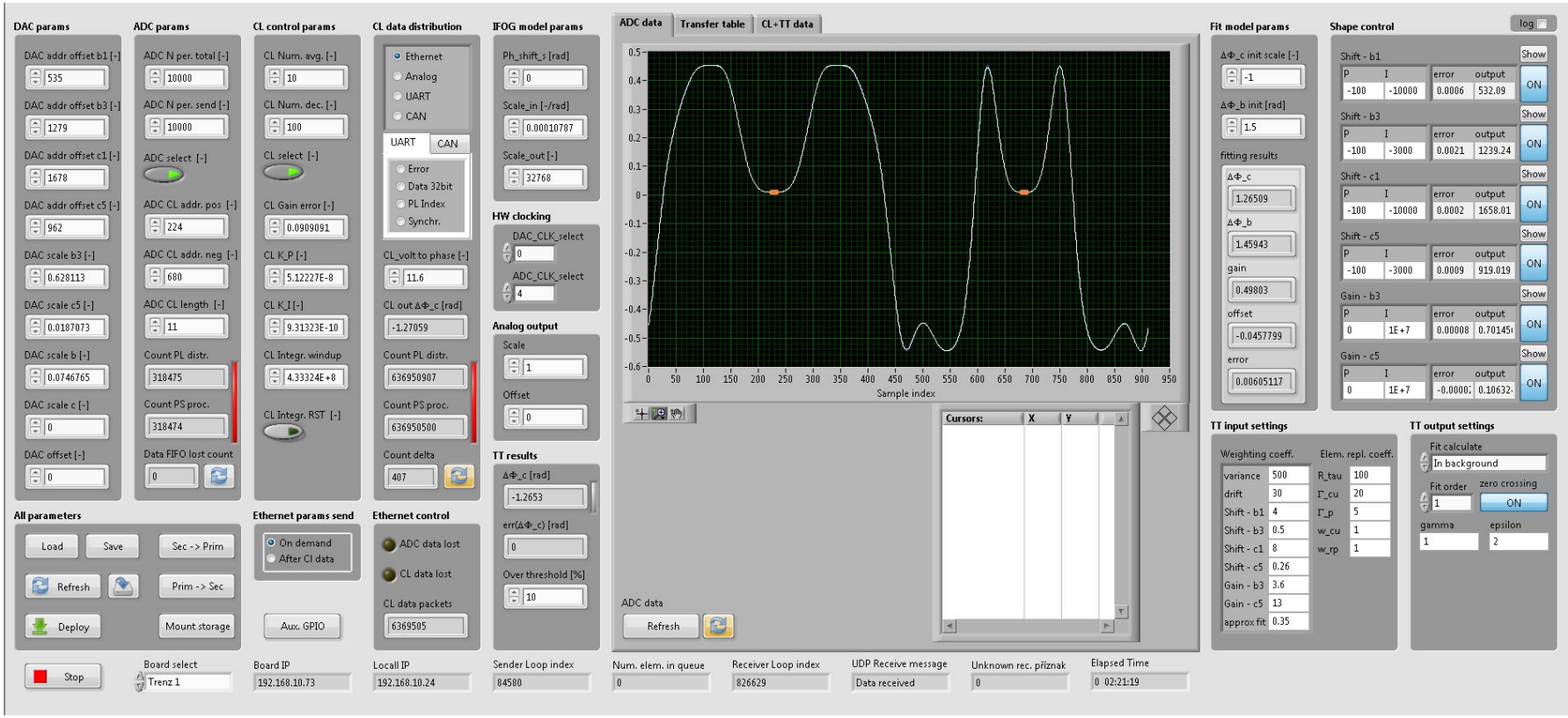
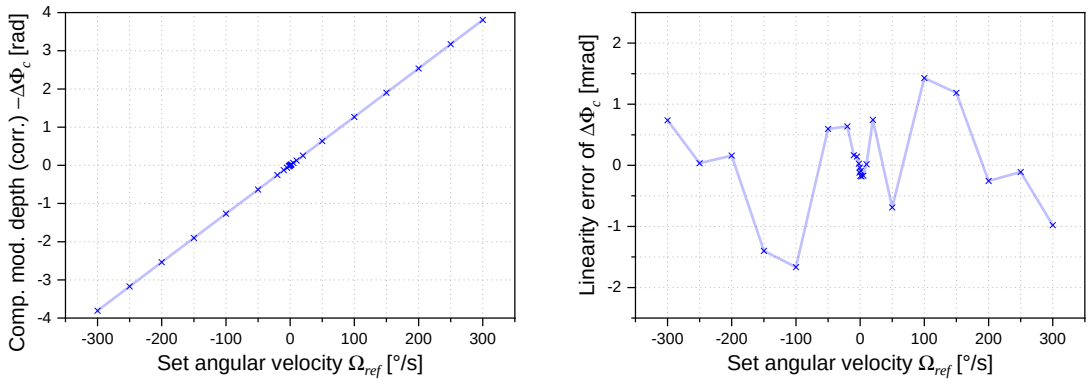
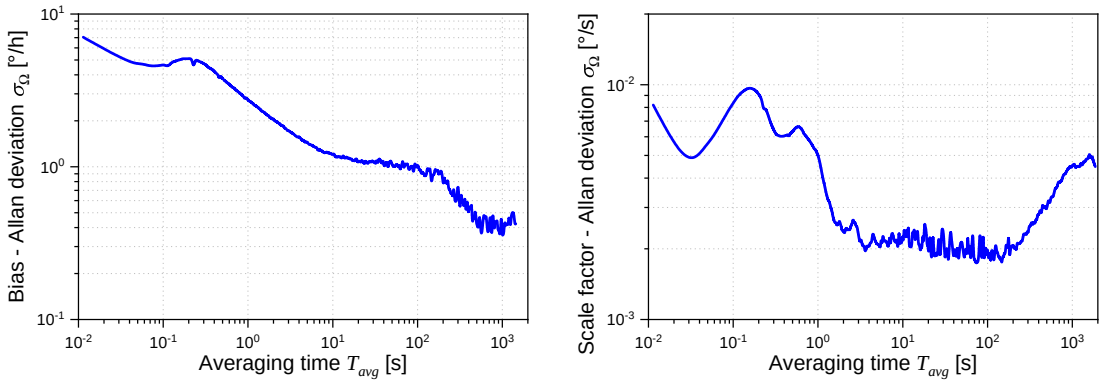


Fig. A.13: A PC application for the P2 IFOG software parameters configuration.



(a) (b)

Fig. A.14: Laboratory verification of the IFOG P2 parameters – scale factor (a) and corresponding linearity error (b).



(a) (b)

Fig. A.15: Laboratory verification of the IFOG P2 parameters – stability of the bias (a) and the scale factor (b).

to +300 °/s. At each angular velocity, the output data were logged for 1000 s. The acquired phase shift with the angular rate is shown in Fig. A.14, including the linearity error. The scale factor SF was determined as a slope of the measured dependency.

The bias measurement was performed at rest, under the effect of vertical Earth angular velocity, equal to $\Omega_{Earth} = 0.00311784$ °/s (11.224224 °/h; location Brno - Královo Pole, Czech Republic: 49° 13' 25" N, 16° 35' 40" E). The measurement of the scale-factor stability was performed at a stable reference angular velocity $\Omega_{ref} = 100$ °/s. The temperature was maintained stable at 25 °C by the temperature chamber. In both cases, the acquired IFOG output data were processed with the Allan variance method, according to [177]. The value of the sensor bias B was

calculated based on the average sensor's output value $\Delta\Phi_c(\Omega_{Earth})$ as follows:

$$B = \frac{\Phi_c(\Omega_{Earth})}{SF} - \Omega_{Earth}. \tag{A.3}$$

Based on the measured data, the bias value was calculated to be $B = 1.71145486\,°/\mathrm{h}$, which is by about one order lower than the Earth's angular rotation rate. The Allan deviation of the measured bias and the scale factor is shown in Fig. A.15.

The key parameters obtained from the measured data are summarized in Tab. A.3.

Tab. A.3: IFOG P2 key measurement parameters.

Parameter	Measured value	Unit
Maximal angular velocity range	±720	°/s
Scale factor	−0.0127	rad · s/°
Bias	1.711	°/h
Bias stability	0.4	°/h
Angle random walk	0.046	$°/\sqrt{\mathrm{h}}$
Scale-factor stability (at 100 °/s)	20	ppm

A.4.2 Practical testing

Alongside the laboratory tests, the IFOG P2 was also tested as an inertial angular rate sensor in a vehicle. For this purpose, an inertial sensor testbench was developed, schematically shown in Fig. A.16. The testbench comprises a commercial high-performance inertial measurement unit (Inertial Labs INS-D), combining a Honeywell HG4930 MEMS IMU with GNSS, to compare the IFOG data to the reference provided by this unit. With the GNSS module, it was also possible to determine the absolute vehicle position. The data from the INS-D IMU were used

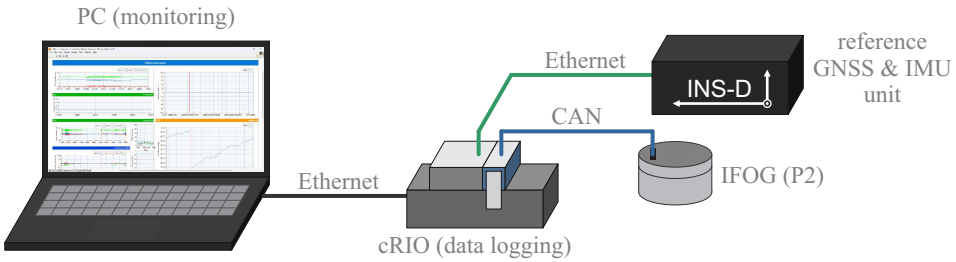


Fig. A.16: Layout of the testbench for a practical verification of the IFOG P2 performance installed in a car.

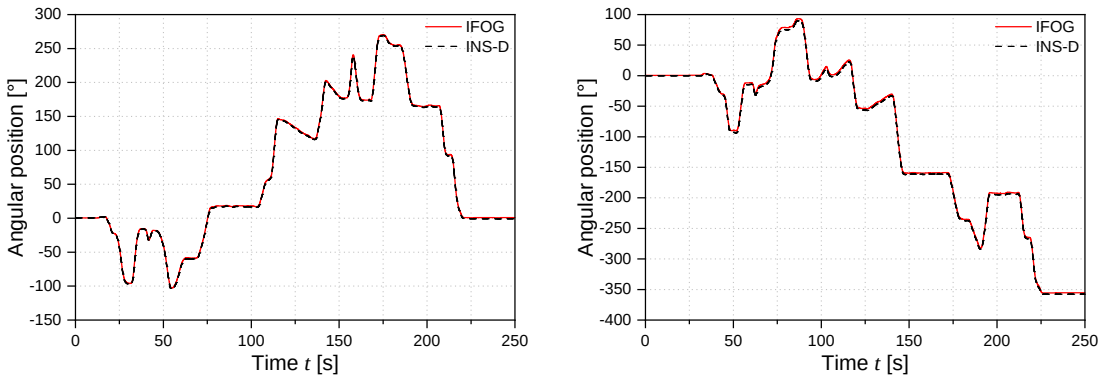


Fig. A.17: Comparison of the integrated angular position for the reference drive in CW (a) and CCW (b) direction.

to compare and assess the performance of the IFOG against the tactical-grade commercial MEMS gyroscope. The data from both sensing units were acquired by the CompactRIO (NI) platform, connected to the PC for real-time data monitoring. The IFOG was connected solely through the CAN interface, emulating a real car implementation.

The data acquired during the reference drive were then post-processed in LabVIEW. By the integration of the measured angular velocity, it was possible to calculate the angular position, shown in Fig. A.17 for both IFOG and INS-D sensors. Of interest were not only the overall courses of the calculated angular position but also the difference between the starting and ending position. After the correction for the Earth's rotation, the difference between the initial and the final angle was for both CW and CCW drive under 2°, which is below a considered error of reaching the original vehicle parking position.

Furhter, the angular rate data were combined with the GNSS to estimate the trajectory of the reference drive as well. The distance traveled in a straight direction was calculated by an integration of the GNSS velocity. The distance was then combined with the angular rate data to obtain the trajectory. These trajectories, computed with the angular velocity measured by the IFOG and INS-D sensors, are compared in Fig. A.18. For the overall assessment, the trajectory data obtained purely by the GNSS-referenced INS-D are also included.

A.4.3 Additional results

During the P2 development, the individual components were also tested extensively to define their ground limitations for the overall IFOG performance. Herein, the

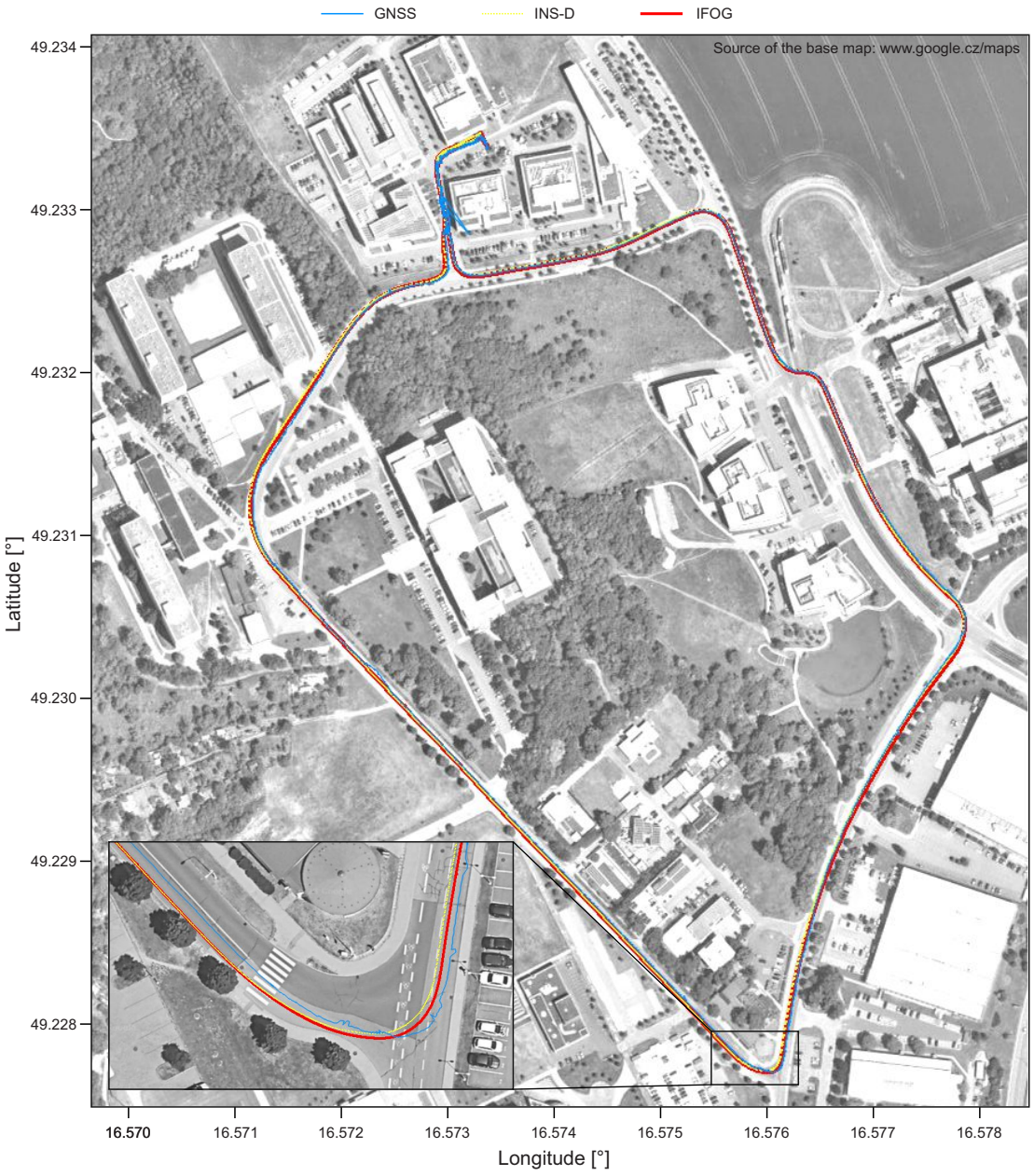


Fig. A.18: Comparison of the measured trajectories for the reference drive in CCW direction.

results for the sensing coil and the light source were picked, as the key components affecting the stability of sensing parameters.

Among other influences, the IFOG bias stability is affected by the light source. Therefore, its effect on the total detected noise and an equivalent angular velocity was measured and computed. A stability performance expressed in terms of Allan deviation of the SFS designed and developed for the P2 was compared to another SFS of similar arrangement with higher pump power, and to a narrow-line LD source

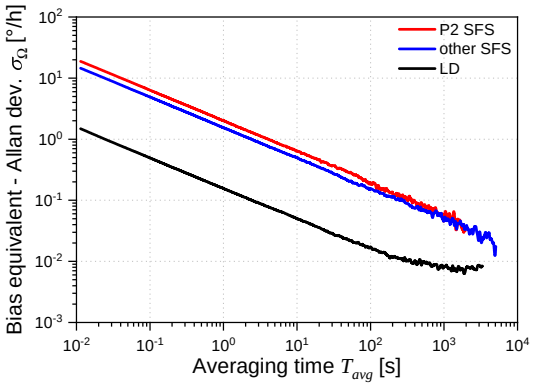


Fig. A.19: An examination of the bias stability limitation posed by various light sources usage within the IFOG P2.

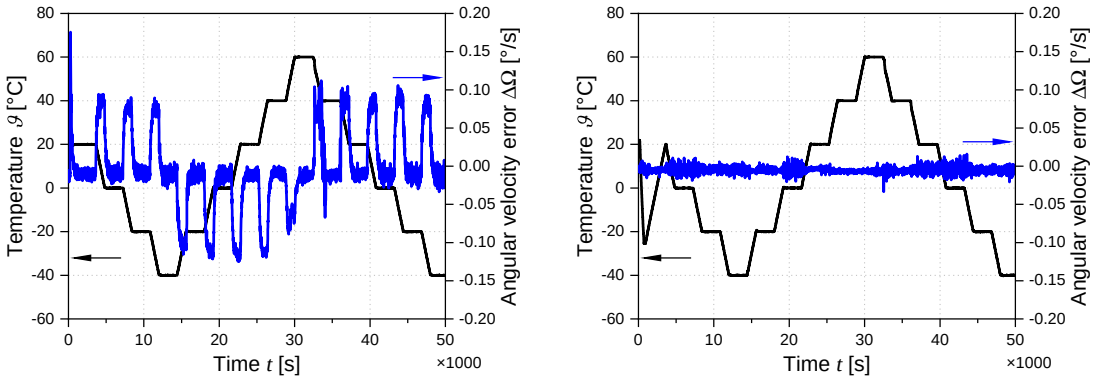


Fig. A.20: An examination of the Shupe effect on the angular velocity error at rest induced by temperature sweep with a singlepole (a) and a quadrupole (b) windings.

with 1550 nm. All the sources were adjusted in their power to an equal level by inserting attenuation components. The results in Fig. A.19 clearly show that the fundamental bias stability limitation of the P2 IFOG is caused in great part by the light source. Namely, the broader the spectrum is, the worse angle random walk is reached, as implied by its inherent physical nature. Nevertheless, despite larger noise, the broadband source brings other undoubtful benefits in some errors' compensation and depolarization, as discussed in Sec. 3.2.1.

Secondly, a sensing coil was studied to test the different fiber winding types and their susceptibility to the Shupe effect induced by the temperature sweep. An angular velocity error $\Delta\Omega$ measured at the Earth rotation rate for a singlepole and a quadrupole coil winding is shown in Fig. A.20 for a rising and a falling staircase temperature profile. Except for the winding method, all other parameters of both

coils were identical. It can be clearly seen from the results that the quadruple winding greatly reduces the temperature-induced Shupe effect and is thus necessary for reliable angular velocity sensing. Note that the residual noise for the quadrupole winding in the $\Delta\Omega$ is due to the mechanical vibrations caused by the temperature chamber.

B Supplementary materials on the closed-loop DBMZI setup

The following materials expand the DBMZI implementation and the test setup description provided in Sec. 4.2 and add further details regarding its optical setup as well as the electronic and control setup. Finally, the additional measurement results are also presented.

As mentioned earlier, the DBMZI setup was modified during its development by replacing some of the optical and the electronic components, their optimization or placement adjustments, to achieve a better performance or facilitate a measurement of a broader range of sample types. The latest DBMZI layout is shown in Fig. B.1. The optical components were placed as tight as possible to reduce the overall setup dimensions. Including the laser, the total dimensions of the optical part are summarized in Tab. B.1. The maximum dimensions of the scanned samples are given by the sample translation stage range, providing a travel of up to 25 mm in each axis, and the L2 lens travel range, allowing the sample thickness up to 25 mm as well.

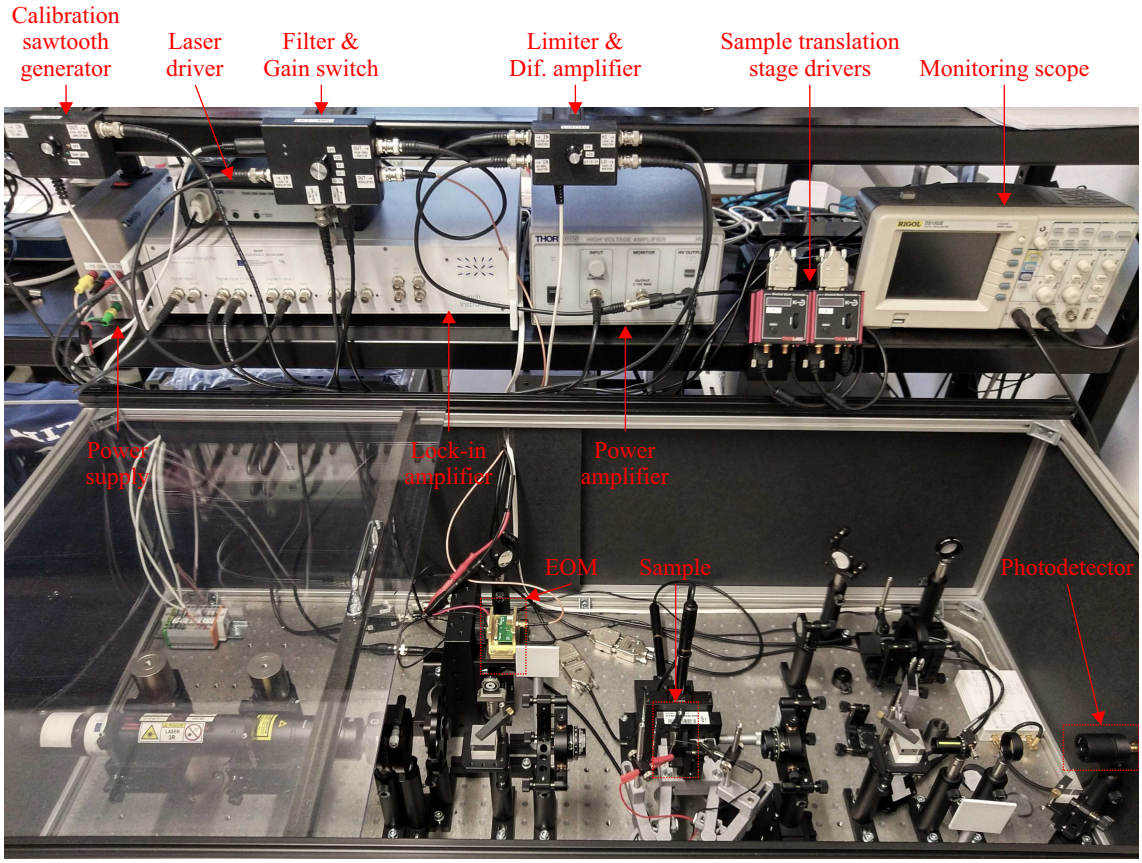


Fig. B.1: An overall DBMZI setup layout.

Tab. B.1: Overall DBMZI optical setup dimensions.

Parameter	
length [cm]	120
width [cm]	55
height [cm]	30
M1 – M2 path [cm]	44.5
M1 – M3 path [cm]	45.5
laser – PBS1 path [cm]	13.2
PBS2 – detector path [cm]	22.0

B.1 Optical setup development

The optical components employed in the displayed DBMZI setup are listed in Tab. B.2. A detailed view of the optical setup (schematically shown in Fig. 4.4) and its components layout is shown in Fig. B.2. Most of the components represent COTS optical elements and accessories. Nevertheless, some of them are partially or fully custom-made, i.e., created specifically for the given purpose. Special attention was paid to the sample clamping and the probing beam focusing.

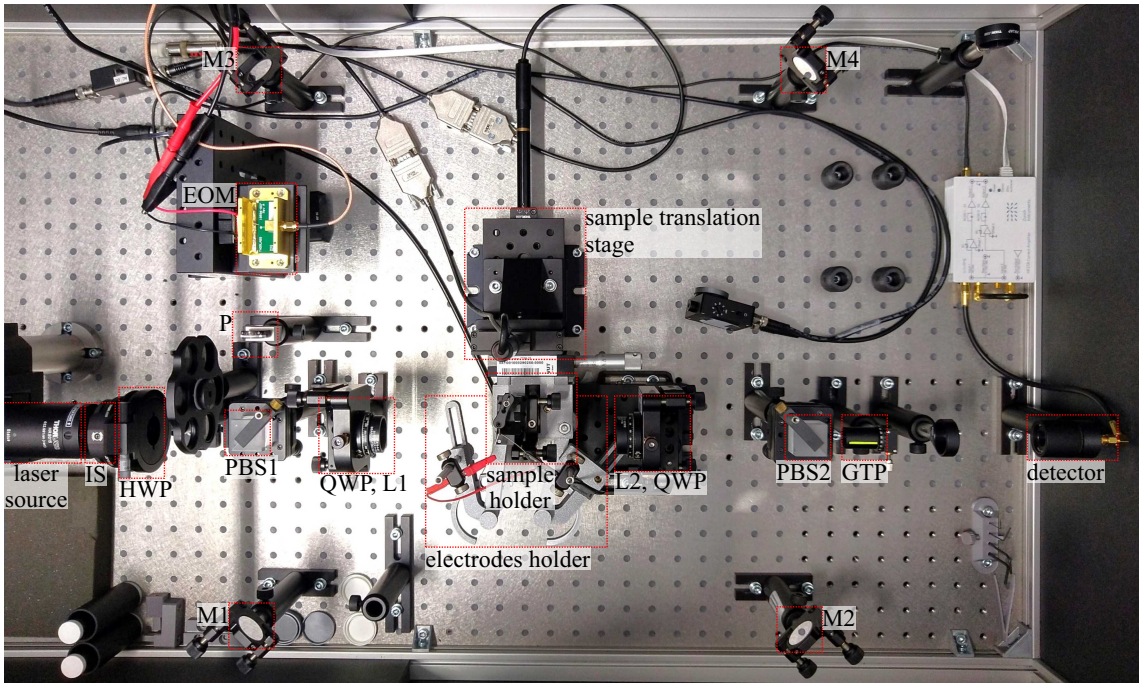


Fig. B.2: DBMZI optical components layout.

Tab. B.2: List of the DBMZI optical components and their key parameters.

Component	Type	Key parameters
laser source	Thorlabs HRS015	633 nm, 1.2 mW, stab., single pol.
laser mount	Thorlabs C1503/M + P200/M + PB2/M	–
isolator	OFR 2A100 + Thorlabs PRM1/M	633 nm
half-wave plate	Thorlabs WPH05M-633	zero-order, 633 nm
quarter-wave plate	Thorlabs WPQ05M-633	zero-order, 633 nm
polarization beam splitters	Thorlabs PBS251	420–680 nm
pol. beam splitters mounts	Thorlabs PBS251 + KM100B/M	adjustable, 2-axis
lenses	Thorlabs LB1676-A-ML / LBF254-040-A / LB1157-A	biconvex, $f = 100$ / 40 / 10 mm
lens mounts	Thorlabs K6XS	adjustable, 6-axis
mirrors	Thorlabs BB03-E02	400–750 nm
mirror mounts	Thorlabs KM100	adjustable, 2-axis
polarizer	Thorlabs PCB-2.5-VIS	ext. ratio 10,000:1, 440–650 nm
Glan-Thompson polarizer	Thorlabs GTH5M + PRM05/M	ext. ratio: 100,000:1, 350–700 nm
EOM	Thorlabs EO-PM-NR-C1	$U_\pi = 135$ V (633 nm), 600–900 nm
photodetector	Thorlabs PDA36A-EC / SM05PD3A	Si, 350–1100 nm, $f_{BW} = 10$ / 23 MHz, switchable / fixed gain
sample translation stage	Thorlabs PT1/M-Z8	range 25 mm, res. ≈ 29 nm
translation stage driver	Thorlabs KDC101	–
sample holder	Thorlabs KS1SC / KM100CL / KM200V/M / VC1/M / custom-made	–
sample electrodes holder	custom-made	adjustable, 2×5-axis

B.1.1 Sample clamping

In the case of the inverse piezoelectric effect measurement, it is assumed that the sample movement is not dampened by any external force. This also concerns the force caused by the sample clamping. In the case of thin layer samples, the piezoelectric film is firmly fixed to the substrate. The substrate is then clamped by the sample holder. The bulk samples, on the other hand, are clamped directly by the sample holder. In both cases, the clamping must be designed carefully so that the measured displacement is not affected by the clamping forces. If the clamping force is too low, there is a risk of a parasitic sample movement, such as tilt, which may also lead to a shift of its central position, leading to a decrease or complete loss of the detected optical signal power. On the other hand, in the case of the tight sample clamping, the induced force may decrease the induced displacement oscillations or, in special cases, lead to the resonance frequencies shift and the vibration profile distortion. Therefore, the clamping should be designed so that the induced forces are distributed symmetrically, and the clamping force should be adjusted for the specific case, according to the studied sample properties.

The Fig. B.3 demonstrates the d_{33} coefficient measurement of a calibration rectangular quartz x-cut sample clamped with a different force. In both cases, the measurement was performed at the same point for frequencies of up to 1 MHz. Whereas there is no observable shift of the resonance frequencies with the clamping force, as shown in the Fig. B.3(a), a detailed view of the first resonance in the Fig. B.3(b) demonstrates the effect of sample oscillation damping when the clamping force is increased.

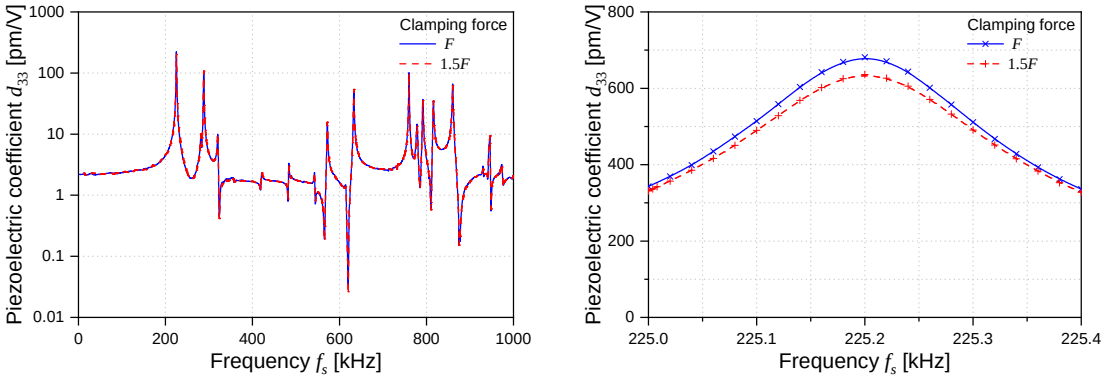


Fig. B.3: The frequency spectrum of the d_{33} coefficient at different clamping forces within the 1 MHz range (a), and a detail near the first resonance frequency (b) (measured at sample center, quartz x-cut, $10 \times 11 \times 1$ mm, $U_s \in \langle 0.01; 0.5 \rangle$ V).

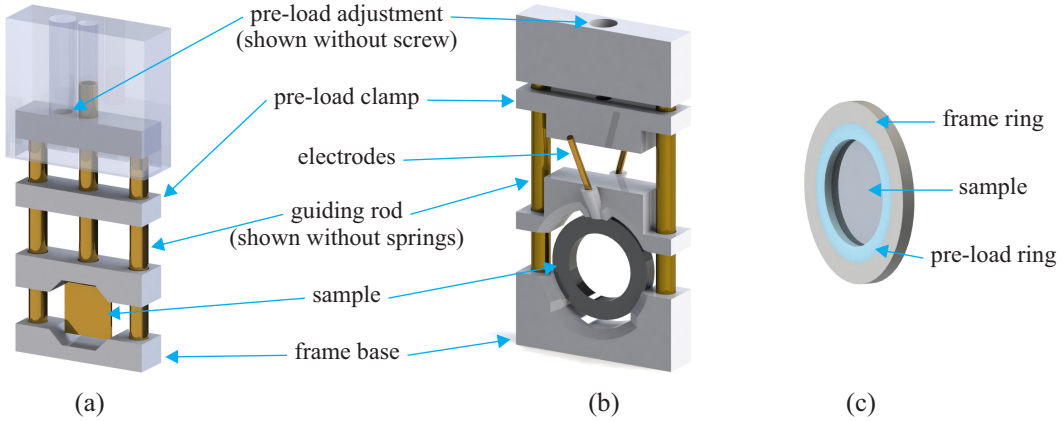


Fig. B.4: Examples of custom-made sample holders with optimized clamping: (a) variable-size square/rectangular sample holder with 4-point force distribution and adjustable clamping force, (b) variable-size disc/ring sample holder with 3-point force distribution and adjustable clamping force, (c) fixed-size disc/ring sample holder with uniform force distribution and fixed clamping force.

For the purpose of the experimental verification and measurements, various types of sample holders have been designed for specific samples' requirements, with some examples shown in Fig. B.4. All of the custom-made sample holders are then attached to the standard kinematic mount, allowing for a small angular adjustment. The sample holders were manufactured by 3D printing using regular PLA and resin (pre-load rings).

B.1.2 Probing beam focusing

Another crucial part of the optical setup is the proper focusing of the probing beam. Unlike the previously published reports, the measurement of the bulk samples was performed without any additional reflective coating. Instead, the surface of the bulk samples was polished by hand using a fine abrasive foil. This technique is simple and increases the reflectivity to a sufficient level. However, the residual surface roughness and scratches lead to relatively high speckle noise in the resulting interference signal behind the GTP. A demonstration of the speckle noise effect can be seen in Fig. B.5, where it results in the parasitic peaks. The speckle leads to a decrease of the interference visibility and also the signal fading during the sample vibrations spatial scanning. Furthermore, the speckle may vary in correlation with the measured displacement changes, which may introduce a significant error in the measured displacement. The optical system was thus designed as modular to mitigate this phenomenon, depending on the sample shape and the surfaces'

properties.

Firstly, three sets of lenses can be installed with different focal lengths of 10, 40, and 100 mm. The shorter the focal length, the lower the depth of field and the susceptibility to the speckle.

Secondly, placing a pinhole of various sizes after the GTP is a commonly adopted technique to shade out large portions of the parasitic speckle. However, such technique also has the limitations of significant fading of the detected signal for some poorly reflective surfaces, making the detection impossible. An example of poorly reflective sample measurement is shown in Fig. B.6, where using a pinhole increases the noise ($\sigma(\Delta d) = 40.2$ pm) compared to the case without a pinhole ($\sigma(\Delta d) = 16.5$ pm) in front of the detector.

Thirdly, if the speckle supressing is difficult, a probing beam defocusing technique

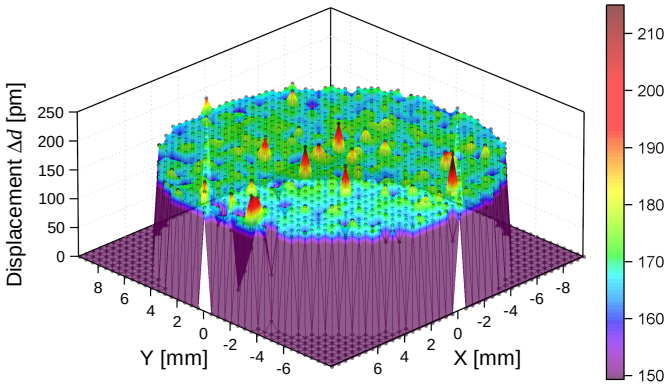


Fig. B.5: Demonstration of the speckle noise effect on the resulting output data (PZT disc sample, 20 mm diameter, measured at $f_s = 20$ kHz).

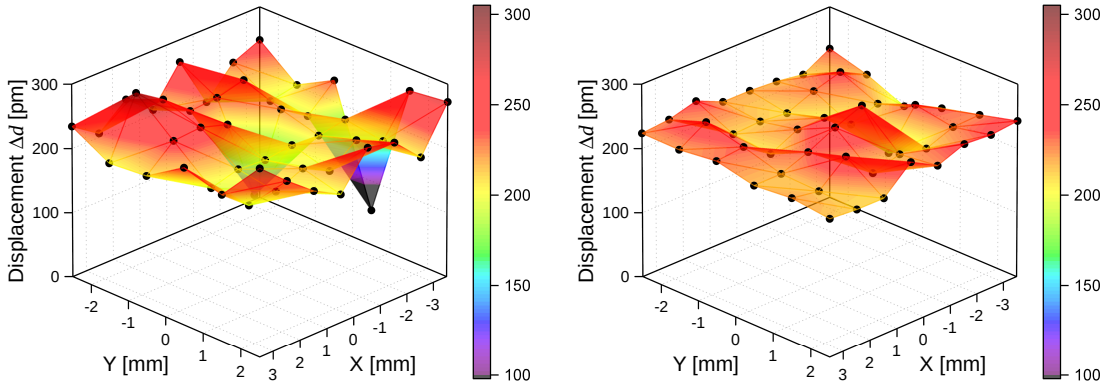


Fig. B.6: Demonstration of measurement with (a) and without (b) using a pinhole in case of a poorly reflective sample producing high speckle noise (PZT NCE40 disc sample, 20 mm diameter, measured at $f_s = 1$ kHz).

may be used. This allows L1 to capture the light from the blured speckle, which is then re-focused by L2 to the opposite sample side. Naturally, the defocusing leads to a reduction of the spatial resolution during scanning. Note that speckle can also be eliminated by the unlensed system; however, as discussed in Sec. 4.2.1, the parasitic sensitivity to the sample deflection during measurement is dramatically increased.

To summarize, each focusing technique may be beneficial for scanning the samples with imperfect surfaces, and should be selected or combined with another technique based on the specific surface roughness and reflectivity. The goal is thus to find a tradeoff between acceptable interference visibility and balanced SNR along the entire scanned area of the sample surface.

B.2 Electronics and control software development

B.2.1 Hardware design

The major components composing the electronic part of the DBMZI setup (schematically shown in Fig. 4.5) are listed in Tab. B.3.

Tab. B.3: List of the DBMZI electronic components.

Component	Type
lock-in amplifier	Zurich Instruments HF2LI
power amplifier	Thorlabs HVA200
filter & gain switch	custom-made
limiter & differential amplifier	custom-made
calibration sawtooth generator	custom-made

As discussed above, the lock-in amplifier is responsible especially for the generation of the EOM and the sample driving signals, and for the intensity signal demodulation and separation of the corresponding components. The analog preprocessing of the EOM driving signal is performed by the custom-made block of the Filter & Gain switch, the functional block diagram of which is shown in Fig. B.7. This block allows either a direct routing of the driving signal from the lock-in amplifier through the power amplifier (with a fixed factor of $\times 20$), or a separation of the low-frequency components $u_{stab} + u_m(t)$ and the high-frequency component $u_c(t)$ with the optional attenuation. The first option is purposed for a coarse resolution detection, with a possibility to set also $\omega_s < \omega_m$. In this case, the driving signal is amplified in the entire frequency range. The resulting signal is directed to the first electrode of the EOM, while the other is connected to ground. The second

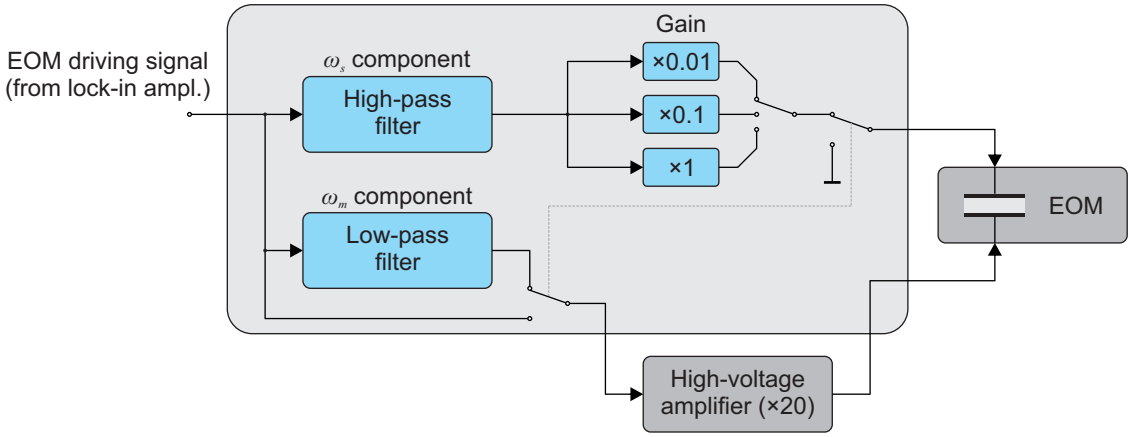


Fig. B.7: Schematic of the Filter & Gain switch module.

option splits the signal from the lock-in amplifier by the low-pass ($f_{cutoff} = 80$ Hz, 4th order, Butterworth, AD8671) and the high-pass ($f_{cutoff} = 300$ Hz, 4th order, Butterworth, AD548) filter into two bands, comprising the $u_{stab} + u_m(t)$ and the $u_c(t)$ components, respectively. Therefore, the modulation frequencies ω_m and ω_s must be set according to the corresponding limits. On the other hand, this solution allows the compensation component $u_c(t)$ to remain unamplified, and it can be further attenuated by a factor of up to 100. Consequently, a much finer resolution in the compensation modulation depth control can be reached, with a corresponding narrowing of the compensation range. The low-frequency and high-frequency paths are then summed together by driving a separate electrode of the EOM. For this purpose, the EOM case must be shielded from the ground.

The second of the custom-made analog processing blocks is the Limiter & Differential amplifier. Its purpose is mainly an exact detection of the actual magnitude of the compensation modulation component $u_c(t)$ and protection of the lock-in amplifier inputs. According to the selected measurement range (×20, ×1, ×0.1, ×0.01), it monitors the corresponding voltage level and transforms it into a differential signal through a limiting amplifier (OPA698).

The electronic setup also includes a calibration sawtooth generator, as an auxiliary module, to generate a $\pm\pi$ phase sweep to observe the interference visibility. This is particularly useful for the fine optical setup adjustments, to align the reference and the probing beam properly. During this process, this module is connected through the high-voltage amplifier to the EOM instead of the driving signal from the lock-in amplifier.

B.2.2 Software design

The DBMZI measurement process is controlled by the LabVIEW application, which runs on a PC. The application is based on the queued message handler architecture, with several parallel processes controlling distinct tasks. The processes are schematically shown in Fig. B.8. The overall measurement control is ensured by the Main control process, which collects the major data and manages the other processes. The Data processing block handles the majority of operations with the raw data, such as filtering or checking the data validity. The User interface involves two sub-processes, one for live data display, and the other one for user action handling. The following processes are responsible for the hardware components control, including the lock-in amplifier, the sample translation stage, and the laser. The Lock-in amplifier control serves not only for the device settings, but also for receiving the measured data in both on-demand (parameters) and polling (data stream) modes.

The front panel of the control application is shown in Fig. B.9. It features an option for a single measurement fully controlled by the operator, as well as a repeated measurement in a defined cycle. The repeated measurement can be performed in the form of frequency sweep, position sweep, or their combination by arbitrary measurement points setting. With the position sweep option, various patterns of scanning are implemented. During the repeated measurement, a probing of each point is performed by averaging a selected number of successive measurements for the cancelation of residual noise in the closed-loop data. Furthermore, a data validity control algorithm is used to check several conditions before the measurement at each point is completed. Firstly, these conditions include residual closed-loop error

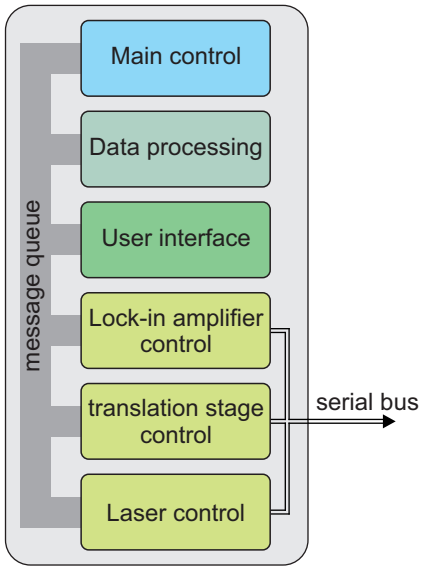


Fig. B.8: Block diagram of the processes in the DBMZI control application.

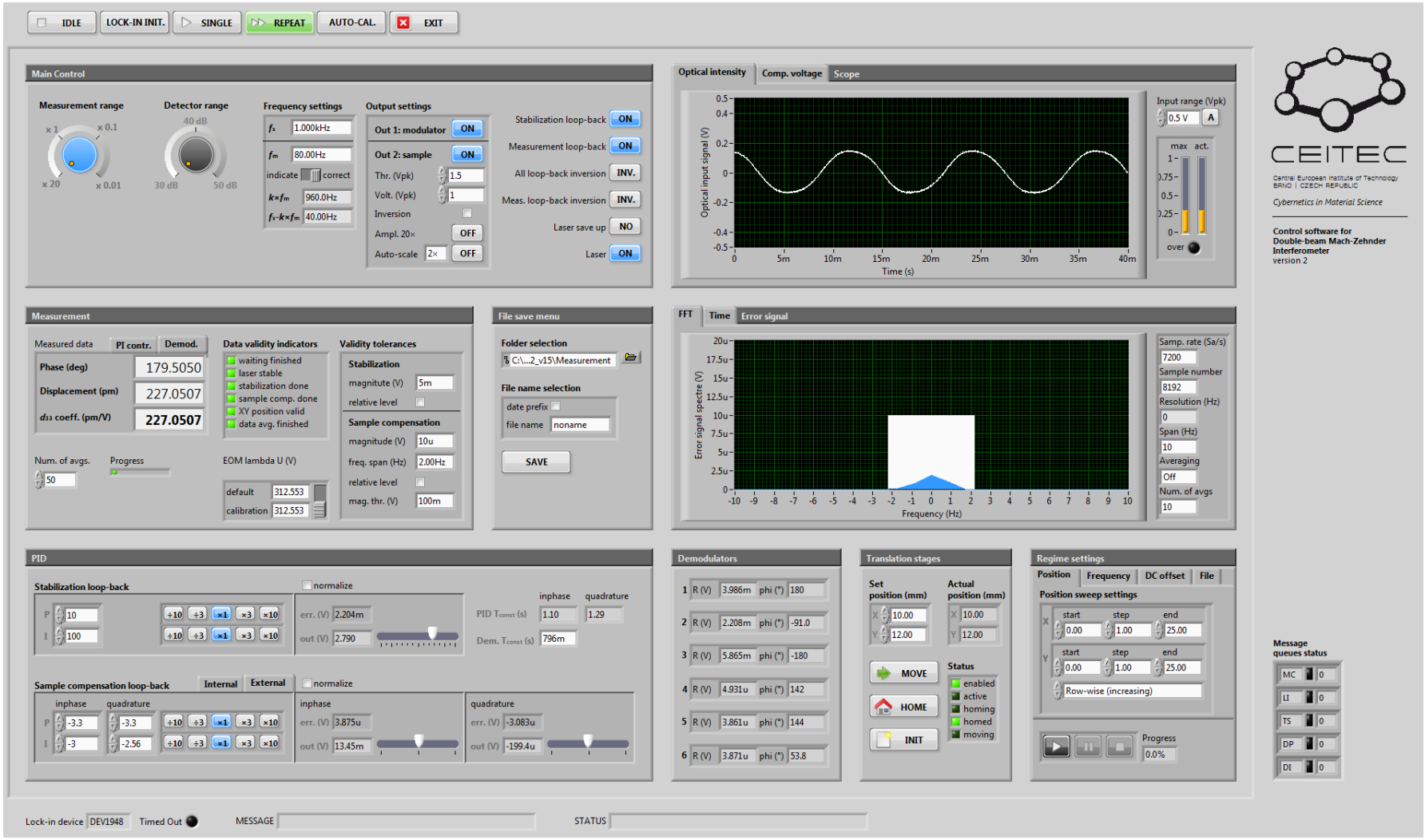


Fig. B.9: A PC application for the DBMZI measurement control.

check. Both quadrature point stabilization as well as sample vibrations compensation closed-loop errors must drop below the desired threshold for the measurement time interval, meaning the measurement is performed during both stationary and stable conditions. The threshold level can also be normalized to an overall intensity signal level. Secondly, the laser status is checked by detection of the overall $\Delta\phi_{stab}$ drift and the quadrature point switching. Temporary laser destabilization may emerge, e.g., with temperature change, and may corrupt the measurement. Thirdly, some of the measurement parameters can change automatically during the measurement, and a settling time is necessary after each change.

The parameters which can automatically change during the repeated measurement depend on the measurement type. With the frequency sweep, the sample displacement near the resonance frequencies may increase by several orders of magnitude, and thus an automatic decrease of the driving voltage U_s is required to avoid exceeding the selected measurement range. In the case of the position sweep, on the other hand, the total reflectivity may vary along the sample surface, leading to fluctuation of the I_i component. The input signal range is thus automatically adjusted for the optimal signal use, and the detected error components are normalized accordingly to maintain the dynamics of the PI controllers.

Next to the discussed features, the application provides a full manual control of all necessary parameters for the closed-loop measurement and stabilization, the demodulators, data filtering, and the sample translation stage control. Among the other functions, it is also possible to mention an automatic control of ω_m to avoid the coincidence of its harmonics with ω_s, or the auto-calibration function, implementing the modulation gain detection, described in Sec. 4.1.3.

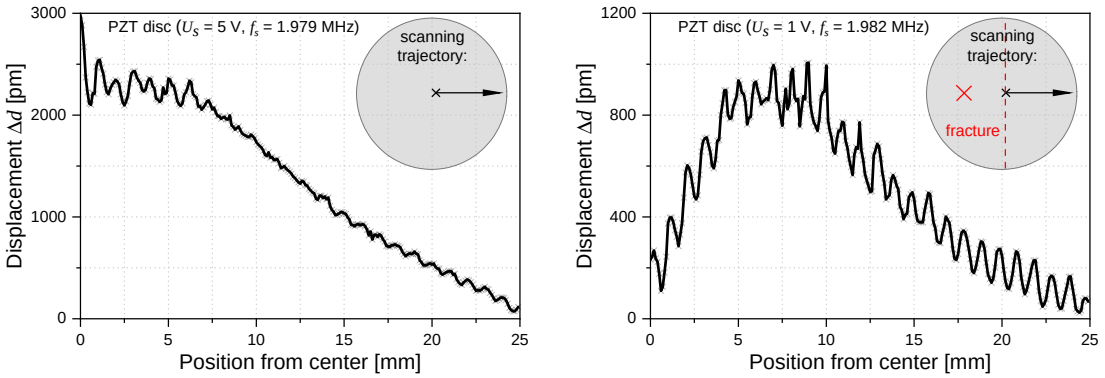
B.3 Supplementary measurement results

Along with the demonstration of the key advantages of the proposed closed-loop stabilization and measurement methods, presented in Sec. 4.3, the developed DBMZI setup was extensively used to study the behavior and properties of various types of piezoelectric samples. Next to the traditionally measured parameters, represented by the material piezoelectric coefficients, the scanning capability facilitated by the sample vibrations closed-loop compensation method brought possibilities of novel and more complex studies, such as analysis of resonance profiles of defects.

In the following section, additional measurement results performed with real samples are provided, demonstrating some of the DBMZI system capabilities enabled by surface vibrations scanning. The first measurement in Fig. B.10 shows the effect of the PZT disc fracture on the thickness vibrations profile at the second (thickness) resonant frequency. This measurement not only confirms that the resonance vibra-

tions profile is strongly related to the sample shape and the corresponding transverse vibrations propagation, but also shows that the defects can be clearly diagnosed, with the possibility of further analysis, e.g., from the distance between the peaks of the vibrations profile ripple or their peak-to-peak value, related to the geometric and material sample properties.

Similar kinds of diagnostics can also be used to detect local disturbances in the sample piezoelectric properties, such as local depolarization or defects in electrodes' deposition. An example of such measurement can be shown in Fig. B.11, where an apparent decrease of the thickness displacement was observed at the edge of the PZT disc. A careful visual inspection revealed that this artifact was caused by the wear of the silver electrode, which led to a loss of electrical contact. Similar artifacts may



(a) (b)

Fig. B.10: Scanning of the PZT disc thickness displacement profile in a radial direction in the original state (a) and after a break along the longitudinal axis (b) (NCE51 material, 50 mm diameter, 1 mm thickness).

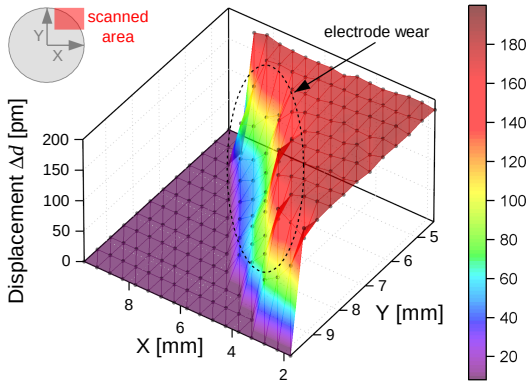
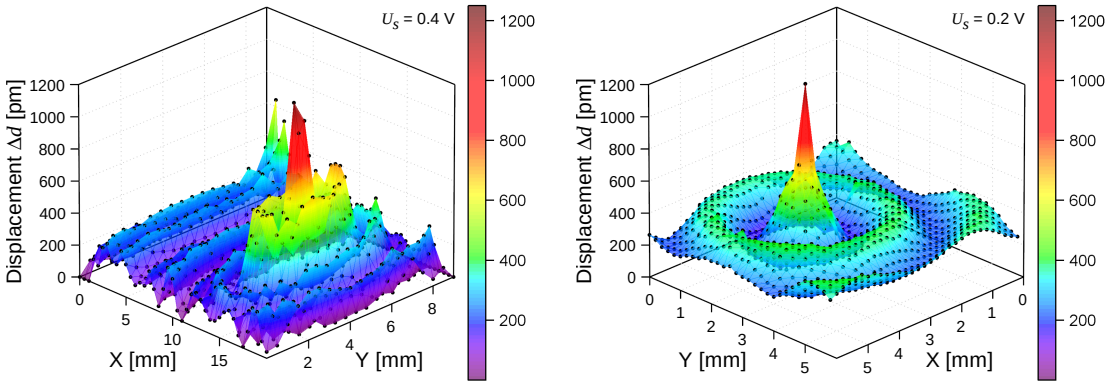


Fig. B.11: Scanning of the PZT disc edge with an electrode wear, resulting in a thickness displacement fading (20 mm diameter, measured at $f_s = 20$ kHz, $U_s = 0.5$ V).

arise not only from a sample wear or damage, but also from an imperfect electrode deposition during the manufacturing process, resulting in uneven piezoelectric properties during its polarization process. Therefore, the vibration scanning is valuable for similar types of diagnostics.

Another type of analysis may focus on determining the piezoelectric matrix coefficient of a given material, requiring a study of the resonant modes vibrations profile of the samples with particular shapes and dimensions. An example of the PZT disc thickness vibrations profile can be seen in Fig. B.12. The measurement in Fig. B.12(a) was performed as a single-side scanning (SBMI configuration), showing an inaccurate profile shape. The double-side (DBMZI configuration) measurement in Fig. B.12(b) then demonstrates a fully symmetrical profile of the disc resonance



(a) (b)

Fig. B.12: Scanning of the PZT disc thickness displacement profile near the center: (a) in a wide area near the thickness resonance frequency, (b) near the sample center at the thickness resonance frequency of $f_s = 1021796.9$ Hz (NCE51 material, 30 mm diameter, 2 mm thickness).

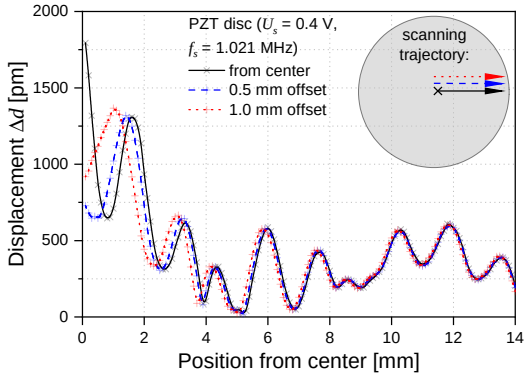


Fig. B.13: Scanning of the PZT disc thickness displacement profile in near lines along the radial axis (NCE51 material, 30 mm diameter, 2 mm thickness).

mode.

Lastly, an example of the thickness displacement profile of the PZT disc near its thickness resonant frequency was measured in its axis and parallel lines with a given offset, as shown in Fig. B.13. This measurement, among other things, demonstrates an excellent repeatability of the results, as the displayed profiles are in close match further from the sample center, even if they are measured in different points, i.e., with a different local reflectivity.